Vulnerability of Rammed Earth structures with respect to hydric conditions

Taini Chitimbo

UNIVERSITÉ SAVOIE MONT BLANC

THÈSE

Pour obtenir le grade de

DOCTEUR DE L'UNIVERSITÉ SAVOIE MONT BLANC

Spécialité : Génie civil et Sciences de l'Habitat

Arrêté ministériel : 25 Mai 2016

Présentée par

Taini CHITIMBO

Thèse dirigée par **Olivier PLE** et
codirigée par **Noémie PRIME**

préparée au sein du **Laboratoire LOCIE**
dans **l'École Doctorale SIE**

Vulnerability of rammed earth structures with respect to hydric conditions

Vulnérabilité des structures en pisé vis-à-vis des conditions hydriques

Thèse soutenue publiquement le **06 Juin 2023**,

devant le jury composé de :

M. Arnaud PERROT
Professeur des universités, Université Bretagne Sud, (Examinateur)
Mme. Céline PERLOT-BASCOULÈS
Professeure des universités, Université de Pau et des Pays de l'Adour, (Rapporteure)
M. Guillaume HABERT
Professeur des universités, ETH Zurich, (Rapporteur)
M. Christopher BECKETT
Assistant Professor, University of Edinburgh, (Examinateur)
M. André REVIL
Directeur de recherche, USMB (Examinateur)
M. Olivier PLE
Professeur des universités, USMB (Directeur de thèse)
Mme. Noémie PRIME
Maîtresse de conférences, USMB (Co-directrice de thèse)

Acknowledgments

This PhD thesis is the result of three years of work whereby I have been accompanied and supported by many people. I take this opportunity for me to thank all the people I met who accompanied, supported and advised me from near or far during this work.

First and foremost, I would like to express my deepest gratitude to my supervisors Prof. Olivier PLE and Dr. Noémie PRIME for giving me this PhD opportunity. I acknowledge their guidance and encouragement throughout the entire period of my work. They have always been finding the time to help me, even through difficult moments. I thank Noémie for her continuous support, every single time I stepped into her office, she took the time to listen to my problems, and I never came out without a solution. She always provided the most perceptive ideas and an enthusiastic way to convey them. I thank Olivier for always providing resources to facilitate my work and also for guiding me through the valorisation of my work, I greatly appreciate it.

I would also like to thank Feras, who was a Post-Doctorate in the same project and became a close friend. We have shared a lot of moments in working during and after the COVID period, to ensure experiments are running for this thesis. I would like to thank Dania, my internee during this project, who also spent a lot of time working with me, her contribution to this work is significant.

Special thanks to our team (Noémie, Olivier, Feras, Dania and me) for all the experimental work that we have done to build walls. I also appreciate the friends who came to help (Julie, Alessia and Arnat), the work was not easy, but through teamwork, we have made it possible.

This thesis was an adventure in social life as well, meeting new people and making new friends at LOCIE, who have supported me during this work. So, I thought of Prince, Julie, Alessia, Arnat, Parul, Yago, Marcos, Guillaume and a lot more that I might forget to put your name, thank you for your contribution to my professional and personal development.

I would also like to thank all the colleagues from the LOCIE laboratory, whom I have been able to meet during these three years of work, having helped me on certain experimental points and with whom I was able to exchange. Not forgetting our social life in the Lab, including pause croissant on Fridays, Football on weekends, and Velo Challenge during Spring. All these made the working environment better.

Finally, my great gratitude is to my family, my parents Mr. & Mrs CHITIMBO, and my brothers and sisters. To Brother Manyanda, who always motivated me to keep moving, especially in difficult situations. I would like to express my deep gratitude for his immense support. I am also grateful to Rhoda, who was always there in difficult and good moments, with a helping hand and an open heart, her support was always there even from afar.

Abstract

Rammed earth is one of the numerous earth building technics. In these days, earth presents a growing interest as a construction material due to its enormous ecological benefits. Despite of them, rammed earth remains sensitive to hydric conditions which affect its mechanical performances. In this context, this thesis deals with the effect of hydric conditions on the mechanical properties of rammed earth structures.

For this, a series of experimental campaigns, at three scales (from material scale to large scales close to a real building), have been undertaken to understand the link between mechanical behaviour and hydric solicitation. The hydric state was represented by a state variable known as suction adopted in this work to facilitate the understanding of water on mechanical behaviour via coupled hydro-mechanical approaches.

The experimental approach aimed to reproduce what happens in real rammed earth building interacting with varying ambient conditions, for example, initial drying after construction and capillary rise of water through the wall. Experimental results show the evolution of mechanical performance with respect to time and hydric state during the initial drying. An increase of both compressive strength and modulus by a factor of 12 from the initial moist state to the dry state was observed, with a rapid increase in the 4 first weeks.

New observations were made on the viscous behaviour (such as creep effect) of rammed earth and their dependency on the hydric state. On the other hand, capillary rise experiments show a decrease in mechanical resistance of 95%. When samples dried after capillarity, they showed restoration in compressive strength by 85% of the original dried samples. In consequence, a loss of strength capacity is observed under the capillary rise cycle. This contributes to explain many pathologies encountered on rammed earth structures, but gives argument for water diagnostic in the field and pathologies solving

Finally, a comparison of results at all scales was done, the parameters required for modelling hydro-mechanical behaviour were then presented at each scale which can contribute to go further in future hydro-mechanical numerical models.

Résumé

Le Pisé est l'une des nombreuses techniques de construction en terre. De nos jours, la terre présente un intérêt croissant en tant que matériau de construction en raison de ses énormes avantages écologiques. Malgré cela, le pisé reste sensible aux conditions hydriques qui affectent ses performances mécaniques.

Dans ce contexte, cette thèse traite de l'effet des conditions hydriques sur les propriétés mécaniques des structures en pisé. Pour cela, une série de campagnes expérimentales, à trois échelles (de l'échelle matérielle aux grandes échelles proches d'un bâtiment réel), a été entreprise pour comprendre le lien entre le comportement mécanique et la sollicitation hydrique. L'état hydrique a été représenté par une variable d'état appelée succion adoptée dans ce travail pour faciliter la compréhension de l'eau sur le comportement mécanique via des approches couplées hydro-mécaniques.

L'approche expérimentale visait à reproduire ce qui se passe dans un bâtiment en pisé réel interagissant avec des conditions ambiantes variables, par exemple, le séchage initial après la construction et la remontée capillaire de l'eau à travers le mur. Les résultats expérimentaux montrent l'évolution des performances mécaniques en fonction du temps et de l'état hydrique pendant le séchage initial. Une augmentation de la résistance à la compression et du module par un facteur de 12 entre l'état humide initial et l'état sec a été observée, avec une augmentation rapide au cours des 4 premières semaines.

De nouvelles observations ont été faites sur le comportement visqueux (tel que l'effet de fluage) de la terre battue et leur dépendance à l'état hydrique. D'autre part, les expériences de remontée capillaire montrent une diminution de la résistance mécanique de 95%. Lorsque les échantillons ont séché après les remontées capillaires, ils ont montré une restauration de la résistance à la compression de 85% par rapport aux échantillons séchés d'origine. Par conséquent, une perte de capacité de résistance est observée lors du cycle de remontée capillaire. Ceci contribue à expliquer de nombreuses pathologies rencontrées sur les structures en pisé, mais donne des arguments pour le diagnostic de l'eau sur le terrain et la résolution des pathologies.

Enfin, une comparaison des résultats à toutes les échelles a été effectuée, les paramètres requis pour la modélisation du comportement hydromécanique ont été présentés à chaque échelle, ce qui peut contribuer à approfondir les futurs modèles numériques hydromécaniques.

Contents

List of Figures

List of Tables

Chapter 1

1. Introduction

1.1. Environmental impacts of the building sector

The building sector plays an important role in contributing to CO_2 emissions. In France particularly, the building sector is the leading consumer of energy representing 44% of the total energy consumed and is responsible for 23% of CO_2 emissions according to ADEME [1]. Globally, the building sector accounts for approximately 39% of total CO_2 emissions in 2018 according to the Global Alliance for Buildings and Construction report [2].

The emission of CO_2 in the building sector can be divided into two sources; First, energy used in the operation of the building (for heating, cooling, and powering the buildings) represent about 28% of all global CO_2 emission. Secondly, the resources consumed during the construction of buildings (for material and transportation) contribute to around 11% of all global CO_2 emissions [3].

As the world's population approaches 10 billion, the global building demand is expected to double in size. Without radical changes to the way the building sector operates, the amount of resources consumed is expected to double thus significantly increasing CO_2 emissions and climate change. Decarbonising the building sector is therefore crucial in an approach to mitigate the worst effects of climate change.

One way toward decarbonising the building sector is to reduce operational energy by adopting energy-efficient buildings. To enforce the construction of energy-efficient buildings, various thermal regulations and energy performance requirements for new buildings have been implemented to limit the CO_2 related to the operation of the building.

For example, France has set an objective of reducing 28% of the energy consumed by residential-tertiary buildings by 2030 as compared to 2010, with the ambitious aim to achieve carbon neutrality by 2050 [4].

The target will ensure proper implementation of the 2012 Thermal Regulations (RT 2012) [1], which made it possible to set a target for reducing energy consumption for new buildings built after 2012 (by a factor of 2 to 4), until its replacement by new Environmental Regulation (RE 2020) [5]. Globally, in 2018 the World Green Building Council launched the Net Zero Carbon Buildings Commitment to inspire and promote advanced climate leadership focused on achieving net zero operational CO_2 of buildings [3].

The emission from operational buildings was first considered because of their predominance, but the emissions directly linked to the construction of the buildings must also be considered. Therefore, another way toward decarbonising the building sector is to reduce emissions during construction (including construction materials and transportation). Currently, the main building material used is cement concrete, and the production of cement involves heating limestone to high temperatures (about 1450°C). This process releases significant amounts of CO_2 into the atmosphere, representing 5% to 10% of global CO_2 emissions making it the second-largest industrial emitter after the steel industry [6], [7]. In addition, transporting raw materials required to cement concrete generates CO_2 emissions due to the fuel consumed by the vehicles used for transportation. These emissions related to construction can be reduced by adopting more ecological and locally available building materials such as earthen materials.

1.2. Earth buildings as an alternative (Why earth buildings?)

Earth building is the technique of construction using raw earth. It is low technology, and easy to work with using simple tools to construct structural walls. Thus, raw earth is considered to be one of the most important construction materials in the history of mankind. It has been successfully used around the world for over 11,000 years [8].

Today, raw earth remains an important building material. Nearly one-third of the world's population lives in buildings made of raw earth [9]. Earth is regaining interest as a building material, not only in developing countries, where due to its low cost, but also in modern societies where, for reasons of sustainability, it has an important advantage as opposed to conventional building materials [10]. The benefits of earth buildings extend from environmentally friendly as well as to the construction industry as summarized below:

- Low embodied energy

The total energy that is expended during the manufacturing of a building is known as embodied energy. This includes mining, manufacturing, and transporting construction materials. These processes consume high energy and result in about 11% of total Green House Gases emissions [11]. Earthen buildings are known to have low embodied energy since they don't require cement for construction, and the availability of earthen material in the nearby local area makes the transportation cost relatively low. To put it in perspective, it is said that earthen materials require about 1% of the energy needed for the construction and transportation of cement-based materials [12].

- Reduced operational energy

Earth buildings can control their indoor environments through the buffering of temperature and relative humidity. These buildings have a high thermal mass and interesting hygro-thermal properties [12] that contributes to the buffering of interior temperature and relative humidity variations. During the hottest hours of the day, earthen structures have a greater ability to store heat and return it during the cold hours of the day. This allows a thermal phase shift between day and night conditions and is responsible for better thermal regulation. More on this can be found in [13]. On the other hand, when the ambient RH is high, these walls absorb moisture due to the presence of clay particles, and the absorbed moisture is released again when the surrounding environment becomes drier. Thus, it helps in maintaining hygroscopic conditions and hence reduces the energy needed for air conditioning in the building [14]. Regulation of relative humidity also increases internal comfort. The quality of the indoor air (relative humidity (RH) and temperature) is very essential for the building's inhabitants because it can significantly influence comfort and health.

- Recyclability

The demolition of buildings contributes to a significant amount of waste. In France for example, the waste from the building sector was around 42.7 million tons, representing nearly 70% of the non-hazardous waste produced according to ADEME in 2017 [15]. Recycling and treatment of this waste require a high amount of energy. Globally, it is estimated that about 35% of the quantities of construction and demolition waste produced are directed to landfills, without any further treatment [16]. Unlike conventional construction materials, unstabilized earth can be easily recycled or safely released into the environment without any treatment. In consequence, a reduction of energy required for recycling earth materials contributes to the overall low Greenhouse gas emissions.

- Acoustic insulation

Earth buildings represent a better improvement in sound reduction due to their high density (around 2000 kg.m3) and big thicknesses (b > 25 cm) [12], [17]. In addition, the porous nature of RE results in excellent sound reverberation characteristics, meaning that it does not generate harsh echoes [18].

- Strength and durability

Earth buildings are known to have relatively low mechanical resistance as compared to conventional construction materials, for instance, concrete, with characteristic compression resistance which reaches more than 20 MPa. However, in most cases, the strength of these buildings is enough for a normal house with few stories. For example, rammed earth building has a characteristic compressive strength of 1 to 2 MPa according to the New Zealand code [19], and Mexico code [20]. it which is sufficient for constructing 2 to 3 storey buildings. A vivid example of a two-story modern rammed earth building can be found in Confluence in Lyon (Figure 1.5). Rammed earth building also appears to have a historically relatively good durability [21], and a satisfactory performance on "very low " to "moderate" seismicity zones [22].

1.3. Rammed earth and other types of earth buildings

There are several types of earth constructions exist depending on the compaction method and soil water proportions. These most common techniques are rammed earth (RE), wattle and daub, cob, adobe, and compressed earth bricks (CEB). Other techniques include; light straw, earthbags, earth bricks, earthen floors, and earth plasters and finishes. The distinction between these techniques according to the classification proposed by Hamard et al. 2016 [23] is shown in Figure 1.1. This classification is based on the manufacturing water content (W_m) and the implementation technique. Based on manufacturing water content, there is a dry method where W_m is less than or near the optimum water content (W_{OP}) and a wet method in which W_m is in between the liquid and plastic limit. Based on the mode of implementation includes masonry units, monolithic walls or infillings.

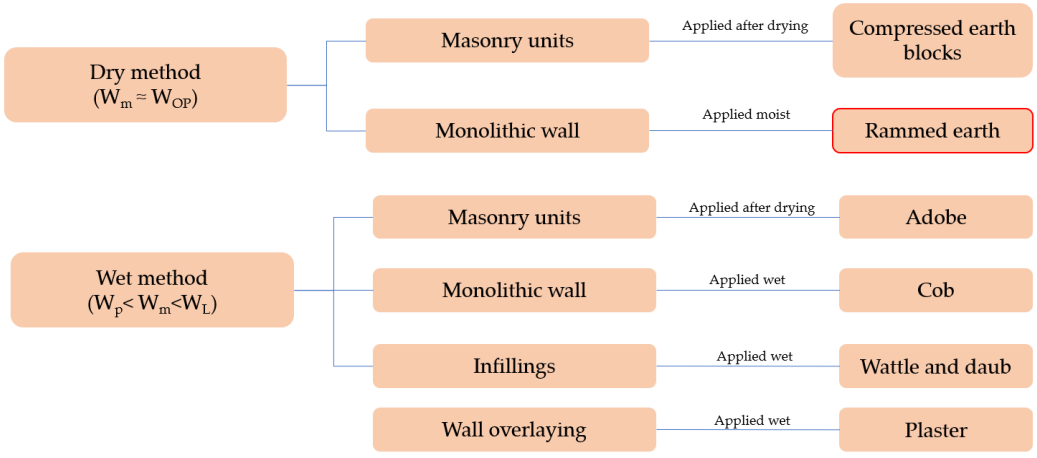

Figure 1.1: The classification of the earth construction process by Hamard et al. (2016) [23]. W_m is the manufacturing water content, W_{OP} is optimum water content, W_P and W_l are the plastic and liquid limit of soil.

a. Wattle and daub

Wattle and daub is the oldest earth construction technique that was used for over 6000 years [8]. This is a technique that consists of a timber frame that forms a load-bearing structure of the building, leaving the open area to be covered and filled by earth material usually made of wet clayey earth, and sometimes mixed with animal dung. Figure 1.2a shows the construction of the wattle and daub wall. The timber frame is known as wattle and the filling material is known as Daub or mud. Depending on the climatic conditions and if well maintained, a wattle and daub panel should last for a long time.

b. Cob

When the cob technique emerged around the 14th century [24], it tended to replace wattle and daub [8]. In this technique, wet clayey earth materials are malaxed, often mixed with organic fibres (e.g. straw, reed) to form a plastic earth mix, a lump of this earth mix is then shaped like balls using hands or towel and is placed directly upon each other to form a structure (see Figure 1.2b). The Cob technique is relatively simple since it requires very few tools and no formwork or mould needed to create a structure. However, the cob technique is time-consuming but offers the flexibility of producing walls of variable shapes.

c. Adobe

When the adobe technique emerged, it largely replaced cob [8], [25]. Adobe is an earth construction technique in which small bricks are made from a mixture of earth with water. The bricks are moulded by hand in a wooden frame and left to air dry under the sun (see Figure 1.2c). The earth typically contains sand, silt, clay, and organic material such as straw. Straw is added to reinforce the brick together and prevent cracking due to uneven shrinkage rate through the brick. Made in a wet state, it corresponds to cob, but with prefabricated units.

d. Compressed earth blocks (CEBs)

From a historical point of view, CEB is considered to be a recent technique that is an improved form of the Adobe technique. It emerged in the 18th century. CEBs are formed by compressing a slightly moistened earth in the desired mould using mechanical or hydraulic presses (see Figure 1.2d). The pressed blocks have higher density and more mechanical resistance than Adobe bricks (compression until a few MPa). Blocks are then assembled as masonry structures to build a load-bearing or freestanding wall.

Figure 1.2: (a) Wattle and daub [26], (b) Construction of a cob wall by stacking mud balls [10], (c)Adobe (source: Archaeology Southwest), (d)Compressed earth blocks [27].

e. Rammed Earth buildings

Rammed earth (RE) structures are built by erecting walls by compacting humid earth layer by layer in between formwork. Figure 1.3 illustrates the fabrication steps of rammed earth. The earth is first mixed with water up to approximately the optimum gravimetric water content, usually ranging from 4% to 12% [28]. The mixture of moist earth is then poured about 15 – 20 cm into a well-braced formwork and compacted into layers of approximately 7.5-15 cm [21], [29], [30]. Compaction is achieved either manually, using a tamper, or mechanically using a pneumatic rammer. New formworks are added above when one is filled, until achieving the required height, then the formworks can be removed. The thickness of the rammed earth wall is between 40 and 80 cm.

Originally, the ramming was done manually by tamping the soil with a long ramming pole, and formwork is usually made of wood, but in modern construction, metallic formwork and pneumatic-powered rammers are employed [31]. This allows higher compaction energy to be applied, thus achieving dense wall structures. Figure 1. shows an example of a traditional rammed earth building. Modern RE structures are making their way into the building sector, thanks to advancements in construction technology. In Lyon, France, for example, RE was recently used to construct a multi-story office structure (Figure 1.5).

Figure 1.3: Manufacturing process of rammed earth; (a) control the water content, (b) fill into the formwork with earth, (c) compact the respective layer, and (d) remove the formwork after all layers were filled in and compacted [32].

Figure 1.4: An example of a traditional rammed earth building located Marsac-en-Livradois, Puy-de-Dôme, France

Figure 1.5: Modern architectural rammed earth building Confluence in Lyon (source: Clement Vergely architects/Fabrice Fouillet).

There are two different types of rammed earth: unstabilized and stabilized rammed earth. When the clay is the only binder agent, and no hydraulic binder is added to the raw earth, it is termed unstabilized rammed earth or simply rammed earth. When additional binding agents such as cement or lime are added to the soil mix, it is termed stabilized rammed earth. Stabilization increases the mechanical strength of rammed earth but comes at a cost of losing most of the environmental benefits, as seen previously. Among all the different types of earth construction techniques discussed, this thesis work will focus only on unstabilized rammed earth and will be labelled as rammed earth or 'RE' in the present document.

1.4. Problem (Challenges hindering the adaptation of earth building)

Despite the numerous environmental advantages, RE buildings still face some drawbacks which hinder their widespread use. One of the biggest limitations is its sensitivity to water which highly affects the mechanical performance of these buildings. RE is made of raw earth which is a non-cementitious porous material, which means that water or moisture can easily penetrate inside it and modify the mechanical equilibrium between grains. Once constructed, RE dries from the initial water content and consequently gains mechanical capacity. In dry climates, RE structures reach high strength. However, in a wet climate, RE structures are exposed to highly fluctuating humidity during the lifespan of the building, which affects the mechanical performance. Also, moisture ingress through the capillary rise, rainfall, and other weathering effects such as freeze-thaw is responsible for most of the humid pathologies which often lead to building deterioration. Despite protection such as overhanging roofs and raised foundations to counteract rainfall and capillary rise, in extreme cases like a flood or possible defects on foundations, water ingress can cause serious structural damage (Figure 1.7), which can potentially lead to building collapse. Therefore, it is absolutely important to address the vulnerability of rammed earth structures with respect to varying hydric conditions.

Figure 1.6: RE structural collapse due to water accumulation at the wall base, Lyon, France [33].

1.5. Research focus and objectives

This thesis is a part of the VBATCH project funded by ANR (Agence Nationale de la Recherche). The main objective of the thesis is to study the influence of water on the mechanical behaviour of RE structures. The study is done through a series of experiments on RE samples, large enough and structured in layers such as they can be considered representative of RE structures inside a real building. The aim is to both, on one hand, apply hydric solicitation and monitor the humidity content and, on other hand, to test mechanical performance. This will help to better understand the coupled hydro-mechanical behaviour of RE submitted to normal or exceptional solicitation during its life, and besides, to further deepen the knowledge concerning the interaction between water and grains in a porous material, in particular in presence of clay.

As said, the experiments aim to test large-scale samples, close to the scale of a real building. In the aim to reproduce realistic conditions of moisture exposition, two scenarios namely drying and capillary rise are considered. This leads us to the specific objectives of the present work:

- Drying experiments – The goal is to study how the mechanical behaviour evolves during the initial drying after the manufacture of RE until reaches equilibrium with the ambient conditions. The hydric state of the sample is monitored and the mechanical test is performed at regular intervals.
- Capillary rise experiments – The goal is to design and perform an experiment for capillary rise on the RE column and wall. This experiment aims at answering these questions: How is the mechanical resistance evolve during capillary rise? What is the kinetic of moisture rise? Is the mechanical capacity restored after drying from capillary rise?

1.6. Thesis layout

This thesis is divided into five chapters as explained below:

Chapter 1 (Introduction): The introduction provides a brief overview of various earthen construction techniques. Among these techniques, a particular focus is made on the RE technique, its advantages, and its limitations. Finally, the main objectives of this thesis are outlined.

Chapter 2 (Literature review): This chapter presents the reviews of existing knowledge on the mechanical behaviours of URE and factors affecting them, notably the hydric state. A detailed review of previous experimental and numerical studies on the hydromechanical coupling of URE is present. Subsequently, gaps were found in the literature which leads this thesis work.

Chapter 3 (Soil characterization, Sample preparation and instrumentation): This chapter aims at identifying the type of earth used, its granulometry, mineralogical composition, and water retention properties. Two methods for proctor tests are presented to determine the sample manufacturing water content. Furthermore, the manufacturing process for samples at three scales (material scale, columns scale, and wall scale) are described. The compaction method at each scale is presented. In additional, different types of instrumentation for monitoring the hydric state inside the samples are detailed.

Chapter 4 (Influence of drying on mechanical behaviour): In this chapter, instrumented samples (columns and walls) are dried under specific boundary conditions just after being manufactured. The hydric state and mechanical behaviour are followed at regular intervals as the sample dries. Results of mechanical behaviour are discussed and linked with their respective hydric state. New findings on the viscous behaviour of rammed earth are also presented.

Chapter 5 (Influence of capillary rise on mechanical behaviour): Another kind of experiment known as the capillary rise is presented. This chapter answers the following questions; how is the evolution of mechanical resistance during the capillary rise? Is the mechanical resistance restored upon re-drying?

Finally, the general conclusion and perspectives present the synthesis of all the experiments at different scales that can be used for numerical modelling, then the contribution of the thesis and proposal for future research work.

Chapter 2

2. Literature review on coupled hydro-mechanical behaviour of RE

The objective of this chapter is to present the review of existing knowledge on the mechanical behaviour of RE and the factors affecting them, notably the hydric state. This chapter will be divided into three main categories: mechanical parameters of RE, factors affecting the RE mechanical behaviour, and modelling of the mechanical behaviour of RE. A detailed review of previous experimental and numerical studies on the hydromechanical coupling of RE is present. Subsequently, gaps were found in the literature which lead to this thesis work.

Chapter outlines

2.1 Mechanical parameters to characterise RE

In order to characterise the mechanical behaviour of RE, various parameters are used such as; compressive strength, Young's modulus, shear strength and tensile strength.

2.1.1 Compressive strength, (fc)

Compressive strength refers to the amount of stress that a material can withstand before it begins to fail. It is the most widely used parameter for the strength of earth building since it needs to resist compressive loading under its own weight and holds the weight of the elements above it. Compressive strength is denoted as fc or UCS (Unconfined Compressive Strength). For RE, there are a lot of works that investigate this parameter. For example, according to New Zealand standards [19] for RE to be

used as a construction material, it should have a minimum characteristic compressive strength of 0.5 MPa, a value that is close to Australian standards [34] that recommends a design value between 0.4-0.6 MPa. However, The Zimbabwe Standard Code of Practice for RE Structures [35] requires at least 1.5 MPa to 2 MPa compressive strength for one-storey to two-storey buildings. Table 2.1 summarises the characteristics of UCS from different standards. It is observed that the minimum UCS required for RE range from 0.4 MPa to a relatively high value of 2.0 MPa for a storey building. The recommended values of UCS by different standards can be achieved by the RE structure according to their fc, found experimentally. Ávila et al. (2020) [28] reviewed the UCS values obtained experimentally from different studies, they observed that the compressive strength of RE range from 1 MPa to 2.5 MPa, excluding some exceptions (Table 2.2). To conclude, compressive strength is the main parameter used to design RE, standards recommend a minimum of 0.4 MPa depending on loading conditions. RE has a compressive strength of up to 2.5 MPa which meets the recommended values.

Table 2.1: Minimum characteristic unconfined compressive Strength recommended by standards.

Minimum UCS required (MPa)	Reference
0.7	(Middleton, 1992) [36]
1 -2	New Mexico Code, 2001 [37]
0.4 - 0.6	Standards Australia, 2002 [34]
0.5	NZS 4298:1998, 1998 [19]
1.5 – 2 (1 or 2 storeys)	SAZS 724:2001, (2001) [35]

Table 2.2**:** Compressive strength (*fc*), Young's modulus (*E*) of RE from various authors.

Specimen size	ρd (kg/m^3)	*fc* (MPa)	*E* (MPa)	References
10 x10 x 10 cm^3	2020-2160	0.75-1.5	-	Hall et al. 2004 [38]
15 x 15 x 15 cm^3	1970-2110	1.8-2	-	Lilley et al. 1995 [39]
Φ= 10 cm, H = 20 cm	1850	2.46	205	Maniatidis et al. 2007 [40]
Φ = 30 cm, H = 60 cm	1850	1.9	160	Maniatidis et al. 2008 [41]
Φ = 16 cm, H = 30 cm	1920	1.7-2.1	460-540	Bui et al. 2014 [42]
30 x 30 x 60 cm^3	1760-2027	0.62-0.97	60-70	Maniatidis et al. 2008 [41]
25 x 15 x 13 cm^3	-	2.55	131	Piattoni et al. 2011 [43]

2.1.2 Young's modulus, (E)

Young's modulus, denoted as E, is important because it gives us an indication of the extent of deformation that will occur based on how much stress is applied. For RE, the recommended design value of E ranges between 150–500 MPa [11], [19], [44], [45].

However, the values of Young's modulus reported in the literature have a high dispersion, which is related to several factors: the heterogeneity of the specimens and the method of measurement (by the displacement sensors [46] or by Digital image technique [22]), the method of calculation (tangent modulus or apparent modulus). Mollion, (2009) [46] used a strain gauge to measure deformation in the middle third of the RE specimen. Bui et al. (2014) [42] also used a strain gauge, they suggested that the young modulus of RE should be determined between 0 and 20% of the maximum stress. Other authors measure Young's modulus using different techniques such as Digital Image Correlation [47] to determine strain during loading test, or a direct measure of the resonance frequencies of specimens [48]. From all these studies, Young's modulus for RE appears to be between 1 and 5.5 GPa which is way higher than the recommended values that lie below 1 GPa. Since RE behave non-linearly with plastic deformation under loading, its modulus of elasticity is approximated by using the secant modulus or apparent Young's Modulus, denoted as E_a in this work.

2.1.3 Tensile strength and Shear strength

Like any type of earth construction material, RE has a weak strength under tension and shear solicitation. This means that RE should not be used for horizontal structure as a lintel or supporting floor, which undergo traction in their bottom part. Despite being weak, tensile strength and shear strength are still important for construction in RE to ensure protection from natural risks such as earthquakes. Although the tensile strength is an important parameter in designing RE, particularly in seismic conditions [49], it is often neglected and rarely studied. Few authors that studied tensile strength have concluded that the tensile strength of RE can be considered equal to approximately 10% of its compressive strength [49], [50]. Based on this criterion and the previous values given for fc, the values of tensile strength range between 0.1MPa and 0.35 MPa.

The shear strength of RE is also very limited, the Australian standards [34] consider the design value of shear strength as zero and others use very low values as 0.035 MPa from the New Zealand code [19]. Only a few experimental studies exist on shear strength. For example, Silva et al. (2014) [51] and Miccoli et al. 2015 [49] conducted a diagonal compression test on RE wallettes to determine the shear strength (see Figure 2.1). Despite this fact, the few studies that have assessed the shear strength of RE have obtained results that, although small, are well above the ones recommended by the standards. These values are between 0.15 MPa and 0.85 MPa [49], [50], [52].

The shear strength is controlled by parameters such as friction angle(φ) and cohesion(c), with the frame of soil mechanics. Chauhan et al. (2019) [53] performed direct shear strength on a prismatic RE sample (60 mm × 60 mm × 30 mm), they found the apparent frictional angle which varies from 43° to 63° and cohesion varies from 0.341 MPa to 0.835 MPa depending on the hydric conditions. El Nabouch et al., (2018) [54] performed a direct shear test on a multi-layered RE sample. The sample was dried in ambient conditions. They found that the apparent cohesion and apparent friction angle obtained at the interface of the layer (c = 24.7 kPa and φ = 32.9°) was lower than in the middle of the layer (c = 30 kPa and φ = 35.3°). This suggests that RE have relatively lower shear strength at the interface than in the middle of the layer.

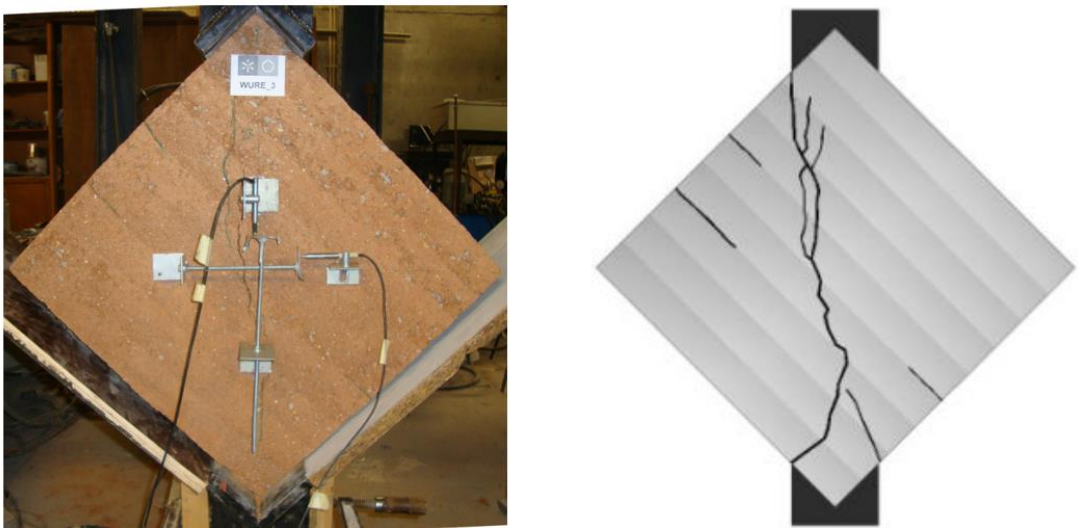

Figure 2.1: Diagonal compression test on RE wallets, on the right is the illustration of crack patterns at failure [51].

2.1.4 Poisson ratio

Poisson's ratio is a measure of the deformation (expansion or contraction) of a material in directions perpendicular to the specific direction of loading. Poisson's ratio provides insights into the behaviour of materials under different loading conditions. For example, a material with a low Poisson's ratio (close to -1 or 0) is generally considered incompressible and does not change much in volume when subjected to external loads. In contrast, a material with a high Poisson's ratio (close to 0.5) is relatively compressible and tends to deform more in the lateral direction when subjected to axial loads. For RE, it is obtained via a uniaxial compression test by measuring vertical and horizontal displacement. Fewer researches about RE Poisson's ratio have been led. Concerned studies show values from 0.22 to 0.3, which is the range for most typical granular material [22], [32], [42]. Champiré et al., (2016) [47] reported a significantly lower value of Poisson's ratio ranging from 0.15 to 0.2. This inconsistency could result due to various factors such as methods for determining strain and the water content of samples at the time of the test.

2.2 Factors affecting the mechanical behaviour of RE

2.2.1 Granulometry

Granulometry analysis investigates the composition of different classes of grains in the soil. Notably, the proportion of fines (clay and silt), sand and gravel can be used for having an idea of the suitability of earth materials for construction. Table 2.3 shows different recommendations for earth composition given by previous studies. They can be summarized as follows: clay up to 20%, silt between 10 and 30%, and sand and gravel between 45 and 75%.

Houben and Guillaud (1994) [55] provided a recommendation for grading range in a granulometric curve, which includes lower and upper limit curves. A recommendation by Houben and Guillaud (1994) [55] was later challenged by Mathew Hall (2004) [38]. In their study, Hall et al., (2004) [38] prepared RE cubes using ten different soil mixes, each mix having a granulometry that agrees with the limits of Houben & Guillaud (1994) [55]. After a series of UCS, Mathew Hall (2003) [38] found that only four of the 10 soil types had suitable compressive strengths to satisfy the minimum requirement of 1.3 MPa outlined in the New Zealand standard [19]. Champiré et al., (2016) [47] has later shown that there

existing RE buildings that are made of earth material whose granulometry was not in agreement with the recommendation of Houben & Guillaud (1994) [55], it was suggested that granulometry alone is not sufficient criteria for selecting earth materials. Therefore, it can be concluded that granulometry can only be used as guidance and that there is no full relationship between granulometry the mechanical capacity.

However, it seems that other factors from granulometric repartition impact compressive strength. Clay content and the binder-to-aggregate ratio of the earth could perhaps be controlling factors for the mechanic capacity of RE. Binder represents the part of clay particles and aggregates represent the part of the sand and gravel.

For example; Aubert et al. (2021) found that the earth material for RE generally contains more than 60% of grains with a diameter greater than 0.063 mm and less than 20% of clay, representing a value of the fine-aggregate ratio of 0.33. The value of the binder-to-aggregate ratio can range from 0.1 to 0.4 from the existing studies in Table 2.3. Further studies are required to determine the relationship between the binder/aggregate ratio to the mechanical behaviour of RE earth structure.

Clay content has been proven to have a particular influence on compressive strength. Lilley et al. (1995) [39] conducted compressive strength tests on cubes with soil mixes with different percentages of clay content. They studied the strength evolution upon drying. Interestingly, for cubes with higher clay content, a reduction of strength was reported from one week to one month of drying, suggesting that shrinkage cracks developed upon further drying weaken the samples. Helson et al. (2017) [56] found that the unconfined compressive strength increases with clay content until reaches an optimum percentage (around 15%) and then decreases which conforming the hypothesis of Lilley et al. (1995) [39].

Table 2.3**:** Recommendations concerning the particle size distribution of soils (in mass proportion) for rammed earth construction (adapted from Gomes et al.(2014) [57]

Reference	Clay (%)	Silt (%)	Sand + gravel (%)
Keable et al. (1996) [58]	5-15	15-30	50-70
Norton et al. (1997) [59]	10-25	15-30	45-75
SAZS 724, (2001) [35]	5-15	15-30	50-70
Keefe et al. (2005) [60]	7-15	10-18	75
Van Gorp et al. (2018)	12	13	75
Walker et al. (2005) [44]	5-20	10-30	45-80
Houben and Guillaud, (2006) [55]	0-20	10-30	45-75

To conclude, the amount of clay in granulometry has been proven to be a critical factor in the mechanical properties of earth structures. Too little quantity of clay results in less binder hence low strength. Too high results in possible shrinkage hence weakening the structure. An optimum clay content seems to be necessary. Further studies show, not only the quantity of clay that impacts the strength but also the nature of clay itself also known as clay mineralogy, which is explained in the next section.

2.2.2 Clay mineralogy

Different types of clays exist. They have variable mineralogic structure and thus variable activity, this last affecting how much they swell when absorbing water and shrink when dried up. Here are classical types of clay: Illite, Montmorillonite, Chlorite, and Kaolinite. In practice, the nature of clays present in a particular earth is characterized using parameters such as the activity index, and the Methylene Blue Value.

Activity value is used as an index for identifying the swelling potential of clay soils. It is defined as the ratio of plasticity index to and the percentage of clay content. Skempton (1953) [61] suggested three classes of clays according to activity as presented in Table 2.4. The nature of clay can also be determined by the Methylene Blue Value (MBV) which is an indicator of the percentage of the swell when wet. The MBV is determined in the laboratory, where a fine soil sample is mixed with methylene blue solution which is more and more concentrated until reaching the saturation of the surface of the fine grains. The saturated amount of methylene blue can be linked to the Clay activity (more details about this experiment will be explained in the next chapter).

Table 2.4**:** Classes of clays based on the activity index

Activity index (AI)	**Classes**	**Example of clay mineral**
<0.75	Inactive	Kaolinite
0.75-1.25	Normal	Illite
>1.25	Active	Montmorillonite

2.2.3 Dry density (ρ_d)

Dry density is defined as the density of soil samples in a completely dry state. Existing studies show that the dry density of RE varies between 1700 kg/m^3 to 2200 kg/m^3 (Table 2.5). This wide range of dry density is mainly due to compositions of soil, water content during manufacture, and compaction method [45]. Dry density plays a significant role in the mechanical behaviour of RE structures. The compressive strength of compressed earth blocks is strongly related to dry density achieved in compaction. The relationship between dry density and compressive strength of RE can be found in the work of Olivier and Mesbah (1986) [62] and has been consistently proven experimentally since then by Houben, 1994, Morel et al. (2007) [55], Kouakou et al. (2009) [63] and Raavi et al. (2020) [64].

Olivier and Mesbah (1986) [62] used static compaction at different pressure levels resulting in different densities. RE samples were cured at constant ambient conditions (RH = 60% and temperature of 27°C), and then tested under unconfined compression until failure. Results showed that compressive strength increases with dry density. Similar observations were made by Morel et al. (2007) [65] who used compressed earth blocks and Kouakou et al. (2009) [63] who used Adobe blocks to perform the study. A closer analysis of different studies in the literature found that compressive strength evolves almost exponentially with the dry density of the material [66]–[69]. For example, Perrot et al. (2018) [69] found an exponential increase in compressive strength with the dry density of raw earth-based mortar samples compacted with different methods (Figure 2.2). Despite the differences in the compaction methods and the type of earth used in the literature, the relationship between strength and dry density seems to remain the same for each study. (see Figure 2.2).

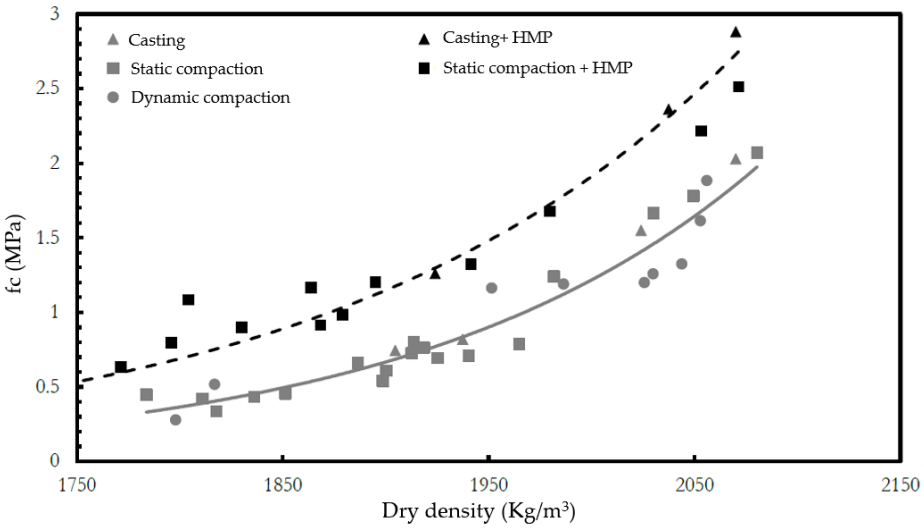

Figure 2.2: Evolution of the mechanical resistance of raw earth samples as a function of the dry density, for different modes of compaction with and without Na-HMP dispersant [69].

Therefore, to attain the maximum strength possible of RE structure, it is important to have the maximum dry density. The maximum dry density can be determined by using the proctor test which highlights the relationship between dry density and water content and allows us to determine the maximum dry density attainable for optimum water content.

Although it would be necessary to estimate the more specifically possible optimum water content and the resulting dry density for earth compaction, there are currently no standards of proctor tests specifically for this application. Studies in the literature show various compaction methods for the proctor test. Some adapt the standards proctor test for soil [70], while others suggest that the modified proctor test provides a compactions effort closer to the one in the site [71]. Others have used proctor tests such as light proctors and specific proctors, and some used site compaction equipment like a Vibrating hammer and Pneumatic rammer for proctor tests. The latter could provide a good approach for the maximum dry density estimation since it uses the same method as in the site.

Table 2.5: Dry density and optimum water content from various experimental campaigns on RE

Reference	Dry density (kg/m³)	Optimum water content (%)	Compaction method
Beckett et al. (2012) [72]	1918 -1948	12	Light proctor
Hall et al. (2004) [73]	2020 - 2160	8	Light proctor
Martinez (2015) [70]	2100	10.1	Standard proctor
Maniatidis et al. (2008)[41]	1850	12.5	Modified proctor
Bui et al. (2008) [74]	1900	10	Pneumatic rammer
Jaquin et al. (2009) [75]	2017 - 2061	12	Vibrating hammer
Gerard et al. (2015) [76]	2000	8	Specific proctor

2.2.4 Effect of sample's geometry and scale

Studies present in literature [22], [41], [77] have reported significant differences in the results for prismatic and cylindrical samples. Cylindrical samples seem to have better compressive strength than prismatic ones for a particular earth. According to the literature, the reason can be the friction between the earth and the formwork during ramming which is greater in the prismatic specimens, especially in the corners [28]. Cylindrical specimens are compacted better and thus have better mechanical strength. Another factor is the slenderness ratio. It is defined as the ratio between height and width (for prismatic samples) or diameter (for cylindrical samples). Generally, for UCS tests, a slenderness ratio of 2 is recommended to have a central tested zone sufficiently far from friction interfaces with loading platens at the top and base [41], [78].

In addition, to geometrical factors, the size of samples also affects the mechanical behaviour of RE. For example, Maniatidis et al, (2008) [41] concluded that there was a reduction of unconfined compressive strength of the columns (Φ = 30 cm; h = 60 cm) as compared to small cylindrical samples of (Φ =10 cm, h=20 cm). One of the reasons was due to the difference in material grading, in the column samples, aggregates greater than 20mm were included. Another reason could be explained by the weakest link theory, that the more the sample is, the more probabilities are to have a default in the sample, which could initiate the failure.

In addition, only a few studies have been done on a large-scale earth structure (some of them are reported in Table 2.6). In one of them, Bui et al. (2009) [74] performed tests at three different scales (compressed earth blocs, structural columns element, and wall scale). The results of the modulus of elasticity calculated from the small-scale samples were close to each other, while for the wall scale, higher results than the other two approaches were reported. Thus, it's clear that there is a significant lack of experimental results at the wall scale, which can give slightly different results and are more representative of the real building scale.

Table 2.6: Summary of experimental studies of mechanical behaviours of URE at large scale

Specimen size	Dry density ρd (kg/m^3)	Compressive strength fc (MPa)	Young's modulus E (MPa)	References
1.0 x 1.0 x 0.3 m^3	Not presented	0.6-0.7	60	Jaquin et al. (2006) [79]
1.0 x 1.0 x 0.3 m^3	2000	1.3 ± 0.2	500±40	Bui et al. (2016) [80]
0.55 x 0.55 x 0.2 m^3	2100	1.26	1034	Silva et al. (2014) [51]
2.5 x 2.5 x 0.5 m^3	1920	0.37	Not presented	Yamin et al. (2004) [52]
1.5x1.5x0.25 m^3	1780 -1850	-	400	El Nabouch et al.,(2017) [22]

2.3 Mechanical behaviour of RE under varying hydric state

2.3.1 RE subjected to varying humid conditions

Several studies focus on the hydric effect on the mechanical behaviour of RE, both numerically [49], [82], [83] and experimentally [47], [53], [72], [75], [84]. Most experimental studies were done at the material scale in the laboratory, with controlled relative husmidity (RH) and temperature.

Champiré et al. (2016) [47] investigated the impact of RH on the mechanical behaviour of compacted earth at a constant temperature. They used three different types of earth named STR, CRA, and ALX, extracted from existing RE construction sites. The earth was sieved at 10 mm, and the mass fraction of clay in each mix was 15%, 16%, and 8% for STR, CRA, and ALX respectively. The sieved earth mixes were compacted at optimum content to form compressed blocks within which cylindrical samples (Φ = 64.4 mm and H = 140 mm). The samples were conditioned in home-designed boxes themselves stored in a climatic chamber at a constant temperature of 24 ± 2 °C. The relative humidity inside these boxes was regulated with saline solutions at three different RH (25%, 75%, and 95%). Once equilibrium was achieved, a series of unconfined compressive strength tests were done with and without unloading-reloading cycles. Figure 2.3 shows the results of the evolution of compressive strength and Young's modulus, evaluated during the first cycle (20% of compressive strength) against relative humidity. From the results, a reduction of mechanical capacity (compressive strength and Young's modulus) ranges from 25% to 50% with an increase in RH from 25% to 75%.

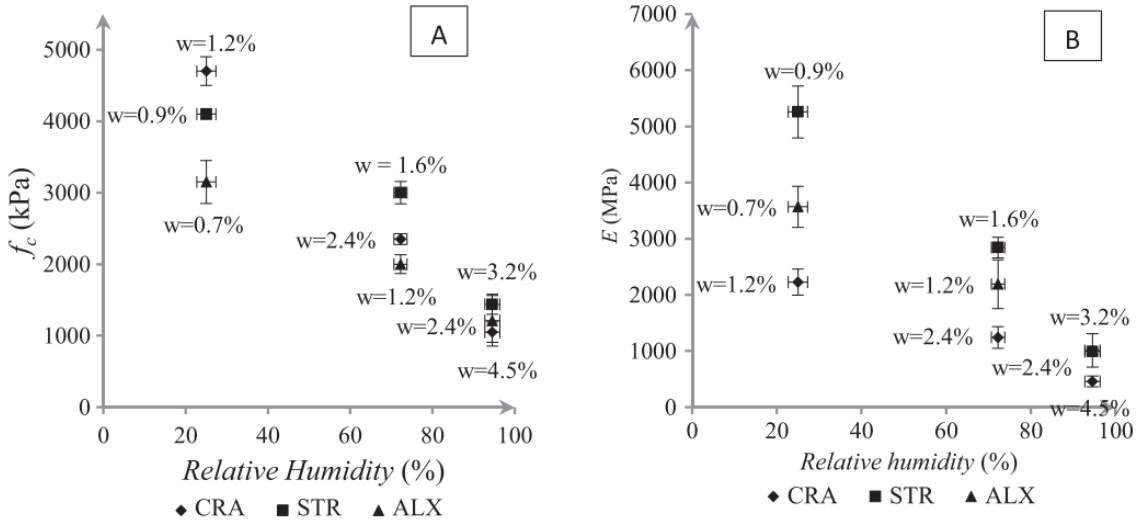

Figure 2.3: Variations of compressive strength (A) and Young's modulus (B) with respect to relative humidity and water content (w) [47].

While Champiré et al. (2016) [47] conditioned the sample at a constant temperature, Beckett et al. (2012) [72] conditioned RE samples by varying both temperature and RH. Their study was performed on two different soils. The first soil contained containing 40% silty clay, 50% sand, and 10% gravel represented as (4-5-1), and the second soil contained 20% silty clay, 70% sand, and 10% gravel represented as (2-7-1). Cubical samples (100 x 100 x 100 mm3) were prepared by compaction in layers at optimum water content. The samples were then conditioned at different temperatures (15°C, 20°C, 30°C, and 40°C) and different RH (30%, 50%, 70% and 90%) to investigate the effect of humidity and temperature on the unconfined compressive strength.

Results are summarized in Table 2.7. It was observed that the compressive strength increases with RH decrease. In fact, the compressive strength at 30% RH was almost double that of 90% RH. It was also found that compressive strength increased with an increase in temperature for the respective RH. However, it was concluded that RH had a greater influence on compressive strength than temperature, a similar observation made by Xu et al. (2017) [85].

Table 2.7**:** Unconfined compressive strength of RE samples (in MPa) conditioned at different temperatures and RH, [72].

Soil		Soil: 4-5-1 (Clay 19.9%) Dry density 1.94 g/cc				Soil: 2-7-1 (Clay 9.9%) Dry density 1.96 g/cc			
Temperature, °C		15°	20°	30°	40°	15°	20°	30°	40°
RH	30%	***1.18***	***1.41***	***1.16***	***1.60***	***1.44***	***1.46***	***1.56***	***1.76***
	50%	***1.00***	***1.18***	***1.40***	***1.13***	***1.12***	***1.16***	***1.55***	***1.39***
	70%	***0.75***	***1.10***	***1.09***	***1.12***	***0.95***	***1.24***	***1.11***	***1.23***
	90%	***0.74***	***0.67***	***0.71***	***0.70***	***0.85***	***0.87***	***0.95***	***0.87***

Xu et al. (2017) [85] studied the hydro-mechanical behaviour of rammed earth at relative humidity and different temperature. Cylindrical samples (Φ = 3.5 cm and H = 7 cm) were fabricated by static compaction method to ensure adequate homogeneity. Samples were cured in a sealed box at three relative humidity (23%, 75%, 97%) imposed by saturated salt solutions, and stored in climatic chambers at a constant temperature of (23°C and 30°C). Once the samples reach equilibrium, triaxial tests were performed at two confinement pressure (1 bar and 6 bar).

The triaxial tests were done with and without unload-reload cycles. The unloading–reloading cycles at prescribed stress levels of 20%, 40%, 60%, and finally 80% of compressive strength. It was found that both the maximum deviator stress and Young's modulus decrease with the increase in relative humidity. The results of deviator stress are summarised in Table 2.8, the deviator stress is reduced by a factor of 2 from low to higher RH while remaining in the same order of magnitude with the temperature change. It was concluded that the mechanical characteristics of rammed earth have a strong dependence on the relative humidity whereas do not seem to be significantly affected by temperature modifications between 23°C and 30°C.

Table 2.8: Maximum deviator stress (MPa) at different test temperatures and RH, confinement pressure of 1 bar (Xu et al., 2017).

	Temperature	
RH	23°C	30°C
23%	***6.8***	***6.6***
75%	***4.1***	***4.3***
97%	***2.8***	***3.0***

Both Xu et al. (2017) [85] and Beckett et al (2012) [72], through different experimental approaches on different soils, have reported that the mechanical performance at low RH (23%, 30%) is almost twice that of high RH (90%,97%). In addition, the RH has a strong influence on mechanical performance whereas temperature has not.

The effect of RH extends also to the shear parameter friction angle (φ) and cohesion (c). To our knowledge, Chauhan et al. (2019) [53] were the first to study the effect of varying RH on shear parameters. They performed a series of unsaturated triaxial tests on cylindrical samples (Φ = 5cm and H = 10 cm). Samples were conditioned at 7 different RH (9%, 22.51%, 32.8%, 57.6%, 75.3%, 84.34%, and 97.3%) and a constant temperature of 25°C. For each RH state, 3 samples were tested at 3 different confining pressures (i.e. 0.2 MPa, 1 MPa and 1.5 MPa). The Mohr-Coulomb failure was plotted for each confining pressure, and φ and c were then determined. It was found the c value increases from 0.5 MPa to 1.8 MPa, and φ from 31° to 37° with the increase in RH.

To conclude, the varying hydric conditions have a strong influence on mechanical performance. Different authors have used RH and water content to describe the hydric state. Unfortunately, RH and water content are not state variables and consequently, cannot account for objective behaviour. In unsaturated soil mechanics, the hydric state is represented by a state variable parameter which is known as suction (more on this is explained in the following part).

2.3.2 Suction as a state variable to describe the hydric state

This work is attached to consider a hydric variable that would be suited for the development of a future hydro-mechanical model, although modelling is not the object of the present work. The state variable chosen is suction since various hydro-mechanical models can be based on it in the unsaturated soils framework. Matric suction, which will be later denoted as "s", corresponds to the part of the total suction due to the capillary and adsorption attraction of water on the porous matrix of the material. It results in a negative value of water pressure, with respect to air pressure such as s can be expressed this way:

$$s = u_a - u_w$$

Where, u_a being the air pressure, and u_w the water pressure. Suction can be linked with the relative humidity (RH) of the pore air through Kelvin's equation (equation 2.1).

Kelvin's equation is defined as:

$$s = -\frac{\rho_w . R . T}{M_w} \ln(RH) \qquad (2.1)$$

Where s is suction at a given temperature T (in Kelvin, K), R is the universal gas constant (R = 8.3143 J/mol/K), Mw is the molar mass of water (Mw = 0.018 kg/mol), ϱw is the bulk density of water (ρ_w = 1000 kg/m^3) and RH is the relative humidity which is defined as the ratio of partial vapour pressure P in the considered atmosphere and the saturation vapour pressure P_0 at a particular temperature (T = 298 K).

Suction can also be linked with water content through the soil water retention curve. The soil water retention curve is a fundamental constitutive relationship in unsaturated soil mechanics that describes the relationship between soil suction and soil water content [86]. The shape of water retention curves

can be characterized by several models, one of them being known as the Van Genuchten (VG) model [87]). It is expressed as follows:

$$\theta(s) = \theta r + \frac{\theta s - \theta r}{[1 + (\alpha|s|)^n]^m} \tag{2.2}$$

Where θ is volumetric water content, s is suction pressure (MPa), θs saturated water content, θr residual water content, α $(MPa)^{-1}$, n and m are fitting parameters.

Therefore, the hydric conditions (RH and water content) can be fully represented by suction. The mechanical behaviour of rammed earth is strongly affected by the suction state inside the pores of RE material. Used in unsaturated models, suction is known to provide apparent cohesion between grains thus responsible for the strength of RE.

It has been notably shown by Jaquin et al. (2009) [75] who performed a series of triaxial tests on samples at different suction values. The suction was measured directly at the top of the sample during the test using a high-capacity tensiometer. The results of both strength and stiffness were linked with the suction values. An increase in maximum deviatoric stress with the suction state was observed (see Figure 2.4).

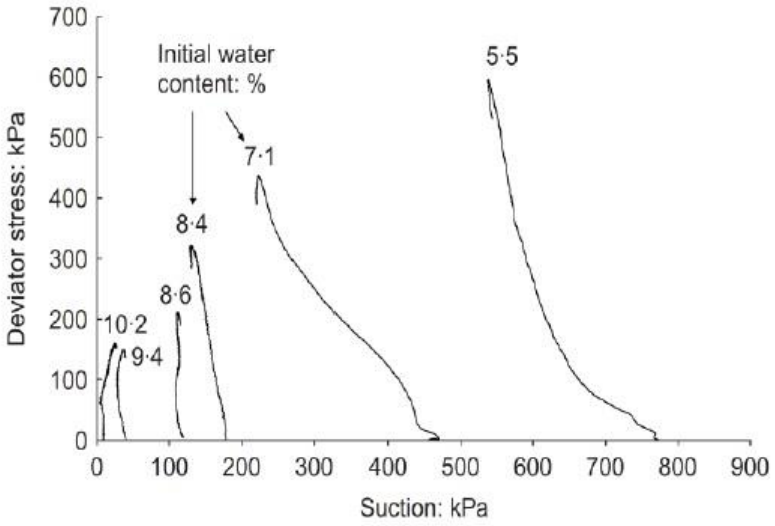

Figure 2.4: Results of the triaxial tests on rammed earth samples linked with the corresponding suction [75].

A similar observation was noted on hyper-compacted earth by Bruno et al., (2017) [67]. Hyper-compacted earth samples are generally compacted at a very high-pressure level and therefore exhibit very high values of compressive strength, which are comparable with those of other building materials such as fired bricks. Bruno et al., (2017) [67] used hyper-compacted samples, compacted to three high-pressure levels of 25, 50, and 100 MPa, then conditioned them at different relative humidity conditions to impose suction values of 7, 36, 66, 112, and 190 MPa and in a constant temperature of 25°C. After a series of mechanical tests, results indicate that both unconfined compression strength and Young's modulus increase with growing suction (see Figure 2.5).

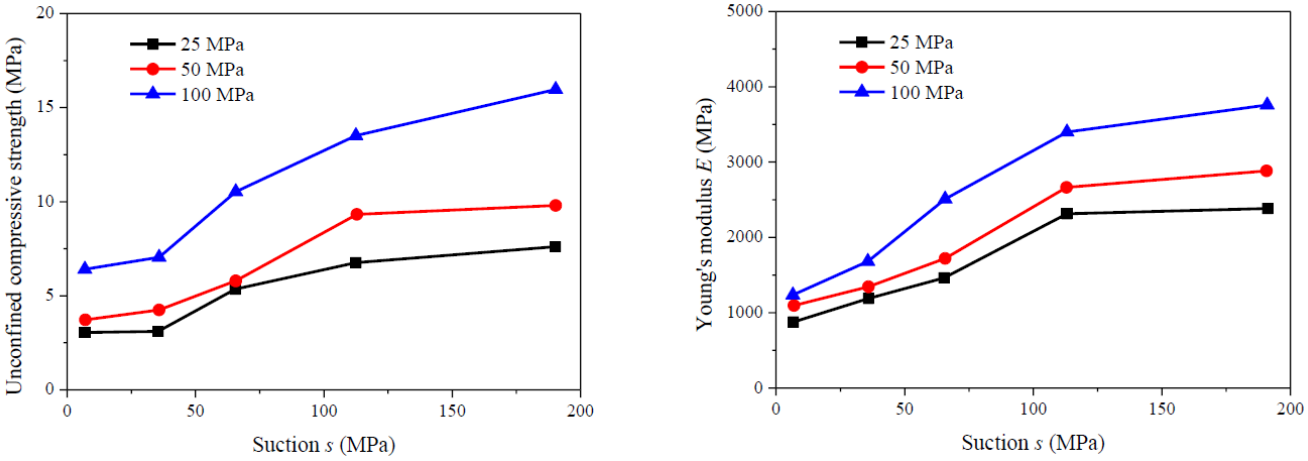

Figure 2.5: Variation of strength and Young's modulus with suction for samples compacted to three high-pressure levels of 25, 50, and 100 MPa [67].

Gerard et al. (2015) [76], François, (2017) [88] and then Chauhan et al. (2019) [53] performed experiments to study the behaviour of RE under varying climatic conditions from the point of view of unsaturated soil mechanics. They used the suction parameter to develop a unified failure criterion for estimating the RE's construction stability under varying atmospheric conditions.

Both Gerard et al. (2015) [76] and Chauhan (2019) [53] experimented on the material scale on a different earth. Gerard et al. (2015) [76] showed a linear relationship between the logarithm of suction with compressive strength. In the same way, Chauhan et al. (2019) [53] found that mechanical performance increases with increases in suction (Figure 2.6). A unified failure criterion including the effect of suction was provided for RE by these two works using the generalized effective stress concept defined by unsaturated soil mechanics. In this last, the intrinsic values of cohesion and fiction angle, obtained in a drained loading path, are unique for a given earth, and suction affects the effective stress tensor, according to Bishop Model [89]. From this unified criterion, Gerard et al. (2015) [76] concluded that the clayey silt studied has the ability to develop sufficient mechanical strength to be used as an unstabilized earthen construction material whatever the relative humidity conditions, except the fully water-saturated state.

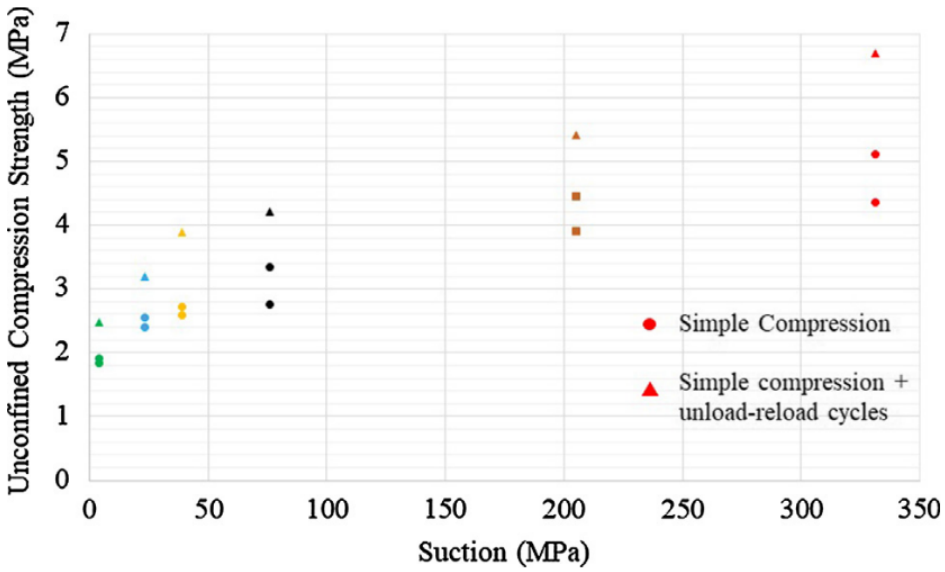

Figure 2.6: Variation of compressive strength with suction, by Chauhan et al.(2019) [53].

This approach was used to build a hygro-mechanical model through finite element simulation, [88], [90]. Finally, experimental results at the material scale were used to validate the previous model described. However, experiments at the material scale, where samples have uniform density without layers and where the earth is sieved to keep the finest granular fraction, are not fully representative of a real RE structure.

Few experimental studies exist at a column scale [42], [90] where RE samples made up of layers were used. Bui et al. (2014) [42] investigated the effect of moisture content on the mechanical behaviour of RE. Cylindrical samples (Φ = 16cm and H = 32) made up of six layers were used. Samples were dried at atmospheric conditions with moisture content varying from manufacturing (11-13%) to dry states (1-2%). After a series of unconfined compressive strength (UCS) tests under different moisture conditions, the strength and stiffness increased by a factor of four from the manufacturing state to the dry state. It was found that a slight increase in moisture content of dry rammed earth did not follow by a sudden drop in compressive strength (Figure 2.7a). In an effort to understand the coupled hydro-mechanical behaviour, Bui et al. (2014) [42] measured the suction of the RE sample after each UCS test. Finally, a linear relationship between suction (in logarithm scale) with compressive strength was observed (Figure 2.7b). In addition, Bui et al., (2014) [42] showed the Poisson's ratio of rammed earth varies from 0.35 to 0.2, in the function of the moisture content, from a humid state after the manufacturing to a dry state.

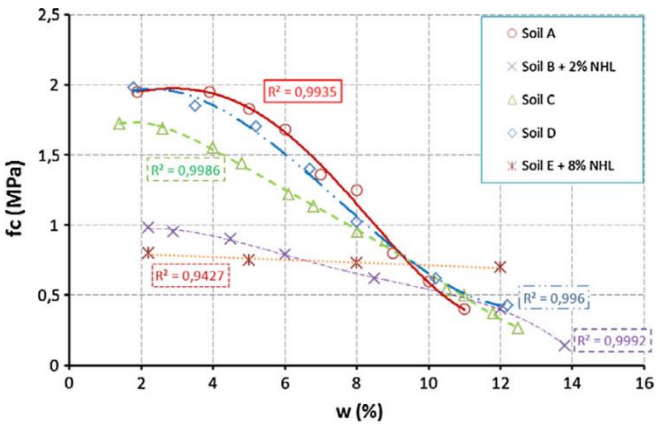

(a)

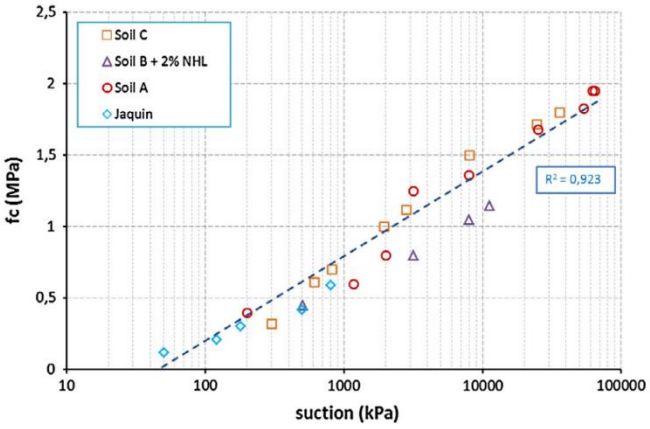

(b)

Figure 2.7: Variation of compressive strength (*fc*) with (a) moisture content (*w*) and (b) with suction, of all soils studied [42].

Chauhan. (2021) [90] also performed experiments at column scale to investigate the influence of hydric solicitation on the mechanical behaviour of drying RE. Prismatic samples (14 cm x 14 cm x 30 cm) made up of four layers were used. Samples were dried in a closed room environment. Upon drying, the hydric state was monitored by RH sensors and UCS tests was then performed at different drying times. The mechanical performances increased with drying time, similar to Bui et al. (2014) [42]. However, only a few tests were done with basic hydric instrumentation. Thus, it's clear that there is a significant lack of knowledge concerning experimental results at the structural scale with realistic conditions.

2.3.3 Elasto-viscoplasticity

As said previously, various studies have highlighted the sensitive nature of RE to moisture conditions [47], [53], [72], [75]. From these studies, it is clear that the compressive strength and Young modulus increase with the decrease in water content. Despite much research devoted to this subject, most of the existing studies tend to be more focused on the elastic parameters (mainly Young's modulus) and compressive strength. To our knowledge, there are no existing studies about the viscous behaviour of RE and its dependency on suction.

Gil-Martín et al. (2022) [91] seem to be the first to show a degradation of elastic stiffness of RE samples when studying the creep effect for 15 days. They used twelve cylindrical columns (Φ = 15 cm, h = 30 cm) that were air-dried for 4 months in atmospheric conditions. Out of twelve samples, six were tested for UCS and the other six were subjected to creep test before UCS. The creep test was done by maintaining a constant compressive stress of approximately 0.1 MPa and it was maintained for 15 days. They found out that, Young's modulus after creep tests was 264.7 ± 65.6 MPa which was lower than the ones tested without creep having Young's modulus of 330.11 ± 133.40 MPa. This show that viscous comportment has a non-negligible influence on the performance of RE buildings, notably in the wet initial state. Therefore, a good understanding of this behaviour is important for the practical design of RE.

a) Background on the rheology of soil materials

Elasto-viscoplasticity is a behaviour that describes strain rate-dependent non-recoverable behaviour. Creep and relaxation tests can satisfactorily allow the characterisation of the elasto-viscoplastic parameters for soil. Stress relaxation is the reduction of stress with time under fixed strain. The visco-elastic behaviour can be modelled by using basic elements such as spring and dashpot arranged in series, known as the Maxwell 1D model (Figure 2.8a) or in parallel also known as Kelvin Voight 1D model (Figure 2.8b). Differential equations for these models are given in 1D on Eqn. (2.3). Where σ is stress, ε is strain, E is Young's modulus and η is the coefficient of dynamic viscosity.

$$\dot{\varepsilon}(t) = \frac{\dot{\sigma}(t)}{E} + \frac{\sigma(t)}{\eta} \qquad \sigma(t) = E\varepsilon + \eta\dot{\varepsilon}(t) \tag{2.3}$$

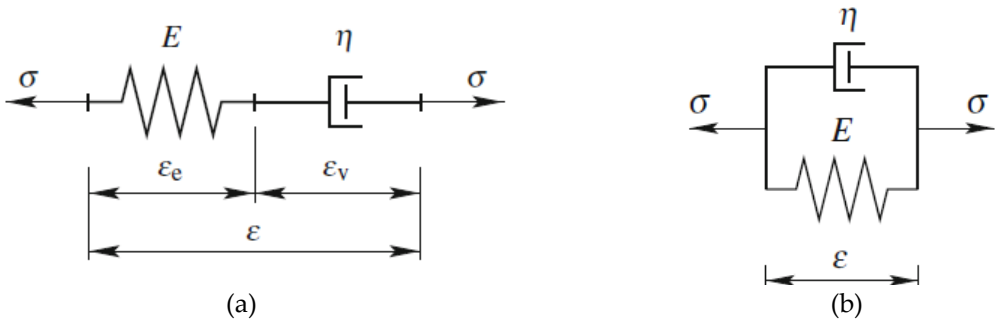

Figure 2.8: (a) Maxwell model and (b) Kelvin Voight model with their respective stress-strain rate equations

b) Stress relaxation

Although Maxwell's body can describe stress relaxation, after a sufficiently long time period, the stress will relax down to zero, which is not realistic for a humid RE structure. In order to describe more realistically the stress relaxation as well as the creep, more complicated models, combined with springs and dashpots, are required. Among these, the three-element model of Figure 2.9a is the simplest allowing to limit of the relaxed stress to a non-zero value (Figure 2.9a, 2.9b). It considers an elastic modulus E1 that is instantaneous, and an elastic modulus E2 that describes long-term elastic behaviour. The differential constitutive relation for this model is given by Eqn. (2.4) [92]).

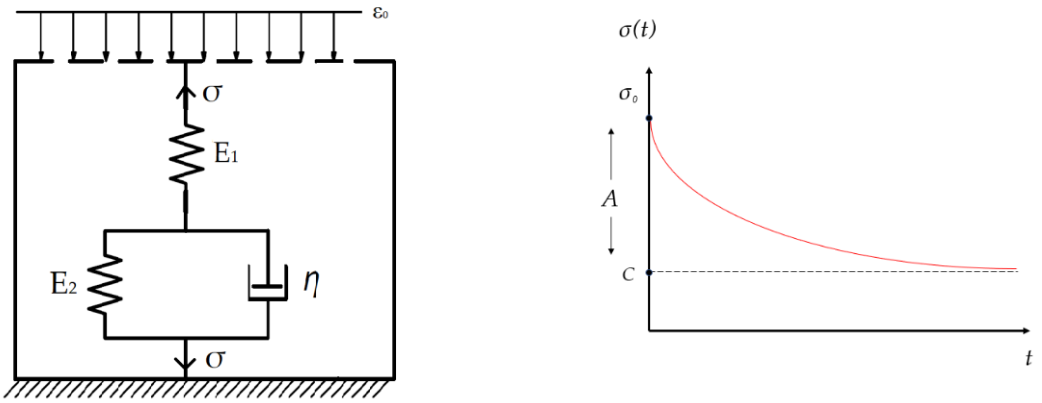

Figure 2.9: (a)Three-element model to describe the visco-elastic behaviour. (b) Stress relaxation function.

$$\sigma + \frac{\eta}{E_1 + E_2}\dot{\sigma} = \frac{E_1 E_2}{E_1 + E_2}\varepsilon + \frac{\eta E_1}{E_1 + E_2}\dot{\varepsilon} \tag{2.4}$$

In a relaxation test, a RE wall is subjected to a constant strain ε_0 at $t = 0$. Therefore $\dot{\varepsilon} = 0$, and Eqn. (2.4) becomes;

$$\sigma + \frac{\eta}{E_1 + E_2}\dot{\sigma} = \frac{E_1 E_2}{E_1 + E_2}\varepsilon \tag{2.5}$$

$$\sigma + \frac{\eta}{E_1 + E_2}\dot{\sigma} = Constant \tag{2.6}$$

$$\dot{\sigma} = -\frac{E_1 + E_2}{\eta}\sigma + Constant \tag{2.7}$$

The homogeneous solution of the differential equation (2.6) is given by:

$$\sigma(t) = Ae^{-\left(\frac{E_1+E_2}{\eta}\right)t} + C \tag{2.8}$$

Equation 2.8 is the stress relaxation function and its curve is illustrated in Figure 2.5b. Where A and C are constants. From the particular solution of the differential equation, we obtain $C = \frac{E_1E_2}{E_1+E_2}\varepsilon$.At time t=0, Eqn. (2.8) becomes $\sigma_0 = A + C$, hence constant A is given by $A = \sigma_0 - C$ (Figure 2.5b).

c) Creep

The same rheological model (Figure 2.5a) can be used to write the long-term creep behaviour. From the previous constitutive equation (2.4), in the case of creep, the wall is subjected to a constant stress σ_0, then $\dot{\sigma} = 0$, therefore Eqn. (2.4) becomes:

$$\frac{E_1E_2}{E_1 + E_2}\varepsilon + \frac{\eta E_1}{E_1 + E_2}\dot{\varepsilon} = \sigma \tag{2.9}$$

$$\varepsilon + \frac{\eta}{E_2}\dot{\varepsilon} = \sigma\ \frac{E_1+E_2}{E_1E_2} \tag{2.10}$$

The solution of the differential equation (2.10) is given by:

$$\varepsilon(t) = Be^{-\left(\frac{E_2}{\eta}\right)t} + \sigma_0\left(\frac{E_1+E_2}{E_1E_2}\right) \tag{2.11}$$

Where B is a constant and can be determined by substituting the boundary conditions: At $t = 0, \varepsilon(0) = \frac{\sigma_0}{E_1}$,

$$\varepsilon(0) = B + \sigma_0\left(\frac{E_1+E_2}{E_1E_2}\right) = \frac{\sigma_0}{E_1} \tag{2.12}$$

thus $B = -\frac{\sigma_0}{E_2}$, and therefore the creep strain equation is as follows:

$$\varepsilon(t) = \sigma_0\left(\frac{1}{E_1} + \frac{1}{E_2}\left(1 - e^{-\left(\frac{E_2}{\eta}\right)t}\right)\right) \tag{2.13}$$

2.3.4 RE subjected to capillary rise

We have seen in the previous section that RE structures gain strength after drying from the manufacturing wet state. Once the RE building is in use, the internal moisture would vary depending on the season or water infiltration through the capillary rise. Indeed, RE walls are porous and consist of interconnected micropores that can absorb and transport water through the capillary rise. Liquid water can penetrate inside the RE structure through capillary rise from the ground, rain infiltration by a roof default, or rare extreme situations like floods. The presence of water in earth buildings, and other types of masonry, is one of the main factors in building deterioration. Franzoni et al. (2014) [93] have shown that rising water leads to bad indoor conditions, poor thermal insulation, and material deterioration. In extreme cases, the capillary rise can cause moisture to accumulate at the base of the wall, resulting in the collapse of earth buildings. For example, Figure 2.10 shows a collapsing RE building resulting from the abnormal increase of pore moisture at the interface between walls and foundations [94].

Figure 2.10: Failure of an earth building in Lyon (France), which was produced by a large increase of water content at the wall base, by Scarato and Jeannet (2015) [94].

The mechanism of capillary rise is well understood for porous building materials such as RE. Hall et al. (1981) [95] studied the water movement in porous building material. It was observed the cumulative absorbed mass of water per unit area of the inflow surface increases linearly against the square root of the elapsed time. A similar observation for RE was made by Hall et al (2004) [73] (see Figure 2.11). From this relationship, parameters such as the coefficient of absorption which reflects the quantity of water absorbed (in kg) per unit area (m^2) and per root of the immersion time ($\sqrt{s}$) can be determined to characterise the capillary rise for porous buildings.

The coefficient absorption is determined experimentally by following the method described by Krus and Holm (1999) [96] and by Hall et al. (2004) [73] with its adaptation of the standard protocol of clay bricks [97] to RE. It consists of plunging the underside of a dry sample into a water tank and measuring, at regular intervals, by weighing, the amount of water absorbed by capillary action in the sample.

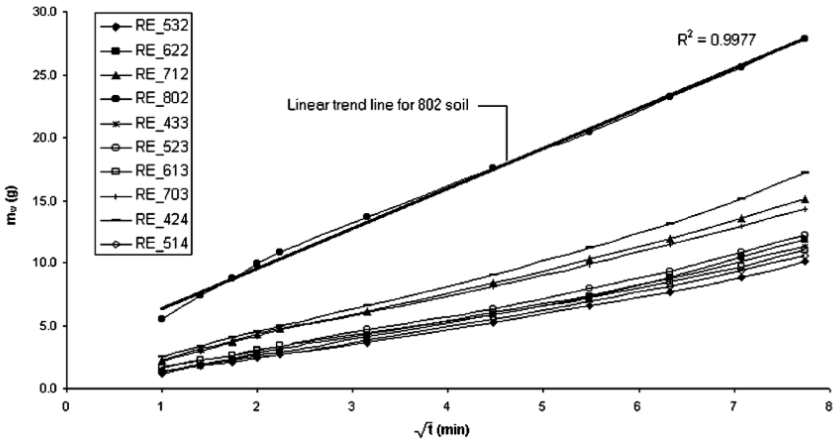

Figure 2.11: Relationship between the mass of absorbed water and the square root of elapsed time for different RE samples.

Particularly for RE, the characterization of capillary absorption properties can be found in studies of Mathew Hall et al. (2003) [73], Chabriac et al. (2014) [98], and Indekeu et al. (2021) [99]. Chabriac, (2014) [98] studied the water absorption coefficient of rammed earth experimentally. The mean values of the coefficient water absorption were 0.37 kg/m²/√s, 0.62 kg/m²/√s and 0.23 kg/m²/√s. Good repeatability was obtained for measurements with the same rammed earth. Hall et al. (2004) [73] showed that capillary absorption on rammed earth is highly dependent on particle size distribution. RE generally outperforms conventional modern masonry materials significantly in terms of the rate and quantity of moisture ingress due to capillary suction [73].

However, the effect of capillary rise on mechanical behaviour has rarely been investigated experimentally or numerically in the literature. Both studies by Hall et al. (2003) [73] confirm that there was no obvious pattern or relationship found between compressive strength and rate of absorption. Other studies have shown the weakening of the horizontal bearing capacity (pushover strength) of the RE structure during the capillary rise. Horizontal bearing capacity is the ultimate horizontal loading during a static push-over test. For example, Zhang & Nowamooz, (2021) [83] did a numerical simulation on the RE wall without capillary rise showing an increase of the horizontal bearing capacity by 47% in 5 years after construction, while this improvement was only 10% with capillarity rise (Figure 2.11).

The interesting findings of the numerical work of Zhang & Nowamooz, (2021) [83] require to be backed up by experimental data for validations, something that is missing in the literature. In addition, practical questions remain unanswered, like:

i) To what extent does the mechanical strength diminish during capillary rise?
ii) Is the strength restored after the drying when the capillary is solved?
iii) Is there an effect of drying-wetting cycles?

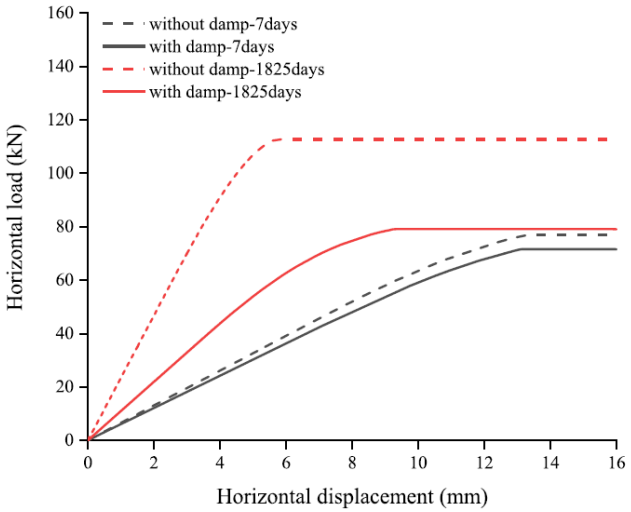

Figure 2.12 Force-displacement diagrams simulated numerically for RE walls with and without capillary rise [83].

2.4 Numerical modelling of RE

Numerical modelling of RE behaviour is suitable to predict the complex behaviour of RE structure. In the design of RE buildings, numerical modelling is quite helpful to estimate safety factors against failure and to optimize their design.

Modelling of RE requires constitutive laws, which are mathematical equations describing the relationship between two or more physical quantities based on the basic principles of continuum mechanics, such as stress and deformation.

2.4.1 Constitutive models for RE materials.

Different constitutive laws have been used in the modelling the mechanical behaviour of RE, some of them are based on the elastoplastic theory [53], [76], [88], [90] whereas others are based on the damage theory [49], [50].

- Elastoplastic models

In elastoplastic theory, the strain is decomposed into elastic and plastic components. Models that are based on elastoplasticity theory include for instance Mohr-Columb, Drucker-Prager, or Cam-Clay failure criteria. These models are developed from unsaturated soil mechanics and can be applied to RE.

Elasto-plastic models are made up of a combination of Hooke's law and the failure criterion. The simplest way is to consider no hardening in models and then the models are based on the assumption that the soil is an elastic perfectly-plastic material (Figure 2.13). The model defined with Mohr's Coulomb failure surface involves then five parameters, with two defining parameters from Hooke's law (E and ν), the two parameters define the Coulomb's failure criteria (the friction angle, ϕ, and cohesion, c) and also a parameter to describe the flow rule (dilatancy angle, ψ which comes from the use of non-associated flow rule).

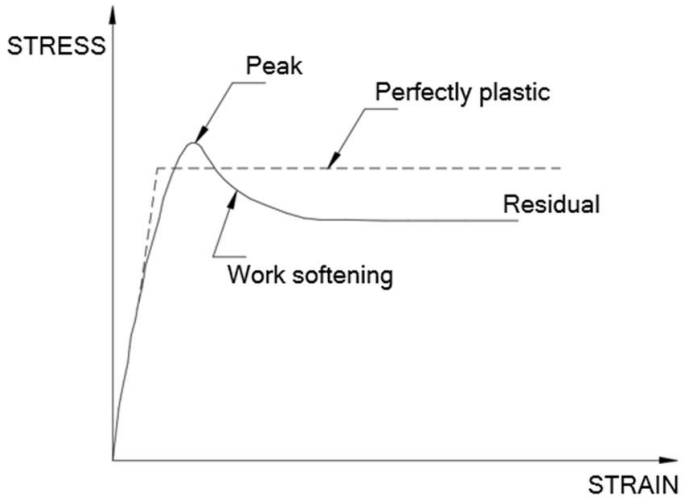

Figure 2.13: Elastic-perfectly plastic assumption

Mohr-Coulomb's elastic perfectly plastic model provides a relatively simple model for simulating the plastic behaviour of soil. The Mohr–Coulomb failure surface in the principal stress space and the octahedral plane is shown in Figure 2.14. Replacing the Mohr-Coulomb hexagonal shape of the failure cone with a smooth cone, with the Drucker-Prager model [100] for instance, allows for avoiding singular points in the numerical modelling. This model was thus used by Francois et al. (2017) [88] to simulate the plasticity behaviour of RE. It was observed that the predictions of stress-strain curves were close to experimental data except for the sharp transition at yield from elastic to elastic-perfectly plastic.

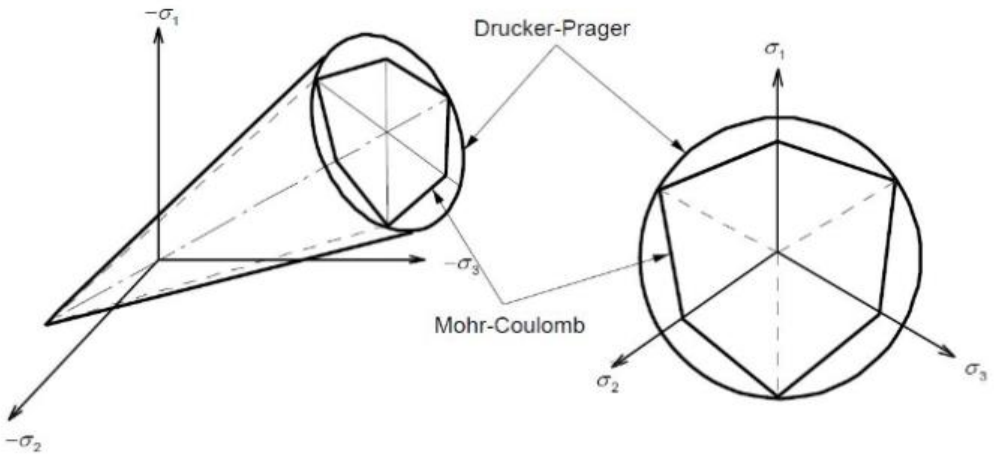

Figure 2.14: Mohr–Coulomb and the Drucker-Prager failure surface in (a) principal stress space and (b) in the octahedral plane.

However, the soil is a complicated material that behaves non-linearly and often shows anisotropic and time dependant behaviour when subjected to stresses [101].

Cam clay model has also been used for the modelling. Developed in the sixties at Cambridge University and later modified by Burland (1965) [102], Cam-clay is well suited to describe normally consolidated or lightly over consolidated soils. Therefore, it is rarely used for RE modelling. Of course, all these models can be enhanced by introducing hardening.

- Time-dependent behaviour

The effect of time on the mechanical response is an important feature of soil as well as earth structure. The time-dependent behaviour could result from the viscous nature of the behaviour and/or the interaction of free pore water with the soil skeleton known as consolidation. The latter is common for soil with low permeability. The viscous properties of soil may lead to creep and relaxation response.

The most popular method for modelling the time-dependent behaviour of materials is based on the viscoelastic approach. Visco-elastic models have already been presented in section 2.3.3. Apart from Gil-Martín et al. (2022) [91], it is a part of the behaviour that is never taken it into consideration in numerical models of RE.

- Damage models

Other kinds of models have been formulated using another conceptual framework: the damage theory, which supposes the development of micro-damages under deformation. The damage model is mostly used to describe the reduction of elastic stiffness. It is well suited for brittle materials, such as concrete and rocks, and due to the high dry density of RE, it can be well suited for its description.

Various authors have adapted the damage model to simulate the mechanical behaviour of RE [49], [50]. Bui et al, 2014 [50] used a damage model called Mazar's model to simulate the behaviour of rammed earth wallets under compression loading. Miccoli et al. (2015) [49] used a damage model called The Total Strain Rotating Crack Model to model the uniaxial compression test for earth block.

After a comparison between experimental data and the corresponding simulations in both studies, it was concluded that the damage model was able to reproduce the initial stiffness and the peak stress. After the peak stress, a smooths stress–strain behaviour observed in the experiments was not reproduced in the simulations. It is worth noting that, as soon as RE get wet, it is not brittle anymore and becomes more plastic. Therefore, there is no perfect model for RE modelling. Elasto-plastic or damage models only describe some limited features of the earth's behaviour.

2.4.2 Incorporating suction parameter in modelling the hydro-mechanics behaviour of RE

As mentioned previously, the hydric state has a significant influence on mechanical behaviour. A state variable chosen to represent the hydric state is suction which is suitable for modelling the hydromechanical behaviour of soil.

Suction can be incorporated into the hydromechanical modelling by using the framework of unsaturated soil mechanics, the effect of suction on effective stress can be introduced by the generalized effective stress [103]. Proposed by Bishop (1959) [89], the generalized effective stress tensor is given by:

$$\sigma'_{ij} = \sigma_{ij} - u_a.\delta_{ij} + \chi(u_a - u_w).\delta_{ij} \quad (2.14)$$

where χ, called the effective stress parameter, varies with the degree of saturation, from 0 for dry soil to 1 for fully saturated conditions. σ_{ij} is total stress component, s is suction and $\delta_{ij}$is the Kronecker symbol (= 0 when $i \neq j$ and = 1 when $i = j$).

When supposing that total suction equals matric suction (few salts in the pore water, thus negligible osmotic suction), we get: $(u_a - u_w) \sim s$. Besides, supposing that pores are connected to the atmosphere, we get $u_a \sim 0$. This way previous equation gets simplified in the following way:

$$\sigma'_{ij} = \sigma_{ij} + \chi . s . \delta_{ij} \tag{2.15}$$

Therefore, using a classical elastoplastic constitutive relation as Mohr-Coulomb, only a single couple of failure parameters (c'; φ') is necessary for any hydric state, since the criterion could be written using apparent cohesion term. Indeed, the failure criterion in total stress is:

$$\tau = c + \sigma_n . \tan \varphi' \tag{2.16}$$

Becomes using Bishop's expression:

$$\tau = c' + \chi . s . \tan \varphi' + \sigma_n . \tan \varphi' = c_{apparent} + \sigma_n . \tan \varphi' \tag{2.17}$$

Various studies have used the concept of generalised effective stress to model the effect of the hydric state on the mechanical behaviour of RE. Some have incorporated this concept into existing elasto plastic constitutive laws. For example, Gerard et al. (2015) [76] and then Chauhan et al.(2019) [53] used a unified failure criterion for RE under variation of suction (see previous equation). These studies were performed experimentally (UCS, DST, and Triaxial tests) and then modelled using Mohr-Coulomb's model. The intrinsic strength parameters (cohesion and friction angle) were determined experimentally from drained triaxial loading. Then triaxial tests at different suction levels were performed to fit the χ parameter. Gerard et al. (2015) [76] formulated a linear Mohr-Coulomb's envelope by using the value of cohesion and friction angle of 6.2 kPa and 36.5° respectively, but both uniaxial compression and indirect tensile tests upon saturated conditions do not fit well the failure criterion. In the same context, Chauhan et al.(2019) [53] used Mohr-Coulomb's failure criterion which fitted well with experimental results at different suction values (Figure 2.15). Both studies, found close fitting of the χ parameter, resulting in a similar expression of generalized effective stress.

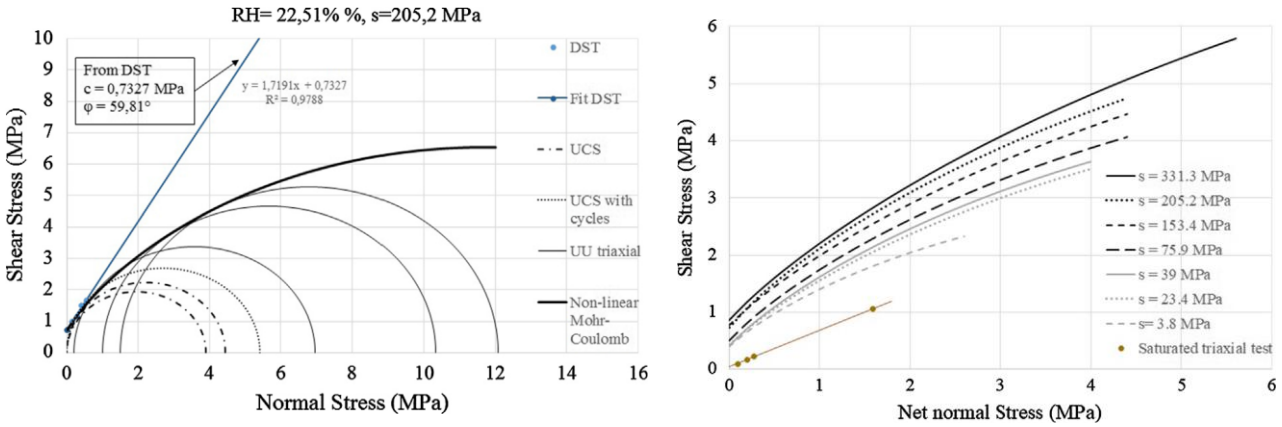

(a) (b)

Figure 2.15**:** Non-linear failure envelope plotted for (a) suction = 205.2 MPa and (b) all suction states, by using the results of UCS, DST and unsaturated triaxial test [53].

To conclude, a unified failure criterion including the effect of suction can be defined for RE using the generalized effective stress concept defined in unsaturated soil mechanics. Suction plays the same role as confining pressure and consequently, additional strength to the material (as seen in Figure 2.13b). A practical application of this approach is the estimation of the RE construction stability under varying atmospheric conditions or humid pathology conditions. Such approaches must be validated on tests on RE structures, with realistic coupled hydro-mechanical conditions, such as the tests performed in the present study.

2.5 Summary of the main problematics

The bibliographic review of previous studies in the literature was presented. It leads to the following synthesis as well as associated remaining unanswered questions:

- The strength of RE is mainly characterised using compressive strength. The values of compressive strength of RE are sufficiently high to meet the requirements proposed in various standards. We have also seen that REs have relatively low tensile and shear strength, thus they are not designed for pure tension.

- Factors that affect the mechanical behaviour of RE were presented. Among them, the hydric conditions of RE are a critical factor during construction as well as during the lifetime of the building. Indeed, when RE walls are wet, their mechanical strength is very low and can lead to catastrophic failure. Once constructed, RE walls have enough strength to carry self-weight, the strength increases as the wall dries, thus allowing further construction to continue as the wall can bear more weight. It would be helping to know more about the drying kinetics and the consequent increase of strength during this phase.

- Only one study in the literature has pointed to the viscous behaviour of RE, but the effect of suction on this behaviour was not covered. Time dependency behaviour such as creep deformation is an important factor especially when walls are moist. Thus, this study will explore the viscous behaviour at different hydric conditions.

- After construction, RE buildings are subjected to varying hydric conditions. Most studies have studied the effect of varying hydric conditions, some experimentally and other numerically. It was concluded that the mechanical behaviour would vary with hydric conditions but would still remain to be able to retain the RE building, except in case of a high level of saturation. This case can occur due to capillary rise. Only a few studies have been carried out on capillary rise and its effects on the mechanical behaviour of RE. The mechanism of capillary rise in porous building materials like RE is well-known in the literature. The effect of capillary rise on mechanical behaviour still needs more research; to what extent does the mechanical strength diminish during capillary rise? Is the strength restored after drying? Is there an effect of drying-wetting cycles? These questions will be answered in this thesis work.

- Furthermore, various existing models for RE have been explored. Generally, most models are adopted from soil mechanics and other used damage modes usually applied for brittle material like concrete. Constitutive laws to describe RE are similar to the ones of soil, such as Mohr-Columb, Drucker-Prager, or Cam-clay models. Time-dependent behaviour was modelled using the viscoelastic models used in solid mechanics. To reproduce the effect of hydric state, other studies have incorporated suction in modelling RE behaviour using generalised effective stress. These models were validated with experimental results from the material scale. A validation using experiments at a scale and boundary conditions that are close to a real building would be more helpful to improve the accuracy of these models. However, there is a lack of such experimental data in the literature, leading to this thesis work.

Chapter 3

3. Characterisation of earthen materials and sample preparation

In this chapter, the origin of the earth used is presented and characterisation was done to know better and classify it. The characterisation by first considering geotechnical properties: granulometry, Proctor analysis, Atterberg's limits and activity of clay. Secondly, by considering the hydric properties: water retention properties and hydraulic conductivity. After the characterisation of soil, a protocol for manufacturing RE samples is presented. Samples were prepared at three different scales (material, representative structural element and wall scale which is ½ of the scale of a real building). Finally, instrumentations for the hydric state are detailed along with their calibration.

Chapter outlines

3.1 Origin of the earthen material

In France, a wide heritage of RE buildings is present in many regions. Many of these buildings can be found in the Rhone-Alpes region where 40% of residential houses old or new are made of rammed earth.

The earth studied in this thesis comes from a recent construction of rammed earth (Figure 3.1). The building is located at Confluence, Lyon. This two-storey building is constructed by using prefabricated load-bearing rammed earth wall elements. The compacted elements are manufactured on the site at the foot of the building and immediately removed from the mould to be lifted and put in place. The construction of this building started in 2019 which is the same time as the beginning of this thesis project. The earth used was excavated from St Quentin Fallavier in the Auvergne-Rhone-Alpes region. All the work realized in this thesis has thus a particular interest since it concerns a real building that is exploited and monitored, and submitted to ambient variation in temperature and relative humidity.

Figure 3.1: Modern rammed earth building at Confluence, Lyon.

3.2 Geotechnical characterisation of materials

3.2.1 Particle size distribution

Granulometry analysis is important for better understanding the material and estimating the suitability of earth material for construction. Considering this study will be carried out on multiple scales (material, structural element and wall scales), the earth which came from the construction site with a maximum grain size (D_{max}) of 50 mm, was sieved at different D_{max} (5 mm, 10 mm, and 20 mm) to have a representative material grain size that fulfils the requirement of dimension scale and homogeneity of a sample at a respective scale.

The granulometric analysis was realised by the wet sieving and sedimentation method (to determine the clay and silt fractions). These tests were done according to French standards NF P 94-057 1992 [104].

3.2.1.1 Wet sieving method

Wet sieving is a method to separate particle fractions by using water. Later the quantity of dried particles is calculated from the retained materials on the sieves. The wet sieving method was performed as follows:

- A mass of 20 kg was chosen according to the D_{max} of the earth as recommended by the standard.
- First, the earth was first dried in the oven at 105°C for 48 hours, until the difference between two successive readings of dry mass is negligible with an accuracy of 0.1%.
- The dried earth was then sieved with the help of running water through sieves arranged in descending order. The different sieve sizes used were 63 µm, 100 µm, 315 µm, 630 µm, 1.25 mm, 2.5 mm, 4mm, 5 mm, 6.3 mm, 10 mm, 20 mm, and 40 mm. The classical geometric series of ratio 2 has been modified with the available sieves, in order to have a sufficiently accurate particle size distribution.

- After the sieving process, the materials retained on each sieve were oven-dried following similar procedures as mentioned before. The dry weight of the grains retained over each sieve was noted and used to find the corresponding percentage (%) passing:

$$\% \ Passing = 100 - cumulative \ \% \ retained \tag{3.1}$$

- The material loss should be checked after wet sieving, and it should be not more than 2% of the total dry earth. In this case, a 0.45% material loss was found which was fulfilling the mentioned criteria.

3.2.1.2 Sedimentation test (Hydrometer test)

A sedimentation test is adopted to calculate the repartition of the finest soil particles (< 0.08 mm) which is not possible by sieving. The sedimentation test was performed using a hydrometer. This test is based on an application of Stroke's law to a soil/water suspension and periodic measurement of the density of the suspension using the hydrometer. The test was done using the material passing a 0.08mm sieve from the previous wet sieving test.

- A 50g of clay and silt material was crushed using a pestle and mortar into fine powder. This mass is sufficient for the test as recommended by the standards.
- The fine soil was then soaked with 300 cm^3 of distilled water and 60 cm^3 of dispersing agent (Sodium Hexametaphosphate) for about 15 hours (overnight). The solution was then mechanically stirred for about 3 minutes before transferring it into a 1 L graduated cylinder.

- The cylinder containing fine soil was filled up with distilled water up to 1 L and another cylinder was filled with distilled water up to 1 L and the same quantity of dispersing agent for hydrometer reading correction.

- The cylinder with the solution was shaken such that the solution is uniformly distributed, then immediately hydrometer was immersed into the solution, and hydrometer graduation values (R) taken from the top of the meniscus on the hydrometer (see Figure 3.2), were recorded at time intervals of 30 seconds, 1, 2, 5, 10, 20, 40, 80, 240 minutes and finally 24 hours.

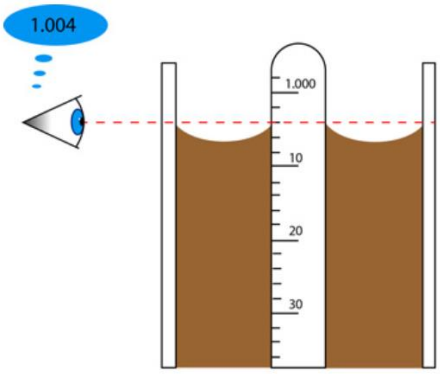

Figure 3.2: Reading the graduation value of the hydrometer at the top of the meniscus.

- After each hydrometer reading, insert a thermometer without disturbing the suspension and record a temperature reading at an accuracy of ± 0.5°C.

- The recorded hydrometer graduation values (R) were then corrected for temperature and meniscus and dispersing agent. This was done by using another cylinder filled with only distilled water, hydrometer was placed in this cylinder at each time of measurement in order to correct the recorded values.

- The corrected value *Rc* is calculated by taking into account the correction factor for temperature (C_θ) and the meniscus (C_m) and dispersing agent (C_d).

$$Rc = R \pm C_\theta + C_m + C_d \tag{3.2}$$

- The percentage of fines was then calculated using the following formula:

$$\%\, Fines = \frac{100 \times Gs}{Ms(Gs - 1)} \times Rc \tag{3.3}$$

Where, Ms is the mass of the earth sample used in the sedimentation test, 50 g, Gs is the soil-specific density which is 2.65, and *Rc* is the corrected hydrometer reading.

- The particle size is determined by Stoke's law which gives the relationship between the falling velocity of a grain of size D in a medium. Stoke's law is defined as:

$$v = \frac{\gamma_s - \gamma_w}{18\eta}.D^2 \tag{3.3}$$

Where v is the settling velocity of particles, γ_s is the specific gravity for a particle, γ_w is the specific gravity of the liquid, and η is the dynamic viscosity of water.

By combining the results from the wet sieving method and sedimentation test, particle size distribution curves for D_{max} = 5 mm, 10 mm, 20 mm and 50 mm are presented in Figure 3.3. The clay fractions were 14%, 12%,10% & 8% for 5 mm, 10 mm, 20 mm & 50 mm respectively. 8 - 15% clay fraction is suitable for most rammed earth soils [41]. For unstabilized rammed earth, the clay content should be sufficient to bind effectively together all other fractions without excessive shrinkage.

Figure 3.3 also illustrates the lower and upper limits of the particle size distribution as proposed by Houben et Guillaud, (1994) [55]. It is observed that the curve of 10 mm and 20 mm maximum grain sizes fit well in between the limits proposed while 5 mm and 50 mm are outside the envelope (see Figure 3.3). However, as discussed in the previous chapter, the limits proposed are not suitability criteria but are considered only for assessments.

It is worth noting that in this thesis, the earth with a D_{max} of 20 mm will be used to manufacture samples at a large scale and a D_{max} of 5 mm for samples at a small scale. The curve of 50 mm represents the whole granulometry for the earth that has been used from a real and recent construction site.

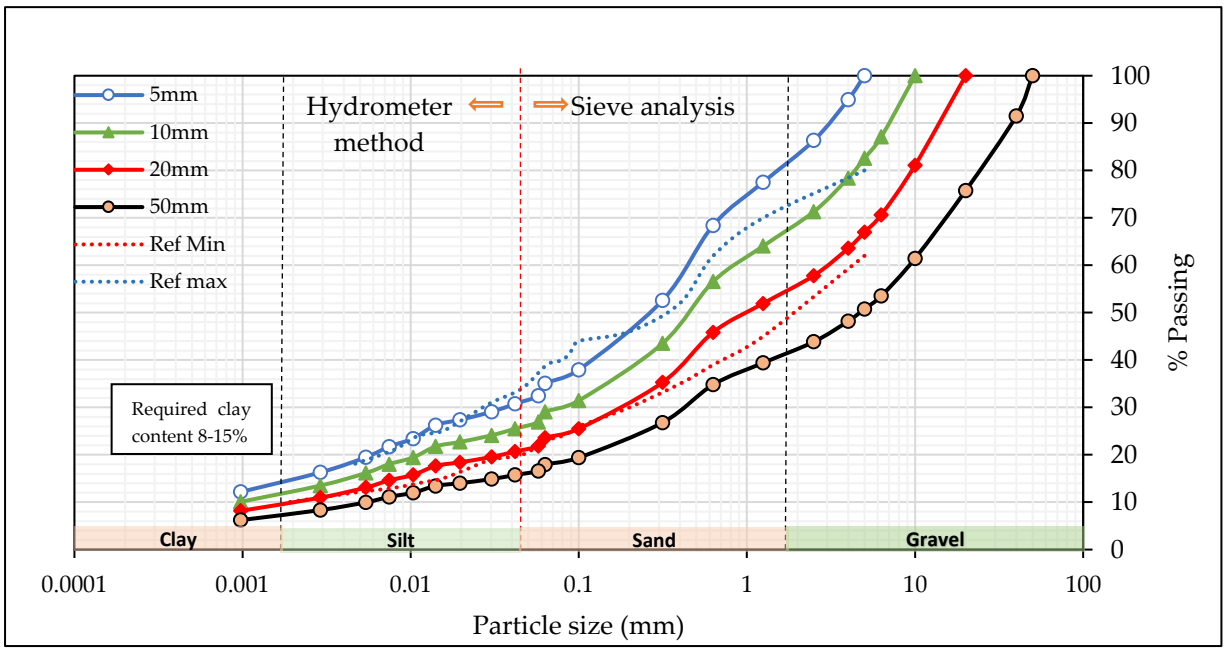

Figure 3.3: The particle size distribution of D_{max} = 5 mm, 10 mm, 20 mm and 50 mm. Illustration of the lower and upper limits for rammed earth proposed by Houben et Guillaud,1994 [55].

3.2.2 Modified and in-situ Proctor test

The Proctor test is used to determine the optimum water content that will lead to a maximum dry density. Optimum Moisture Content (OMC) is the moisture content at which the maximum possible dry density is achieved for a particular compaction energy or compaction method. The OMC from the Proctor test will then be used as a manufacturing water content for sample preparation.

The Proctor test is divided into standard and modified Proctor, depending on the compaction energy [105]. From the literature review, the modified Proctor test seemed to provide a closer simulation of compaction using on-site ramming equipment [71]. Therefore, a modified Proctor test was chosen and was done in the laboratory. The modified Proctor test was then compared to another Proctor test done by using on-site ramming equipment, called the "In-situ Proctor test".

- **Modified Proctor test**

According to the French Standard NF P 94-093, (1999) [105], the modified Proctor test is done with compaction energy between 2.56 MJ/m³ to 2.8 MJ/m³, depending on the type of mould used. The compaction energy is calculated by:

$$(E) = \frac{\mathrm{H} \times \mathrm{m} \times \mathrm{g} \times \mathrm{N1} \times \mathrm{N2}}{V} \tag{3.4}$$

Where *E* is the compaction energy (MJ/m³), m is the mass of ram (4.5 kg), H is drop height (457 ± 3 mm), N_1 is the number of layers (5), N_2 blows per layer (56) and V is the volume of the mould. A standard CBR mould (Φ = 150 ± 1 mm, H = 120 ± 1 mm), corresponds to a compaction energy of 2.66 MJ/m³. However, in this study, a CBR mould (Φ = 150 ± 1 mm, H = 151 ± 1 mm) was used. This mould has a higher volume compared to the standard one, so to obtain the same compaction effort, it was proposed to increase the number of blows per layer from 56 to 72. The resulting compaction energy was:

$$E = \frac{0.457 \times 4.5 \times 9.81 \times 5 \times \mathbf{72}}{(\pi/4 \times 0.152^2 \times 0.15)} = 2.663\ \mathrm{MJ}/m^3$$

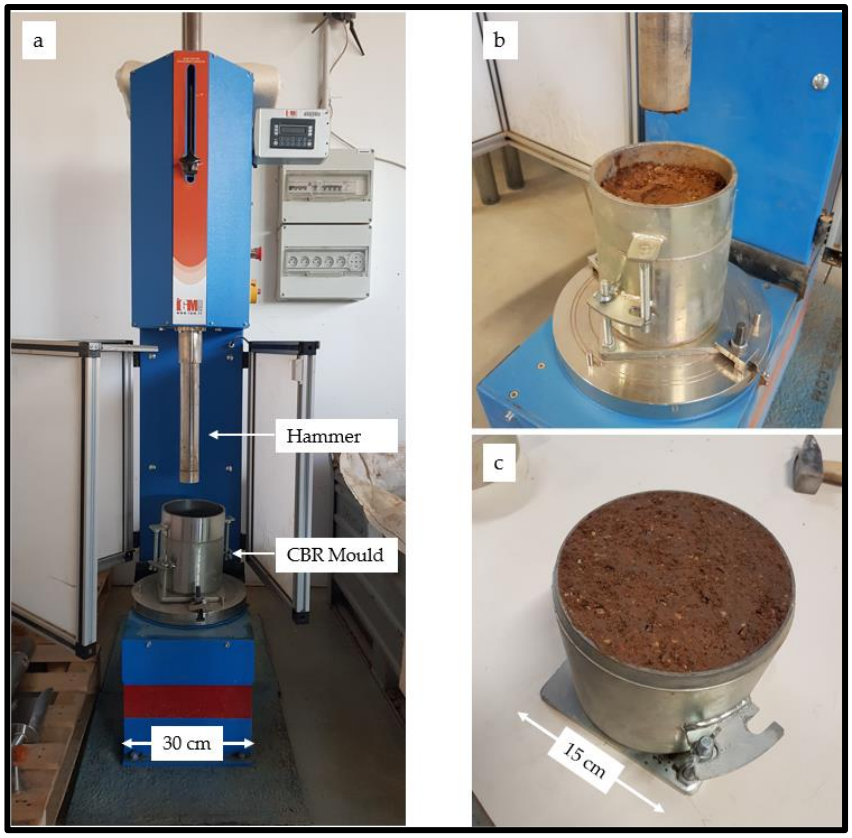

Figure 3.4: Modified Proctor test (a)automatic Proctor machine and CBR mould, (b) earth compacted in CBR mould, (c) excess earth trimmed after compaction.

An automatic mechanical compactor was used for the compaction test (Figure 3.4a). The modified Proctor test was done in soil passing through 5 mm, 10 mm and 20 mm. The procedures were as follows:

- About 7 kg of the earth was prepared for compaction points with increasing water content (w = 6%, 8%, 10%, 12%, and 14%) which will bracket the estimated optimum water content.
- The mixed earth was placed into five sealed containers and left overnight to ensure moisture homogenisation.
- A CBR mould with a base plate is first weighed, and then they are assembled with an upper collar (Figure 3.4c).

- The moist soil is then poured into the mould and the compaction is performed by a mechanical compactor according to the parameters (layers, mass of hammers) presented before to fulfil the required compaction energy.
- After compaction, the upper collar is removed from the mould, and the excess soil is trimmed using a flat knife until the compacted soil is at a flat level with the top of the mould. Small voids can be manually filled with excess samples (see Figure 3.4c).
- The mould with the sample is then weighed and recorded and the soil is taken out from the mould. A piece of the specimen was then used to determine the exact water content by oven drying, and the process is repeated for subsequent samples.

Figure 3.5 shows the results of the modified Proctor test for the earth sieved at 5 mm, 10 mm and 20 mm. 5 mm soil has a maximum dry density of γ_d= 1990 kg/m³ at w = 10.7% water content. 10 mm soil has a maximum dry density of γ_d= 2040 kg/m³ at w = 8.6%, and 20 mm soil has a maximum dry density of γ_d= 2045 kg/m³ at w = 9.6%. It can be observed from Figure 3.5 that the dry density increases with the D_{max}, representing about a 2.7% increase in dry density from a D_{max} of 5 mm to 20 mm. This could be attributed to the low porosity in large granular of 20 mm soil as compared to the one of 5 mm soil.

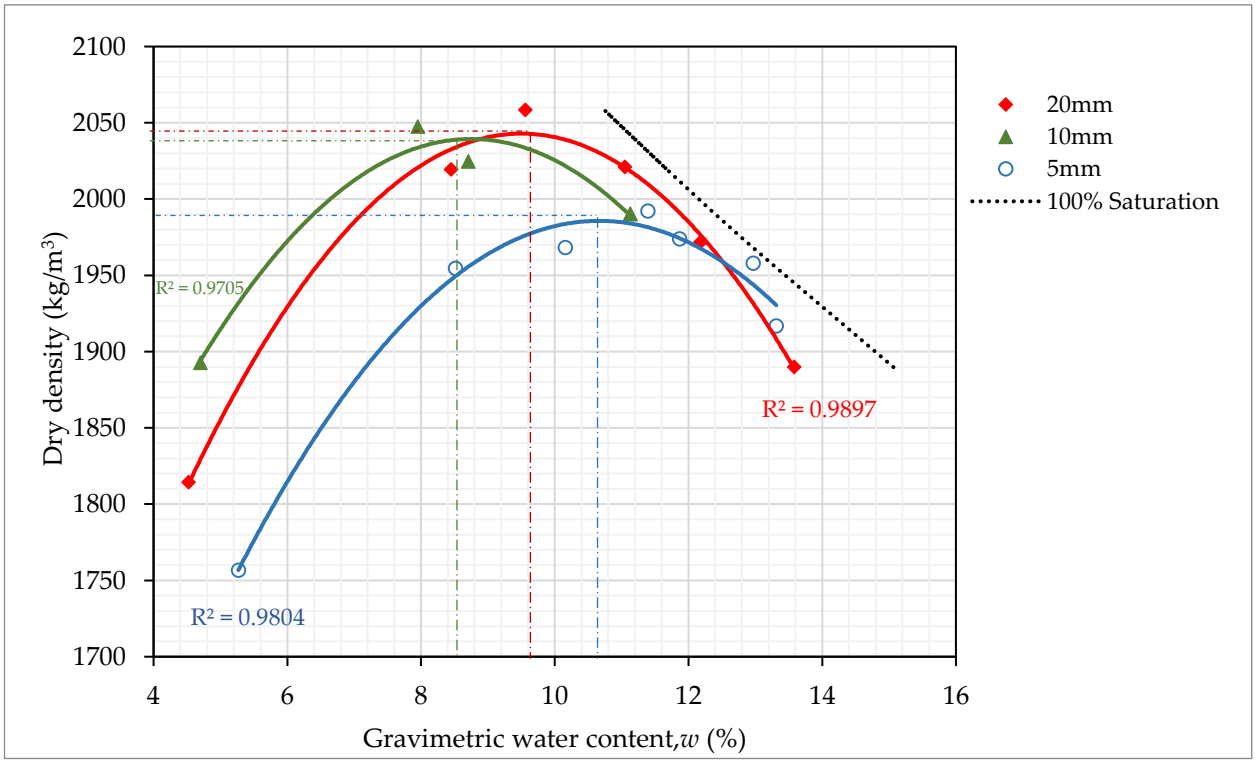

Figure 3.5: Modified Proctor test for soil with D_{max} = 20 mm, 10 mm and 5 mm.

- **In-situ Proctor test**

The in-situ or on-site Proctor test was performed to determine the compaction parameters using the onsite ramming equipment. As the compaction energy in the site may not the be same as in the Modified Proctor test since the method of compaction is not the same, it is important to compare them. Only the earth sieved at 20 mm, was used for the in-situ Proctor test, representing the grain size of the earth material that will be used to manufacture large samples. The compaction was done in a CBR mould (Figure 3.4c) by using a pneumatic rammer. The earth was compacted in two layers of thickness of 7.5 cm, the size of the layer was chosen to be representative of the one used in-site. The water content varied between 6% and 14%. The results of the in-situ Proctor are presented in Figure 3.6. The maximum dry density is 1995 kg/m^3 at an optimum water content of 10.4%.

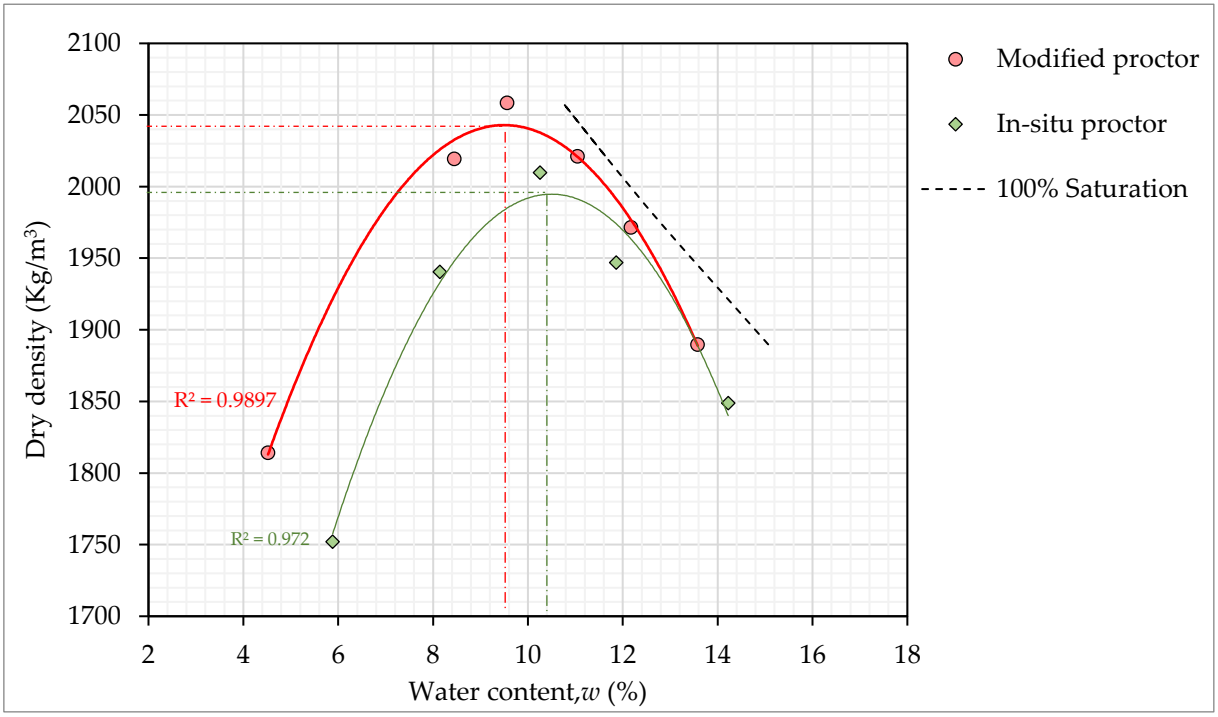

Figure 3.6: Results of in-situ and modified Proctor test for soil sieved at 20 mm

Table 3.1: Summary of Proctor test results

Type of Proctor test	Dmax	Optimum moisture content	Maximum dry density (kg/m^3)
Modified	5 mm	10.7%	1990
Modified	10 mm	8.6%	2040
Modified	20 mm	9.6%	2045
In-situ (20 mm)	20 mm	10.4%	1995

To conclude, both the modified and In-situ Proctor test was then done. A slightly lower value of maximum dry density (1995 kg/m^3) was found in the in-situ Proctor test as compared to the modified Proctor test (2045 kg/m^3), representing a difference of 2.4%. It can be noted that the difference in dry density is relatively low, which explains that the compaction energy from the modified Proctor test can be representative of the one used on the site. This observation confirms that the modified Proctor test is one of the most efficient methods in the laboratory to determine the maximum dry density and OMC for RE. The OMC from the modified and in-situ Proctors were comparable (w = 9.6% and 10.4%, see table 3.1), the mean value of OMC was 10% and was therefore used as a manufacturing water content for large samples (more on this later on).

3.2.3 Atterberg's limits

In raw earth, fine particles act as a binder for coarse particles. It is important to determine how consistency changes with water content., which is done by using Atterberg's limits. An Atterberg limit corresponds to the moisture content at which soil changes from one consistency to another. These limits are Liquid Limit, Plastic Limit and Shrinking Limit. The shrinking limit has not been established in this work because shrinkage is negligible on this earth.

i. Liquid limit (LL)

Liquid limit is defined as the water content w of soil at the state of transition from a liquid to a plastic state. In this study, the Liquid Limit test is conducted using two methods on the fine particles (<0.4 mm) These methods are Casagrande's method in agreement with the norm NF P 94-051 1993 [106] and Cone Penetrometer method NF P 94-052-1, (1995) [107].

Using Casagrande's method, the Liquid Limit is defined as the water content at which the two halves of a plaster of soil, placed in a cup and divided into two parts by a groove, come into contact with a fixed length as the result of a fixed number of blows (25) delivered to the cup. Figure 3.6a shows the Casagrande tool used.

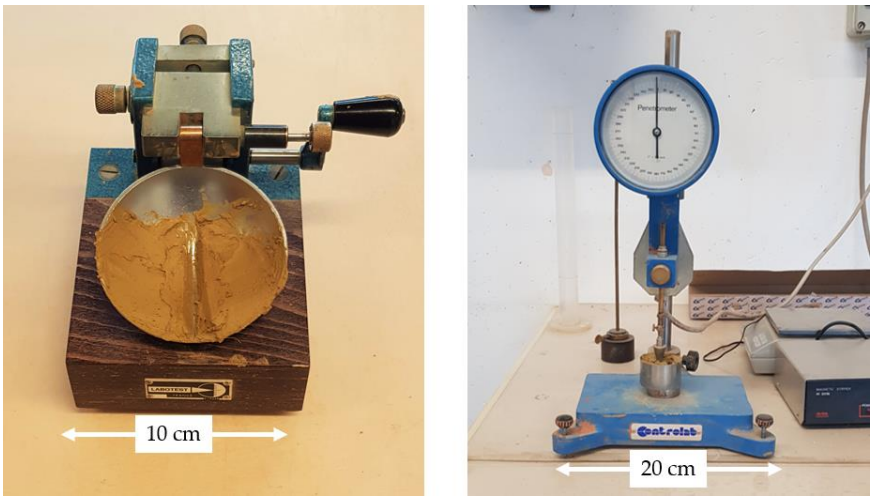

(a) (b)

Figure 3.7: Method for determining the liquid limit of soil; (a) Casagrande method where moist soil is grooved in Casagrande tool. (b) The cone penetrometer method shows a cone penetrating moist soil sample.

Another method for determining liquid limit is by using the cone penetrometer test method (see Figure 3.7b). Using this method, the Liquid Limit is based on the relationship between the moisture content and the penetration of a cone into a soil sample. This method provides improvements over the Casagrande method since it eliminates uncertainties that come from operator skills and provides a visual measurement of penetration. In the cone penetrometer method, the Liquid Limit is taken as the water content at which a standard cone will penetrate the soil sample at a distance of 20 mm in approximately 5 sec. Figure 3.8 shows the results of both the Casagrande and penetrometer methods. Both methods are in good agreement with the Liquid Limit values of w_L =30,5% and 30% [108].

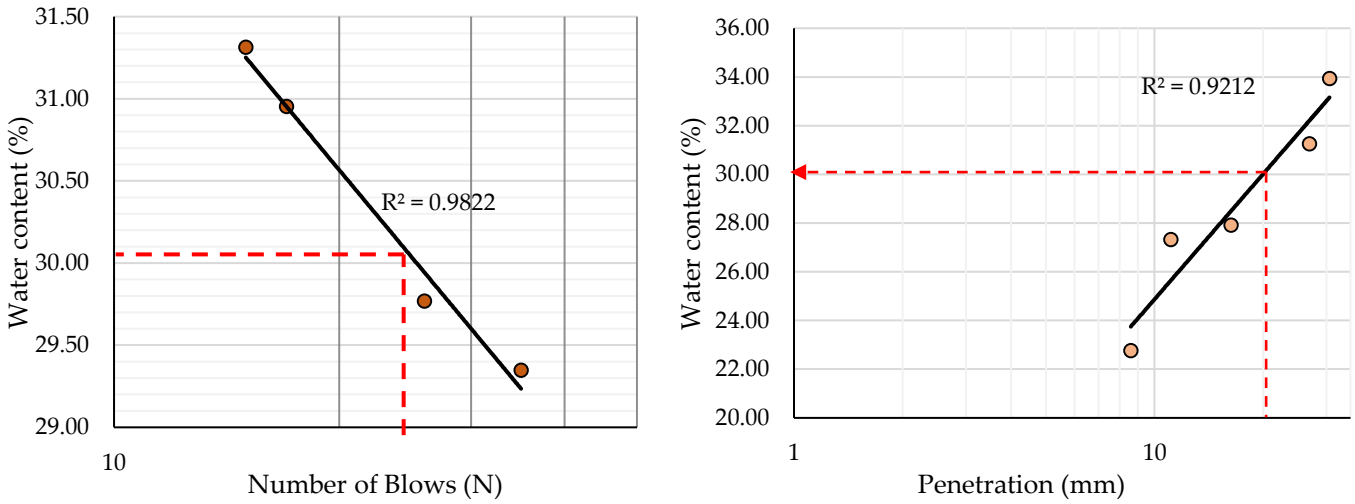

Figure 3.8: (a)Flow curves showing the water content and the corresponding number of blows using Casagrande's method. (b)The curve of water content with the penetration depth of the cone using the Cone penetrometer method.

ii. Plastic Limit (*Wp*)

The plastic limit is defined as the moisture content of soil at the state of transition from a plastic state to a solid state. The plastic limit is determined by repeatedly remoulding a small ball of moist plastic soil and manually rolling it out into a 3 mm diameter thread without cracking. The water content at which the thread crumbles when lifted, is taken as the Plastic Limit. The Plastic Limit was determined according to standards NF P94-051, (1993) [106] and was equal to 19% [108].

iii. Plastic Index (PI)

The difference between the Plastic Limit and Liquid Limit defines the range of the plastic zone called the Plastic Index (PI). Soils with a high PI have a higher clay content. From equation (3.5), the plastic index was evaluated as equal to 11%.

$$PI = w_L - w_P \tag{3.5}$$

The plastic index and liquid limit values obtained were then used to classify the soil. Casagrande defined an A-line in order to separate inorganic clays from silt and organic soils (Figure 3.9). The A-line represents the relationship between the plasticity index and the liquid limit of soil. According to Casagrande's Plasticity chart, the soil lies above the A-line which means the soil is inorganic and it is in the transition from inorganic clay with low plasticity to medium plasticity (Figure 3.9). Also according to the French Classification of Soils GTR (Guide de Terrassements Routier) [109] for fine-grained soils (i.e. more than 35% of grains passing 80 μm and no grain size over 50 mm), it is classified as A1, i.e. low plastic silt (Ip < 12%). It means that the soil has low plasticity.

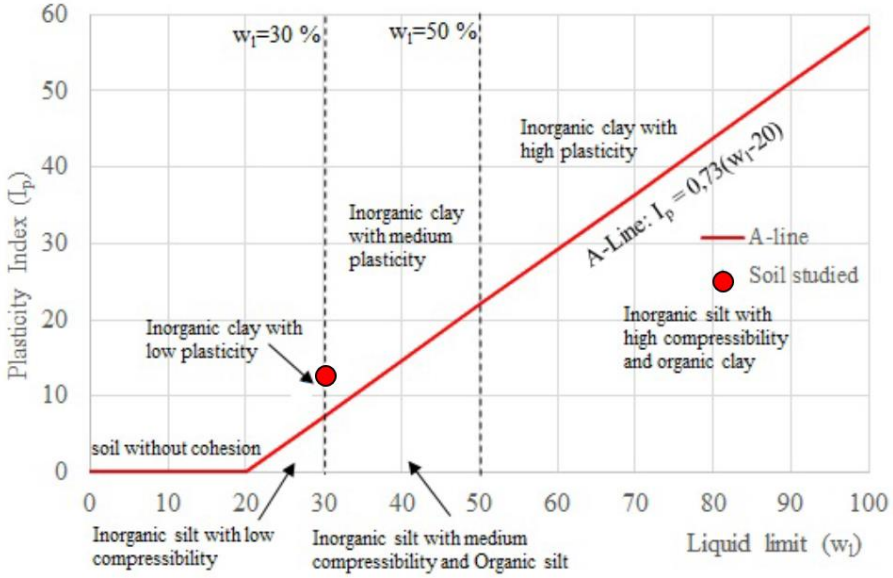

Figure 3.9: Casagrande's plasticity chart for the classification of fine-grained soils

Furthermore, the plasticity index (PI) value was used to characterize the swelling potential of clay soils, determined by activity value. Activity (A_c) is defined as the ratio of plasticity index to and the percentage of clay content.

$$A_c = \frac{P_I}{f} \tag{3.6}$$

Where f is the percentage of the clay content of Recalling the percentage of clay content in 5 mm, 10 mm and 20 mm soil is 14%, 12% and 10% thus the activity was found equal to 0.79, 0.92 and 1.1 respectively. Using this value, the soil activity is in the normal range (0.75 < Ac < 1.25) and can be considered as slightly active soil. The activity of the soil was further determined in the laboratory by using the methylene blue analysis.

3.2.4 Methylene Blue analysis

The aim of the methylene blue value (MBV) test is to estimate the presence and activity of clay mineral present in the soil. The MBV test quantifies the ionic adsorption capacity of soil by measuring the quantity of methylene blue necessary to cover the total (external and internal) surface of the clay particles contained in the soil.

To do so, clay and silt fraction (<0.08 mm) was taken as testing sample and the standard NF P 94-068, (1998) [110] was adopted.

Procedures:

i. 30 g of dry fine particles (clay and silt) passing through a 0.08 mm sieve are placed in a container with 500 mL of distilled water, dispersed in the water, and maintained in suspension by means of a stirrer. (Figure 3.10a).

ii. With a burette, unit doses (5 mL) of the methylene blue solution, with a concentration of 10 g/L, are added to the suspension.

iii. After adding each unit dose, a small quantity of the suspension is collected with a rod and a small drop is made to fall onto standard filter paper; this produces a dark blue stain, surrounded by a colourless wet area (Figure 3.10b).

iv. Further unit doses of the solution are then added and more drops are deposited on the filter paper until a light blue halo is seen to form inside the wet area and around the blue stain. This reflects the presence of an excess quantity of methylene blue that is no longer adsorbed by the clay mineral surface and remains in suspension.

v. At this point, no more methylene blue is added and the suspension is checked at 1 min intervals to determine the stability of the light blue halo; if the halo persists after 5 mins, a sufficient quantity of methylene blue has been added. Otherwise, the titration process is continued until the halo becomes stable enough.

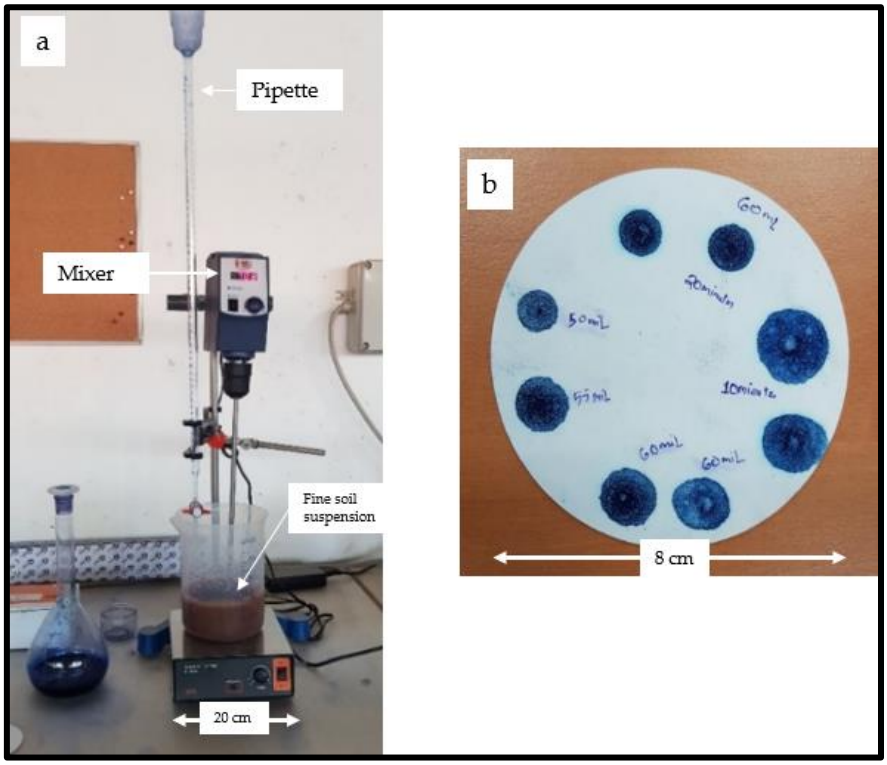

Figure 3.10 (a)Experimental procedure and apparatus for methylene blue value test. (b) Spot tests for finding the end point and total volume of methylene blue added.

The index supplied by this testing method is referred to as the blue value of the soil (M*V*B, in g/100 g), for soil with D_{max} > 5 mm and is given by:

$$MVB = \frac{B}{m_o} \times C \times 100 \tag{3.7}$$

where m_0 is the mass of dry soil (g), B is the mass of methylene blue (concentration of 10 g/L), C is the proportion of 5 mm in 50 mm fraction.

Because the blue value test is carried out on fine particles (a mixture of clay and silt), *MVB* does not only reflect the clay content of the sample but also indicates the activity of clay minerals. Accordingly, the index of activity is defined to purely reveal the activity of clay fraction in soil:

$$A_{CB} = \frac{MVB}{C_B} \tag{3.8}$$

where A_{CB} is the index of activity (in grams of methylene blue in a 100 g clay fraction), *MVB* is the blue value for the testing sample (in grams of methylene blue per 100 g of dry soil), and C_B is the clay content (<0.002 mm) in the 0-0.08 mm fraction.

Table 3.2: Methylene blue value results and classification of clay contained in the earth

Test No.	**1**	**2**	**3**
The volume of MB adsorbed (mL)	61	60	60
Blue value (MBV) (g/100g)	1.36	1.34	1.34
Clay content (C_B), in the 0-0.08 mm fraction	0.4	0.4	0.4
Clay activity (A_{CB})	3.4	3.5	3.5
Evaluation of clay activity	Slightly active	Slightly active	Slightly active

From the results (Table 3.2), the blue value of the earth was 1.35 g/100g which is in the category of Loam soil according to NF P 94-068, (1998) [110]. The earth presents a low value of methylene blue adsorption which indicate low swelling activity [111]. This was confirmed by the index of activity of clay which was 3.5 and classified as slightly active (3<ACB<5) [110]. The PI, computed from Atterberg Limits, also gave a lowly plastic clay/loam (from the Casagrande classification).

Other characterization tests of clay soil including measuring the cation exchange capacity (CEC) were done in another laboratory**.** CEC is a measure of the ability of soil to retain and exchange cations which are retained on negatively charged sites that are found on the surface of particles of clay. The cation exchange capacity (CEC) of the material was measured with the cobalt-hexamine method [112]. The obtained value of CEC = 9.2 ± 0.4 meq/100 g at a pH of 7.0, this means that the soil has moderate retention capacity.

3.2.5 Summary of geotechnical properties of the raw earth used

The soil of max grain size (D_{max}) of 50 mm was sieved to different D_{max}, 20 mm, 10 mm and 5 mm according to the required size of samples. Table 3.3 shows a summary of the geotechnical properties of the earth used. A focus is made for soil with D_{max} of 5 mm and 20 mm which will later be used for making small and large samples respectively. From the granulometry, the clay content is from 8 to 14%, which is a sufficient binder content for RE construction. Atterberg's limit test show that the clay has a PI of 11% meaning the soil contains lowly plastic clay/loam according to the Casagrande classification and the French Classification of Soils GTR (Guide de Terrassements Routier). Furthermore, the activity of clay was estimated by using the PI value and was classified as slightly active similar classifications were confirmed by using a methylene blue test. The modified Proctor test was done to determine the optimum water content (OWC) that will be used as a manufacturing water content during the compaction of samples. The OWC was 10.7% and 9.6% for 5 mm and 20 mm producing a maximum dry density of 1990 kg/m^{-3} and 2045 kg/m^{-3}. From these OWCs, the corresponding manufacture water content will be taken as 10% for 20 mm and 11% for 5 mm since they are more practical.

Table 3.3: Summary of geotechnical properties

Soil property					
Soil maximum grain size		5 mm	10 mm	20 mm	50 mm
Granulometry					
Gravel fraction		16%	32%	45%	58%
Sand fraction		52%	42%	33%	26%
Silt fraction		18%	14%	12%	18%
Clay fraction		14%	12%	10%	8%
Compaction Characteristics					
Modified Proctor test	dry density (kg/m3)	1990	2040	2045	-
	Water content (%)	10.7%	8.6%	9.6%	
In-situ Proctor test	dry density (kg/m3)	-	-	1995	-
	Water content (%)	-	-	10.4	
Manufacturing water content		11%	-	10%	
Atterberg's Limit					
Liquid limit		30%			
Plastic limit		19.%			
Plasticity index (PI)		11%			
Activity					
Activity from PI		0.79 to 1.1		Slightly active	
Methylene Blue Value		1.35 g/100g		Slightly active	
CEC		9.2 ± 0.4 meq/100 g			

3.3 Hydric properties

The soil-water properties that are essential to this study are the water retention properties describing how much can the soil retain and hydraulic conductivity describing how easily can water infiltrate through the soil. First, it is important to recall several variables are used to describe the water present in the soil matrix:

- Water content

Represents the amount of water present within a soil matrix either by mass or volume. Gravimetric water content is defined as the ratio of the mass of water to the mass of solids whereas volumetric water content is the ratio of the volume of water to the volume of solid.

- Degree of saturation

The degree of saturation refers to the volume of water occupying the soil's pores. When soil is fully saturated, the void space is completely occupied by the water and the saturation is equal to 1.

- Relative humidity (RH)

Relative humidity is defined as the ratio of the partial pressure of water vapour in the air to the saturation vapour pressure of water at the same temperature, usually expressed as a percentage.

Unfortunately, water content, degree of saturation and RH are not state variables and consequently, cannot account for objective behaviour. One of the state variable parameters that is used to quantify the hydric state of unsaturated soil is known as suction (more detail in the next section).

3.3.1 Suction

In unsaturated soil, total suction is defined as the combined effect of matric suction and osmotic suction. Matric suction arises from the difference in pressure at the air-water interface. Matric suction refers to the net interparticle force generated within a matrix of unsaturated granular particles due to the combined effects of negative pore water pressure and surface tension. The macroscopic consequence of suction stress is a force that tends to pull the soil grains toward one another. Osmotic suction is due to the dissolved solutes in the soil pore water. Suction can be linked with the relative humidity (RH) of the pore air through Kelvin's equation (2.1) (see Chapter 2, section 2.3.2).

3.3.2 Soil water retention curve

The soil water retention curve is a fundamental constitutive relationship in unsaturated soil mechanics that describes the relationship between soil suction and soil water content [86]. The soil water retention curve was estimated by measuring the earth's water content for a known (controlled) suction or, else, measuring suction for a known water content. According to the level of water content targeted, different methods also exist for controlling the suction or measuring it. A summary of various instruments used for measuring soil suction is presented in Table 3.4. Therefore, measurements were done using two methods, the Liquid-vapor equilibrium method and the filter paper method. Experimental results were then modelled by using Van Genuchten and the GAB model.

Table 3.4: Summary of common techniques for controlling and measuring soil suction

	Method	Suction Range (MPa)	References
Controlled suction	Isopiestic humidity control	4 – 400	Young (1967) [113]
	Axis translation techniques	0–1.5	Bocking and Fredlund (1980) [114]
Measurements	Contact filter paper method	Entire range	Houston et al. (1994) [115]

3.3.2.1. Experimental determination of soil water retention curve

a) Controlling suction, thanks to Saline solution method

This method consists in applying a given suction state within the porous material, through liquid-vapour equilibrium obtained in a climatic chamber containing different kinds of saturated saline solutions. By using Kelvin's thermodynamic equilibrium equation (2.1), the suction imposed at the corresponding relative humidity was determined (see Table 3.5).

Table 3.5: Saline solutions with their corresponding relative humidity and suction values at 25°C.

Saline solution	KOH	CH_3CO_2K	$MgCl_2$	NaBr	NaCl	KCl	K_2SO_4
Relative humidity (%)	9	22	32.8	57.6	75.3	84.34	97.3
Suction (MPa)	331.3	205.3	153.4	75.9	39	23.4	3.8

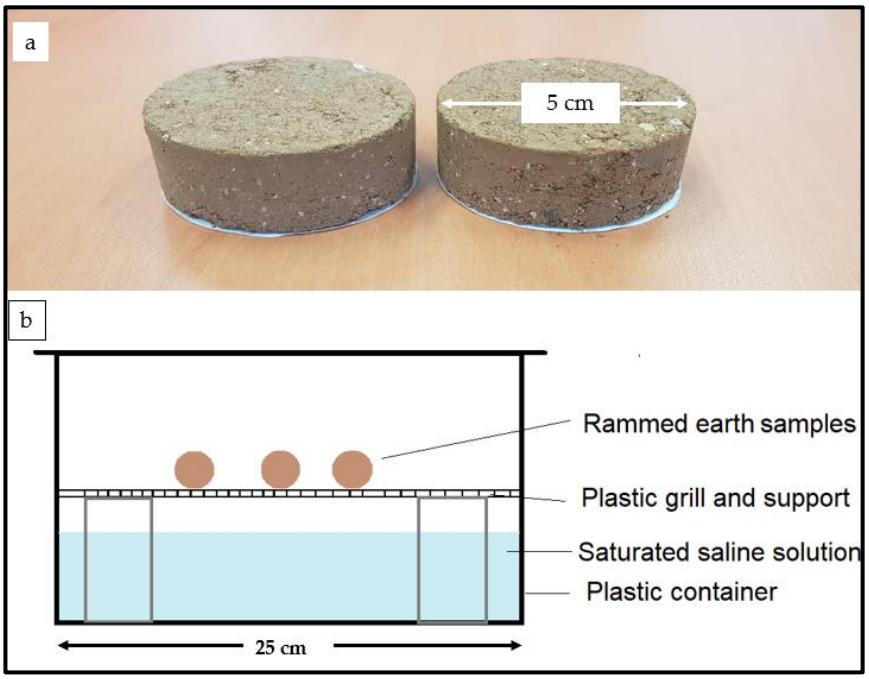

Figure 3.11 (a) RE samples used for soil water retention curve. (b)A scheme representing the relative humidity boxes.

Experimental protocol:

1. Four small cylindrical samples (Φ = 5 cm, H = 1 cm) and an average mass of 56 ± 0.5% g were used. These samples were manufactured by static compaction (Figure 3.11a).

2. The samples were oven-dried at a temperature of 70°C for several days until the mass was stabilized. The mass of a sample is considered at equilibrium when the variation of mass is less than 0.05% for 24 hours. This is also adopted by Chauhan et al. (2019) [53] and it is close to the one adopted by Champiré et al. (2016) [47] which was lower than 2% for at least one week.

3. Samples were then covered with a thin permeable sheet to avoid losing soil mass during the process and allow the water vapour to transfer in the meantime.

4. Seven different saline solutions (Table 3.5), were prepared in a saturated state. This was achieved by adding salt to the solution while mixing with a magnetic agitator until the salt crystals remain undissolved. Saturated solutions were poured into a sealed plastic box (see Figure 3.11b), and then place in a room with a constant temperature of 25°C. It was made sure that the salt solutions are always saturated during the experiment.

5. The test began with the lowest relative humidity (9%), and samples were placed in the box containing KOH saline solution. Samples were weighed periodically (once per day) using a balance with an accuracy of 0.01 g. When equilibrium was reached at this RH level, samples were then transferred to the next higher relative humidity box.

6. A similar process continued until all samples were placed successively inside 7 boxes having an increasing RH until the last box.

7. Once equilibrium was reached in the last box with the highest relative humidity (97.3%), the data points for the sorption curve were obtained.

8. The samples were again transferred towards lower relative humidity boxes in descending order until the lowest relative humidity (9%). In this way, the points for the desorption curve are obtained.

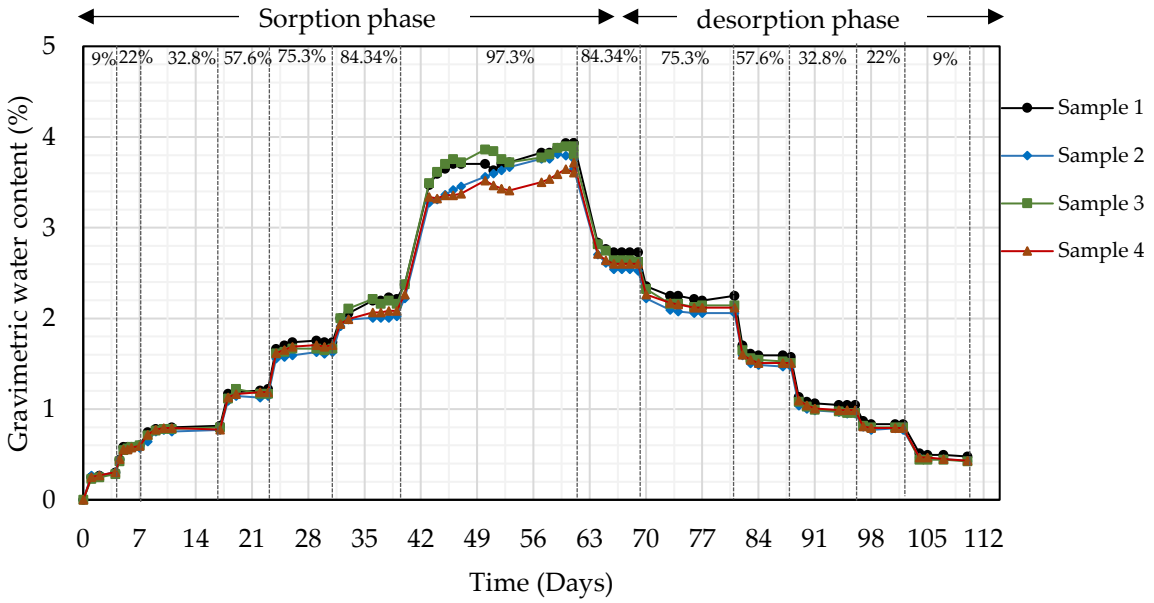

Figure 3.12: Variation of gravimetric water content with time when the samples were moved from RH of 9% to 97.3% for the sorption phase and vice versa for the desorption phase.

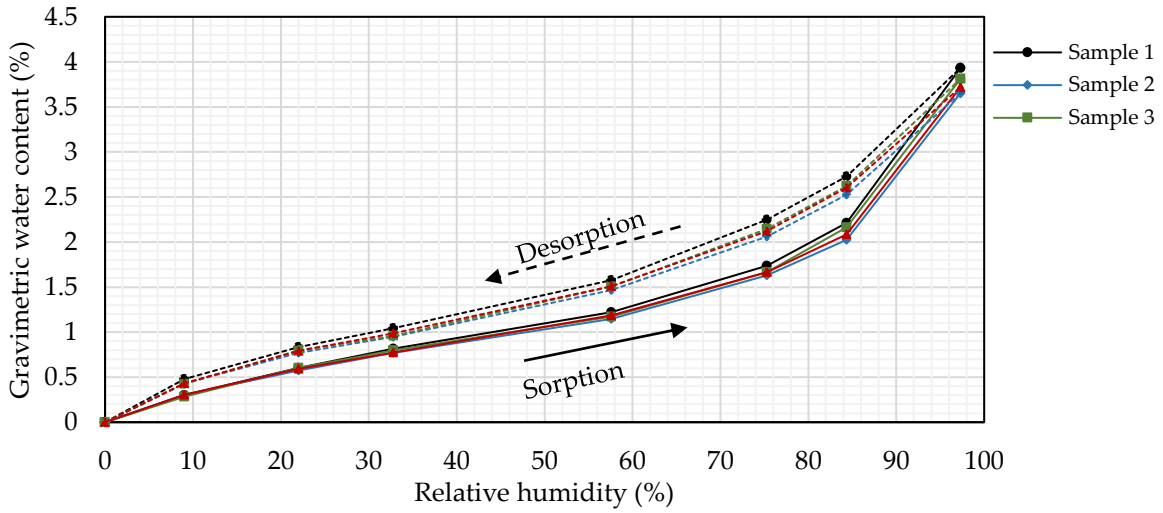

Figure 3.13: Variation of water content with respect to RH, showing sorption and desorption phases.

In total, it took about 16 weeks for the sorption and desorption phases to complete. Results of the four samples are summarized in Figure 3.12 showing the variation of gravimetric water content (w) with time at each RH. A good consistency in w is observed between the four samples, except for the highest RH of 97.3% where inconsistency in w is observed (Figure 3.12). At a relative humidity of 9%, the water content was at 0.3% for the sorption phase, and then it increased up to 3.8% at 97.3% relative humidity (see Figure 3.13). In the desorption phase, for the same relative humidity of 9%, the water content is 0.44%, highlighting the hysteresis effect. Hysteresis is defined as the difference in water content of the soil at the same corresponding suction obtained under the wetting and drying process. This phenomenon arises due to the non-uniformity of the pores.

The equilibrium water contents were then related to the corresponding suction from Table 3.5 to realise the water retention curve (Figure 3.14). The suction from the saline solution method gives 7 points between s = 3.8 MPa and s = 331.3 MPa, for these states, mass water content w varies between 0.4% and 4% (Figure 3.14). By using this method, the hydric state is modified only through equilibrium with the gaseous phase. No high-water content (low suction values) can therefore be reached with this method. To complete the retention curve with even lower suction values, another method "Filter paper" that covers the entire suction range will be used.

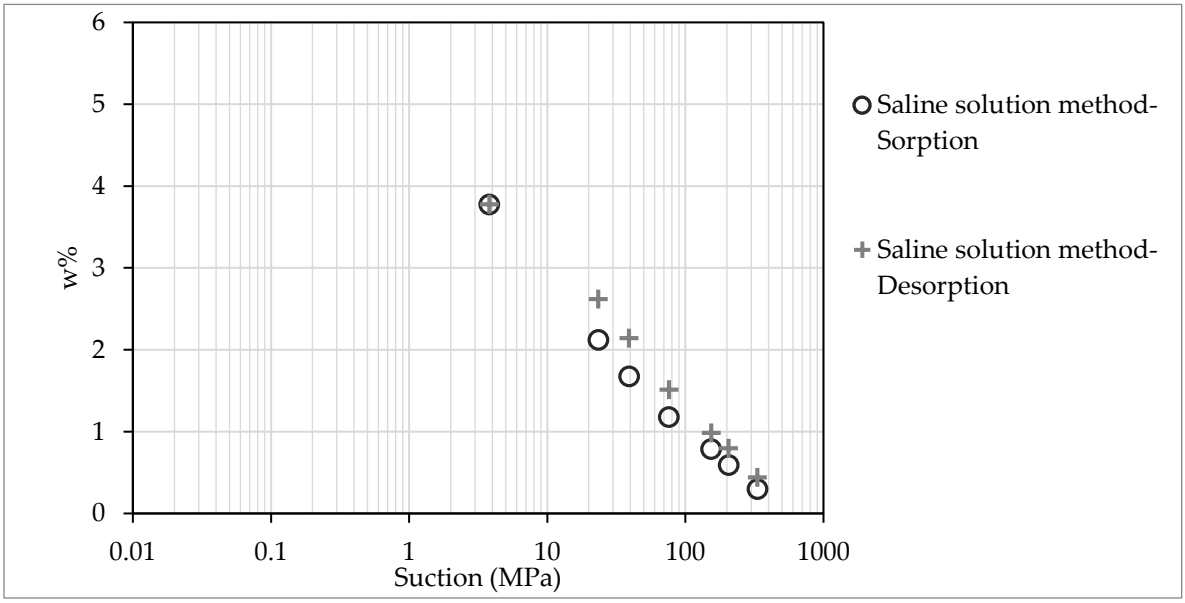

Figure 3.14: Soil water retention curve using the saline solution method

b) Measuring suction thanks to the filter paper method

The second method focused on a specific suction, corresponding to the manufacturing stage. Indeed, this state is very moist and thus is out of the range of suction controlled by saline solution (it cannot be reached through equilibrium with the atmosphere). However, because this state corresponds to the initial one for the rammed earth structures done with this earth, it is essential to know the corresponding suction. Therefore, the filter paper method was used to determine it [116].

The filter paper method is a soil suction measurement technique It is the only method which covers the full range of suction measurements (Table 3.4). The working principle behind the filter paper is basically that the filter paper comes into equilibrium with the soil either through vapour flow or liquid flow. At equilibrium, the suction value of the filter paper and the soil will be the same.

Furthermore, both matric and osmotic suction measurements are possible with the method. Matric suction arises from the difference in pressure at the air-water interface whereas osmotic suction arises from the osmotic effects due to dissolved solutes in the pore water.

In this study, the osmotic suction could be negligible, since distilled water was used to prepare samples, and the solute concentration is expected to be very low. Therefore, only matric suction is measured using "Whatman 42" filter paper. The calibration chart for Whatman 42 filter paper proposed by (ASTM D5298-03 2003) is given in Figure 3.15, the calibration chart corresponds to both total and matric suction.

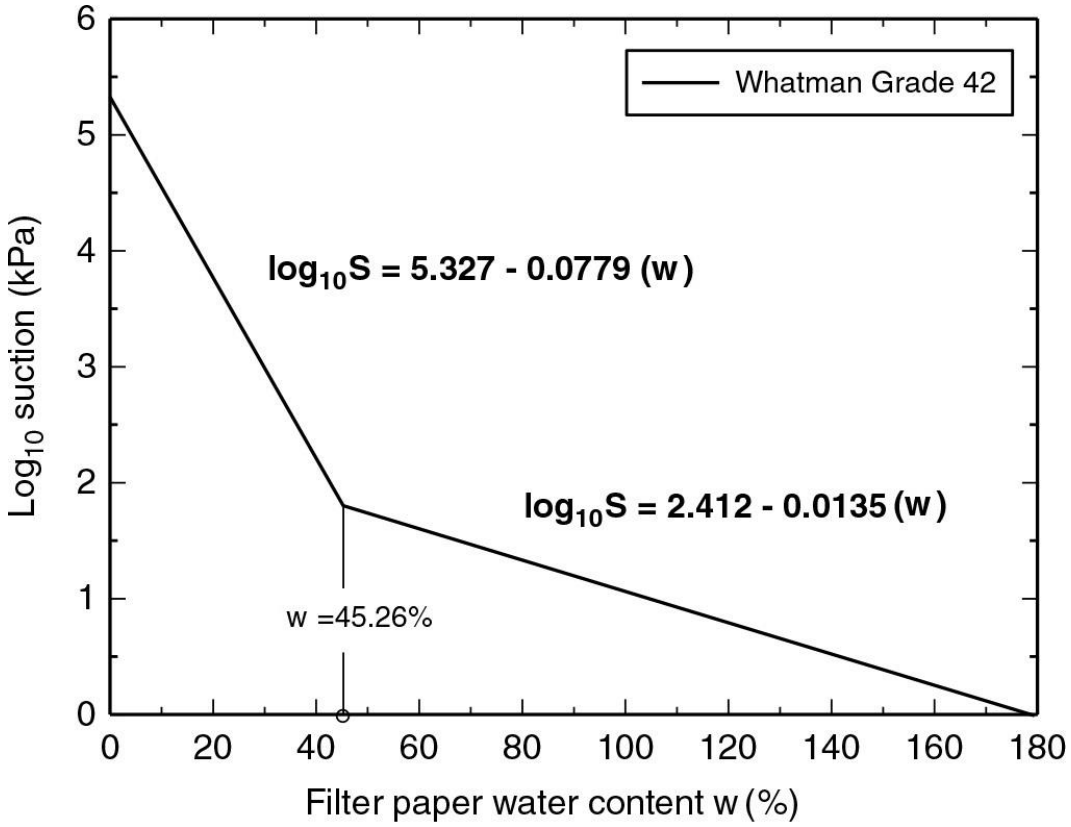

Figure 3.15: Calibration curves for Whatman 42 Filter Paper (ASTM D5298-03 2003)

To measure the matric suction with filter paper, the following experimental procedures were followed:

- Six small cylindrical samples with (D = 5 cm, H = 2 cm) were prepared by static compaction. Their mass varies between 81g and 84 g (Table 3.6). The surfaces of the soil samples are smooth and flat for establishing good contact between the soil sample and the filter paper.

- Wathman.42 filter paper was protected from direct contact with the soil by using two larger protective filter papers. This will prevent the soil grain from sticking directly to the filter paper but still allows the water or vapour to transfer between the sample and filter paper.

- Three sandwiched samples were prepared (Figure 3.16a), each using two RE samples. In between the two samples, the filter paper was carefully placed in the middle by using tweezers. The interface between sandwiched samples is covered by duct tape.

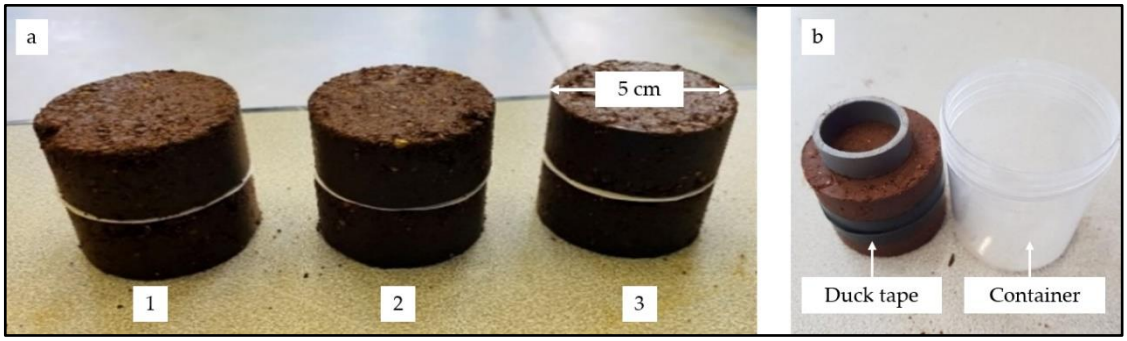

Figure 3.16: Filter paper method to measure suction of RE samples. (a)The filter paper is placed in between two pieces of samples, (b) Each sandwiched sample is sealed by duct tape and placed in a sealed container.

Table 3.6: Summary of the cylindrical sample of size (Φ = 5 cm, H = 2 cm) used in the filter paper test.

Sandwiched samples	Individual Sample	Mass (kg)	Dry density (kg/m³)	Porosity (-)
1	SF1	82.81	1900.73	0.28
	SF2	83.53	1917.25	0.28
2	SF3	81.62	1873.41	0.29
	SF4	84.11	1930.57	0.27
3	SF5	83.4	1914.27	0.28
	SF6	83.72	1921.62	0.27
	Mean	**83.20 ± 1%**	**1909 ± 1%**	**0.28 ± 3.4%**

- In total, three sandwiched samples with filter paper were prepared and put in sealed plastic containers to prevent any moisture exchange between the air inside and the air outside of the container (see Figure 3.16).

- Then, the sealed containers were put in a relatively constant temperature environment for seven days until equilibrium was reached.

- After equilibrium was established between the filter paper and samples, the filter papers were weighed to the nearest 0.001 g accuracy and were kept at 105 ± 5°C temperature for 24 hours inside the oven for water content measurement.

Table 3.7 summarizes the results of water content and the corresponding matric suction. The matric suction values were calculated from the calibration curve (Figure 3.15). Since the values of water content obtained (Table 3.7) are inferior to 45.3%, then the equation for determining suction from Figure 3.15 is given:

$$s(Log\ kPa) = 5.327 - 0.0779w \tag{3.9}$$

In simplified form:

$$s(kPa) = 10^{(5.327-0.0779w)} \tag{3.10}$$

Where *s(kPa)* is the suction and *w (%)* is the water content. Using equation 3.10, the matric suction was calculated and presented in Table 3.7. From the results, the mean suction for the initial state was $s_{0,m}$= 0.62 MPa with a standard deviation of 16%. We observed that this suction is below the suction induced by the KOH saline solution (3.8 MPa), it is logical since the samples are very moist in the manufacturing state. The results of suctions by using filter paper were added to the retention curve as shown in Figure 3.17.

Table 3.7: Results of matric suction using filter paper method

Filter paper	Mass of wet filter paper (g)	Mass of dry filter paper (g)	Water content (%)	Suction (MPa)
1	0.207	0.155	33.55	0.517
2	0.204	0.154	32.47	0.628
3	0.208	0.158	31.65	0.727

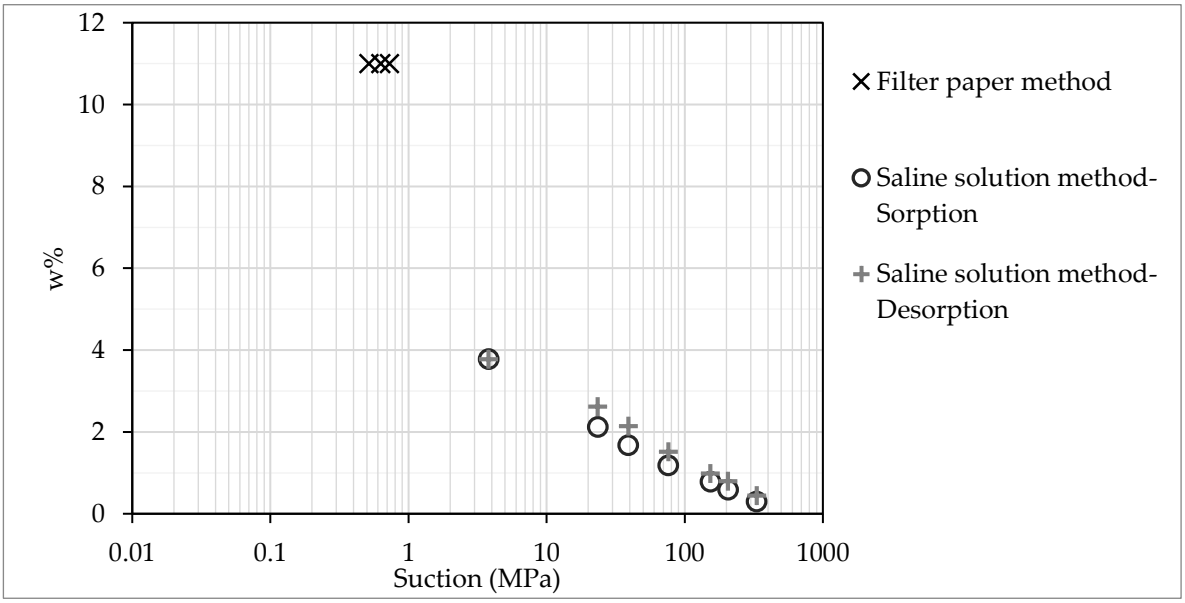

Figure 3.17: Soil water retention curve using saline solution method and filter paper method.

3.3.2.2. Modelling of the water retention curve

Modelling of soil water retention curve helps to predict the water retention properties over a larger range of suction. Numerous approaches have been proposed for modelling retention behaviour. An effective and commonly used for geo-mechanical applications relating water content to the matric suction was proposed by Van Genuchten [87], and is expressed as follows:

$$\theta(s) = \theta r + \frac{\theta s - \theta r}{[1 + (\alpha|s|)^n]^m} \tag{3.11}$$

Where θ is volumetric water content, s is suction pressure (MPa), θs saturated water content that describes the point where all of the available pore space in the soil matrix is filled with water. θr residual water content that describes the minimum water content beyond which there is no appreciable change in water with suction and extremely large changes in suction is required to remove additional water from the soil. α $(MPa)^{-1}$, n and m are fitting parameters. Another important parameter is known as the air-entry, this describes the suction where air first starts to enter the soil's largest pores and desaturation commences. The air-entry value marks the transition between the saturated and unsaturated state of the soil.

In this work, the Van Genuchten model was used to express the hydric state in a suction value. To model the whole retention curve Van Genuchten model (equation 3.11) was used. The model fitting parameters obtained by the mean square method were evaluated as α =1.507 MPa^{-1}, n=1.556, and m = 0.357. The Van Genuchten curve is shown in Figure 3.18, the air-entry value is 0.3 MPa. This model is classical for unsaturated soil mechanics and is suited even for a saturation state close to 100%.

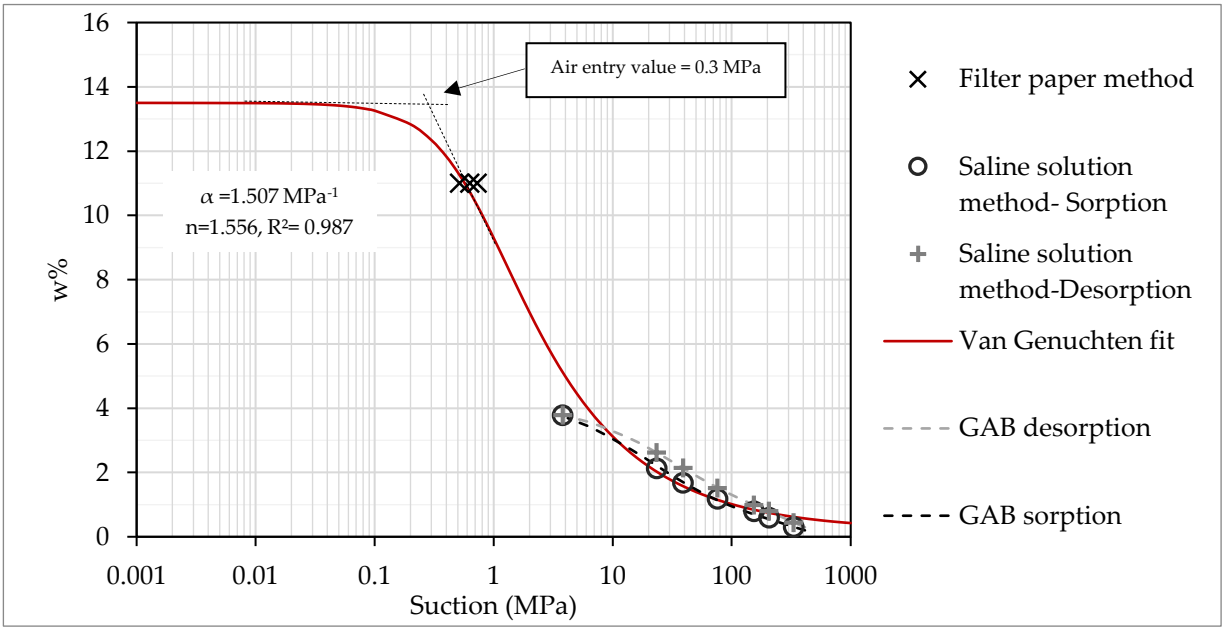

Figure 3.18: Soil water retention curve using saline solution method, filter paper method, Van Genuchten, and GAB models at 25°C.

In addition, another kind of model, namely the GAB model [117] was used. It is well suited for hygro-thermal applications of RE. The GAB model is described as follows:

$$w = \frac{C_1\, C_2\, RH}{(1 - C_2\, RH)(1 - C_2\, RH + C_1 C_2\, RH)}\, Wm \tag{3.12}$$

Where w is the gravimetric water content, RH is relative humidity (-), while C_1, C_2, and W_m are fitting parameters. The model fitting parameters obtained by the mean square method were evaluated as C_1 = 10.58, C_2 = 0.86, and W_m = 0.64 for sorption and C_1 = 10.58, C_2 = 0.78, and W_m = 0.94 for desorption. This model is a sorption isotherm classically used to describe the hygroscopic behaviour of isolation

materials. It is plotted in Figure 3.18 for sorption and desorption and is limited within the range of suction imposed by saline solutions because it is not suited for high levels of saturation.

By considering the two curves, it appears that only the VG model describes the high saturation degrees which concern the compaction wet state, but the GAB model is maybe more suited for the dryer hydric state during the exploitation of the earth building. Indeed, the difference between the 2 models is that the GAB model is a model for the 'sorption isotherm' relation whereas the VG model is a 'soil water retention' model.

3.3.3. Hydraulic conductivity

Hydraulic conductivity is a measure of how easily water can pass through soil, high values indicate permeable material through which water can pass easily; low values indicate that the material is less permeable. Permeability properties are important for studying the liquid water movement in the RE. Hydraulic conductivity was determined on a small cylindrical sample using a triaxial device.

- First, the sample of size Φ = 5 cm, H = 10 cm was prepared by using a double compaction method, which is well detailed in section 3.8.1.
- Rammed earth sample was inserted into the triaxial cell after the sample is covered with the rubber membrane fixed with O-rings (Figure 3.19).
- Before the beginning of the saturation stage, it was made sure that air bubbles were removed from all the connecting pipes and the pressure meters connected for cell pressure and pore water pressure. The method of saturation used here was stepped saturation. In this method, cell pressure increments of 100 kPa were applied, and the evolution of pore water pressure was monitored.

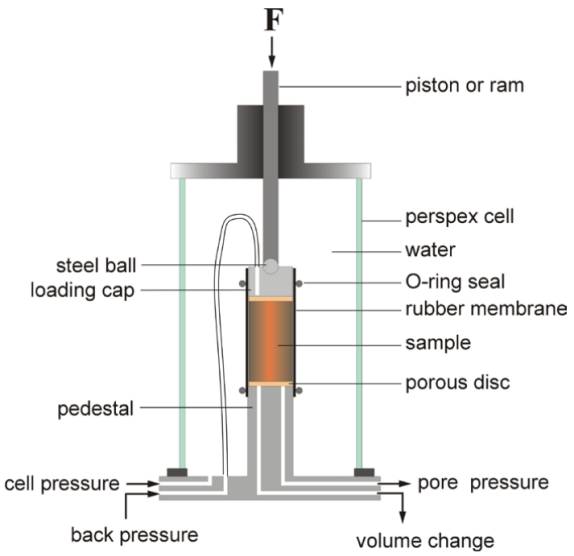

Figure 3.19: Triaxial cell used for permeability test [118].

- To check for saturation, the saturation of the sample was monitored by the value of pore pressure parameter $B = {\Delta u}/{\Delta \sigma_3'}$ where Δu is the change in pore pressure and $\Delta \sigma_3$ change in cell pressure = 100kPa. The criterion B ≥ 0.95 is usually accepted as an indication of near-saturated conditions.
- Once saturation is reached, a pressure difference of 20 kPa was imposed between the top and bottom of the sample, to establish a steady flow.

- The change in the volume of water flowing through the sample was recorded with time (Figure 3.20), and the test lasted for 20 min.

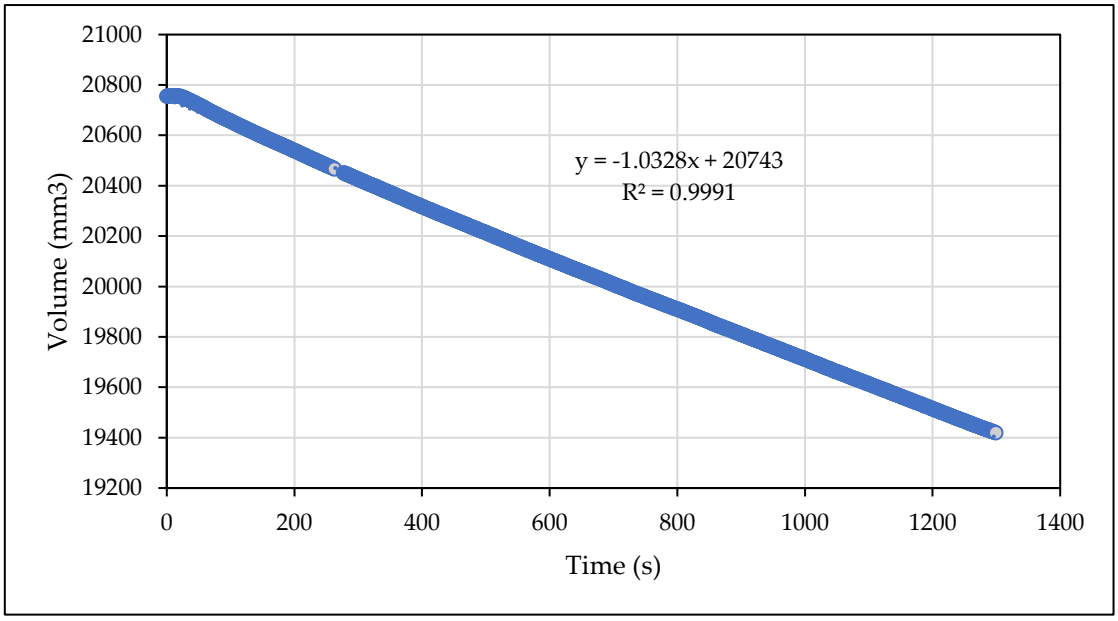

Figure 3.20: Evolution of volume of water passing through a sample during the permeability test.

The saturated hydraulic conductivity was calculated using the following expression of Darcy's law:

$$k_{sat} = \frac{\rho g \Delta L \Delta V}{\Delta u \Delta t A} \tag{3.13}$$

where ΔV is the change in volume recorded within a certain time Δt, A is the cross-sectional area of the sample, k_{sat} is the saturated hydraulic conductivity, ρ is the density of water, ΔL is the length of the flow path (i.e. length of the sample), and Δu is the pressure difference applied between the top and bottom of the sample (taken as 20 kPa, enough to create a flow path). The value of $\frac{\Delta V}{\Delta t}$ is taken from the slope in Figure 3.20. The calculated saturated hydraulic conductivity of the earth used is equal to 2.4 × 10^{-8} m/s. This value will be applied to determining the rate of capillary rise of RE, which will be described later in Chapter 5.

3.4. Sample Preparation and Instrumentation

After earth characterisation, the samples were then manufactured. Three sizes of samples were prepared (material scale, structure scale and wall scale shown in Figure 3.21). During manufacturing instrumented, intending to monitor the liquid water content inside the sample. At each scale, samples where manufactured with the water content adapted from the optimum water content obtained in Proctor test.

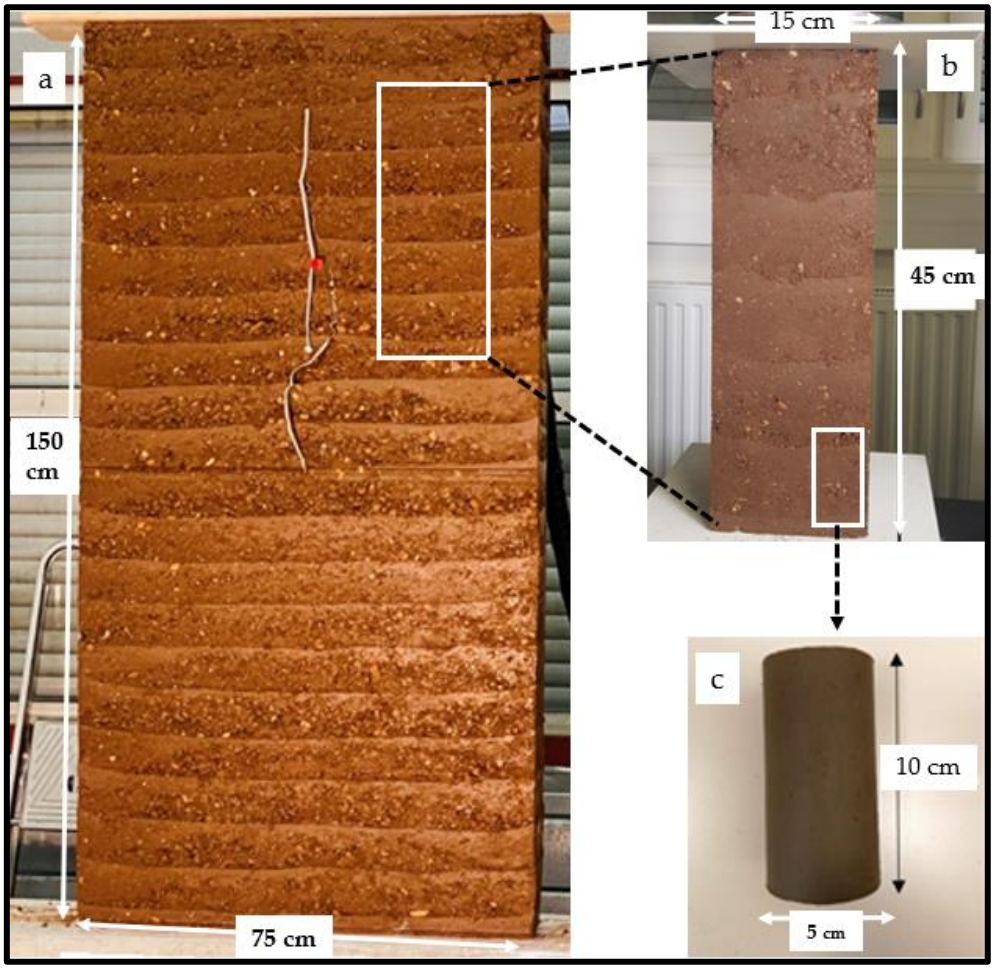

Figure 3.21: Different scales of samples manufactured, (a) wall scale, (b) representative elementary volume scale (REV) and (c) material scale.

3.4.1.Small cylindrical samples

18 samples were manufactured at material scale, and cylindrical samples (Φ = 5 cm, H = 10 cm) were prepared using the static double compaction method adopted by Chauhan, (2021) [90], with a total compaction pressure of 5 MPa.

Following are the steps for the preparation of the sample:

- Firstly, the soil which is sieved at 5 mm was mixed thoroughly at an optimum moisture content of 11% and left for water content homogenization for 1 day in a sealed container.

- Two cylindrical disks of 5 cm diameter and 1 cm height are inserted at the bottom of the mould. These cylindrical disks are used to facilitate the insertion of cylindrical pistons once the mould is turned.
- Around 430 g of moist earth estimated to obtain the desired dry density and height of the sample is poured inside the mould.
- A cylindrical piston labelled *A* (diameter 5 cm and height 12.5 cm) in Figure 3.21 is inserted at the top and pressed manually to be at least 1 cm inside the mould (2). The piston is rotated about the vertical axis to confirm that the piston is not getting stuck and is vertical in orientation. If the piston is not vertical, there can be abrasion between the piston and the inside of the mould, which can completely halt the process and damage the mould.
- Firstly 80% of the total compaction pressure, i.e. 4 MPa is applied at a displacement rate of 2 mm/s. The first stage of compression can be seen in (2) to (3) in Figure 3.22.
- The specimen is unloaded and the 2 cylindrical disks at the bottom of the mould are removed by holding the complete assembly up. Then the mould is carefully rotated so that piston *A* is now at the bottom of the mould assembly.
- Another piston *B* (diameter 5 cm and height 12.5 cm) is inserted from the top in the gap that was created before by the cylindrical disks (4)
- The loading plate is made to come in contact with piston B and 100% of the total compaction pressure, i.e. 5 MPa is applied from the top at a displacement rate of 1 mm/s (5).

The double compaction process is complete. In order to remove the sample from the mould, piston *B* is removed. In order to create a gap at the bottom of the mould, the mould is placed on a mechanical nut, a diameter of which is less than 5 cm. This assembly is pressed downwards, and piston *B* is inserted at the bottom. In order to move the mould downwards and not compress the specimen, another hollow cylindrical mould of an inside diameter of 10 cm is placed at the top of the assembly. The physical properties of all the samples are summarized in Table 3.8.

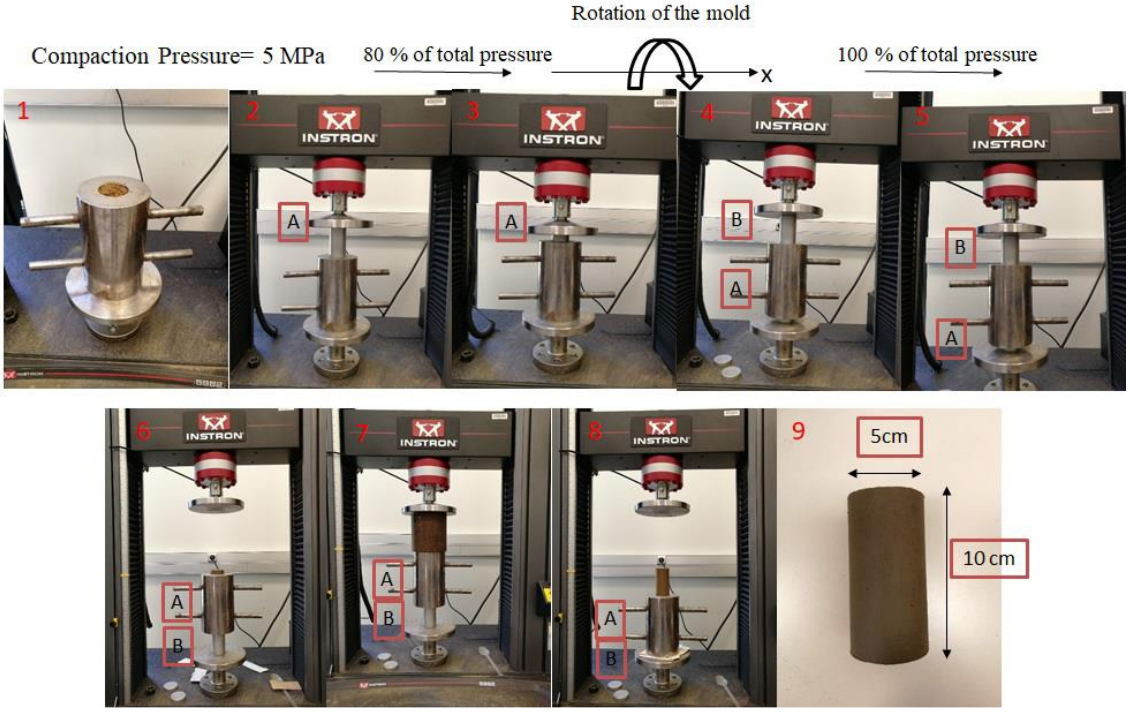

Figure 3.22: Procedure for cylindrical sample preparation using the static double compaction method adapted from Chauhan, (2021) [90].

Table 3.8: Summary of the cylindrical sample of size (Φ = 5 cm, H = 10 cm)

Sample Name	Mass (g)	Dry density (kg.m^{-3})	Porosity (-)
SS1	425.00	1951	0.26
SS2	422.83	1941	0.27
SS3	425.90	1955	0.26
SS4	426.80	1959	0.26
SS5	428.40	1967	0.26
SS6	395.60	1816	0.31
SS7	397.40	1824	0.31
SS8	394.00	1809	0.32
SS9	395.04	1813	0.32
SS10	391.77	1798	0.32
SS11	394.30	1810	0.32
SS12	397.20	1823	0.31
SS13	394.50	1811	0.32
SS14	402.88	1849	0.30
SS15	393.70	1807	0.32
SS16	391.10	1795	0.32
SS17	393.60	1807	0.32
SS18	425.92	1955	0.26
Mean	**405.3 ± 3.7%**	**1861 ± 3.7%**	**0.30± 8.8%**

3.4.2. RE columns (prismatic and cylindrical)

24 RE samples were manufactured. 21 Prismatic samples (15 cm × 15 cm × 45 cm) and 3 cylindrical sample (Φ = 16 cm, H = 32 cm) were manufactured by dynamic compaction of method. To do so, the following tools were used; soil mixer, metallic moulds (prismatic and cylindrical), and pneumatic rammer. The pneumatic rammer was used (Figure 3.23a), working by using compressed air that moves the piston up and down. The pneumatic rammer was connected to an air compressor by using a flexible tube for a compressed air supply. The piston is connected to a rubber hammer (square or round) which can be changed depending on the type of compaction.

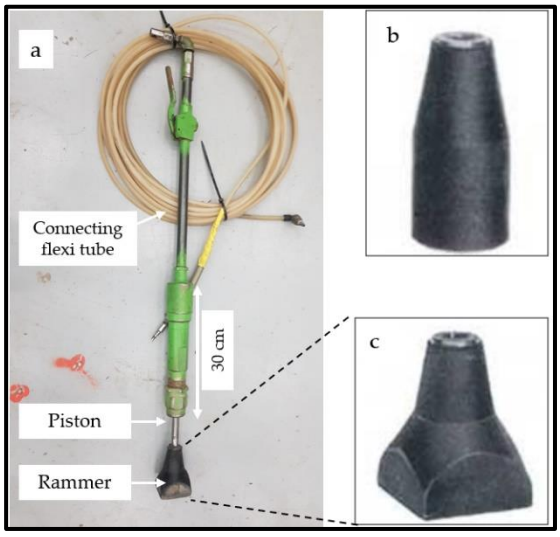

Figure 3.23: (a) Pneumatic rammer used for compaction, (b) Round rammer and (c) Square rammer.

The following procedures were adopted for the preparation of the rammed earth columns:

- Soil preparation

First, the earth was sieved at 20 mm using a large metallic grid sieve (Figure 3.24b). About 25 kg of sieved earth, which was enough to make one sample was taken. The mass of soil required was estimated using the dry density (obtained from Proctor) and the volume of samples, an excess amount of soil can be added to compensate for the loss of material during manufacture. A sufficient amount of water was added to the earth to achieve the optimum water content of w=10%. The earth was thoroughly mixed in a mechanical mixer, (see Figure 3.24c), and then covered for at least 1 day to allow the moisture to be homogenized. A choice of 1 day was made because it's practical since it assures the good distribution of water. A similar approach was done by Beckett, (2012) [72] and Xu et al, (2017) [85] who let the soil mix for 1-2 days in sealed bags to achieve water content homogenization.

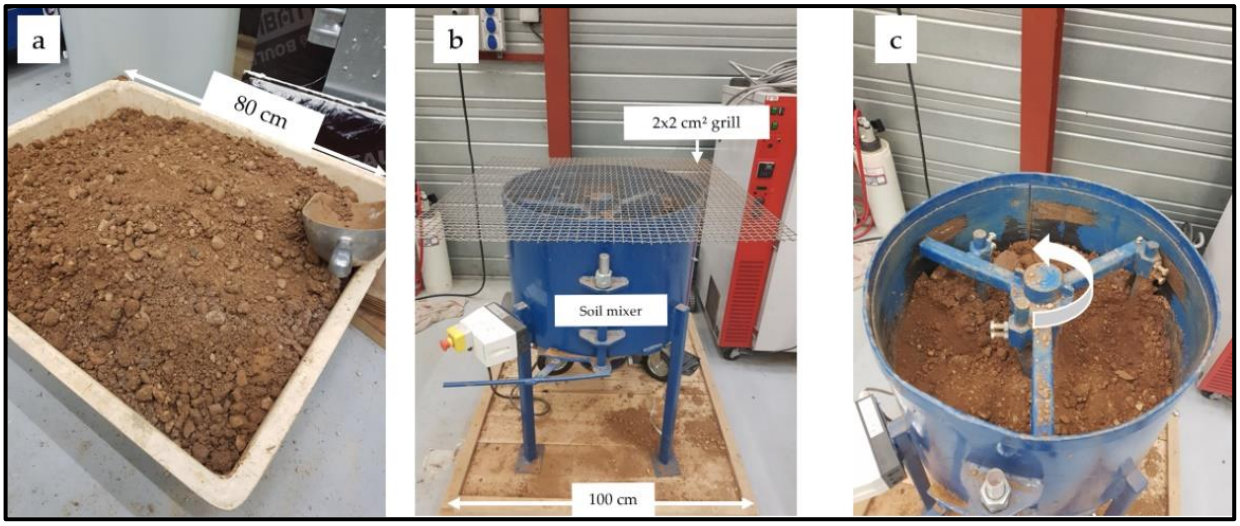

Figure 3.24: Soil preparation steps; (a) Preparing the earth (b)Sieving and directing to the mechanical mixer (c) Mixing the soil with water.

- Compaction

We designed a specific steel mould, able to manufacture 15x15x45 cm samples, while it sustains the dynamic compaction. It has a vertical extension in order to make possible the levelling of the surface once compaction is finished (Figure 3.25). The mould was assembled then for each layer, moist soil (with a water content of 10%) was poured inside it with a thickness of about 14 -16 cm. The soil layer was rammed using a pneumatic rammer starting from the edges to the centre of the sample until reaching a levelled surface. This compaction procedure was repeated until the 6th layer. The top surface was levelled flat using a straightedge metal, and the mould was carefully dismantled (Figure 3.25c). All prismatic samples are summarised in Table 3.9.

Similar procedures were adapted for manufacturing cylindrical samples (Φ = 16 cm, H = 32 cm). The compaction was done in an existing metallic mould (Figure 3.26). The pneumatic rammer was equipped with a round rammer, (see Figure 3.23b) suitable for cylindrical mould. The moist earth was poured into the mould and compacted up to 4th layer. Then the top was trimmed to have a flat surface and the mould was dismantled (Figure 3.26). All cylindrical samples are summarised in Table 3.10.

After manufacturing, the sample's humid density (ϱ_h) was determined at a moist state, and then the dry density was calculated from the relation between the dry density(ϱ_d), humid density(ϱ_h), and water content(w) described in equation (3.11).

$$\rho_d = \frac{\rho_h}{(1+w)} \tag{3.11}$$

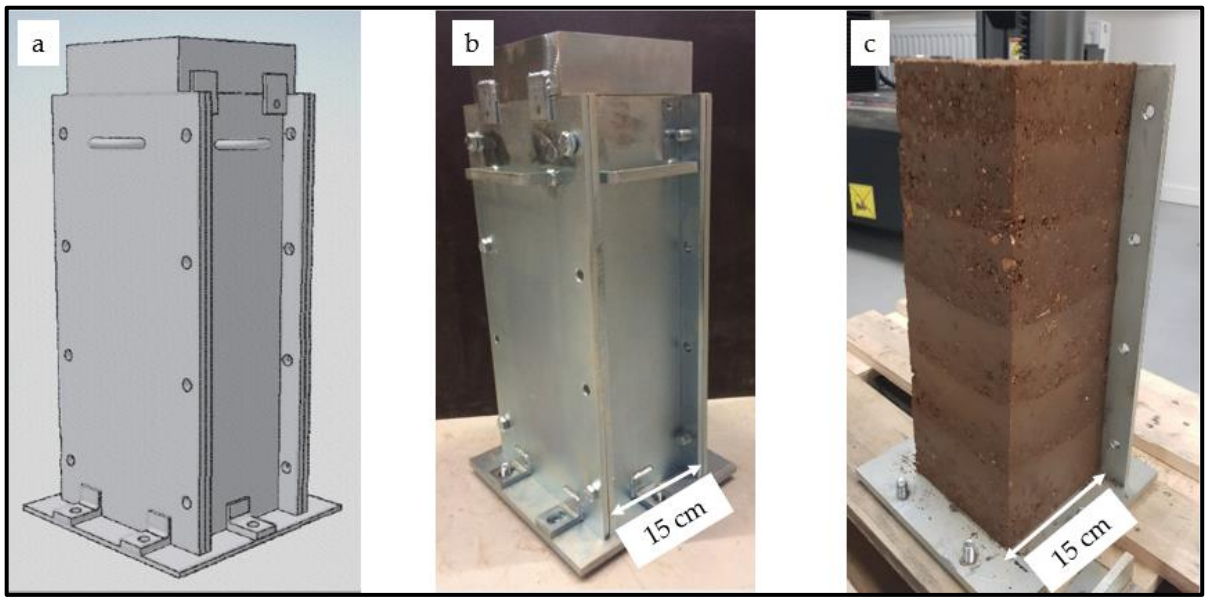

Figure 3.25: Prismatic RE samples manufacturing; (a) Designed mould, (b)Steel mould (c) Compacted sample

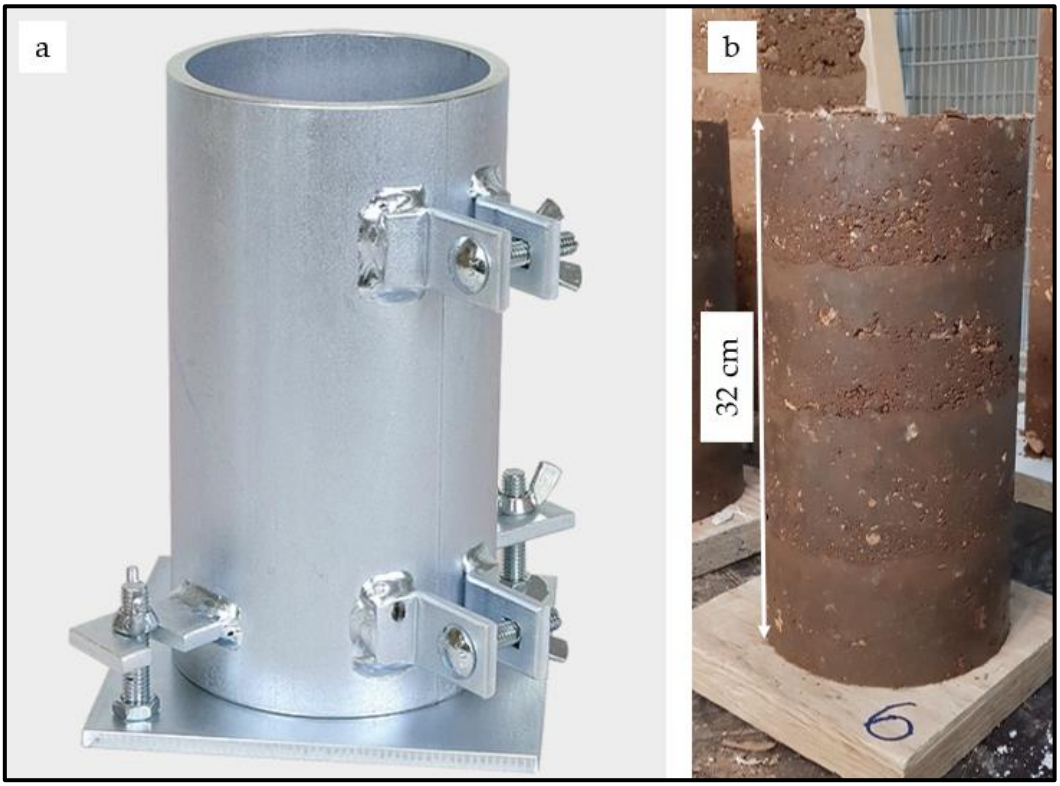

Figure 3.26: Cylindrical RE samples manufacturing; (a)Steel mould (b) Compacted sample

Table 3.9**:** Summary of prismatic samples (15 cm × 15cm × 45 cm) manufactured.

Sample Name	**Initial mass (kg)**	**Manufacturing water content (%)**	**Dry density (kg/m³)**	**Porosity (-)**
S1	21.5	10	1930	0.27
S2	20.8	10	1868	0.30
S3	21	10	1886	0.29
S4	21.967	10	1972	0.26
S5	21.627	10	1942	0.27
S6	20.64	10	1853	0.30
S7	21.05	9.95	1891	0.29
S8	20.51	10	1842	0.31
S9	21.327	10	1915	0.28
S10	20.697	10	1858	0.30
S11	21.401	10	1922	0.27
S12	20.927	10	1879	0.29
S13	20.52	10	1842	0.30
S14	20.95	10	1881	0.29
S15	21.3	10	1912	0.28
S16	20.6	10	1850	0.30
S17	20.35	9.5	1836	0.31
S18	20.7	10	1859	0.30
S19	21.117	10	1896	0.28
S20	20.827	10	1870	0.29
S21	21.04	10	1889	0.29
Mean	20.99±1.9%	9.97±1.1%	1885±1.9%	0.29±4.8%

Table 3.10**:** Summary of cylindrical samples (Φ = 16 cm, H = 32 cm) manufactured.

Sample	Dry density (kg/m³)	Porosity
C1	1990	0.25
C2	1926	0.27
C3	1976	0.25
Mean	1951 ± 1.7%	0.26 ± 5%

3.4.3.RE walls

Three identical walls (W = 0.75 × H = 1.5 × b = 0.2 m^3) were manufactured in the laboratory. The following tools were used in the manufacturing:

i. Metallic grid sieve- 20mm (Figure 3.24b)

ii. Soil mixer (Figure 3.24c)

iii. 8 Formwork with dimensions 75 cm × 130 cm

iv. Compactor -Pneumatic rammer with a square ram (8 × 8 cm^2) (see Figure 3.23).

v. Concrete beam base (180 cm x 40 cm x 20 cm)

vi. Sealing tape for the formwork.

The following procedures were adopted for the preparation of the rammed earth walls:

- Soil preparation

About 1.5 tonnes of earth sieved at 20 mm using a large metallic grid. D_{max} = 20 mm is indeed the maximum size of grains if we want to consider 'continuous' walls of 20 cm width. This size is smaller than in the real building, but the wall has a scale between $\frac{1}{2}$ and $\frac{1}{3}$ with respect to an element of elevation of 50 cm width and 3.5 m height. 500 kg of sieved earth, which was enough to make one wall was taken each time. The mass of soil required was estimated using the dry density (obtained from the Proctor test) and the volume of samples. An excess amount of soil can be added to compensate for the loss of material during manufacture. A sufficient amount of water was added to the earth to achieve the optimum moisture content of 10%. The earth was thoroughly mixed in a mechanical mixer and then covered for at least 1 day to allow the moisture to be homogenized (see Figure 3.24).

- Formwork assembling

A concrete beam was placed on two pieces of wood to keep them elevated from the floor. The formwork was then assembled on a concrete base. Two types of formwork were used metallic and wooden formwork. Wooden formwork was placed to support the side of the wall while metallic ones were used to covering the front and back. The metallic formwork used constituents of two parts; the top and bottom part. The bottom half was first assembled to facilitate compaction (Figure 3.27a). After compacting the first half of the wall, the second half of the metallic formwork was assembled (Figure 3.27b) and then compaction continued.

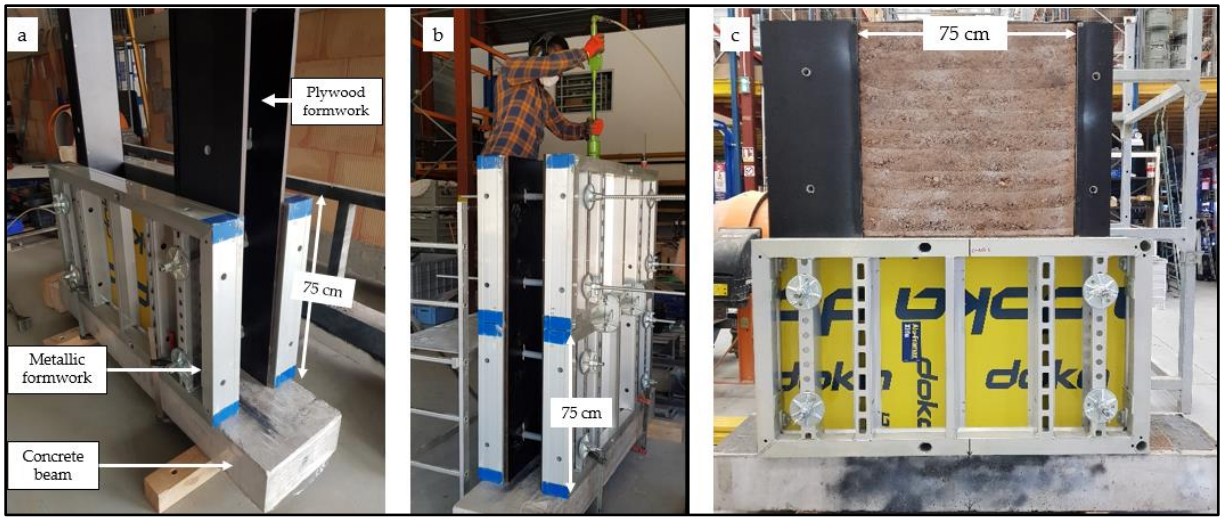

Figure 3.27: Protocols for manufacturing RE wall (W = 0.75 × H = 1.5 × b = 0.2 m^3); (a) Assembly of metallic and plywood formwork, (b) Compaction by using pneumatic rammer and (c) Removing formwork after compaction.

- Compaction

Moist soil was poured with a thickness of about 14 -16 cm into the mould. The soil layer was rammed using a pneumatic rammer starting from the edges to the centre of the sample. After compaction, the thickness of each layer was around 7 cm to 8 cm.

When compaction reaches half of the wall, another part of the formwork is stacked on top and compaction continues until reaching a top level (H = 1.5 m). In the end, the disassembling of the formwork was carefully done after the manufacturing by sliding each shutter to avoid any damage to the wall. In total, each wall is made of 20 compacted layers (Figure 3.28), the properties of all three walls are presented in Table 3.11

Figure 3.28: Three Rammed earth walls just after manufacture.

Table 3.11: Summary of walls properties after manufacture

Wall Name	Mass of wall (kg)	Dry density (kg/m^3)	Porosity (-)
W1	461	1862.63	0.29
W2	461.5	1864.64	0.29
W3	463	1870	0.29
	461 ± 0.2%	1865 ± 0.2%	0.29

3.5. Instrumentation for monitoring the hydric state

During the tests, the hydric state inside RE samples is recorded as the water content and the relative humidity (RH). A direct approach to determining water content is by measuring the mass of a sample and deducing the amount of water present, this is known as gravimetric water content. A balance with a maximum load capacity of 30 kg and an accuracy of 0.01% was used. This method was employed for small cylindrical samples and RE columns whose mass can be easily measured. However, this method was not possible for the three walls due to its impracticality considering the mass of each wall was 461 kg.

Other techniques were used to monitor the hydric state by equipping the samples with various instrumentation. These instrumentations include:

- Capacitive sensors - for RH and temperature measurements
- Time Domain Reflectometry (TDR) - for volumetric water content measurements
- Induced polarization (Electrical measurements) using geophysics technique – for water content.

3.5.1. Capacitive sensors

To be able to record the relative humidity (RH) and temperature inside the sample, capacitive sensors were used. A capacitive humidity sensor measures relative humidity by a variation of the capacitance of the capacitor. A capacitor is a sensitive element whose dielectric constant consists of a hygroscopic substance (polymer) a few micrometres thick which absorbs the water molecules contained in the air environment. A variation of the dielectric constant of the thin layer is then observed and, consequently a variation of the capacitance of the capacitor [119].

There are different kinds/brands of capacitive sensors, in this work, an SHT75 sensor type was chosen because of its small size, cost-effectiveness and relative ease to use (see Figure 3.29).

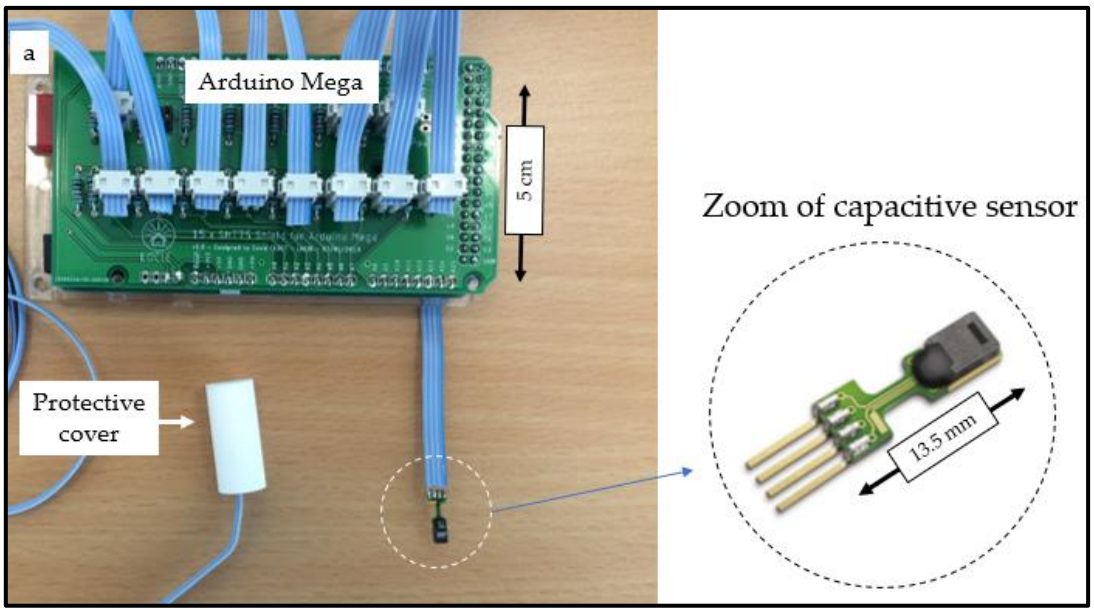

Figure 3.29: The capacitive sensor used for relative humidity and temperature measurement. The sensor is covered using a permeable protective filter. Data acquisition is done by a microcontroller (Arduino Mega).

The operating range of this sensor is from 0 to 100% RH. The typical accuracy of SHT75 sensors for the measurement of relative humidity is 1.8% RH for the range of 10 to 90% RH. The uncertainty in the measurement rises to 4% RH at either very low RH (less than 10%) or very high RH (greater than 90%) as shown in Figure 3.30a. The sensor offers a wide range of temperature (from -40 to 123.8 °C) (Figure 3.30b), but only a temperature range between 10°C to 40°C can be measured with a good accuracy of less than ±0.4 °C. Our temperature measurements will stay in that range.

However, long-term exposure to conditions outside the normal range, for example at humidity greater than 80% RH, may temporarily offset the RH signal (+3% RH after 60h). The sensor gradually returns to the calibration state after returning to the normal range.

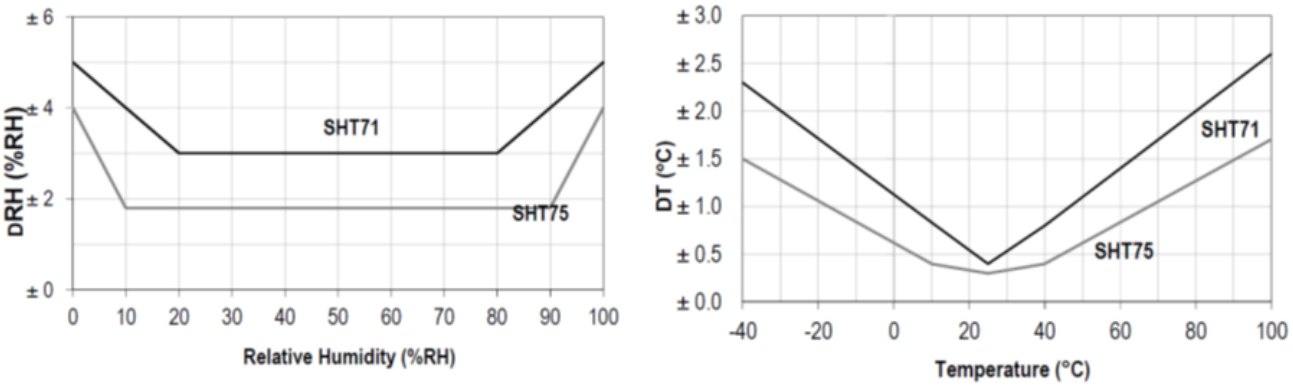

(a) (b)

Figure 3.30: The RH-tolerance at 25 °C (a) and temperature tolerance for the SHT sensor(b) (data given by the Sensirion SHT75, (2011) [120].

SHT75 sensors were calibrated in a small insulated and confined chamber, in the LOCIE laboratory. Each sensor was protected with a filter (Polyethylene sintered) (see Figure 3.29) which prevents damage during compaction, since sensors are included in the earth at a given depth, during the sample manufacture process. This filter also prevents the contact of the SHT with direct moist soil but is very permeable to the water vapour such as the relative humidity in the earth's pores is the same as the relative humidity inside the protective filter. Sensors were connected with "Arduino Mega" for data acquisition (Figure 3.29). The calibration chamber in Figure 3.31 was designed in the laboratory. The calibration was done in two stages firstly, the temperature was calibrated at a constant humidity and then humidity was calibrated at a constant temperature. A high-precision cooled mirror hygrometer was used in parallel with the SHT sensors to record TH and temperature which will serve as reference data for calibration.

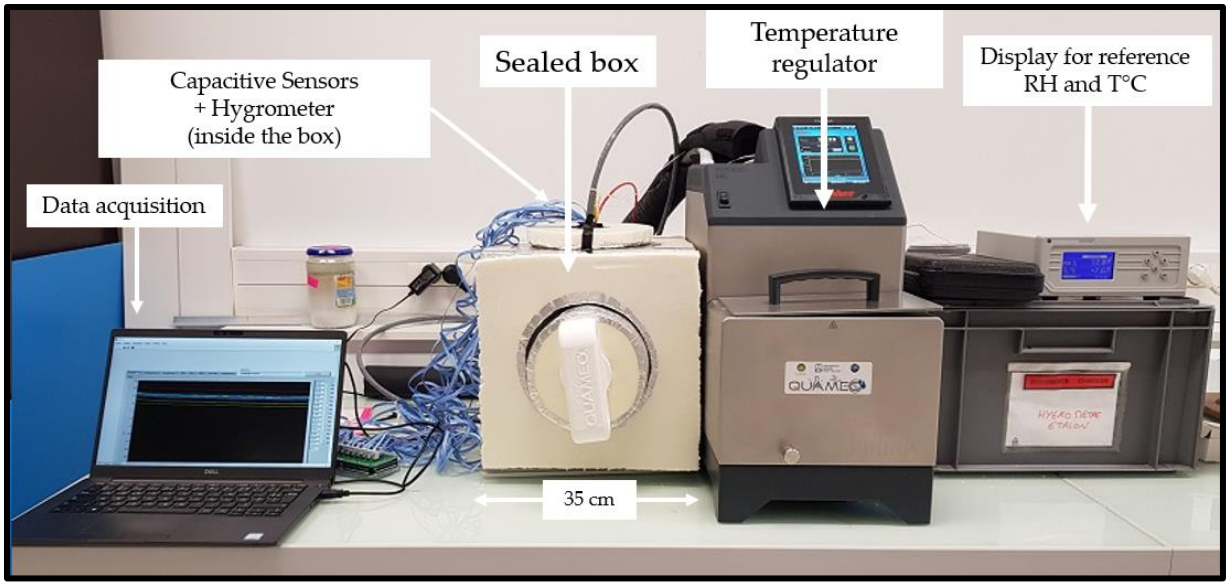

Figure 3.31: Calibration chamber for SHT capacitive sensor for RH and temperature.

For temperature calibration, the humidity in the chamber was kept as low as possible by using silica gel which absorbs ambient moisture, this helps to reduce uncertainty in the calibration. The temperature inside the calibration chamber was varied from 5°C to 30°C with steps of 5°C. The temperature recorded by SHT75 sensors is plotted along with the real temperature measured by the cooled mirror hygrometer as shown in Figure 3.31. The calibration curve shows a very good correlation (with a regression value of 0.999) between the temperature measurements by SHT sensors and the ones from reference data (Figure 3.32). A discrepancy in measurement is observed for temperatures less than 10°C (Figure 3.32), this has already been noted by the supplier in Figure 3.30b. In humidity calibration, the temperature inside the calibration chamber was maintained constant at 25°C. By using saturated saline solution, different RH were attained inside the calibrating sealed box. At each respective RH, data from SHT75 sensors were recorded and plotted against the RH of the box measured by a cooled mirror hygrometer (Figure 3.33). From the results of the calibration of RH, a very good correlation between the SHT measured value and a reference RH value was observed with a regression value of 09999. This means that, the SHT capacitive sensors provide accurate measurements of RH and temperature, and were then used in the experiments.

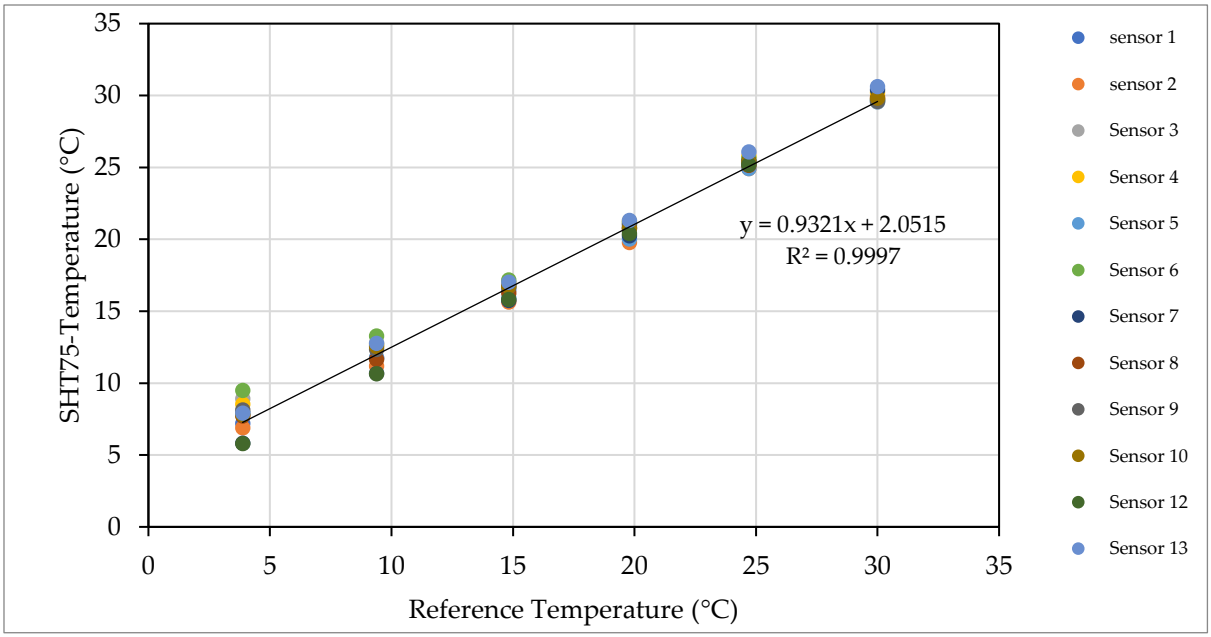

Figure 3.32: Capacitive sensor calibration for temperature

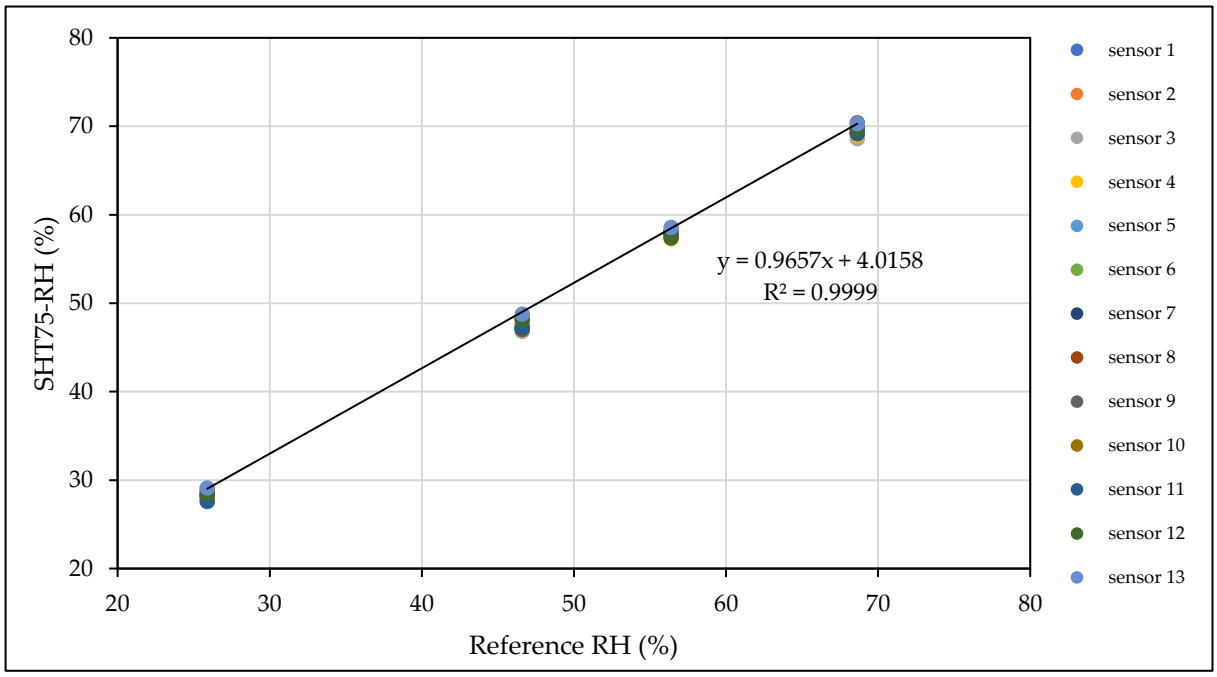

Figure 3.33: Capacitive sensor calibration for relative humidity

3.5.2. TDR

Time Domain Reflectometry (TDR) method is a technique applied to determine the volumetric water content inside the wall [121]. TDR working principle is based on the determination of the apparent permittivity of porous materials using the measurement of electromagnetic pulse propagation time along the rods of the measuring probes. The dimensionless value of the apparent permittivity is the main factor evaluated during the measurement.

Apparent permittivity is a measure of a material molecule's behaviour under alternating electromagnetic fields and after its release. The dipolar character of the water molecule causes a high value of the apparent permittivity that equals 80. On the other hand, the apparent permittivity value of air equals 1 and that of solid materials is between 2 and 9. The difference between the values of the apparent permittivity of water and other phases is essential for moisture evaluation in the moist porous media [122].

One of the most essential pieces of equipment in TDR measuring is the TDR probe (Figure 3.34), they consist of, (i) measuring rods, inserted into the measured material, (ii) coaxial cable connecting the sensor to the TDR-meter, and (iii) dielectric cover, where the rods are fixed and connected to the coaxial cable. The TDR probe used in this study was TRIME-PICO-32 (Figure 3.34b), having measuring rods 10 cm long. This TDR was first calibrated by measurements on saturated sands and compacted soils of known volumetric water content. It was found that the TDR provides a measurement of the volumetric water content with an accuracy of ±2% in the entire volumetric water content range (0 to 100%).

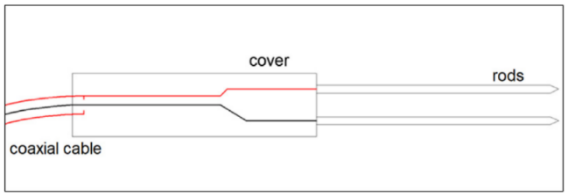

(a) (b)

Figure 3.34: (a)Typical TDR probe design, (b) TDR probes used in this study for volumetric water content measurement.

3.5.3. Induced Polarization (Geophysical technics)

Induced polarization is a non-destructive method for imaging the water content of soil or rocks through electrical surveying. This method is commonly used in geophysics. This method was done by Feras Abdulsamad. who was a Post-Doctorate working in parallel with this thesis on the same VBATCH project.

Abdulsamad et al. (2020) [123] proposed to use of the induced polarization method for imaging the water content distribution of RE materials. In this method, the measurement could be realized in the frequency domain (using alternative current varies between 0.1 and 1KHz), or in the Time domain (continuous current). The latter was used to measure the water content of the RE sample in the present study (Figure 3.35).

Samples were equipped with electrodes held firmly by a rubber band. Four electrodes are used to carry on the measurements. One pair of electrodes will inject the electric current and the other for measurement of the electrical conductivity and normalized chargeability. Electrical conductivity describes the ability of a porous body to conduct an electrical current. Normalized chargeability describes the ability of a body to store reversibly electric charges under the action of an external (primary) electrical field [124], [125]. These measured electrical properties can be connected to the density of the material, its clay content, and its volumetric water content [126]–[128]. More about the induced polarization method can be found in Annex 1 and 2.

The induced polarization method was used in parallel with other methods discussed previously. An advantage of using this method is, its non-destructive nature of measurements making it possible to detect the hydric state from the surface of the wall, a technique that can be employed in the site to a real building.

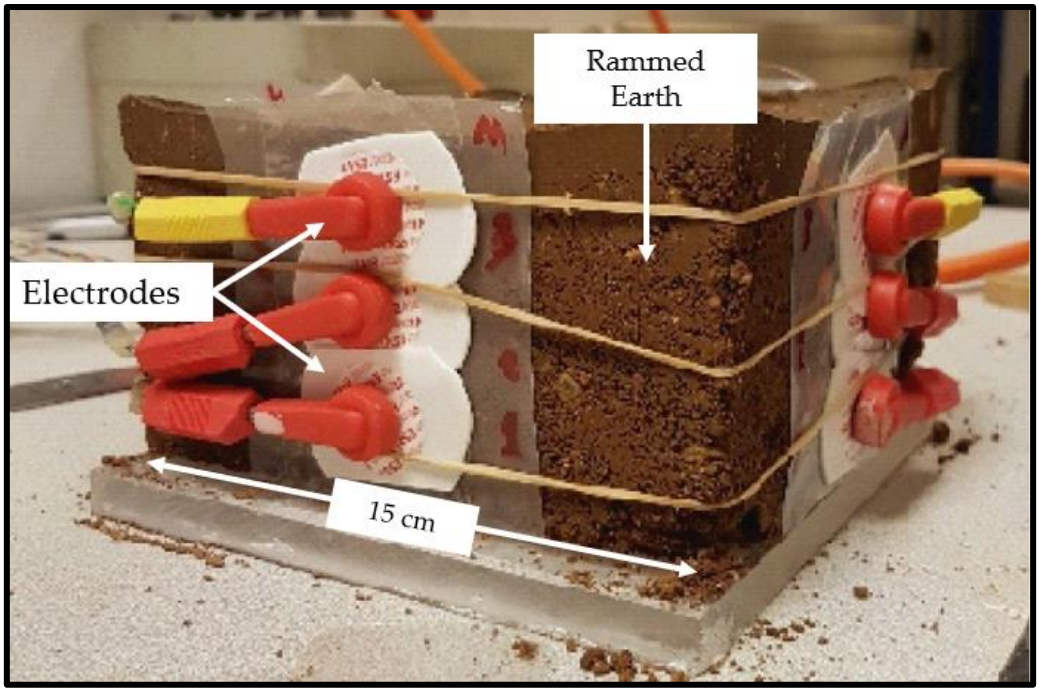

Figure 3.35: Measurements of water content in RE sample by using Induced polarization method (a geophysical method)

Chapter 4

4 Influence of drying on the mechanical behaviour

This chapter deals with the impact of hydric state evolution on RE mechanical behaviour during the earth's 'young age'. Indeed, as already explained, manufacturing RE structures implies wet compaction, which has as consequence to have an initial hydric state of the earth that is not yet in equilibrium with the surrounding HR conditions. In particular, compressive strength, elastic modulus, and dynamic viscosity coefficient will be focused on during this initial drying. It was decided initially to work on three scales which are: Material scale which is equivalent to a single layer in a RE building, 'Columns scale' which is considered as a representative elementary volume with multiple layers, with respect to the D_{max} considered (20 mm), and wallets whose scale is equivalent to half of a real RE building's wall. At both scales, samples were placed to dry in ambient conditions. The objective of the present work was then to follow, at the same time, their hydric state and their corresponding mechanical characteristics at regular intervals of time.

Chapter outlines

4.1 Research problematic

Once constructed, RE structures always have a non-uniform hydric state. First, they dry from the initial moist state due to wet manufacturing water content. Later, during their lifetime, they are subjected to varying relative humidity of the surrounding climatic conditions (indoor-outdoor). Finally, they can potentially undergo accidental wetting from rainfall roof infiltration, capillary rise or other hydraulic damage inside the building. This creates a non-uniform hydric state of the indoor-outdoor RE wall.

The experimental studies presented in the literature review have made it possible to highlight the evolution of mechanical behaviour with respect to varying drying conditions. From the literature review, it was observed that most of these studies were done on a small scale with homogenous samples (with respect to their density) and uniform hydric state (equilibrium reached each stage of the drying). Indeed, real RE buildings are made of several layers, with non-uniform density, dry under varying atmospheric conditions, and with a non-uniform water content field. Therefore, investigation at the material scale and equilibrated hydric states are not sufficient to understand the RE response.

The evolution of mechanical resistance along drying has already been studied in the literature. However, in order to enhance construction technology, more practical questions are left unanswered in the literature with proper quantification. For instance, with the prefabrication process, large prefabricated RE panels are produced on the ground before being lifted to be placed on top of each other to form a wall-bearing structure (see Figure 4.1) in the building site of Orangery Confluence building. Questions raised in this case are thus the following:

- How long does it take for RE panels to attain sufficient strength for the next wall elevation?

- Does the current answer based on the builder's experience well estimated or is the drying time overestimated?

- Are there quantifications of how much the strength increases at a particular time?

- Can the other mechanical characteristics (elastic modulus, viscosity) be quantified as well?

This chapter will thus present an experimental campaign focused on the initial drying of RE after manufacture. Suitable boundary conditions are adopted, which represent what's happening in a real construction scenario. Mechanical characteristics will be investigated at regular intervals of drying time.

In the last part, this work will be carried out in order to move towards the development of a hydromechanical model, thus the hydric variable chosen is suction since various hydro-mechanical models can be based on it in the unsaturated soils framework.

(a) (b)

Figure 4.1: RE construction using prefabricated RE panels, (a) onsite compaction of prefabricated wall panels, (b) RE panels being placed on top of each other to form a wall-bearing structure. (source: Le pies, Nicolas Meunier)

The theory behind drying of porous building materials

Drying is defined as the transfer of liquid water or vapour from the pores of a solid material to the surrounding air. Drying kinetics depends markedly on external factors as well as on intrinsic material properties. Drying of porous building materials such as RE occurs in two distinct stages, called in the drying process domain, the constant drying rate period (stage I) and the falling drying rate period (stage II) [129]–[131].

- Stage I

In the first stage, the water content is high, there is a continuous supply of liquid water across the material to the drying surface where the vapour diffuses to the external environment (Figure 4.2). The liquid migrates towards the drying surface by unsaturated capillary flow. In this stage, the drying rate is strongly controlled by external conditions (ambient RH, temperature, and airflow) above the drying surface.

- Stage II

The decrease of the water content in the material causes the formation of a drying front which is defined as the interface between the wet and dry zone (Figure 4.2). After a certain moment, the liquid flow to the drying surface becomes insufficient to compensate for the evaporative demand and, therefore, the drying front recedes into the material (Figure 4.2). In this stage liquid transfer by capillary flow prevail beneath the drying front and the rate of unsaturated flow within the porous solid limits the drying rate.

The drying front goes on receding as evaporation proceeds and, hence, the water content in the wet zone decreases further, increasing the path length for vapour diffusion across the material resulting in a falling drying rate.

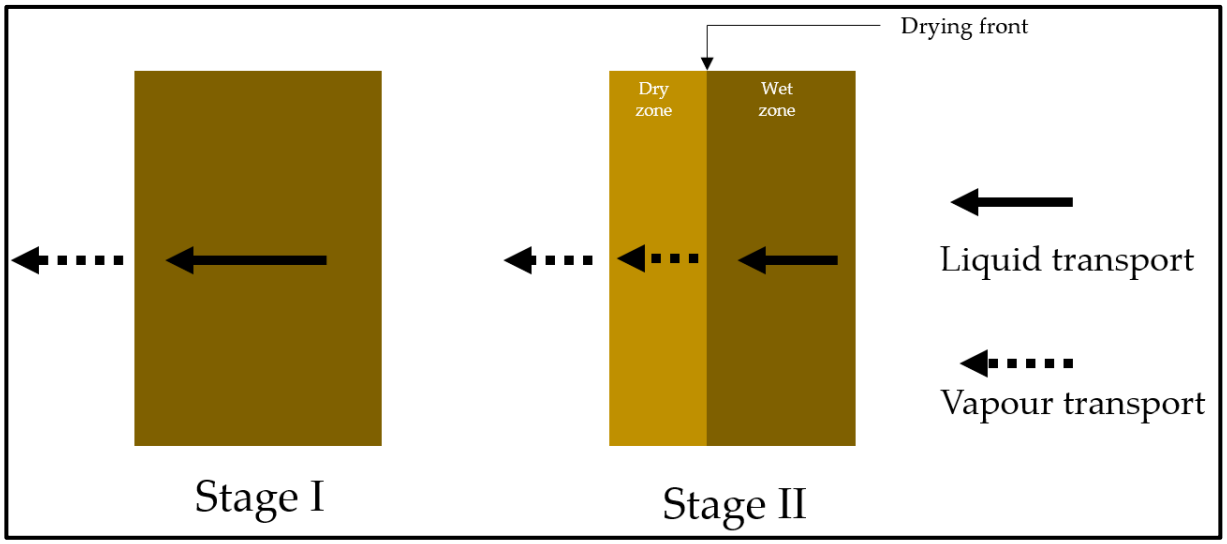

Figure 4.2: Representation of the two main stages of drying porous building materials.

In the next section, the experimental campaign will be presented. The schematic plan, of different kinds of experiments, is shown in Figure 4.3. The experiments will be done at three scales, where the hydric state and mechanical performances will be monitored.

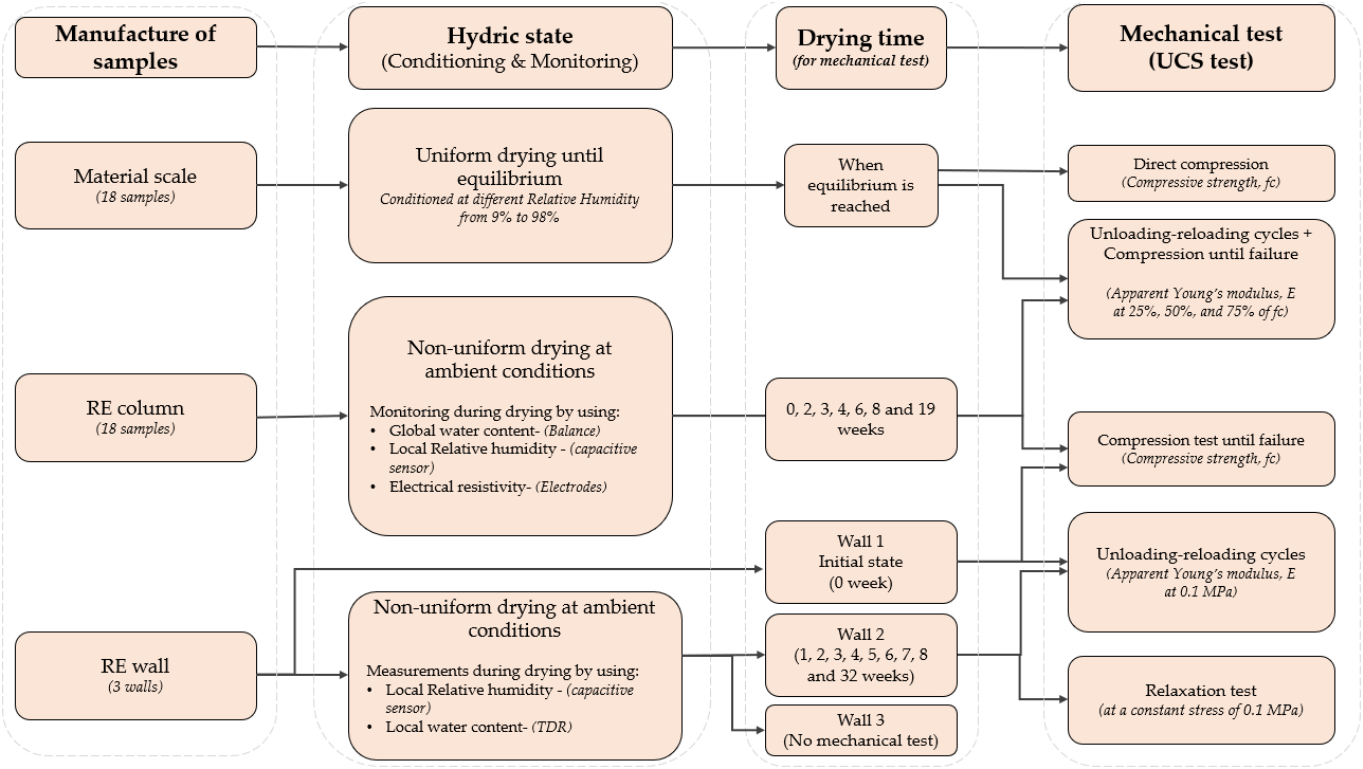

Figure 4.3: Schematic plan of the experimental protocol

4.2 Experiments at the material scale

The experimental campaign started with samples at material scale (H = 10 cm), which is equivalent to one layer of a RE wall (see Chapter 3, section 3.4). The aim is to quantify the influence of suction on the mechanical behaviour at the material scale. At this scale, the samples used have a uniform density and will be conditioned in a homogeneous hydric condition. Indeed, this scale is not representative of a real RE building, but the results will help us to compare with experiments done at a larger scale (to be described later on). Cylindrical samples (Φ=5 cm, H = 10 cm) was used, and the samples were manufactured by using a double compaction method as explained in the previous chapter 3 (section 3.4.1). This part of experimental work was realised by Dania EL SAHMARANY, who was an intern.

4.2.1 Experimental protocol

a) **Sample conditioning at different suction**

Samples were first conditions at different suction. A protocol similar to the one used in Soil water retention behaviour was used where the samples were placed in RH-controlled boxes with saline solutions (see Chapter 3, section 3.3.2). In total, 18 samples were used. 15 samples were conditioned in five different boxes (3 samples in each box) equilibrated at the following RH of 32.8%, 57.6%, 75.3%, 84.34% and 97.3%, at a constant temperature of 25°C. Table 4.1 shows the different saline solutions with their corresponding RH and suction imposed at a constant temperature of 25°C. The other 3 samples were not conditioned, instead, they were used at the initial manufacturing state with their suction corresponding to 0.62 MPa, determined by using filter paper (see Chapter 3, section 3.3.2.1). Figure 4.4 shows the samples inside the boxes, placed on top of the plastic mesh to separate them from the saline solution Each box was then closed and sealed to maintain their respective RH. The samples were weighed regularly to follow the variation of water content with time. Every time, the saturation of the saline solutions was checked, in order to ensure that samples equilibrate to the desired suction states. The equilibrium in the samples is supposed to be achieved when the variation of mass becomes less than 0.05% for more than 24 hours.

Table 4.1: Saline solutions with their corresponding RH and suction at 25°C

Saline solution	**$MgCl_2$**	**NaBr**	**NaCl**	**KCl**	**K_2SO_4**
RH (%)	32.8	57.6	75.3	84.34	97.3
Suction (MPa)	153.4	75.9	39	23.4	3.8

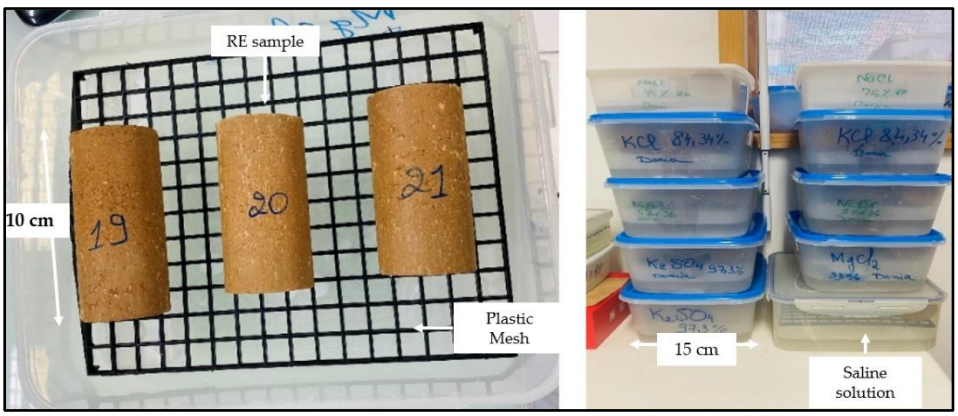

Figure 4.4: Cylindrical RE samples placed inside a box with a controlled RH

b) Mechanical testing

When samples reached equilibrium at different suction values, they were then tested mechanically. Unconfined compressive strength (UCS) test was performed to determine the compressive strength (fc), and Apparent Young's modulus (E_a). UCS testing was done on 18 samples, i.e., 3 samples for each 5 suction/RH conditions and 3 samples at initial condition. Firstly, 2 samples from a batch were compressed with monotonic loading to obtain the fc. Then, 1 out of every 3 samples from the batch, was compressed with unload reload cycles in order to obtain Young's modulus. The unload-reload cycles were done at 25%, 50%, and 75% of the fc. The samples were compressed with displacement control at a rate of 0.005 mm/s to remain in quasi-static condition. The displacement control was chosen because the failure is less sudden, and the post-peak behaviour can be observed.

4.2.2 Results and Discussion

The stress-strain curve for 3 samples conditioned at 23.4 MPa suction is shown in Figure 4.5. It shows the results of two samples compressed without unload-reload cycles and one sample compressed with unload-reload cycles. The mean value of fc was 3.77 MPa from all three samples (Figure 4.5). The modulus E_a was calculated on three reloading-loading E1, E2 and E3 corresponding to 0.66 GPa, 0.77GPa and 0.82 GPa. All the stress-strain curves for the UCS test are shown in Appendix A.

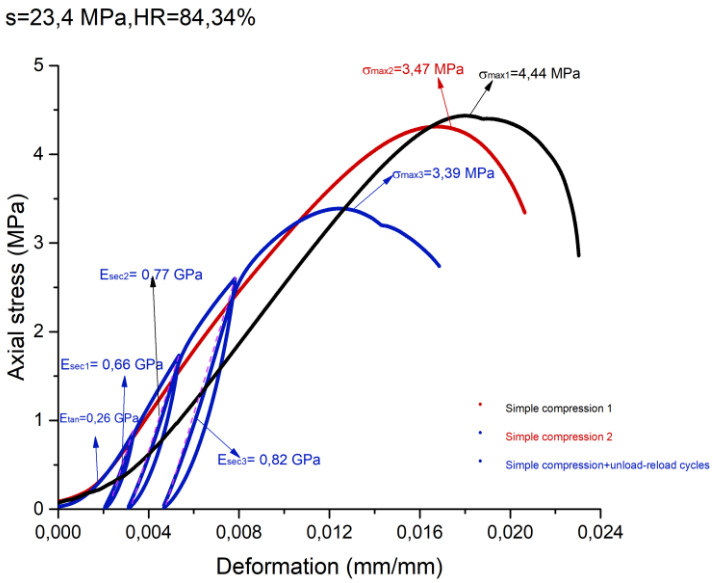

Figure 4.5: Axial stress-deformation curve during unconfined compressive strength test for 3 samples conditioned at 23.4 MPa suction

The results of compressive strength (*fc*) with their corresponding suction are presented in Figure 4.6. A global trend of the variation of *fc* with suction can be seen, the compressive strength increases significantly with the increase of suction (Figure 4.6). Suction is reported on a logarithmic scale. A linear relationship between the logarithm of suction and fc is observed. The value of *fc* varies from 0.33 MPa to 5.56 MPa for suction increasing from 0.62 MPa to 153.4 MPa. This behaviour is also consistent with the literature [53], [132]. The variation of the apparent Young's modulus with suction for all samples is

shown in Figure 4.7. A significant increase in the value of E_a is observed with an increase in suction. The trend is similar to the variation of the fc with the log suction. This can be related to the gain of mechanical resistance of RE building upon drying. Inversely, this can also be related to the loss of mechanical strength for unusual water entry in the RE building.

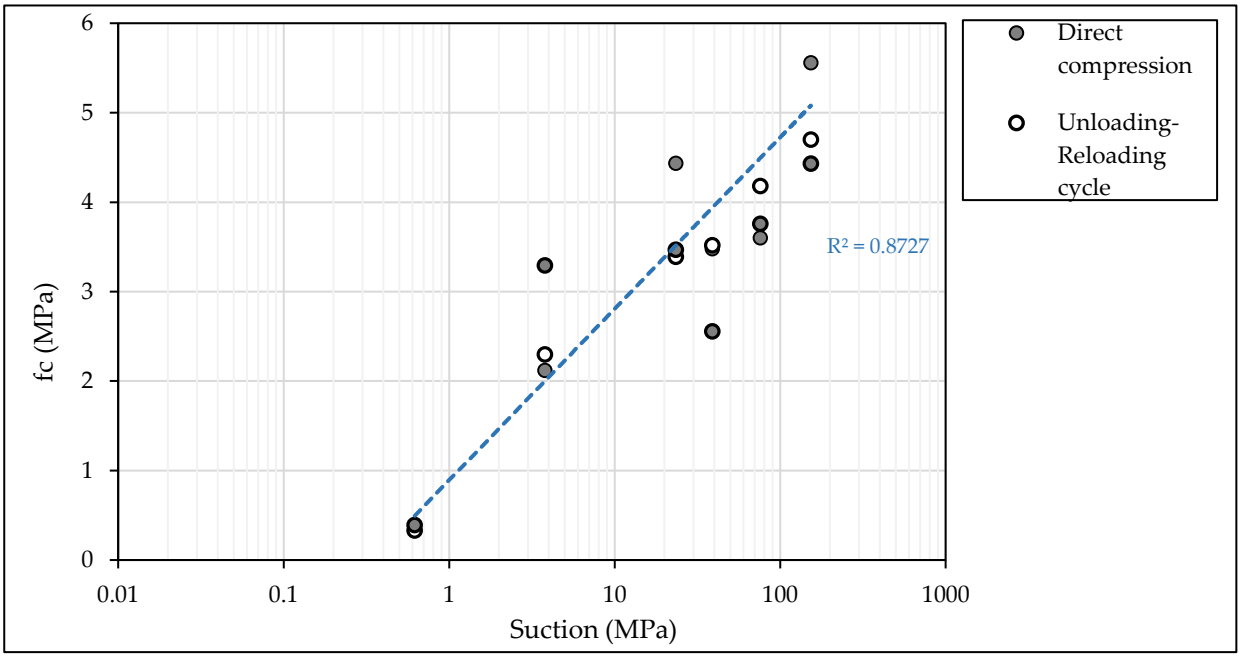

Figure 4.6: Variation of compressive strength with suction (in log) for samples at material scale

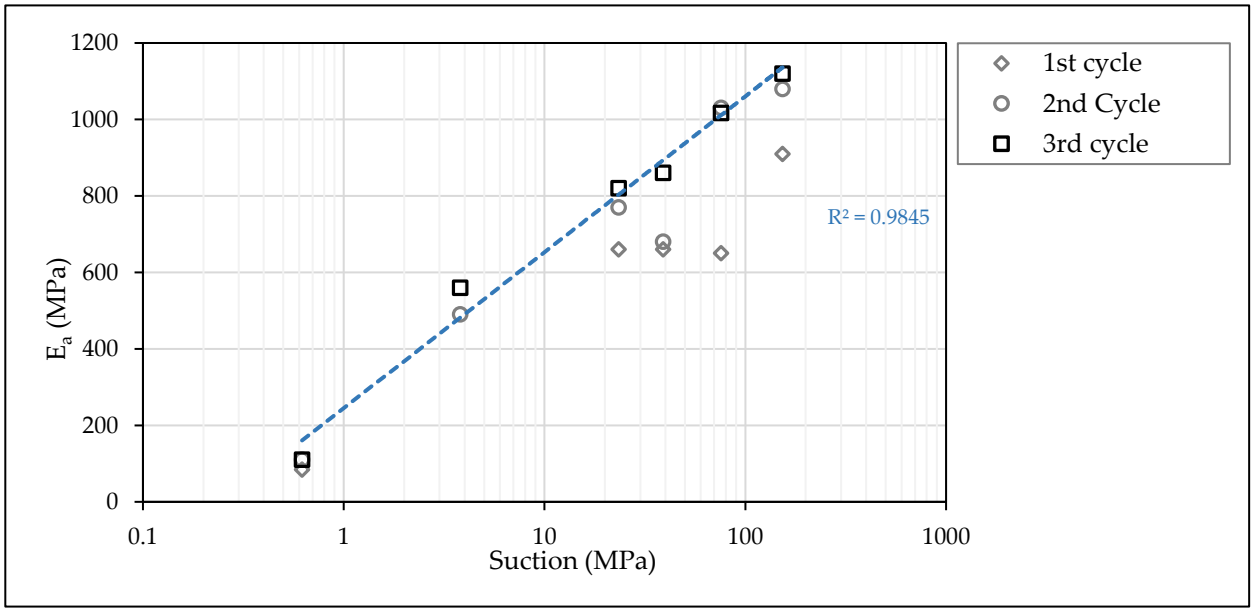

Figure 4.7: Variation of apparent modulus E_a with suction (in log) for samples at material scale

4.3 Experiments at column scale

In total, 15 prismatic samples were used in this experimental campaign. The preparation of these samples was previously described in Chapter 3, section 3.4.2. The experimental campaign includes monitoring of hydric state and mechanical behaviour during drying.

4.3.1 Experimental protocol

4.3.1.1 Water Monitoring

a) Boundary conditions

Samples S1, S2 and S3 were tested mechanically on the manufacture state. Other samples (S4 to S15) were then placed in a closed room to dry, up to be tested mechanically at different stages of drying, the drying being stopped after 2 to 19 weeks, depending on the sample considered (see table 4.8). The temperature and relative humidity of the room were continuously recorded and ranged around 15°C/25°C and 40%/80% respectively. In order to simulate what happens in the site where a wall structure, where only 2 faces are submitted to drying conditions, rammed earth samples were covered with plexiglass on two opposite sides and top. The bottom surface was covered by an impermeable base on which the sample was placed. This was done to constrain the drying of samples in one direction as shown in Figure 4.8.

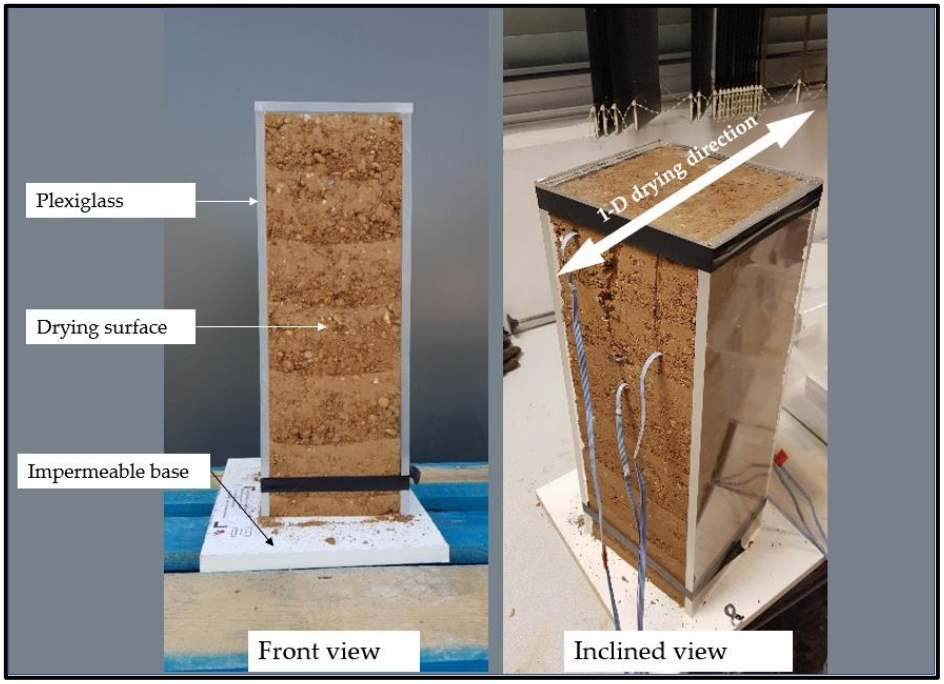

Figure 4.8: Rammed earth samples covered by plexiglass to allow drying on one direction.

b) Position of Relative Humidity sensor inside the sample

The kinetic of sample drying was followed by using two methods. First, by continuous measurement of the global mass of each sample at a regular time interval of one day; secondly, by using relative humidity sensors (capacitive sensors) which were placed inside the sample (see Chapter 3, section 3.5.1). Capacitive sensors record data each day.

Capacitive sensors were used for measuring relative humidity and temperature. First, they were calibrated by using a cooled mirror hygrometer in a calibration chamber for both relative humidity and temperature with ranges of 5°C/30°C for temperature and 9%/98% for relative humidity (see Chapter 3, part 3.5.1). Calibrated sensors were placed in the sample during manufacture. They were covered by a polyethene filter as protection from damage. In each sample, a total of 6 sensors were used. These sensors were placed in the middle of each layer at a distance of 3 ± 0.5 cm, 5 ± 0.5 cm, and 7.5 ± 0.5 cm from the drying surfaces. Figure 4.9 below illustrates the layout of the sensors.

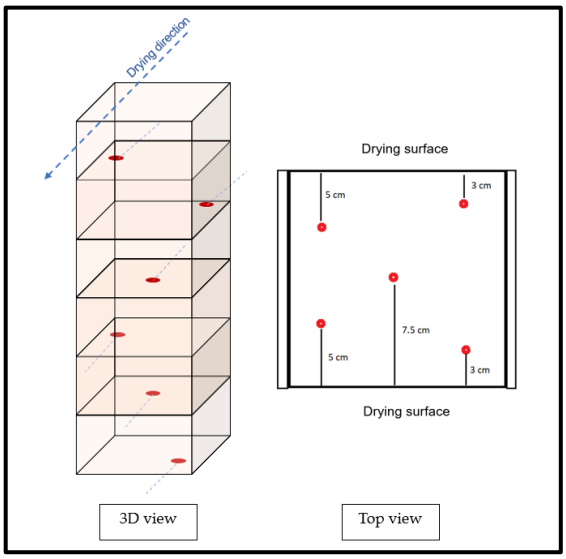

Figure 4.9**:** Position of the sensor inside a rammed earth sample: 2 sensors placed at each depth of 3 cm, 5 cm and 7.5 cm [133].

4.3.1.2 Mechanical testing

The mechanical test performed in this experimental campaign is the unconfined compressive strength (UCS) test. The UCS tests were performed on 18 samples as follows:

- At its initial moist state (3 samples, S1 to S3, see table 3.10)
- After drying for 2, 3, 4, 6 and 8 weeks (2 samples at each time period, S4 to S13)
- At dried state after 5 months of drying (2 samples, (S14 and S15), and 3 cylindrical samples (C1, C2, and C3)

a) **UCS test setup**

The prismatic samples, after removing plexiglass, were tested in compression between two hardened steel plates of 100 kN capacity press (Figure 4.10). To reduce friction at the interface between the steel plate and sample Teflon layers were used on the top and bottom of the sample. The vertical force and displacement were recorded during the test. Samples were loaded by displacement control at a constant rate of 1.2 mm/min [134]. At each drying time defined, two kinds of compression tests were performed: a first test by monotonous compression, to determine UCS, and a second compression test with 3 cycles, in order to determine the stiffness modulus, at 25%, 50%, and 75% of UCS found in the first test. The second test is then finally carried on until the failure of the sample.

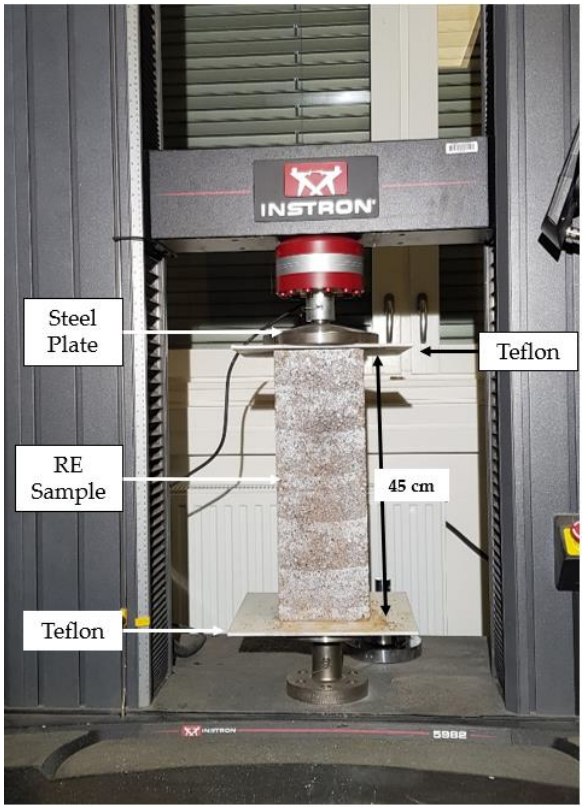

Figure 4.10**:** RE sample compression between two hardened steel plates of 100 kN capacity press for UCS test.

b) **Digital image correlation**

In parallel to the UCS test, performed with or without cycles, Digital Image Correlation (DIC) technique was used. DIC is a non-contact and non-interferometric (without interfering waves or rays to the specimen) optical method used for measuring the displacement field within a solid material subjected to external loading. In this method, the deformation is determined by comparing the changes in the image of the surface of a tested object before and after the solicitation. The DIC technique was introduced in the 1980s [135]. The measurement of the displacement field (and thus strain field) using the DIC system requires the following consecutive stages:

- **Patterning**

A random speckle pattern was applied on the surface of all the samples using black and white spray paint (Figure 4.11). First, the white paint was sprayed evenly on the surface of the sample to provide good contrast, then finally the black paint was randomly diffused to obtain patterns. The diffusion was carefully done manually by using spray cans at medium pressure. The mean size of the dots is around 4 mm.

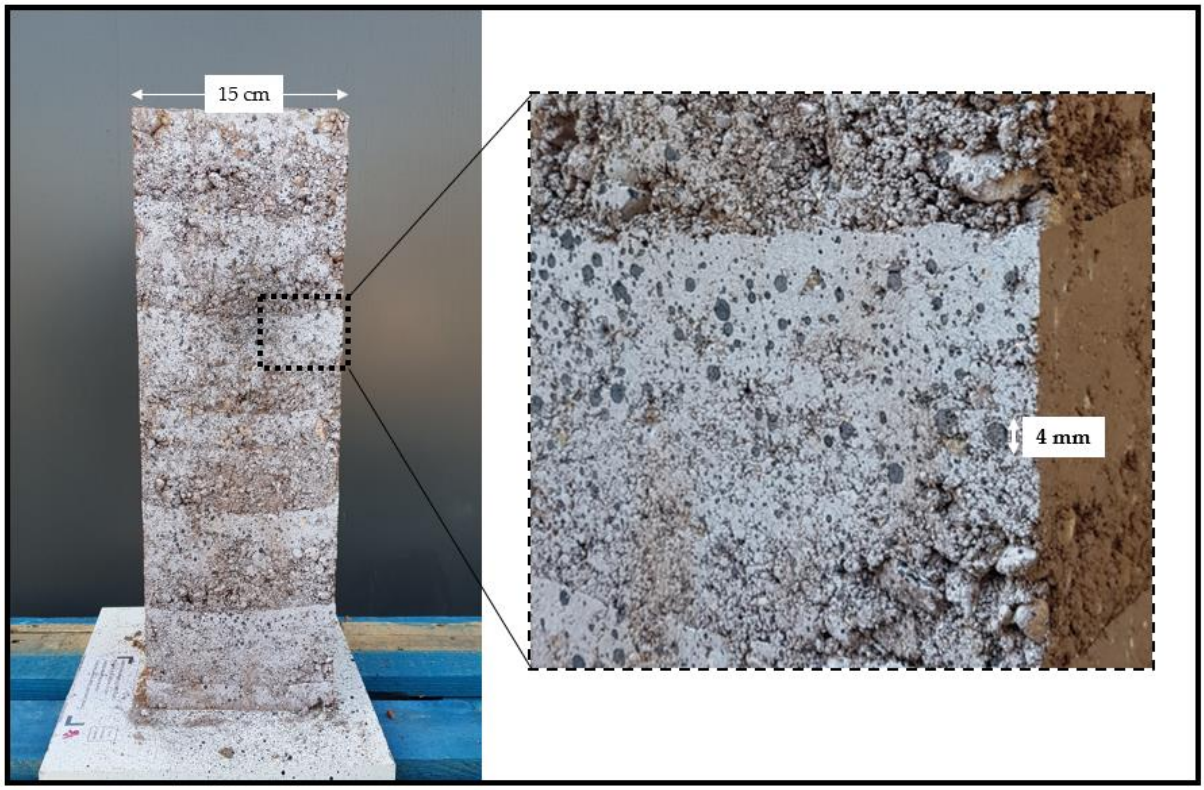

Figure 4.11: One surface of the RE sample was sprayed with black and white paint to make a random pattern. On the right side, a zoom of the sample shows a pattern of black dots on the white background on the surface of the sample.

- **Camera and Lighting setup**

A single-camera system was applied to measure in-plane deformations, this configuration is thus a two-dimensional DIC. The camera used in this study has a 3248x4872 pixels resolution, with an almost 16 million megapixels white and black camera system. The camera is placed with its optical axis normal to the sample's surface (Figure 4.12). During the tests, a light projector and LED light source were used to provide constant illumination on the specimen.

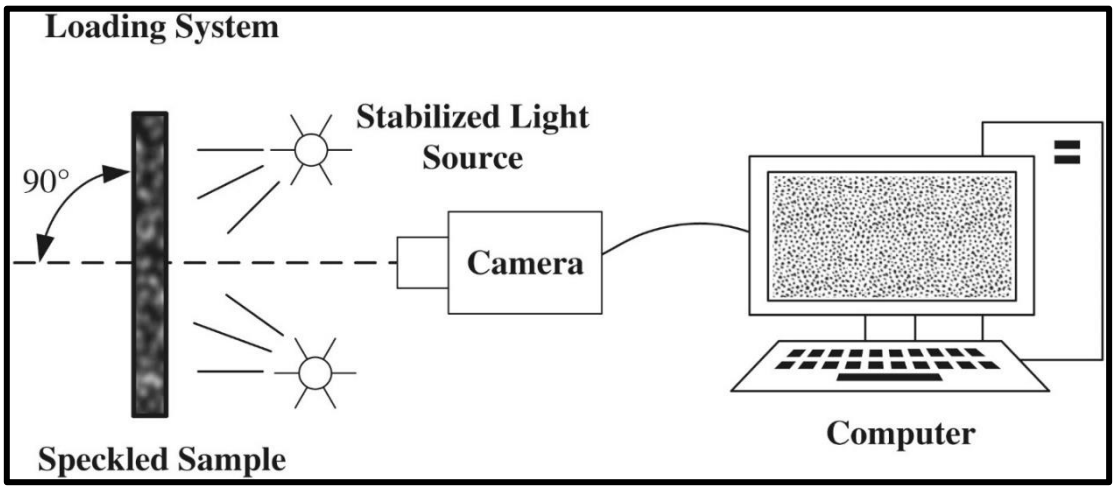

Figure 4.12**:** Two-dimensional DIC setup showing a camera is perpendicular to the sample's surface, image acquisition is done by a special program in the computer [136].

- **Images acquisition and analysis**

Images were recorded at different steps during reloading and unloading UCS tests at the following stages of the mechanical test (see Figure 4.13):

i. The first images were taken before loading the sample, point O,
ii. Then for each cycle, at peak stress during loading and the lowest stress during unloading, therefore, points AB, CD, and EF.
iii. Finally, multiple images were recorded at regular intervals during the post-peak phase of the sample failure.

Image analysis was done by using a specialized computer program for two-dimensional DIC. In this study, 7D software developed by the laboratory SYMME from USMB was used to analyse the images [137]. The analysed region was in the middle third of the sample, in order not to be constrained by friction at the top and bottom supports. The region was divided using a virtual grid into a small square pattern where the deformation can be calculated (Figure 4.14). Using this technique, the vertical strain and thus Young's modulus were calculated.

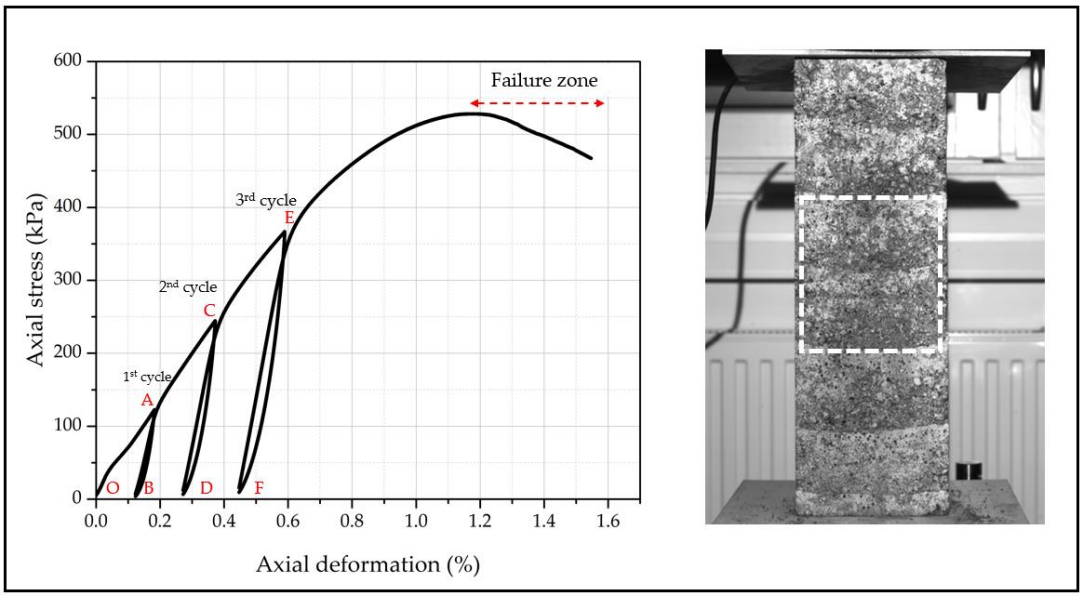

Figure 4.13**:** The points where images were recorded in the stress strain curve. On the right, the middle third region of the sample used for analysis of deformation of the RE column.

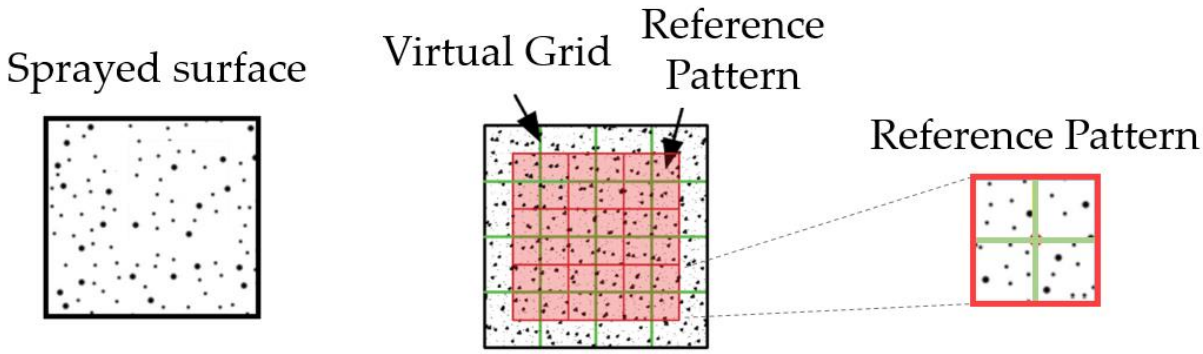

Figure 4.14: DIC method, illustration of image analysis by dividing the image using virtual grids and obtaining a square pattern. Reference pattern, marked with red squares and its centre points located at the intersection of the green virtual grid [138].

4.3.1.3 Summary of all tests on RE columns

The samples properties, type of instrumentation and the type of mechanical test are summarized in Table 4.2.

Table 4.2: Summary of RE columns samples used for drying experiments

Sample Name	Drying duration (Weeks)	Initial mass (kg)	Dry density (kg/m³)	Date of manufacture	Mechanical test	Hydric monitoring method	
					Cyclic loading-unloading		
						RH	Water content
S1		21.5	1930	24/09/2020	No cycles	No	No
S2	0	20.8	1868	30/09/2020	No cycles	No	No
S3		21	1886	09/11/2020	Cycles	No	No
S4		21.96	1972	03/12/2020	No cycles	Yes	Yes
S5	2	21.63	1942	03/12/2020	Cycles	Yes	Yes
S6		20.64	1853	05/07/2021	No cycles	No	Yes
S7	3	21.05	1891	02/07/2021	Cycles	No	Yes
S8		20.51	1842	08/04/2021	No cycles	No	Yes
S9	4	21.33	1915	25/03/2022	Cycles	No	yes
S10		20.69	1858	08/12/2020	No cycles	Yes	Yes
S11	6	21.40	1922	17/03/2021	Cycles	Yes	Yes
S12		20.93	1879	30/10/2020	Cycles	Yes	Yes
S13	8	20.52	1842	02/11/2020	No cycles	Yes	Yes
S14		20.95	1881	09/12/2020	No cycles	Yes	Yes
S15	19	21.3	1912	18/03/2021	Cycles	Yes	Yes
Mean		21.08 ± 2%	1890 ± 2%				

4.3.2 Results

4.3.2.1 Results hydric monitoring

c) Evolution of RH

With the help of capacitive sensors, it was possible to locally follow the relative humidity in the sample. Figure 4.15 presents the evolution of RH with time for samples dried for 6 weeks and more (i.e. sample number S10 to S15 as outlined in Table 4.1). Indeed, samples dried between 2 to 4 weeks showed no significant variation of RH and thus were not presented. From Figure 4.15, it was also observed that no variation of RH can be measured from the first 2-3 weeks although it is where the mass loss is more intense (see Figure 4.15). The RH value measured by sensors stays at 100%. This was due to the limitation of capacitive sensors. In very humid conditions (RH>98%) capacitive sensors have very low sensitivity to changes in relative humidity [86].

Then, after 2-3 weeks of drying, a significant decrease in RH was observed for each sample depending on the ambient condition. It was also observed that the sensors placed near the drying surfaces recorded a higher drying rate and responded quickly to the change in environmental humidity.

For samples that were dried for 6 weeks (S10 and S11), S11 was observed to dry at a significant rate reaching RH between 70% and 80% whereas RH for S10 dried to RH between 80% to 94% in 6 weeks (Figure 4.13), this difference in RH was probably attributed from the ambient condition, the samples were not dried at the same season, S10 dried in winter and S11 in spring (see table 4.2). Both samples (S12 and S13), dried for 8 weeks recorded a decrease in RH until reaches RH between 86% to 92%. Samples S14 and S15, dried after 19 weeks recorded a constant decrease of RH until the samples reach equilibrium with the drying environment (Figure 4.15). S14 for example, after 3 weeks of drying, recorded a constant rate of decrease in RH of 4.1%, 4.3%, and 5.6% per week for sensors placed at a depth of 7.5 cm, 5 cm, and 3 cm from the drying surface. Similar observations were made by Chauhan. (2021) who used the same type of RH sensor (Figure 4.16) with a similar rate of decrease in RH that was observed after 2-3 weeks, ranging from 4.5 – 5% RH per week for sensors placed at depth of 7 cm, 5 cm, an 3 cm (see Figure 4.15) [90]. A hydric equilibrium state was achieved depending on the drying environment, sample S14 (dried in winter) tends to reach equilibrium after 15 weeks of drying while sample S15 (dried in spring) stabilized after 10 weeks.

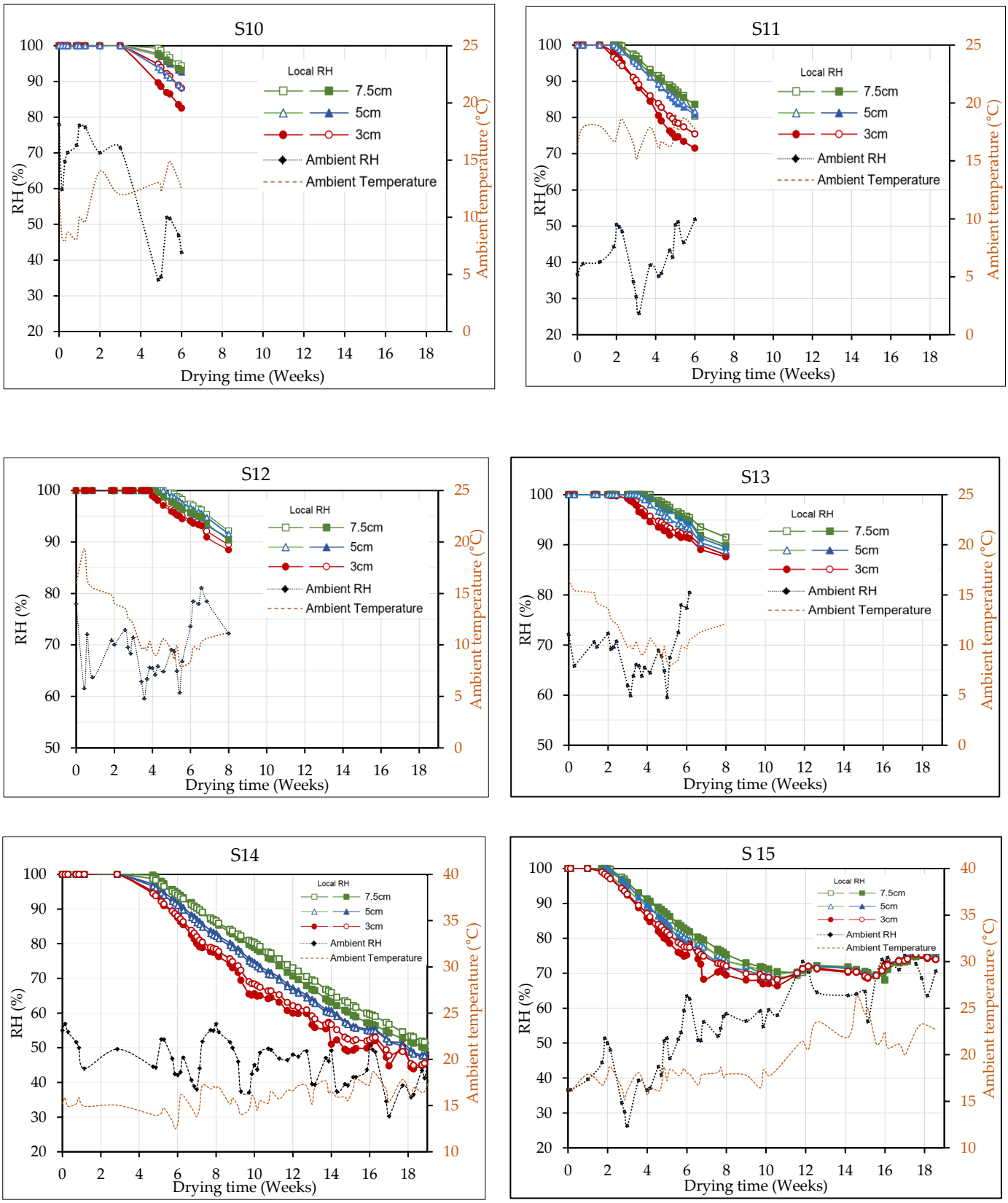

Figure 4.15: Evolution of RH with time for samples dried after 6,8 and 19 weeks along with the variation of ambient RH and temperature (RH in samples measured by capacitive sensors at different depths: 3 cm, 5 cm and 7.5 cm) [133].

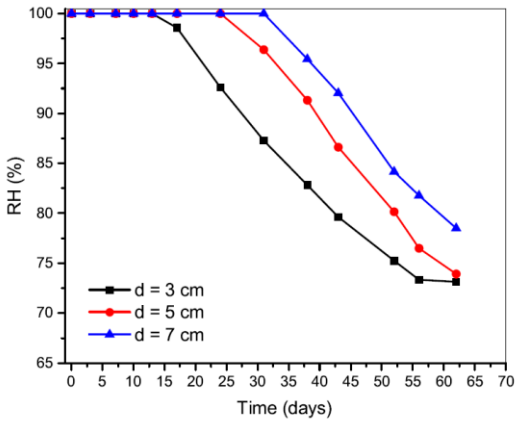

Figure 4.16**:** RH in RE samples measured from capacitive sensors at different depths (3 cm, 5 cm and 7 cm) [90].

d) **Water content measurement**

While capacitive sensors provided local measurement of relative humidity, it was essential to find global information on the hydric state during drying. This was done by periodically weighing the sample, and thus the evolution of global gravimetric water content was determined. The water content was determined by the ratio of the actual water mass in the sample to the dry mass. Drying curves expressed in water content are presented in Figure 4.17. It was noted that the first part of the drying curve is approximately linear, until 3 weeks. This is known as the first stage of drying and is associated with a constant drying rate period [129]. The second stage of drying is associated with the falling drying rate. Good repeatability in the evolution of water content was observed in the first stage of drying for a majority of samples (Figure 4.17f). Only samples S11 and S15 were observed to dry faster in the first stage of drying at an evaporation rate of 3% per week compared to 1.6% per week for the rest of the samples. This difference is certainly due to the difference in ambient conditions, visible in Figure 4.15. Indeed, it must be pointed out that all samples have not been tested in the same period of the year (see Table 4.2).

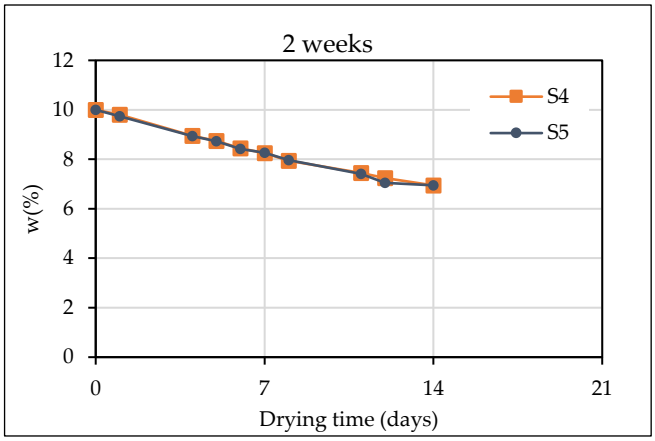

(a)

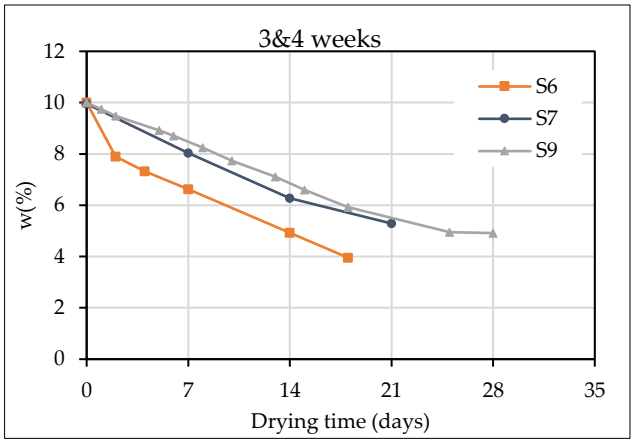

(b)

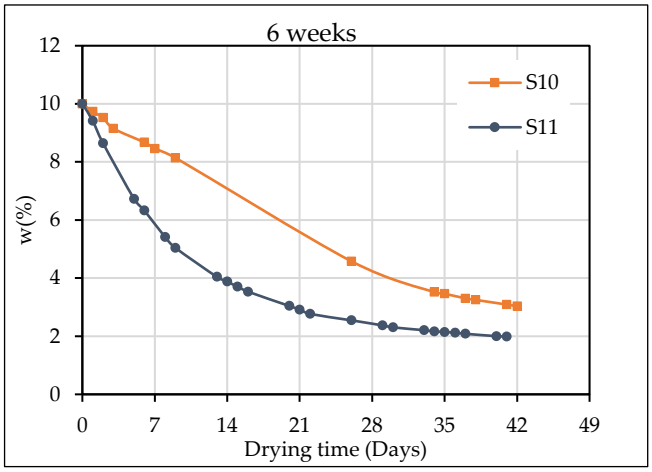

(c)

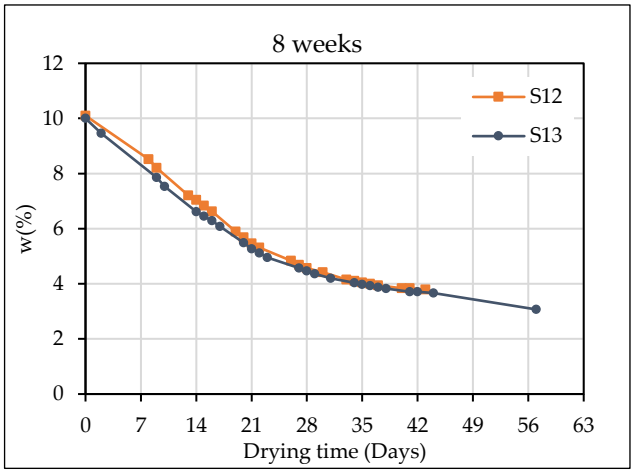

(d)

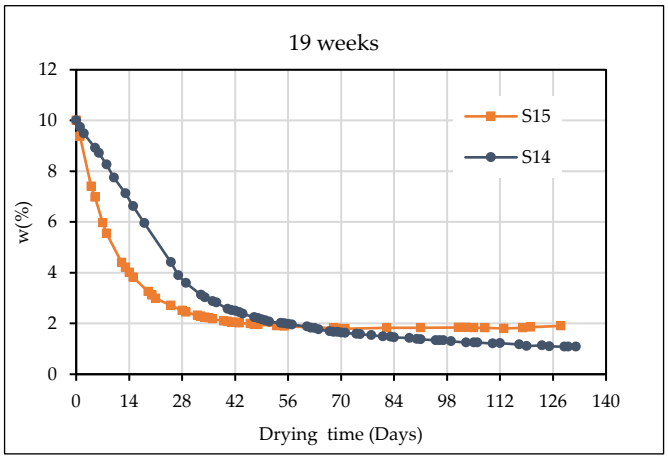

(e)

Figure 4.17: Evolution of water content with drying time for all samples. All curves are combined in (f)+(g-zoom).

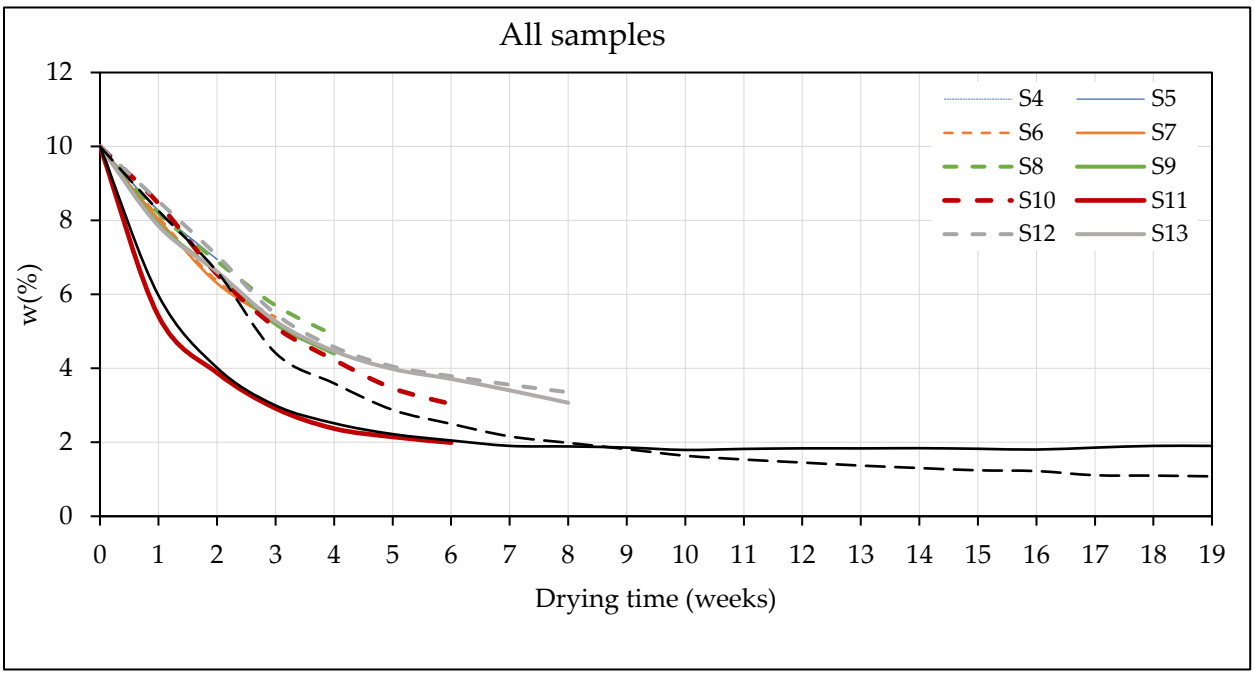

(a)

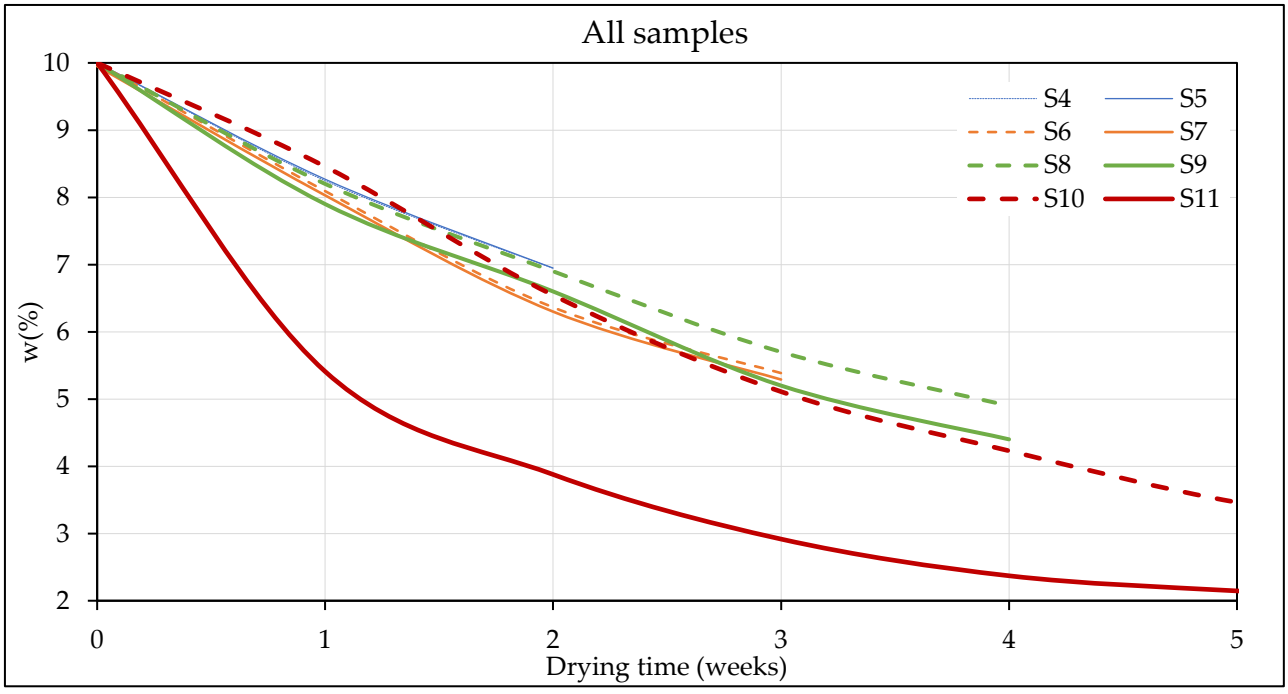

(b)

Figure 4.18: Evolution of water content with drying time for all samples combined (a), and a zoom (b)

e) Comparison of the local and global methods for monitoring hydric state

As mentioned previously, the hydric state of the RE sample was monitored by using RH capacitive sensors (local measurements) and water content measurement by global weighing. To compare the two methods discussed, the results of sample S14 were selected because it presents enough data for a long drying time, less fluctuation of ambient conditions (Figure 4.15) and has a similar drying behaviour to most of the samples (see Figure 4.18), hence representative. Figure 4.16 shows the evolution of water content measured direct (Figure 4.17) and computed from local RH (Figure. 4.13). The RH values were linked with suction using Kelvin's equation, and suction was finally linked to water content using the Van Genuchten model for the retention curve (see Chapter 3, section 3.3.4). To recall, the parameters used from the model were: α =1.507 MPa-1, n=1.556, and m = 0.357.

From Figure 4.19, it was observed that computed local water content presents no variation as long as the RH was constant at 100% which is not the case as shown by the global water content. Results can thus be considered from 5 weeks. In addition, the retention curve was prepared at a constant temperature of 25°C while the sample dried at a varying ambient temperature (between 15 and 20°), thus the results computed of local water content are not exact. Thus, it can be concluded that the hydric state of a very humid sample is better represented in a global way by the water content obtained by weighing. However, the local measure of RH and the deduction of w allows distinguishing the different amount of liquid water, to have an estimation of w, which is suitable when the hydric state get far from 100%RH (for w lower than 3% here). When the water content is below 3% (5 to 6 weeks), both methods were fairly close to each other (Figure 4.19). Finally, it appears that both results are tending toward a similar value of final water content, around 1%.

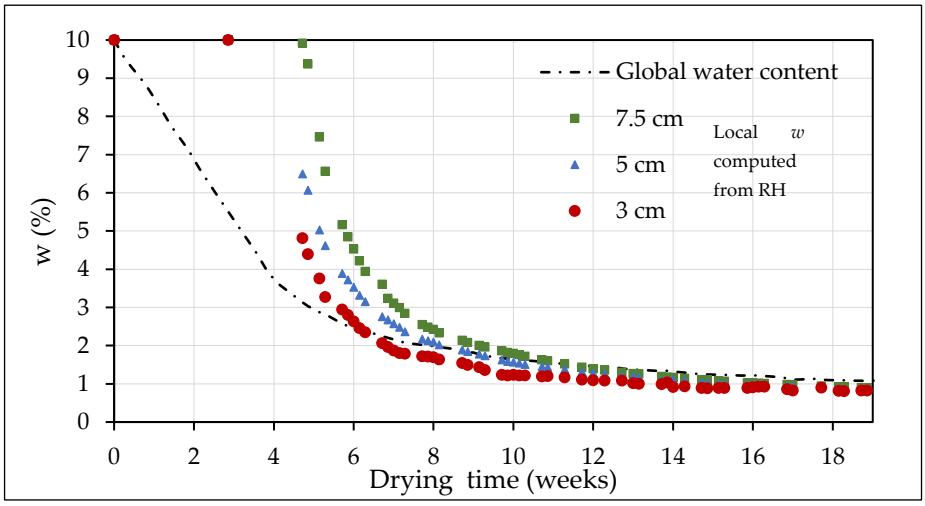

Figure 4.19: Evolution of gravimetric water content for sample S14, obtained experimentally together with the one determined from RH measurements [133].

f) **Induced Polarization method**

Only sample S8 was equipped with electrodes, that were used to survey the volumetric water content through electrical measurements. A resistivity meter "ABEM Terrameter SAS-4000" was used to acquire the electrical conductivity and changeability of sample S8. The electrical conductivity decreases with drying (loss of water content). The normalized chargeability has the same trend as the electrical conductivity.

The conductivity and chargeability were then converted to volumetric water content, more about this is found in Annex 1. The measurements were carried out at four distinct times during the drying process [139]. First measurements were performed at the initial state just at the manufacture, then after 5 days, 13 days, and 25 days. Figure 4.20 shows the distribution of volumetric water content at the different elapsed times during the drying process. The drying profile represented from left to right corresponds to the following elapsed times t = 0, 5, 13, and 25 days, respectively.

It can be observed, after 5 days of drying, the upper part of the block looks dried more than the lower part. In the same time period, the influence of the layer porosity gradient is very important, the looser part of the block (at the base of the compacted layers) is losing more water by volume unit than the denser part of the block (at the top of each layer). After 13 days of drying, this effect starts to be less visible. After 25 days the block is almost dry with the volumetric water content of less than 7% ($w \approx$ 3.5%).

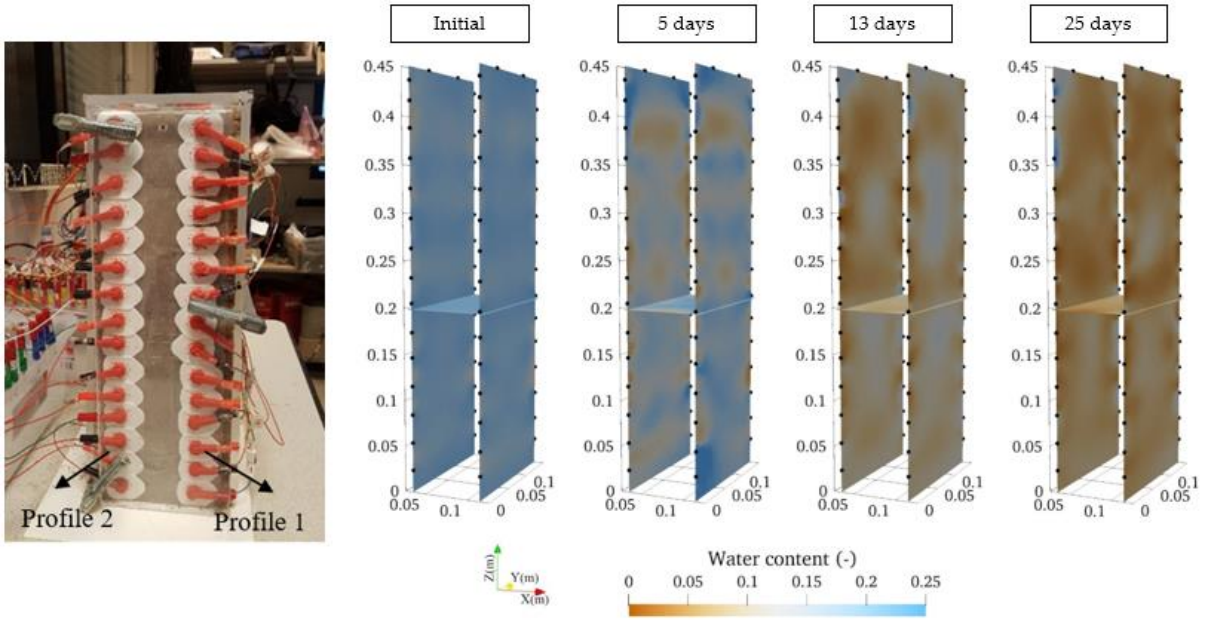

Figure 4.20: Imaging of the distribution of volumetric water content at different elapsed times during the drying process. By using the induced polarization method [139].

g) Effect of gravity

It was observed that the samples dried faster on the top part than on the bottom. The effect of gravity is seen visually, as shown in Figure 4.21, where the top layer seems drier (clearer colour) than the bottom one (darker colour). A similar effect was observed for all samples during the early stages of drying. In addition, the same effect of gravity was recorded by capacitive sensors. Figure 4.21 shows for instance the results of RH from sample S14; it can be seen that for sensors placed at the same depth of 7.5 cm below the drying surface, the RH recorded at the 3rd layer becomes higher than the one of the 5th layer from the first weeks. This effect emphasizes from weeks 8 to 12 and then becomes less pronounced as soon as equilibrium water content tends is reached.

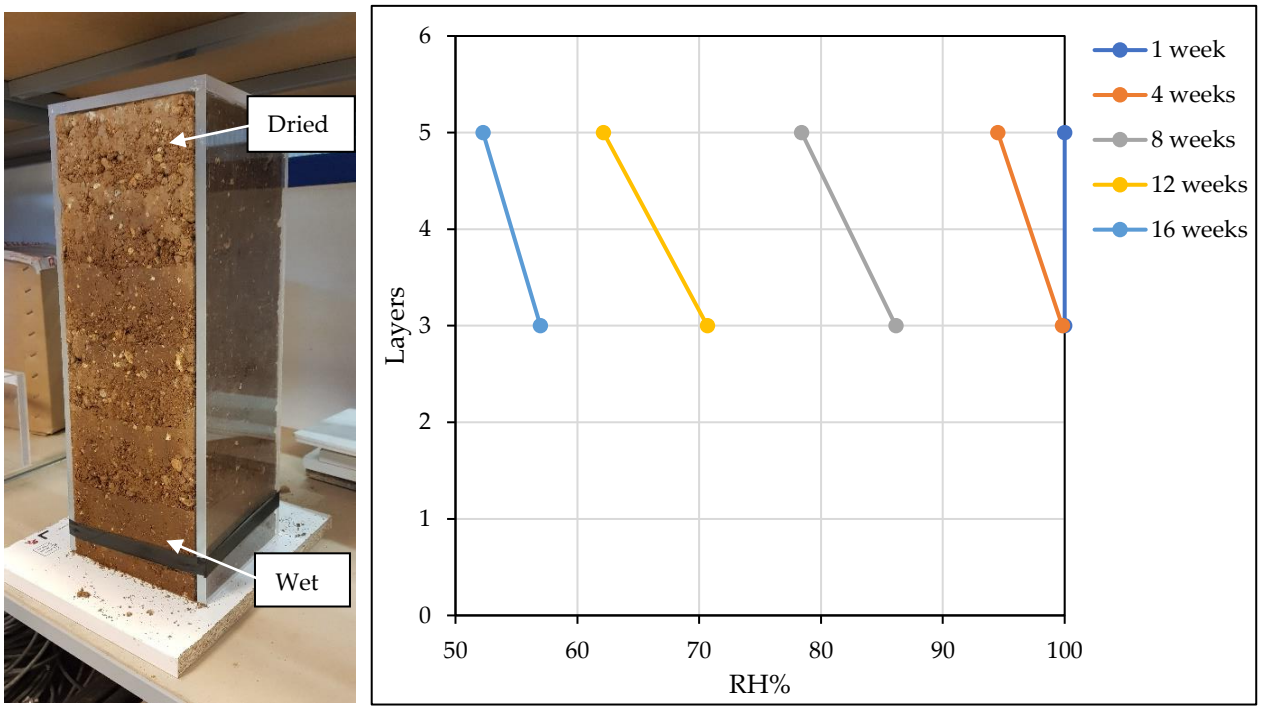

Figure 4.21: RE sample dried faster at the top than at the bottom due to the effect of gravity. This effect is recorded by capacitive sensors on sample S14, placed at depth of 7.5 cm from the drying surface, showing RH at the 3rd layer is always higher than that of the 5th layer, except for the 1 week where the sample is still moist.

4.3.2.2 Results of Mechanical testing

a) Results of the UCS test

The results of UCS tests for all samples, including compressive strength (fc) and apparent Young's modulus (E_a) have been collected in Table 4.3. The modulus E_a calculated from the 1st cycle (between A and B states as shown in Figure 4.11), the 2nd one (between C and D) and the 3rd one (between E and F) are represented by E_a 1, E_a 2, and E_a 3 respectively.

Figure 4.23a shows the mechanical response of samples S1, S2, and S3 which were tested just after compaction at their manufacturing water content of 10%. The fc were 116.23 kPa, 110.24 kPa, and 137.77 kPa for S1, S2, and S3 respectively. Results of fc for all samples are in the same order of magnitude,

showing good repeatability with an average fc of 121 ± 11.9% kPa. A similar observation was made for the modulus E_a, which was determined by the DIC technique on S3 where the test was done with unload-reload cycles. The results of E_a, from 3 cycles, were 190.07 MPa, 183.01 MPa, and 190.7 MPa for E_a1, E_a2, and E_a3, with an average value of 187 ± 2.3% MPa.

After two weeks of drying, samples S4 and S5 showed values of fc that are close to each other (509kPa and 527kPa) (see Figure 4.23b). A slight dispersion in the results of E_a, evaluated from S5, the results were 523.71 MPa, 417.76 MPa, and 432.33 MPa.

After three weeks of drying, the fc of samples S6 and S7 (753.97 kPa and 758.98 kPa) (Figure 4.23c) were observed to increase by a factor of 7 compared to the initial manufacturing state. The E_a calculated from sample S7, the results were 619.62 MPa, 502.75 MPa, and 550.16 MPa.

The samples dried for four weeks, S8 and S9, showed a compressive strength greater than 1 MPa (Figure 4.23d), with a significant difference in the E_a between the loading-unloading cycles. The values of compression strength were 1064 kPa and 1186.16 kPa for S8 and S9 respectively. The values of E_a were calculated as 944.02MPa, 925.09 MPa, and 694.54 MPa as E_a1, E_a2, and E_a3 respectively.

The results of the compression test for samples S10 and S11, which were tested after six weeks of drying period have been shown in Figure 4.23e. The fc of sample S10 which was compressed by direct loading until failure (fc = 1246.59 kPa) was slightly lower than the fc of sample S11 (fc = 1400 kPa) which was tested with unload-reload cycles.

Samples 12 and 13 dried after 8 weeks showed a significant drop in both fc (973.33 kPa and 1139.35 kPa) (Figure 4.23f), and apparent Young's modulus (831.42 MPa, 845.98MPa, and 965.49 MPa). It is worth noting that, samples S12 and S13 were not well manufactured. There was a segregation of gravels during the earth mixing. Hence the top part of the sample contained more gravel while the bottom part was mainly sand and fine (Figure 4.22). This explains the sudden drop in mechanical strength for these samples (Table 4.3, Figure 4.19f, 4.22, 4.23).

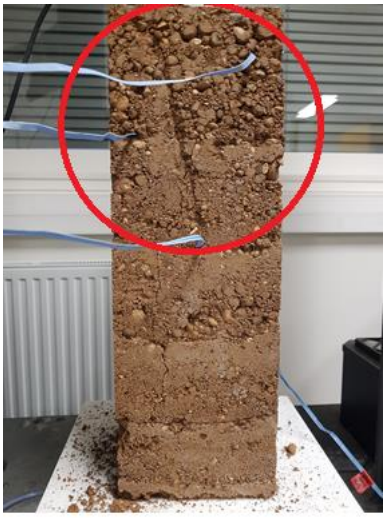

Figure 4.22: A segregation of aggregate during soil mix for samples S12 and S13, causing the upper part of the sample to contain more aggregates while the bottom part is mainly sand and fine.

Figure 4.24 shows the compression results of samples S14 and S15, which were tested after 19 weeks of drying. The fc of sample S14 which was compressed by monotonous loading until failure (fc = 1356kPa) was close to the one of sample S15 (fc = 1391.55 kPa) which was tested with unload-reload cycles. A similar order of magnitude was obtained for sample S11 (fc=1400 kPa) which was dried for 6 weeks, suggesting that, an asymptote of mechanical capacity was reached around 6 weeks. Also, after 19 weeks, both samples exhibited a greater value of E_a compared to the previous samples (see Table 4.3).

Table 4.3**:** Results of Compressive strength, Apparent Young's modulus for all samples.

Sample Name	Drying duration (Weeks)	Compressive strength, fc, (kPa)	Apparent Young's modulus, E_a (MPa)		
			E_a 1	E_a 2	E_a 3
S1	0	116.23	-	-	-
S2		110.24	-	-	-
S3		137.77	190.07	183.01	190.7
S4	2	509	-	-	-
S5		527	523.71	417.76	432.33
S6	3	753.97	-	-	-
S7		758.98	619.62	502.75	550.16
S8	4	1064	-	-	-
S9		1187.16	944.02	925.09	694.54
S10	6	1246.59	-	-	-
S11		1400	1051.62	753.78	1141.07
S12	8	973.33	-	-	-
S13		1139.35	831.42	845.98	965.49
S14	19	1356	-	-	-
S15		1391.55	1310.98	1535.43	1162.02

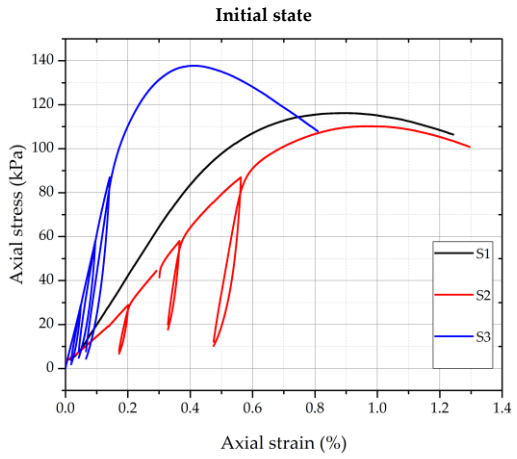

(a)

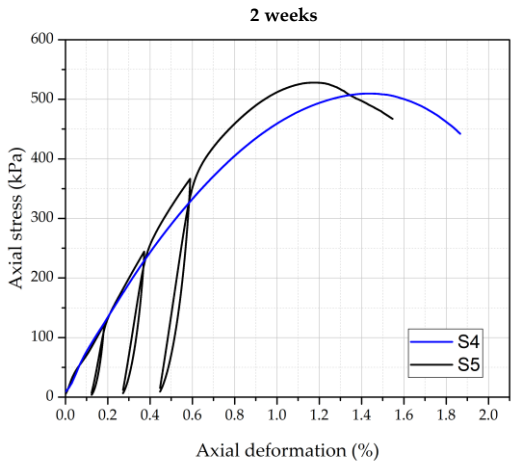

(b)

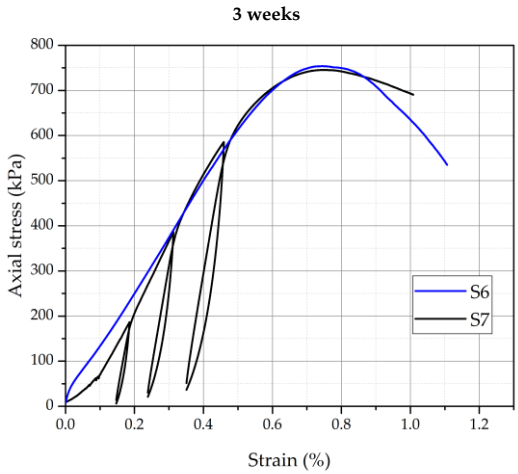

(c)

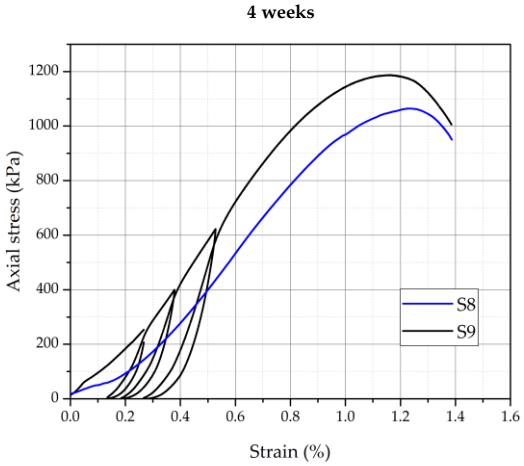

(d)

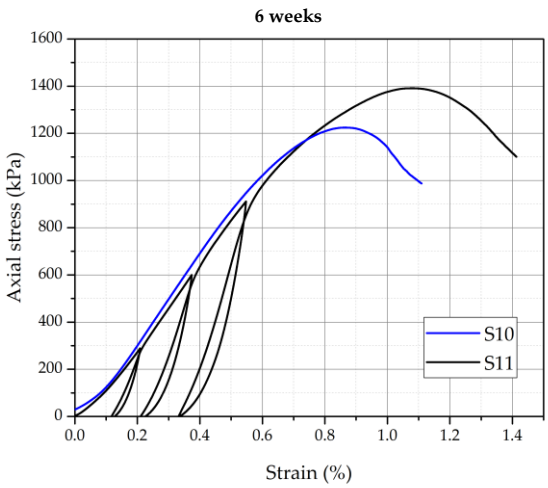

(e)

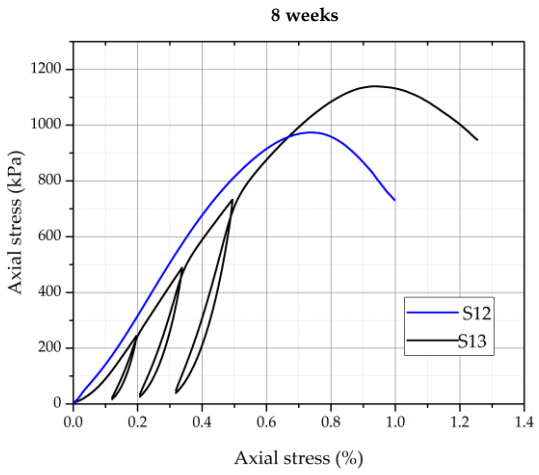

(f)

Figure 4.23: Axial stress-strain curve for samples after 0 (a), 2 (b), 3 (c), 4 (d), 6 (e), 8(f) weeks of drying with and without unload-reload cycles.

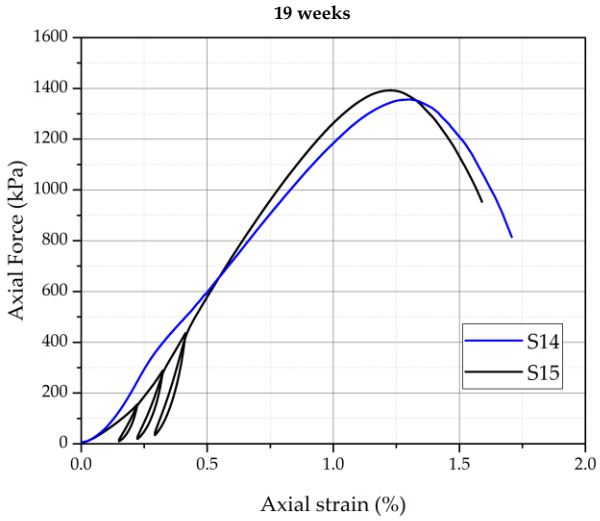

Figure 4.24: Axial stress-strain curve for samples after 19 weeks of drying with and without unload-reload cycles

The stress-strain curves for all the samples tested are assembled in Figure 4.25 without cyclic loading and in Figure 4.26 with unloading-reloading cycles. It can be observed from both figures that the mechanical behaviour of a RE sample changes from more plastic at humid conditions to more brittle failure at dry conditions, similar observations were noted in [75], [90], [132]. A transition between plastic to more brittle behaviour can be observed after three weeks. It can also be observed from Figure 4.25 that the slope of unloading-reloading cycles increases as the sample dry (Young modulus is getting higher)

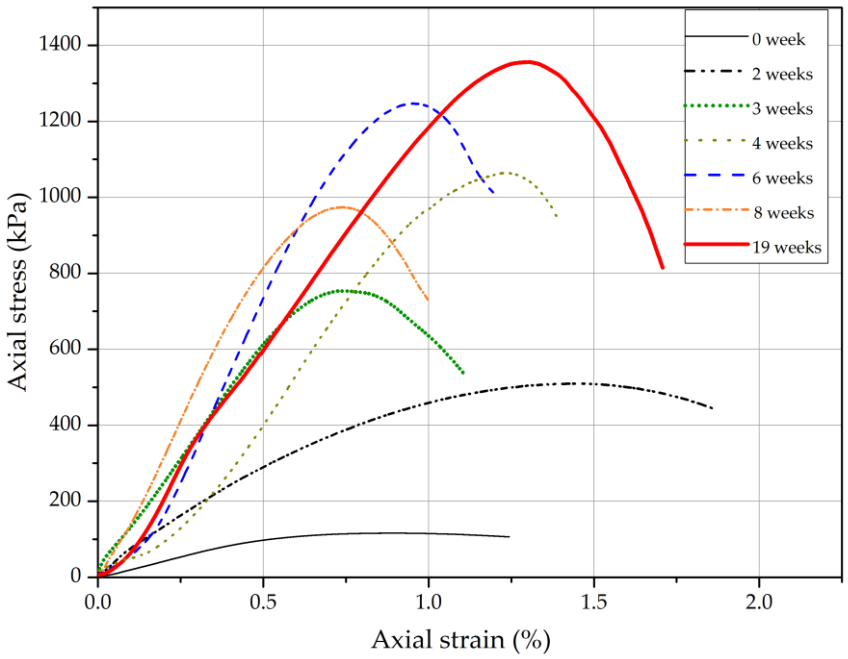

Figure 4.25: UCS of samples at different drying times without cyclic loading-unloading [133].

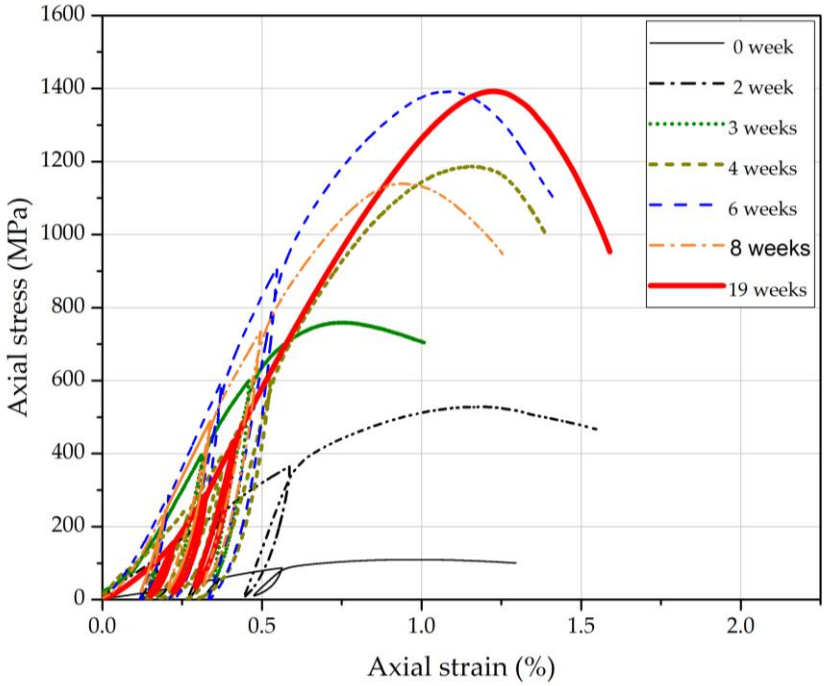

Figure 4.26: UCS with loading and unloading cycles of samples at different drying times [133].

4.3.3 Discussion

4.3.3.1 Evolution of mechanical performance with drying time

Results of compressive strength and apparent Young's modulus for 0, 2, 3, 4, 6, 8, and 19 weeks are summarized in Figure 4.24 and Figure 4.25. As expected, both compressive strength and the apparent Young's modulus were observed to increase with drying time. Compressive strength was observed to increase by a factor of 12 from the moist state (manufacturing state) to the dry state (see Figure 4.27). It means that once the RE building is manufactured (with a water content of around 10-12%), it will gain mechanical resistance 12 times more after several weeks of drying (with a water content of about 1-2%). The factor obtained in this work is a huge factor compared to similar studies, for example, Bui et al, 2014 reported an increase in compressive strength by a factor of 4 from the moist state to the dry state.

In the first 3 weeks of drying, the sample has gained 60% of maximum compressive strength, this is where the sample loses most of its water (around half of it) as shown in Figures 4.7 and 4.8. After 6 weeks of drying, the compressive strength reaches around 1400 kPa which meets the minimum characteristic compressive strength (1.-1.3 MPa) for construction [19], [37]. As pointed out before, samples tested after 8 weeks of drying were not well manufactured which explains the sudden drop in mechanical strength for samples tested after 8 weeks. After 19 weeks, a little variation of the compressive strength was observed compared to samples dried after 6 weeks. In addition, the sample compressed with reload-unloading cycles showed a higher compression strength than those compressed in a monotonous way during the entire drying period (Figure 4.27). In detail, the difference is minor for humid samples (before 3 weeks), although a significant difference was observed after 4 weeks, maybe due to different humid stages reached for variable drying kinetics.

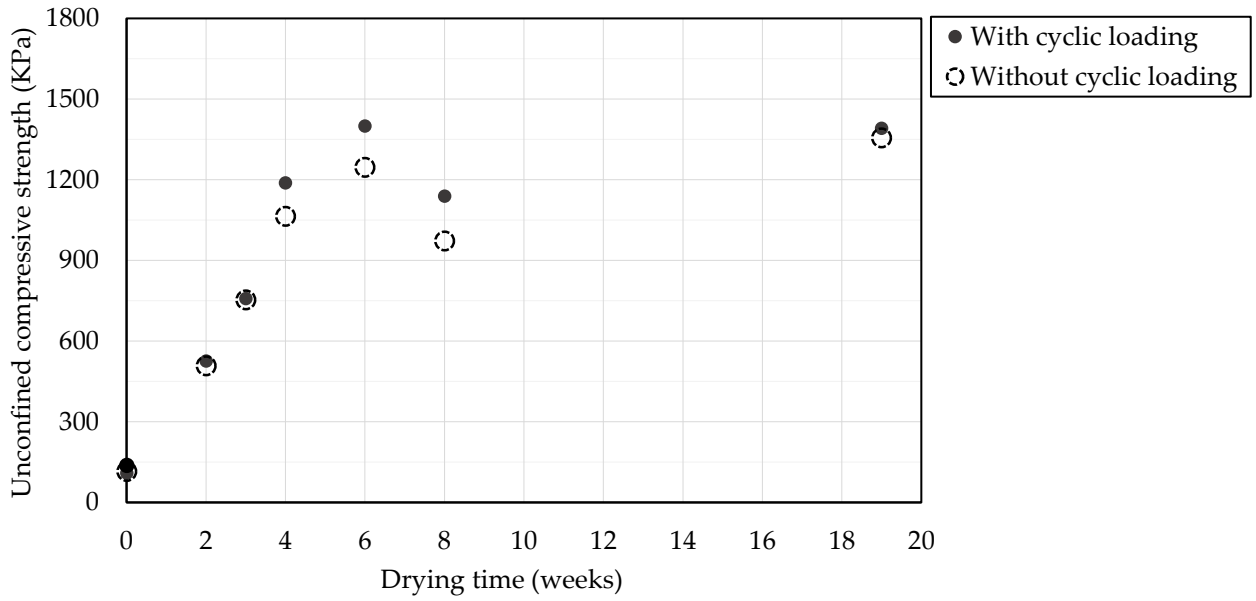

Figure 4.27: Compressive strength with respect to drying time.

Figure 4.28 shows the apparent Young's modulus calculated from three loading cycles. The modulus E_a for all cycles was generally observed to increase with drying time (Figure 4.28). The modulus was observed to increase by a factor of 7 from the manufacturing state (E_a = 190 MPa) to the dry state (average E_a = 1340 MPa).

The difference in modulus between cycles was more prominent on dry samples (from 4 weeks of drying). There was no regular pattern between loading cycles and the modulus even though some studies reported a gradual decrease in modulus with the increase in axial stress of cycles [53]. As explained previously, the results of 8 weeks are not consistent. The maximum apparent Young's Modulus of 1535 MPa is obtained after 19 weeks.

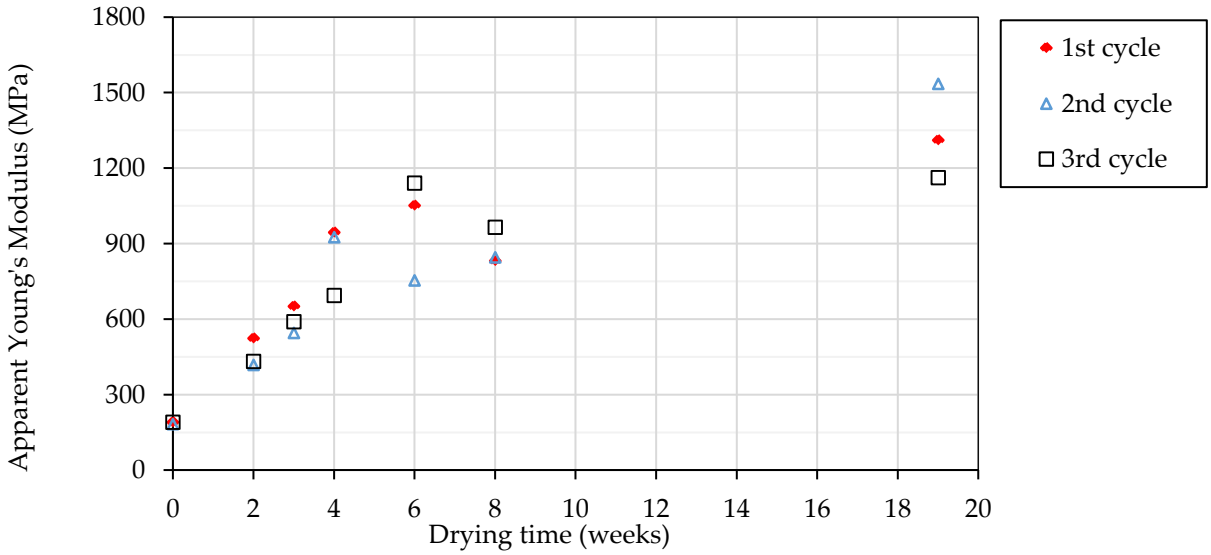

Figure 4.28: Apparent Young's with respect to drying time.

4.3.3.2 Correction of fc geometry

The slenderness ratio is defined as the ratio between height and width (for prismatic samples) or diameter (for cylindrical samples). According to the standard ASTM-D2166 (2016) [134], the UCS test, the recommended sample geometry is cylindrical with a slenderness ratio between 2 and 2.5. The effect of samples geometry and slenderness is well explained in the literature (Chapter 2, section 2.4), it was recommended to use cylindrical samples with a slenderness ratio of 2 to avoid additional friction between the loading platen and the sample top and bottom surfaces [41], [140].

In this study, prismatic geometry (15 cm × 15 cm × 45 cm) was chosen since it provides a better representation of the wall-drying problem as explained in section 4.2.1. It was then necessary to compare the results UCS test on prismatic samples and the recommended cylindrical sample, to quantify the difference between UCS and Young modulus due to geometry. To do so, three cylindrical samples (Φ=16 cm and H=32 cm) with a slenderness ratio of 2 were used. The preparation of these samples (named C1, C2, and C3) is detailed previously in Chapter 3, section 3.4.2. The cylindrical samples have similar dry density, and granulometry, and were compacted using a similar method (see Table 4.4).

After manufacture, cylindrical samples were placed to dry for 19 weeks in the same drying environment as the prismatic sample. The samples dried up to an average final water content of 1.32%. The UCS was done with monotonous compression and with unloading-reloading cycles according to the same procedure as explained in section 4.2.3.1. The results are summarized in Table 4.4, the average compressive strength of cylindrical samples was 1771 kPa, whereas for prismatic samples was 1373.5 kPa. Figure 4.29 shows a comparison of the UCS results for prismatic and cylindrical samples. It was observed that the cylindrical sample shows 22 % higher compressive strength compared to the prismatic sample. Therefore, applying a coefficient of 1,22 to fc would maybe make the values determined more representative. The modulus E_a for cylindrical samples showed high dispersion in results, this could be due to the curved surface of the cylinder making it extreme complex to determine the strain by using 2-D DIC. So, the results of E_a for cylindrical samples are not presented. Although prismatic samples underestimate the mechanical capacity with respect to the cylinders, they seem to be well representative of the wall. The choice of slenderness, size (with respect to the D_{max}) and section (square) was made to have a multilayer representation of the wall.

Table 4.4: Results UCS of cylindrical samples

Sample	Dry density	Porosity	fc (kPa)
C1	1990.5	0.248	1691
C2	1926.99	0.273	1791
C3	1976.39	0.254	1830
Mean	1951 ± 1.7%	0.26 ± 5%	1771 ± 4%

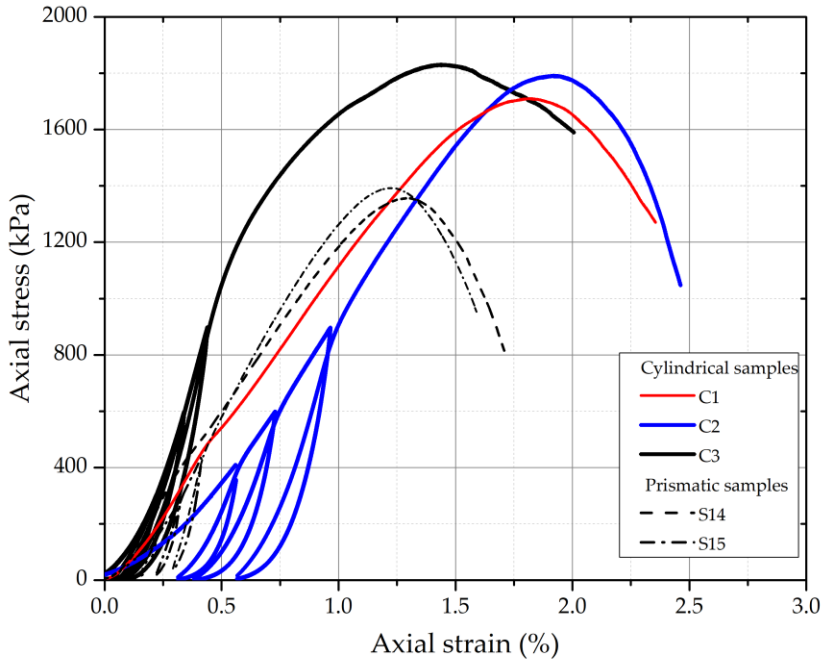

Figure 4.29: Comparison of compressive strength for the cylindrical and prismatic sample in the dry state.

4.3.3.3 Cracks pattern at failure using DIC

Thanks to the DIC, the displacement field during different stages of the UCS was recorded. Then strain field could be deduced with the help of DIC software. Figure 4.30 show the failure pattern of rammed earth at different drying time. For samples at the initial state and 2 weeks of drying, cracks mostly appeared on a propagating top or bottom edge. Shear bands are thicker at the initial time which can be explained by the more ductile behaviour of the earth at this hydric state. For more dry samples (6 and 19 weeks), localized strains are localized both at the interface between layers and with an inclination of about 30° with respect to the vertical direction.

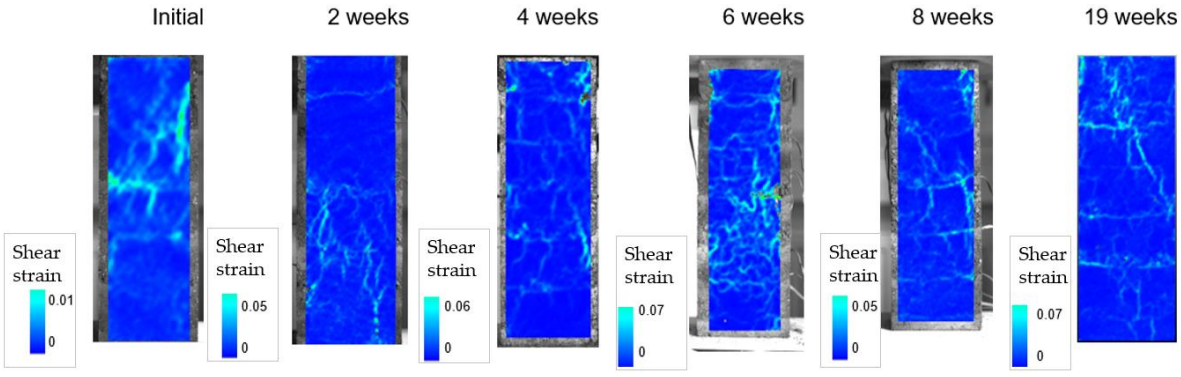

Figure 4.30**:** Failure pattern of a RE samples at the peak stress, represented by fields with maximum shear strains [133].

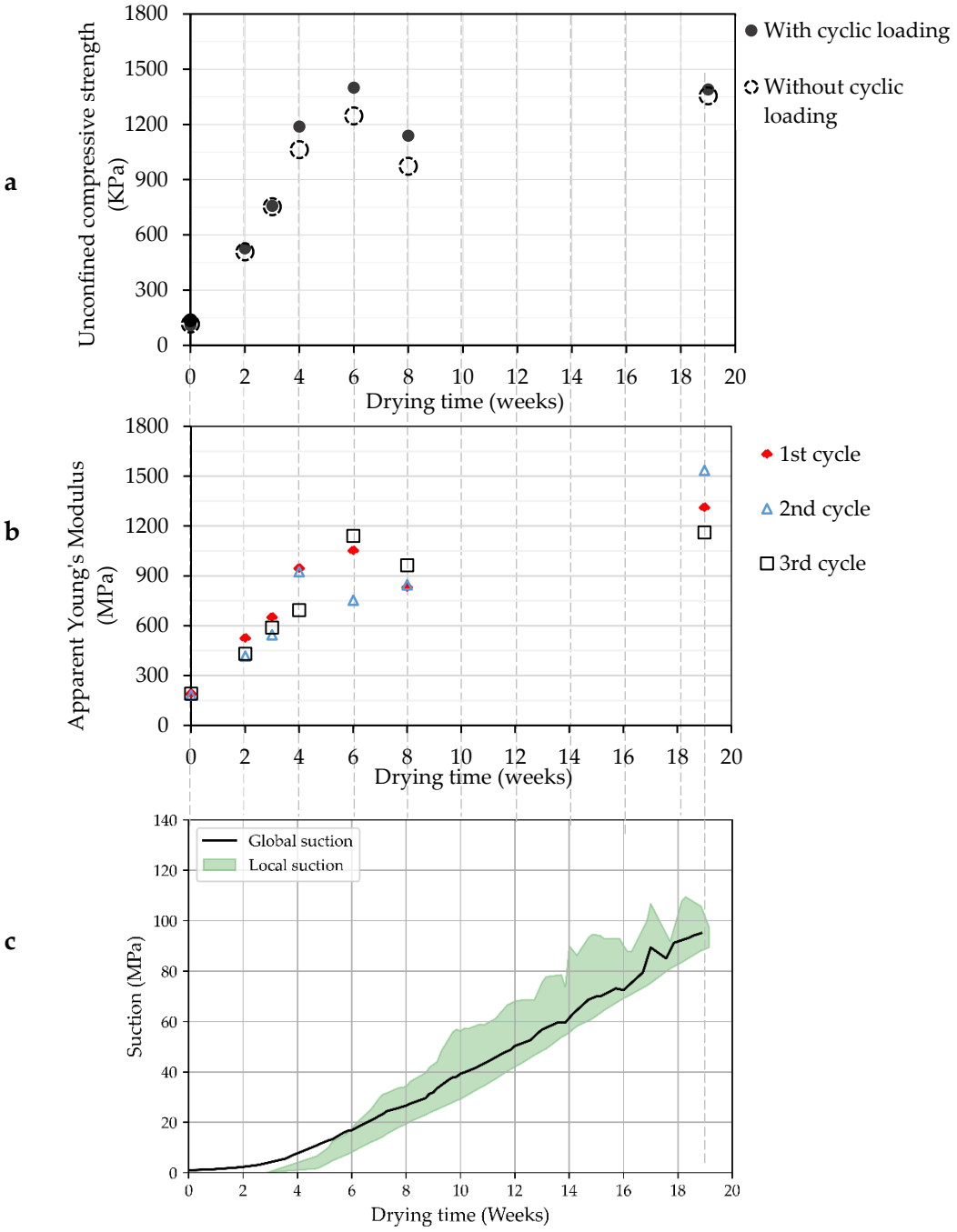

Figure 4.31: Link between the mechanical properties and suction development

4.3.3.4. Evolution of mechanical performance with suction

The evolution of mechanical behaviour was linked to the hydric state within the samples as presented by its suction values (see Figure 4.31c). The hydric results of sample 14 were used. As discussed, the RH (Figure 4.15) and their corresponding temperatures were expressed in suction by using Kelvin's equation (1). The suction values correspond to local values at depths of 3 cm, 5 cm, and 7.5 cm are represented in Figure 4.31c. Indeed, the suction in the sample is non-uniform, so local suctions are represented as a field of suction with minimum values in the middle of the sample and the maximum near the surface (Figure 4.31c). In addition, global suction in Figure 4.31c was obtained from the evolution of water content thanks to the Van Genuchten model (chapter 3, section 3.3.4). Figure. 4.31c shows, in the early drying stage, the development of global matric suction up to 10 MPa was correlated

with a substantial increase in the compressive strength from 100 kPa at manufacture to 1000 kPa after 4 weeks (Figure 4.31a). From 6 weeks, a significant increase in matric suction from around 20 MPa to 90 MPa had little to no influence on mechanical behaviour. This confirms the results of Bui et al., 2014 [42] that a slight change in the hydric state of an almost dried sample produces a minimum effect on its mechanical properties.

4.3.3.5 Validation of results of mechanical strength with suction

The results from this study were further compared with other studies on a similar scale (column scale). Bui et al. (2014) [42] performed a UCS test on drying RE columns and then used the filter paper method to measure respective suction values just after the UCS test. In this thesis, suction values were linked with the Kelvin equation and Van Genuchten model similar to Chauhan, (2021) [90]. Figure 4.32 shows the results of compressive strength with the corresponding suction from different authors. In this thesis work, it was observed that the logarithm of suction is linearly correlated to the compressive strength. This linear relation is well correlated for all results regardless of the soil composition. This underlines again the important role played by the development of suction for low values, whereas the same increase at high values has few influences on fc.

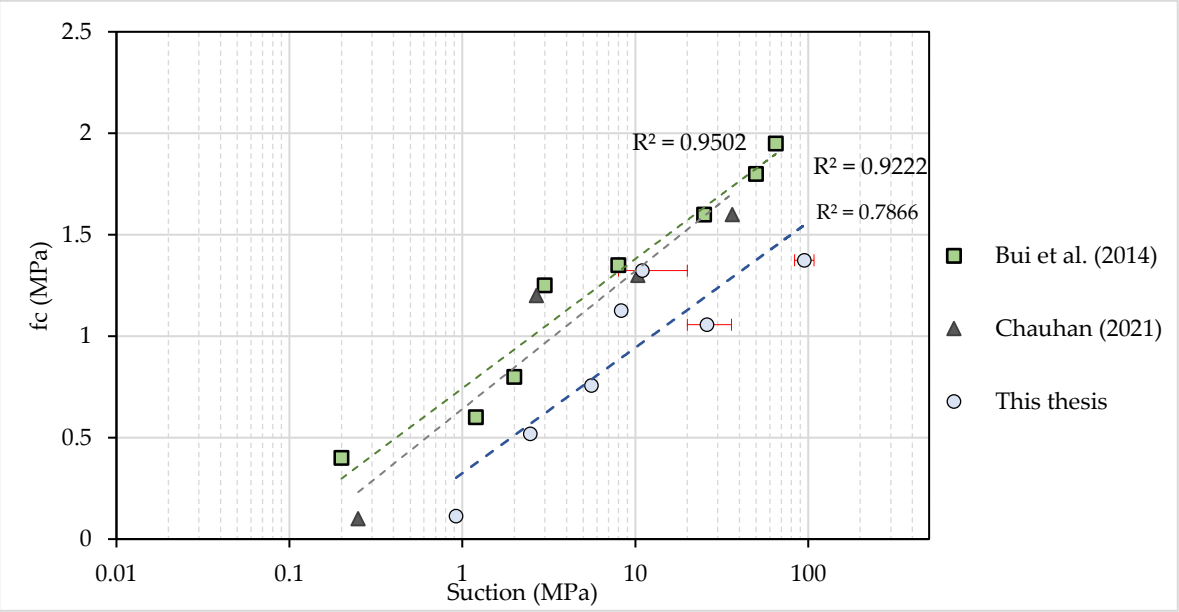

Figure 4.32: A linear relationship between compressive strength and suction. Comparison with studies of Bui et al. (2014)[42] and Chauhan (2021) [90].

4.3.4 Synthesis

Rammed earth samples were dried in a closed room before they were mechanically tested. The boundary conditions adopted constrained the moisture transfer in the sample to one direction mimicking a real wall equilibrating with ambient climatic conditions. While drying, periodic monitoring of the hydric state was performed. Thus, the evolution of water content, as well as RH, were obtained. In the first week, the drying rate was constant with a high evaporation rate, then followed by a fall in evaporation rate after 3 weeks. Capacitive sensors were placed to measure relative humidity inside the sample. During the first weeks of drying, there was no change in RH recorded by capacitive sensors. This is due to their limitation in very humid conditions. However, after 3 weeks the relative humidity inside the sample was falling at a constant rate. In addition, a comparison between the two methods (balance and capacitive sensors) for hydric monitoring was done, and a good agreement was observed at water content below 3%.

In the meantime, compressive strength was evaluated. It was observed both compressive strength and apparent Young's modulus were increasing rapidly during the first 3-4 weeks. After 6 weeks of drying the maximum strength was attained with a slower rate of gain in stiffness, although, the drying time depends on the temperature and HR conditions. Moist samples were more ductile while dried samples showed more brittle behaviour. Furthermore, the hydric state was represented with a matric suction variable. The evolution of mechanical behaviour with respect to suction was presented. A slight increase in suction was correlated with a significant increase in mechanical capacity at the early stage of drying, which is why the semi logarithmic graph for the fc(s) curve is more suited, where a linear relationship was observed. Results were validated by previous studies on a column scale [42].

4.4 Experiment at wall scale

Previously, a drying experiment on RE columns was performed, and a link between hydric state and mechanical properties was obtained. Now, this section will proceed similar experimental campaign but at a wallet scale (1.5 × 0.75 × 0.2 m^3) (Figure 4.33), in order to evaluate a geometric configuration which is closer to a real RE structure than the prismatic samples. The scale here is about ½ in width and height with respect to a real wall scale. Three walls named W1, W2 and W3 were fabricated as mentioned previously in chapter 3.8.3. Their properties are summarized in Table 4.5 with the type of test and monitoring, hereafter presented

Figure 4.33**:** Experimental protocol for RE walls

Table 4.5**:** Summary of walls properties, type of mechanical test and instrumentation.

Wall No	Dry density (kg.m3)	Porosity (%)	Date of manufacture, Drying time	Mechanical test	Instrumentation
W1	1862.6	29.6	01/04/2021, 0 week	Initial state after manufacture	Non
W2	1864.6	29.7	28/06/2021, 32 weeks	Periodic test during drying and after drying	Capacitive sensors
W3	1870	29.4	17/05/2021, 8 weeks	Mechanical test after capillary rise	Capacitive sensors+ TDR+ Electrodes
Mean	1865 ± 0.2%	29.6 ± 0.5%			

4.4.1 Experimental protocol

a) **Water monitoring**

The kinetics of drying of two walls W2 and W3 was followed by relative humidity sensors (capacitive sensors) and water content sensors (Time Domaine Reflectometer, TDR), whose principles are detailed in Chapter 3, section 3.5. Calibrated sensors were placed in the sample during manufacture. In each wall, a total of 9 of them were used. They were placed in the mid-height of each layer at a depth of 3 ± 0.5 cm, 5 ± 0.5 cm and 10 ± 0.5 cm from the drying surfaces (see Figure 4.34).

The TDR probe used in this study was TRIME-PICO-32, which provides a measurement of the volumetric water content with an accuracy of ± 2%. The device was calibrated by measurements on saturated sand and compacted soil of known volumetric water content. After calibration, the TDR was placed until a depth of 10 cm on the right side at mid-height of the wall.

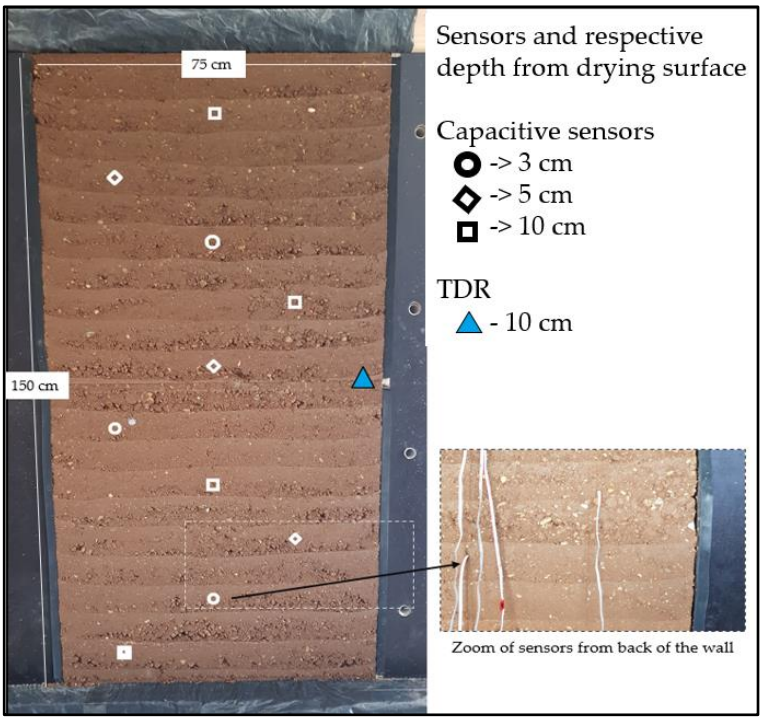

Figure 4.34: Layout of the position of the sensors with their respective depth in the wall. Zoom of the sensor's final position taken from the back of the wall.

b) **Mechanical testing**

A series of compressional tests were performed on large walls. At this scale, and with the huge mass of the walls, setting up experiments can be challenging. Thanks to the LOCIE Lab, which provided proper equipment to facilitate such experiments. The experimental setup is illustrated in Figure 4.35. The testing platform consists of a portal frame steel structure. The compression was done by electric actuators fixed on the top horizontal beam. An electric actuator that can push up to a maximum capacity of 120KN was used for compression. This way, according to the force necessary, one or two actuators were used. Transporting the walls to the testing platform was challenging. Indeed, walls had to be transported together with the concrete beam at the base, the wood beam at the top and the manufactured metallic formworks. In total, they weighed together about one tonne. To transport such a heavy wall, an electric forklift was used and operated by a skilled person.

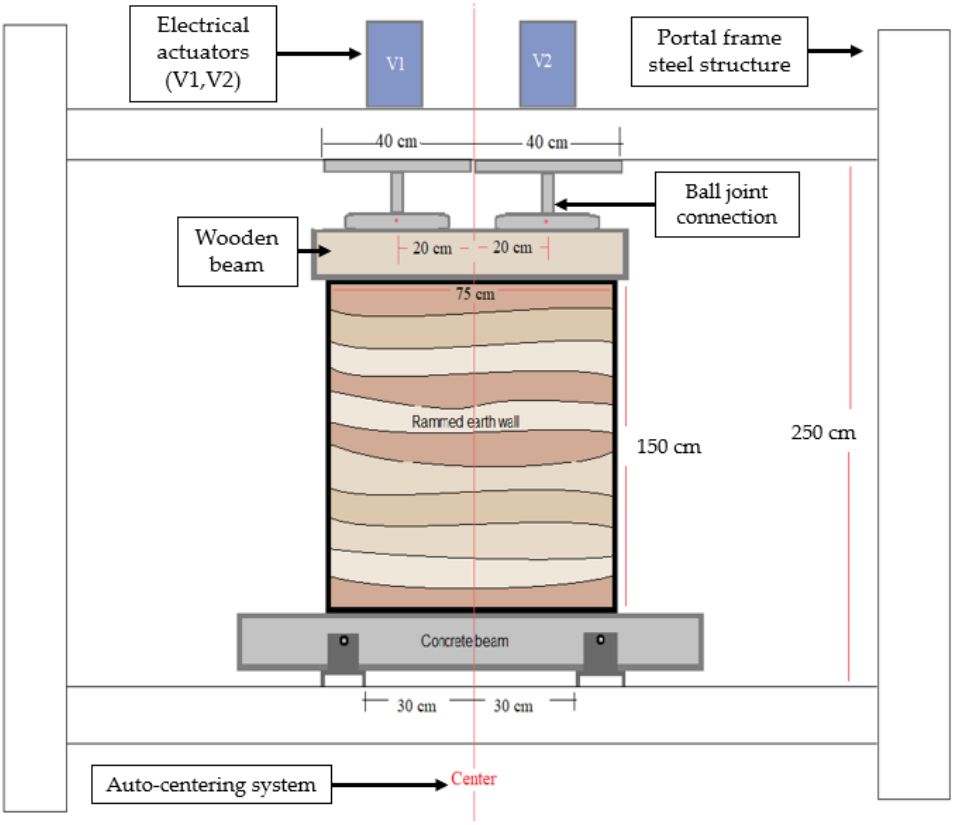

Figure 4.35: Experimental setup for mechanical testing

- **Periodic mechanical test (Elasto-viscoplastic behaviour)**

In order to determine the compression strength of the wall at the initial state, wall 1 (W1) was tested directly after manufacture in its moist state (w=10%). Whereas wall 2 (W2) was kept to be periodically tested with small loading-unloading increments to evaluate rigidity evolution. W2 was not tested at time 0 (in order to avoid damage at such a weak state) but from 1 week up to 32 weeks. Displacement controlled mechanical test is adopted. The loading path is illustrated in Figure 4.36 [141]: a first load until 0,1 MPa were performed (OA in Figure 4.36), then an unloading-reloading up to 0,1 MPa is done to determine the elastic behaviour (ABC). Lastly, it was decided to keep the displacement fixed for 100 to 500 seconds in order to determine the viscous component of the behaviour in relaxation (CD). The maximum loading, 0,1 MPa both prevent damage on the wall and is representative of a classical vertical apparent stress for a one-story building. The loading was controlled at a constant displacement of 1.2 mm/min (quasi-static loading). From Figure 4.36 points OAB represents the loading-unloading path with corresponding plastic and elastic deformation. The strain was calculated using field displacement coming from (DIC) technique as explained in section 4.2.3.2. The wall was sprayed with black dots to make patterns as shown in Figure 4.37. Images were recorded at points O, A, B, C, and D in Figure 4.36. The strains were determined in the central part of the wallet in order to avoid border effects.

Stress relaxation shows the dependency of stress on time, while displacement is fixed. The relaxation test is represented by points C and D (see Figure 4.36) and its corresponding stress-time dependency.

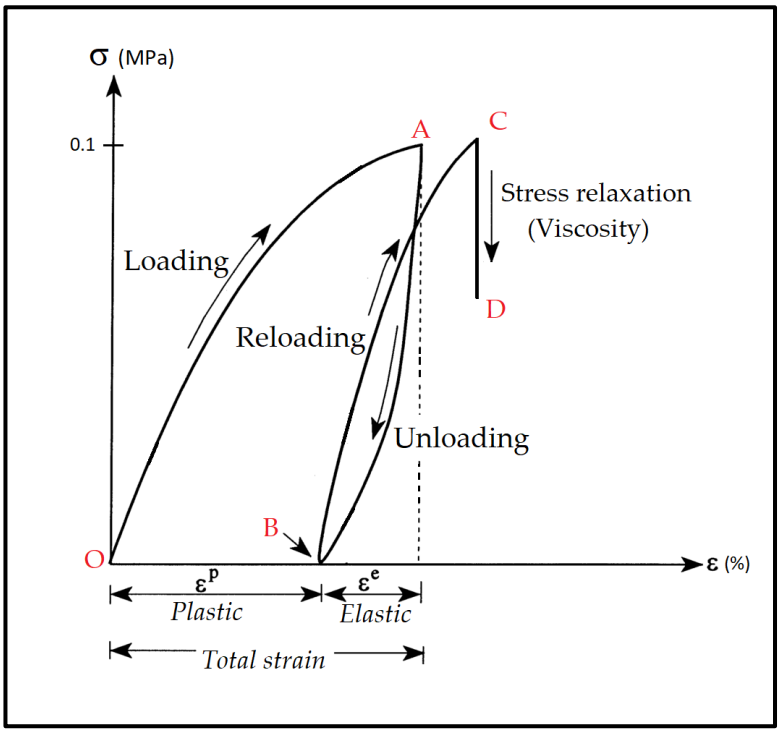

Figure 4.36: Loading path: Loading-Unloading cycle (OAB), and stress relaxation (CD) [141].

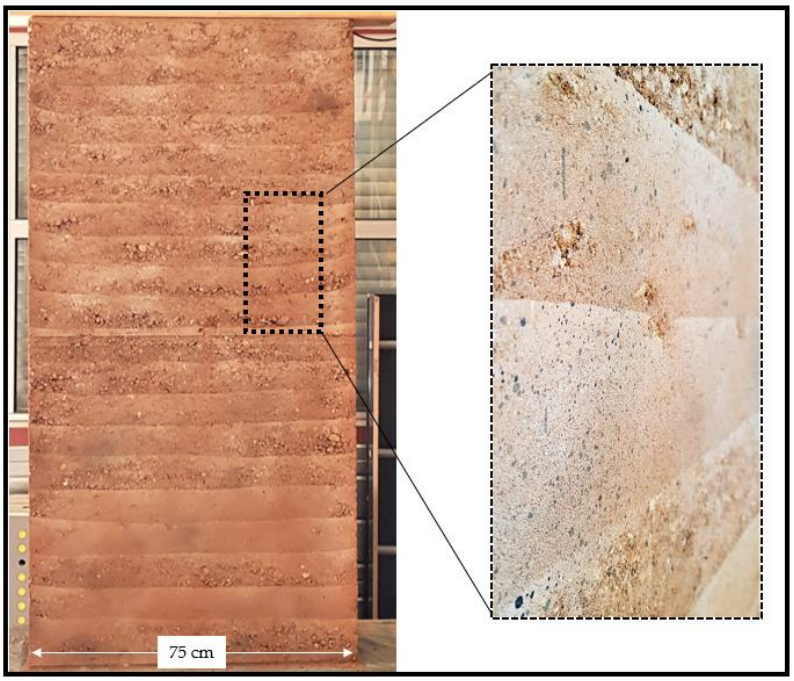

Figure 4.37: Black dots patterns on wall W2 for DIC during mechanical testing.

4.4.2 Results

4.4.2.1 Results of hydric state

With the help of capacitive sensors, relative humidity was followed in walls W2 and W3, results are shown in Figure 4.38 and 4.39 respectively for 8 weeks. In wall W2, it was observed that no variation of RH can be measured from the first 3 weeks although it is where the mass loss seems to be more intense according to TDR results (see Figure 4.40). At 8 weeks, both walls had RH ranging from around 80% to 90%. W2 was further dried, up to 32 weeks were it was mechanically tested, at this time the RH in the wall W2 was between 50% to 65%, reaching equilibrium with the drying environment. As for the prismatic columns, this was due to the limitation of capacitive sensors: in very humid conditions (RH>98%). Similarly, to the columns, after 3 weeks of drying, a constant decrease in RH was recorded from each sensor. It was also observed that the sensors placed near the drying surfaces recorded a higher drying rate and responded quickly to the change in environmental humidity.

Although measurement of global water content was not possible due to the large size and weight of the walls, it was possible to measure local water content using TDR. Figure 4.40 shows the evolution of water content determined by TDR in the core of wall W3. This Local value of water content decreased from a manufacturing water content of about 10.7% to 4.5% in 8 weeks. This value is higher than the global water content reached by prismatic samples S12, S13, S14 and S15 after 8 weeks of drying, which was between 2 to 3.5% (Figure 4.15f). However, this is consistent since the TDR is placed at the core of the wall thickness. That explains the higher water content.

It was noted that the first part of the drying curve is approximately linear, until four weeks. This is known as the first stage of drying and is associated with a constant drying rate period [129], where the ambient drying conditions (globally constant) are the limiting factor to the drying kinetics. The second stage of drying is associated with the falling drying rate, from weeks 5 to 8, where the internal water transfer from the core to the surface is the limiting phenomenon to the drying kinetics.

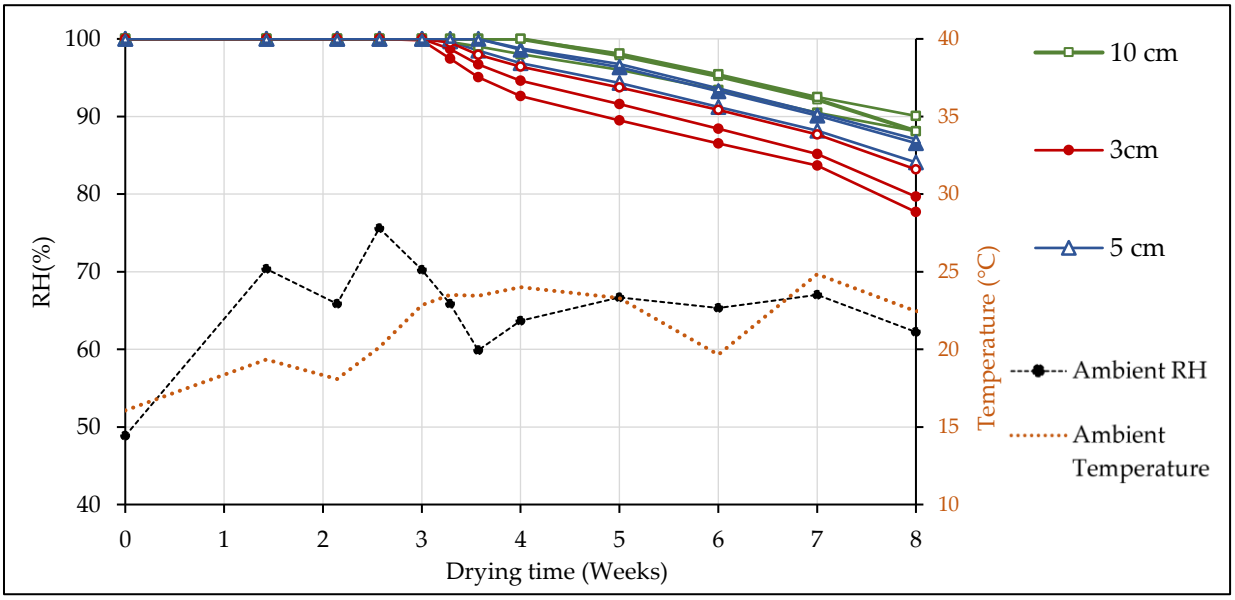

Figure 4.38: Evolution of RH with time for wall W2, RH recorded by capacitive sensors placed at a depth of 10 cm, 5 cm and 3 cm.

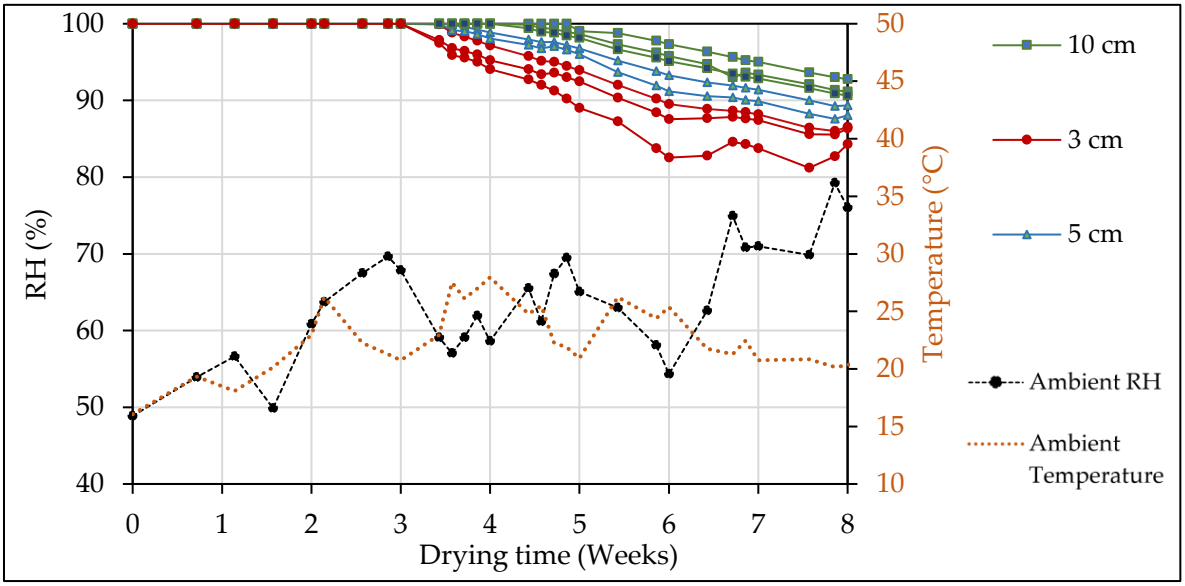

Figure 4.39: Evolution of RH with time for wall W3, RH recorded by capacitive sensors placed at a depth of 10 cm, 5 cm and 3 cm.

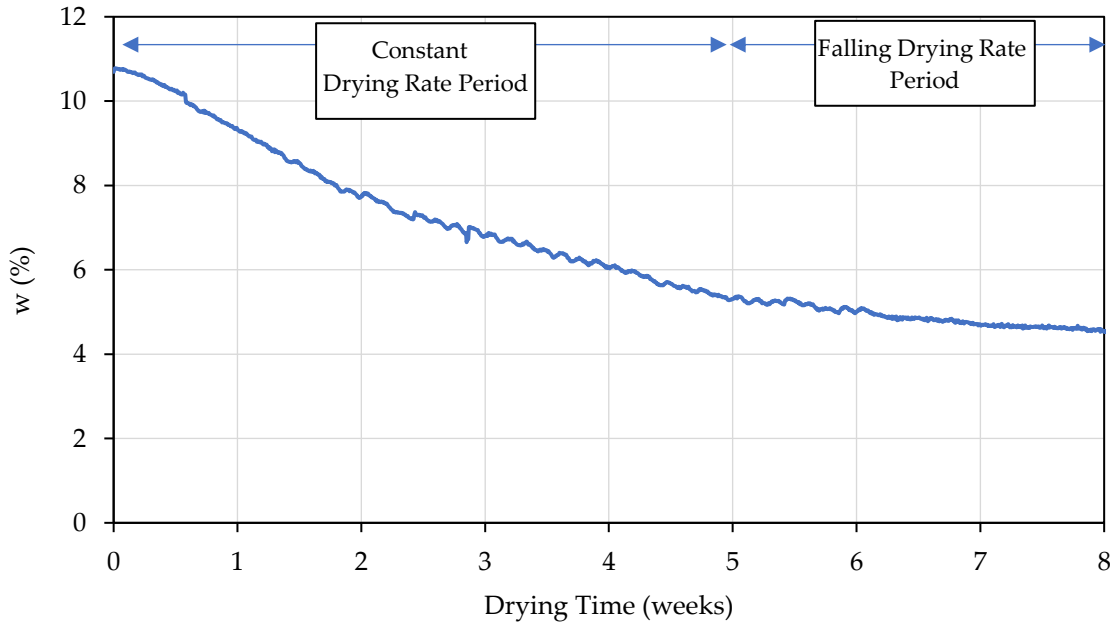

Figure 4.40: Evolution of water content with drying on wall W3, water content was measured by TDR probe placed middle side of the wall at a depth of 10 cm.

4.4.2.2 Results of Mechanical tests

a) **Initial and final compressive strength**

The mechanical resistance was determined on wall W1 in the moist state and on wall W2 after 32 weeks by compression until rupture. Results are presented in Figure 4.41. At the initial moist state, the compressive strength found was 0.1MPa, and at a dried state it was found 1.15MPa. An increase in compressive strength by a factor of almost 12 from the moist state to the dry one, a similar factor was observed in the RE columns presented in the previous section. The behaviour of the dried wall (W2) was more brittle observed by a sudden drop of axial stress during the rupture, while a moist wall (W1) presented a slow plastic deformation at the failure zone (Figure 4.41). Finally, the stress-strain curve of both shows that the dried wall (W2) has a large slope compared to the moist wall (W1) suggesting that the modulus of W2 is greater than W1. This modulus will be quantified in the next section by using the DIC technique to analyse the deformation and hence the modulus.

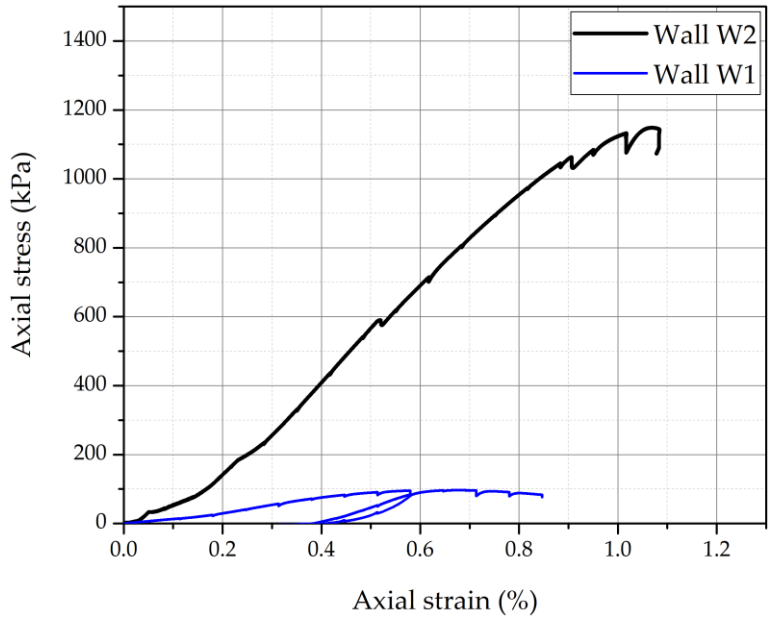

Figure 4.41: Stress-strain curve for wall W1 tested at moist state, and wall W2 tested at dry state after 32 weeks.

b) **Apparent Young's modulus of wall W2**

The apparent Young's modulus was determined from the unloading path AB where elastic deformation is found (see Figure 4.36). The images recorded at points A and B were analysed by 7D software to determine the strain. In this case, image B was used as a reference. Figure 4.42 presents the strain calculation using DIC on W2 dried after 8 weeks. All curves for all drying periods are presented in Appendix B. The displacement field between images A and B was determined, with 3 vertical profiles of vertical displacement (dy) represented in Figure 4.42. A non-uniform vertical strain can be observed in the Figure since the repartition of dy is not linear. The top part has deformed greater than 0.2 mm (seen by the bluish colour in Figure 4.42) and the near bottom part has deformed by 0.05 mm (seen by the reddish colour in Figure 4.42), it is worth noting that, the negative sign on the dy scale indicates the

downward direction. The strain was calculated in the third middle zone, marked by a dashed box in Figure 4.42. To ensure that the strain is calculated from the same region at each drying period, displacement profiles were made on the left, centre and right of the wall (see Figure 4.42). From these displacement profiles the strain was always determined between 500 mm to 1000 mm, the strain was calculated from the slope of displacement (dy) to the corresponding height on the wall. After 8 weeks of drying, and for $d\sigma_{yy} = 0.1$ MPa, we got $d\varepsilon_{yy} = 0.0119\%$, 0.0115% and 0.0149% for the left, centre and right of the wall respectively. It leads to an average value of apparent Young's modulus of $E_a = 721.7$ MPa.

The results of all weeks are summarised in Figure 4.43. Results show that the $E_a$of the walls increased from 190 MPa to 721.7 MPa after 8 weeks of drying from manufacture and then to 1024 MPa after 32 weeks. It was observed that the results of the evolution of apparent Young's modulus are very comparable to those obtained on RE columns presented in Figure 4.20, for very comparable densities, only the scale differs.

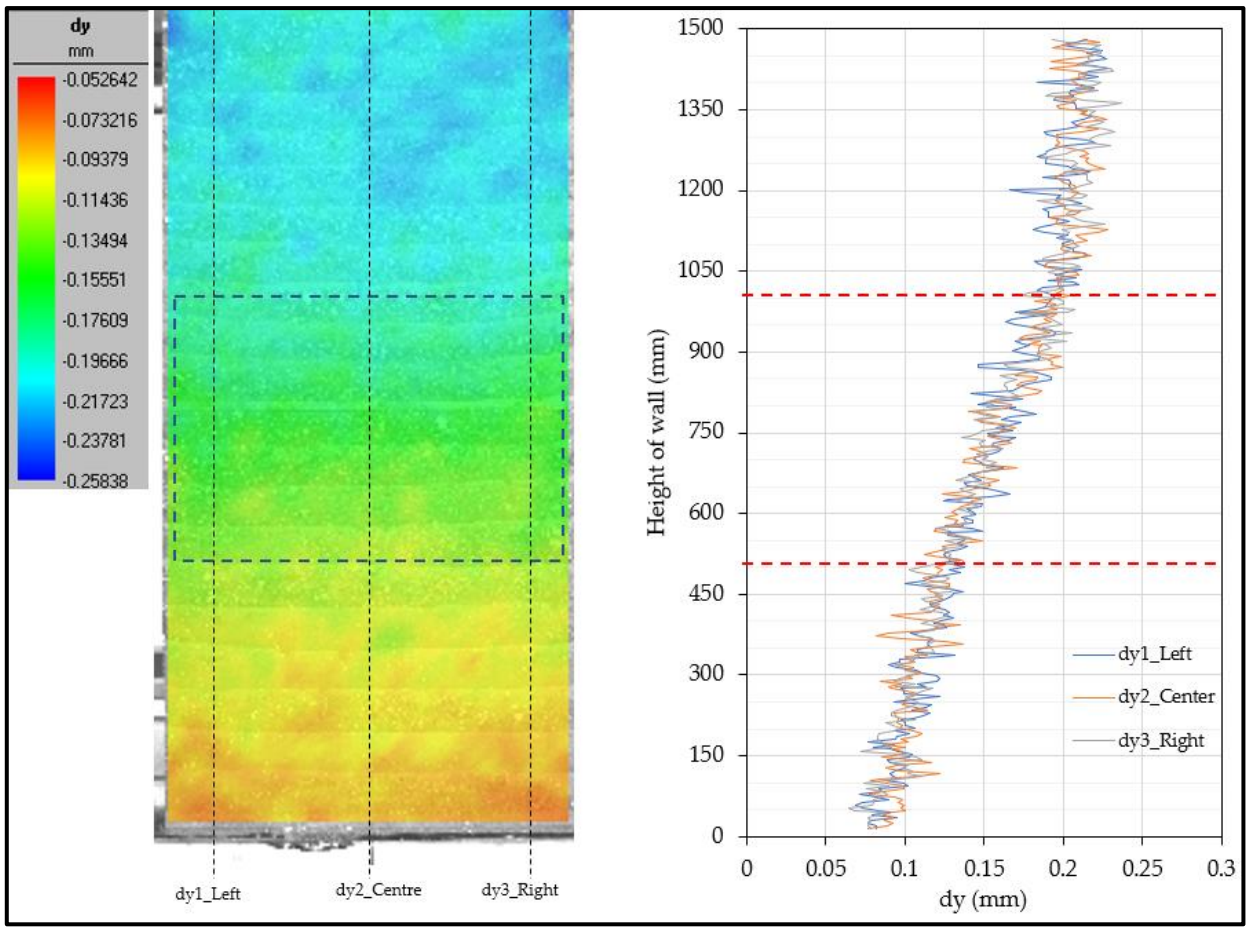

Figure 4.42**:** Image analysis of wall 2 (W2) dried after 8 weeks. On the left, is the displacement map of the wall during the unloading of 0.1 MPa. The strain is calculated in the third middle zone. The curve on the right shows the displacement profile on the left, centre and right of the wall, where the strain is determined between 500 mm to 1000 mm.

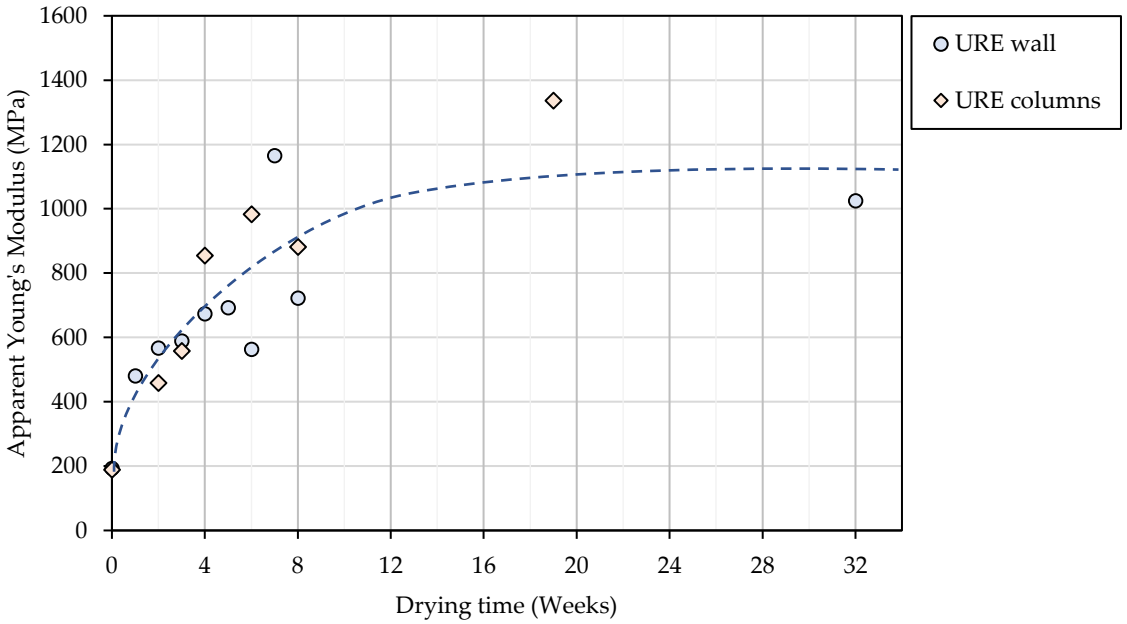

Figure 4.43: Evolution of Apparent Youngs' modulus with drying time along with its tendency shown by the dashed line.

c) **Viscous behaviour of RE and rheological models**

Figure 4.44 shows the evolution with drying weeks, of the stress relaxation curve during phase CD of the loading path (W1 at t=0, and W2 for one week and after). It was observed that, on each curve, the stress reduces with a pattern that seems to be exponential. For 8 weeks, the relaxation has been realized for a sufficiently long time of all and it can be seen that stress evolution seems to approach a fixed asymptotic value. Using the three-element model for relaxation (Figure 4.45), explained in Chapter 2, recalling the model equation as follows:

$$\sigma(t) = Ae^{-\left(\frac{E_1+E_2}{\eta}\right)t} + C \qquad (4.1)$$

Where σ is stress, ε is strain, E is Young's modulus, η is the coefficient of dynamic viscosity, and A and C are constants. From equation 4.1, the relaxation behaviour was modelled for each week and represented by the dashed line in Figure 4.44. From the model, the dynamic viscosity was determined for each test to fit the more accurately possible experimental data. Results are presented in Figure 4.46.

An increase of the coefficient of viscosity (η) from 8.15×10^9 to 1.53×10^{11} Pa·s during 8 weeks of drying is observed, after 8 weeks, η tends to an asymptotic value as shown in Figure 4.46. A significant change of η by a factor of almost 20, suggests the viscous behaviour should be considered in modelling the coupled hydro-mechanical behaviour of URE. When the wall is dried, the value of the viscosity was ranging around 1.3×10^{11} Pa.s. A similar order of magnitude of the coefficient of viscosity (4.834×10^{12} Pa.s) was reported by Gil-Martín et al. (2022) [91] studying a RE cylindrical column (Φ=15 cm and H=30 cm) during a creep test using the same rheological model (see Figure 4.45). From Figure 4.46, it is clear that the viscous behaviour of rammed earth is highly dependent on the hydric state. In the first week, it may be significant, and it was noticeable (noise made by rearranging of grains) even for the low

increment of loading. In real buildings, viscosity can take place when the wet earth is loaded, and strain can develop by creep. Therefore, it could be s necessary to estimate the creep strain.

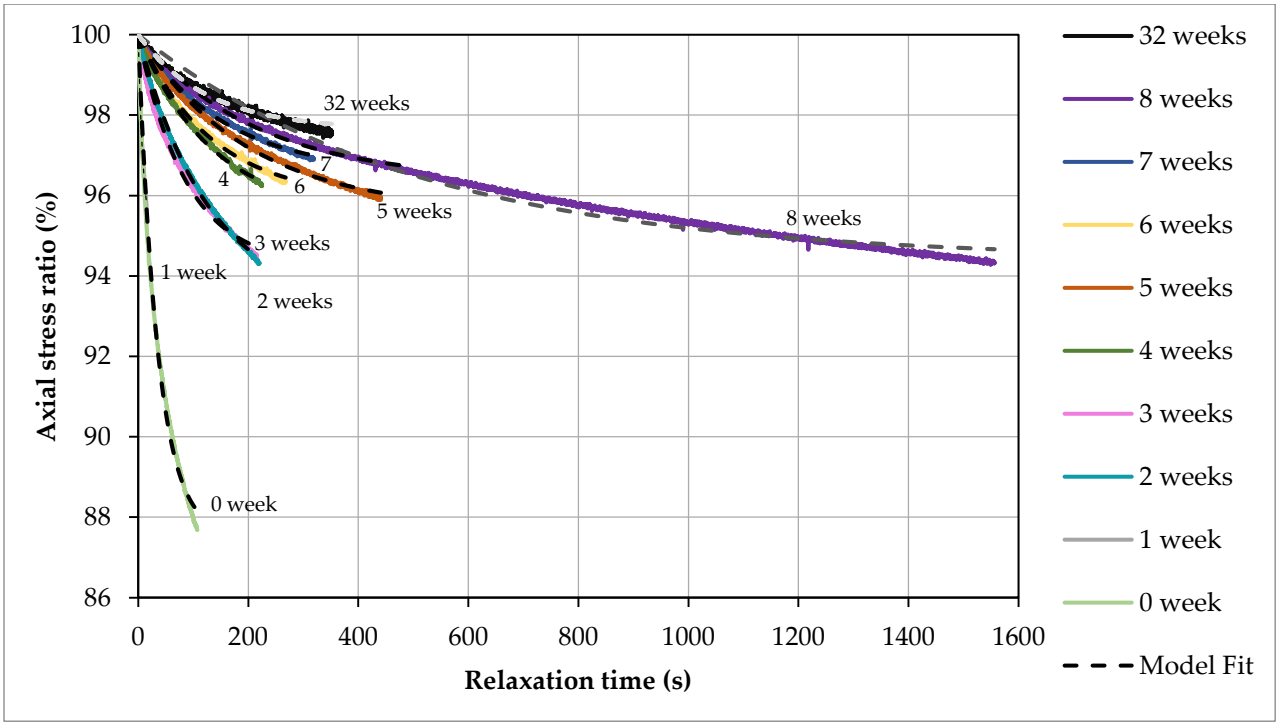

Figure 4.44: Stress relaxation test results showing experimental and modelled curve each week on a drying URE wall [141].

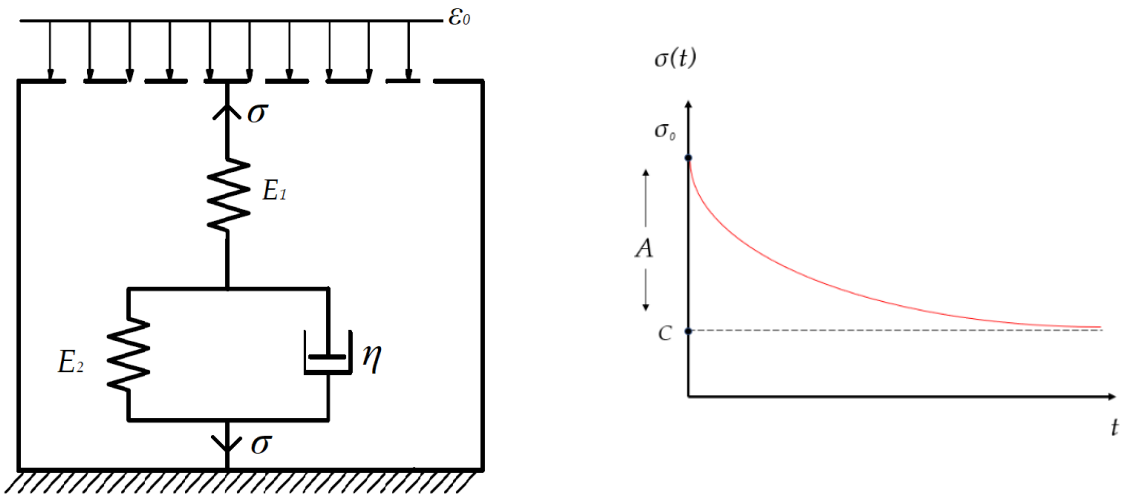

(a) (b)

Figure 4.45: (a)Three-element model to describe the elasto-viscoplastic behaviour. (b) Stress relaxation function.

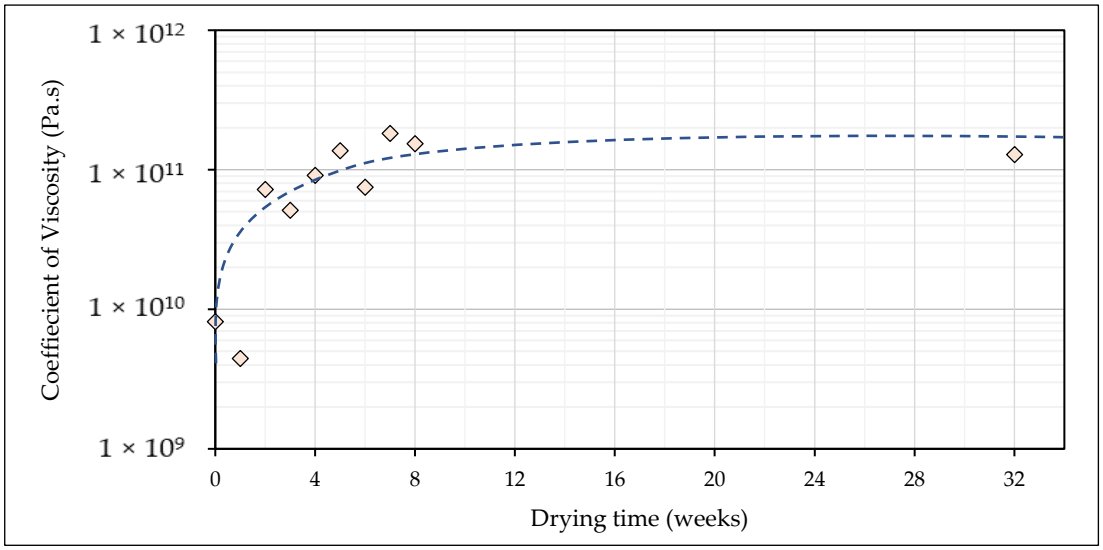

Figure 4.46**:** Evolution of coefficient of dynamic viscosity with drying time, along with its tendency shown by the dashed line.

Using the same three-element model (Figure 4.45a), creep strain $\varepsilon(t)$ was calculated from equation 2.13 (more explanation in Chapter 2, section 2.3.3). We recall:

$$\varepsilon(t) = \sigma_0 \left(\frac{1}{E_1} + \frac{1}{E_2} \left(1 - e^{\left(\frac{E_2}{\eta}\right)t} \right) \right)$$

Where σ is stress, ε is strain, E is Young's modulus and η is the coefficient of viscosity. The evolution of creep strain developed at a constant load of 0.1 MPa at different drying times is shown in Figure 4.47. At the initial state, where the wall is moist, it was observed that the creep strain developed increased to 0.125%. While a dry state, (32 weeks), a gradual increase in creep strain to 0.097% was observed in about two hours. A significant reduction of creep strain from moist to dry state by a factor of 1.3. It can be observed in Figure 4.47 that the asymptotic values seem low. It means that a 3 m fresh wall would only creep for about 3 mm. The values of creep strain might seem negligible at first glance, but it's worth noting that these values are proportional to the constant load applied, the higher the load, the higher the creep strain. Doubling the constant load will double the creep strain.

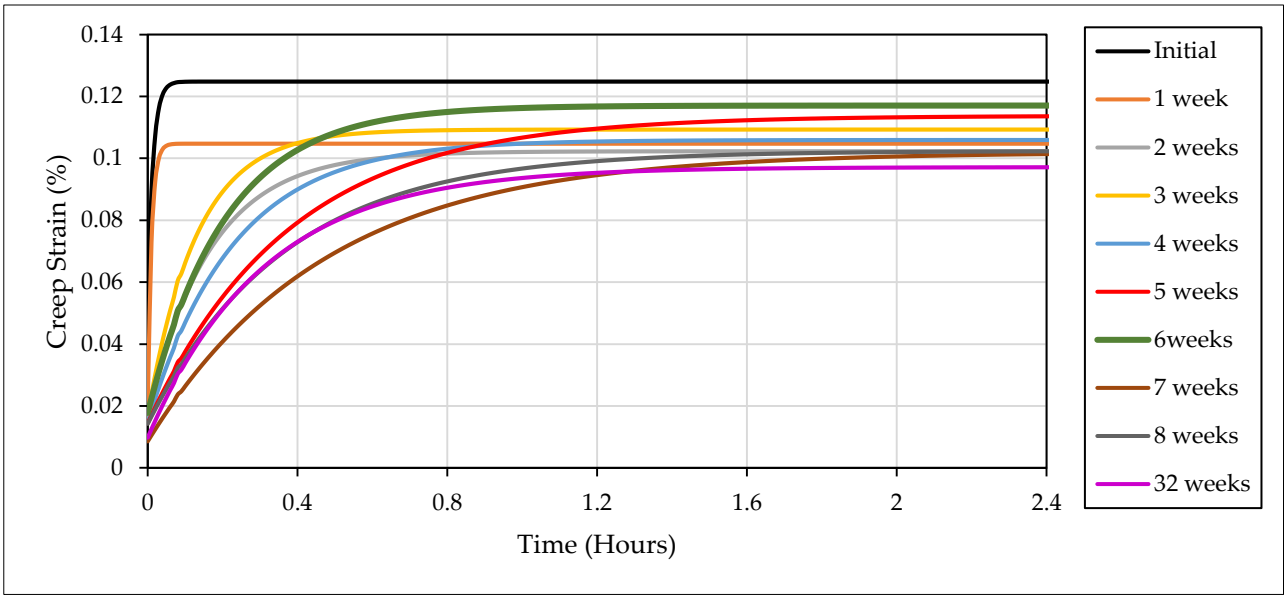

Figure 4.47**:** Evolution of creep strain at a constant load of 0.1 MPa with drying time. The strains are calculated from Three element model (Burges model) using the coefficient of viscosity obtained experimentally.

4.4.3 Discussion

a) **Study of suction as a state variable to represent the hydric state**

Suction has been shown to be a very suitable parameter in order to understand and model the unsaturated hygro-hydro-mechanical behaviour of the earth's porous medium [84]. It is thus important to adopt it as a single variable to stand for the hydric state. The RH (Figure 4.38) and their corresponding temperatures were expressed in suction by using Kelvin's equation (8). Kelvin's equation was previously defined in Chapter 2, section 2.3.2. The suction values were computed locally at depths of 3 cm, 5 cm, and 10 cm (position of capacitive sensors), and represented in function with drying time (Figure 4.48). In addition, suction evolution deduced from TDR water content (Figure 4.48) was obtained thanks to the Van Genuchten model of the water retention curve. These curves show a consistent evolution, except for the first 3 weeks on which the SHT sensors cannot measure the very slight evolution of RH, responsible for a not negligible variation of water content, once the Kelvin equation is used. We can observe that the suction value deduced from TDR stays low during the drying period (consistently, it was observed previously that the water content measured was still high after 8 weeks). However, it is close, during the last weeks, to the values of suction deduced by SHT, at the same position (10 cm under the surface). It means that measurements can be trusted and that the core of the material stays very humid, even after 8 weeks.

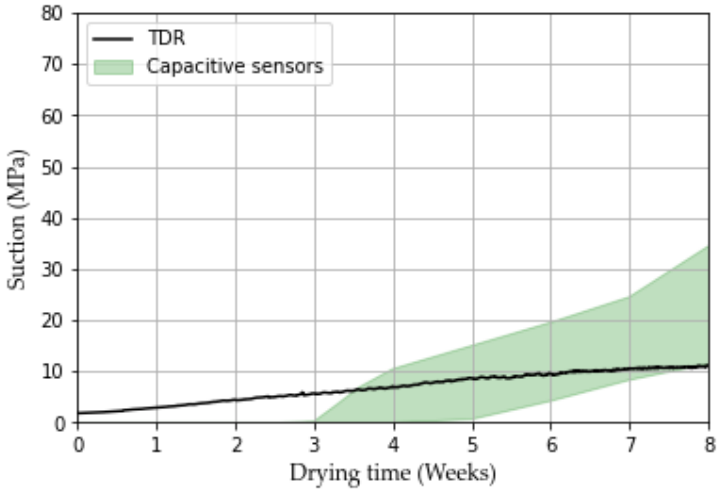

Figure 4.48: Evolution of suction in RE wall deduced from RH and water content evolution

b) **Mechanical properties vs suction**

The evolution of total mechanical behaviour can be linked to the hydric state within the wall through its suction values. Only local suctions in the wall were evaluated by using TDR and capacitive sensors as shown in Figure 4.48. To relate, the mechanical behaviour with the corresponding suction, the local suctions from TDR were used in the first three weeks. Then after three weeks, both TDR and RH were considered, and the suction was taken as the mean value of suction with an error bar representing the lower and upper values of suction at each stage. Figure 4.49a. shows the results of apparent Young's modulus with the corresponding suction. In this work, it was observed that the logarithm of suction is linearly correlated to the apparent Young's modulus, similar relation was observed from the RE column. The low R^2 of 0.64 value in Figure 4.49a can be explained by some points that are way off-set from the rest, such as the one near E_a of 1200 MPa, this could be due to technical errors in the measurement of strain. In addition, the suction value is not uniform and may vary in between the error bar represented in Figure 4.49a which can vary the R^2. On the other hand, the coefficient of viscosity (η) was also linked to the suction (Figure 4.49b), a linear relation, with an R^2 of 0.54 correlation was shown in Figure 4.49b, similar results η are observed on soil material containing clay [142].

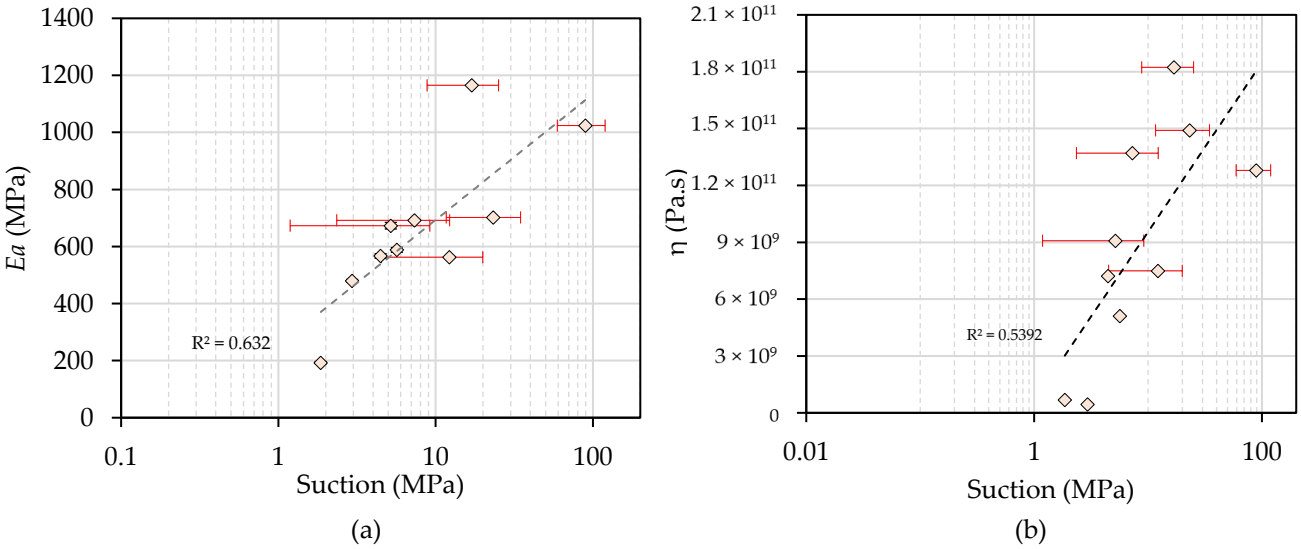

Figure 4.49: (a) Evolution of apparent Young's modulus with log(s) at wall scale (b) Evolution of coefficient of viscosity η with the log(s) for RE wall.

c) Effect of scale

The results of the influence of hydric conditions on mechanical performance have been presented at each scale (i.e. material scale, column scale and wall scale). The study has been done by using the same soil and the same clay nature. At the material scale, the soil was sieved at 5 mm, while at both large scales, the soil was sieved at 20 mm. The samples in all three scales had comparable dry densities with standard deviation of 0.8%. As discussed previously, suction is a parameter chosen to represent the hydric state. A uniform suction was controlled at the material scale. At large scale, the distribution of suction is not uniform, therefore, the global and local repartition of suction was measured.

In all three scales, the mechanical performances increased linearly with the log of suction. The results of fc with the log of suction at three scales are shown in Figure 4.50. It is observed that the fc at the material scale is significantly larger than both column and wall scales. The reduction in strength at a large scale was attributed to higher gravel content and size according to the weak link theory. At large scale, both columns and wall show a similar fc at moist state (suction around 2 MPa), at this state samples were more ductile as we have seen previously in Figure 4.25 and 4.41. When dried, the behaviour was more brittle (suction near 100 MPa), and columns were found to have a higher fc of 1.2 as compared to the wall (see Figure 4.50). This highlights the effect of scale and can be explained as that the more the sample is, the more probabilities are to have a default in the sample, which could initiate the failure. On the other hand, the apparent Young's modulus, E_a, showed the same trend with the log of suction at three scales (Figure 4.51), but the values of E_a were in the same order of magnitude at all suction levels, with minor exceptions.

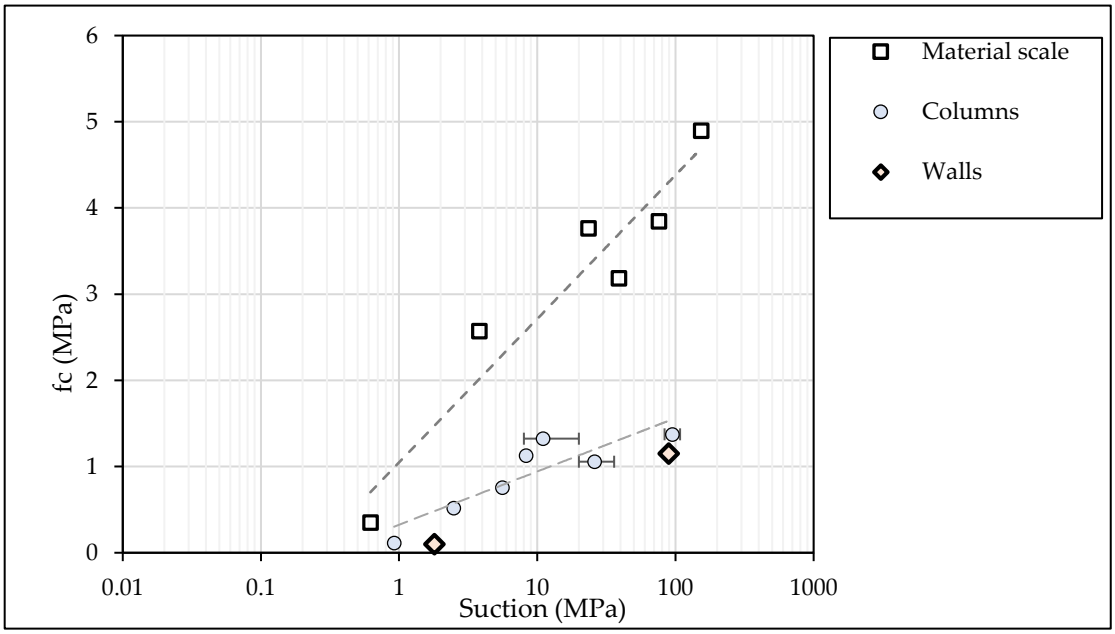

Figure 4.50: Evolution of compression strength with the log of suction, presented for material, columns and wall scale.

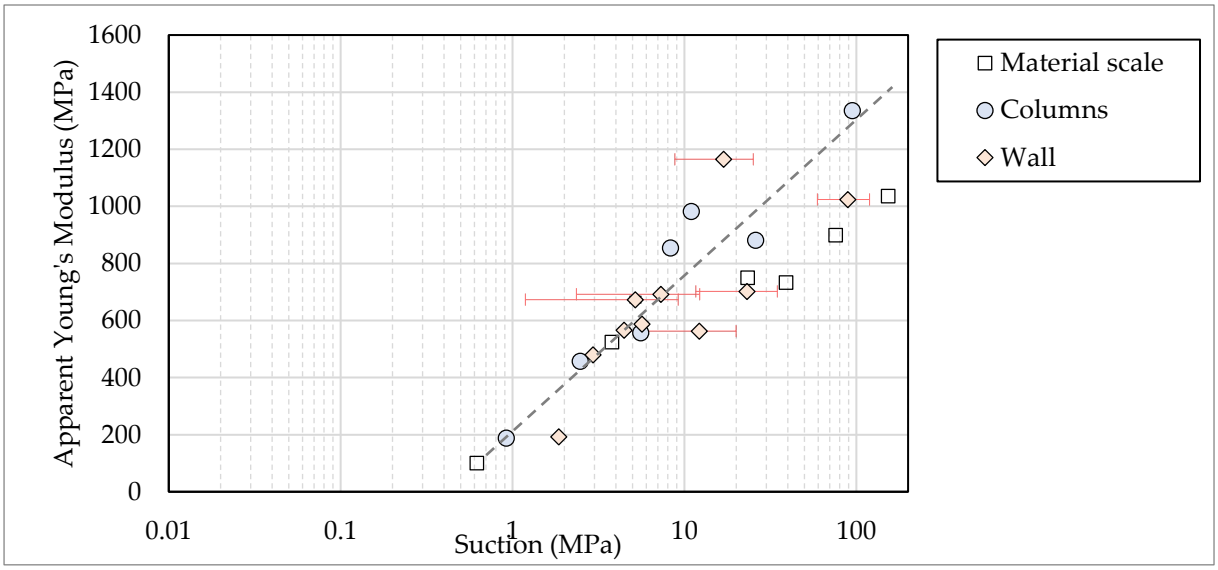

Figure 4.51: Evolution of compression strength with the log of suction, presented for material, columns and wall scale.

4.4.4 Synthesis

The mechanical behaviour of RE has been studied at a wall scale close to a real building scale. The RE walls were dried after manufacture and while drying, periodic monitoring of the hydric state was performed. Thus, the evolution of water content, as well as RH were obtained. The walls were then subjected to mechanical tests including Loading-unloading cycles (elastoplastic behaviour) and stress relaxation (viscous behaviour). These tests were performed each week for 8 weeks of drying and then at the dried state, thus the evolution of mechanical behaviours with respect to time and hydric state were presented.

This chapter includes some major contributions to the unsaturated behaviour during RE drying. First, it highlights the viscous behaviour of RE and its evolution with the hydric state. Considering that, none of the existing studies has ever shown the variation of visco-elastoplastic behaviour of RE, this work will pave the way for taking into consideration the viscous part of the mechanical behaviour of URE. In particular, it provides the order of magnitude for the coefficient of viscosity (η) for RE, which is scarce in the literature. The influence can be taken into consideration, and the creep effect has been estimated to be limited for limited increments of axial load.

Secondly, the size effect on the mechanical response of RE has been investigated. The results of apparent Young's modulus at the wall scale were compared to the ones at the material and column scale that used the same soil. A close relation was observed in the evolution of apparent Young's modulus with time between the three scales. However, some variations were noted on the apparent Young's modulus when considering the suction in the samples, but it could be due to the non-uniform distribution of suction in walls and columns, thus the suction is presented as a global and local value of suctions. Semi-logarithmic functions are obtained between suction and, apparent Young's modulus and coefficient of viscosity. Similar results are obtained on soil material containing clay.

4.5 General conclusion of the drying experiment

In this chapter, the mechanical behaviour of RE has been studied with respect to hydric conditions in an early stage of drying. The study was performed experimentally at three scales, from material scale to large scale of columns and walls which is half of a scale of a real building scale.

The main protocol was to link the change in mechanical response with the hydric state. To do so, First, the hydric state was monitored and then mechanical tests were performed.

The hydric state at the material scale was monitored by conditions samples at different RH between 32.8% and 97.3%, at a constant temperature of 25°C. At both large scales, RE samples and walls were dried in an ambient condition, and continuous measurements of water content and RH were done.

The kind of mechanical tests performed at all scales were UCS to determine the compressive strength (fc) and apparent Young's modulus, and relaxation test (viscous part) to determine the coefficient of viscosity for the wall.

Attention was paid to the presentation of the hydric state (RH and water content) using the suction variable which is a state variable. Finally, the link between the hydric state and mechanical characteristics was established. The evolution of mechanical behaviour with respect to suction was presented at all three scales. A slight increase in suction was correlated with a significant increase in mechanical capacity at the early stage of drying. A linear relationship was observed between mechanical capacity and logarithmic of suction. It means that, close to the saturation, the effect of a few variations of the suction has much more important than a few variations of suction, for a low saturation degree. It may be understood by the fact that at high saturation, the suction is developed in a larger amount of liquid into the pores, whereas at low saturation, only a small volume is concerned by this stress. This is the sense of the Bishop expression of unsaturated effective stress (where: $\sigma'_{ij} = \sigma_{ij} + Sr.s.I_{ij}$, see the equation in Chapter 2, section 2.4.2).

In addition, from the wall, the viscous part of them had a similar response with suctions, the equivalent creep effect calculated was about 0.1% for a fresh wall, meaning that a 3 m fresh wall would only creep for about 3 mm.

A comparison of all three scales was done showing that the fc at the material scale was significantly larger than both column and wall scales. While, the apparent Young's modulus, E_a, showed the same order of magnitude at all suction levels.

4.6 Summary of parameters necessary for modelling the thermal hydromechanical behaviour of RE

In this section, the parameters required for modelling the thermal hydromechanical (THM) of the RE wall are presented. These parameters are obtained experimentally with boundary conditions close to a real building. Parameters are categorised as physical, hygro-thermal, hydric and Mechanical parameters. These parameters are summarised in Table 4.6 as follows:

Table 4.6**:** Parameter summarized from this work necessary for modelling the thermo-hydro-mechanical behaviour.

	Factors	**Units**	**Values**	
Materials	Fine contents	-	0.1	
	Fine/Gravel ratio	-	0.3	
	Porosity	-	0.29	
	Dry density	$kg \cdot m^{-3}$	1865	
Dimension	Wall thickness	m	0.2	
	Wall height	m	1.5	
	Wall width	m	0.75	
Hygro-thermal	Initial saturation of walls	-	0.71	
	Average ambient RH	%	60	
	Average ambient temperature	°C	15	
Water retention properties	Air entry suction	MPa	0.3	
	VG parameters: α, m and n	α (MPa^{-1})	α =1.507, n=1.556, m= 0.357	
	GAB parameters: C_1, C_2 and W_m		C_1 = 10.58, C_2 = 0.78, W_m=0.94	
	Hydraulic conductivity	m/s	2.4×10^{-8}	
			Moist	Dry
Mechanical	Suction	MPa	1.8	60 to 115
	Compressive strength	MPa	0.1	1.15
	Apparent Young's Modulus	GPa	0.19	1.024
	Coefficient of viscosity	Pa·s	10^9	10^{11}

Chapter 5

5 Influence of capillary rise on mechanical capacity

This chapter presents a second experimental campaign where RE columns and a wall are subjected to capillary rise. During the capillary rise, the hydric state of the sample was recorded thanks to various instrumentation methods and therefore the kinetic water rises and water absorption parameters to characterise capillarity are presented. In parallel, samples are tested mechanically just after the capillary and others were left to re-dry after the capillary rise and then tested mechanically. This chapter answers the following questions:

What experimental method is suitable to follow the capillary rise, and which kinetics can be observed?

How evolves the mechanical resistance during the capillary rise?

Is the mechanical resistance restored upon re-drying?

Chapter Summary

5.1 Research motivations and the theory of capillary rise in porous building

Capillary rise, also known as rising dampness, is a common problem in masonry buildings, caused, respectively, by the humid state of ground soil and ambient conditions such as rainfall. Usually, a damp-proof course and raised foundation are used to prevent groundwater to access the ground floor walls, and overhanging roofs to reduce the wetting of wall surface from rainfall. In case of a broken, bridged, or missing damp-proof course, groundwater will gain access to ground floor walls through capillary action. Also, in extreme cases like a flood or unexpected heavy rainfall, water rise through capillarity can still cause serious structural damage, especially for earth buildings like RE.

As discussed in the literature review, the effect of capillary rise on mechanical behaviour RE is significant but rarely studied. In addition, the impact of drying-wetting cycles on the mechanical

performance of RE has not been yet accurately quantified and understood. The study aims to experimentally quantify the effect of capillary rise on the mechanical performance of RE at a scale that is representative of a multi-layer structure of rammed earth. To do so, capillary experiments adapted for the large scale were designed, and the kinetic of capillary rise and evolution of mechanical strength were followed before and after capillary rise.

The interactions between water and porous building materials are complex and numerous. First, it's important to understand the mechanism of capillary rise in a porous building.

a) Height of capillary rise

The internal molecular force of attraction between molecules of the same substance is termed cohesion and the force of attraction that exists between the molecules of dissimilar materials is known as adhesion. Water molecules stick together because of cohesion forces, and stick to other materials such as glass or cloth because of adhesion forces. When the adhesion force is greater than the cohesion forces within the water, then the surface of the solid material becomes wet. At the air/water interface, the surface of a given quantity of water behaves as a thin tight membrane due to surface tension. Therefore, capillarity is a phenomenon that describes the movement of water within the spaces of a porous material due to the forces of cohesion (holding water molecules together), adhesion (sticking water molecules to the other material), and surface tension (holding the surface intact). The classic example to illustrate capillary rise is that of a hollow open-ended glass tube in a container of water (Figure 5.1). Capillarity is a consequence of the surface tension between the surface liquid film and the wall of the capillary tube. The height of capillary rise reached by the liquid depends on the surface tension of the liquid and the radius of the capillary tube (Figure 5.1).

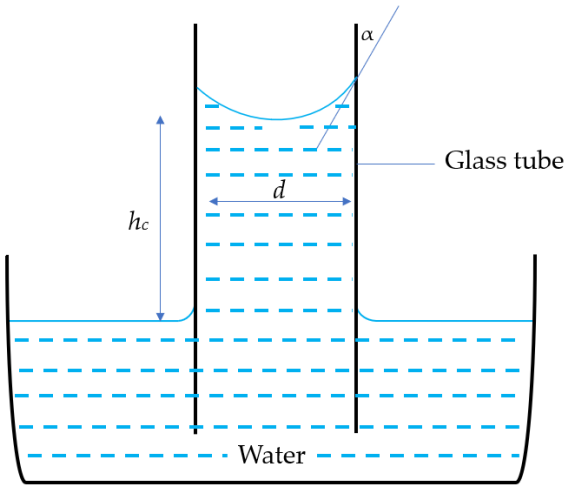

Figure 5.1: Capillary rise of water in a small-diameter glass tube

From a simple analysis of mechanical equilibrium for the capillary rise in a small-diameter tube, the ultimate height of capillary rise, h_c, is given by Jurin's law [86]:

$$h_c = \frac{4T_s \cos\alpha}{d\rho_w g} \tag{5.1}$$

Where:

ρ_w is the density of water (1 g/cm3), g is the gravitational acceleration (980 cm/s²), α is the contact angle (low for water, air, and glass contact and *Ts* is the surface tension of water (72 mN/m at 25 °C), d is the diameter of the tube. Imposing these values, and considering a zero value of α equation 5.1 simplifies to:

$$h_c(cm) = \frac{0.3}{d(cm)} \tag{5.2}$$

However, capillary rise in porous building material is far more complex than the simple capillary tube model (Figure 5.1, thus equation 5.2 is not sufficient to estimate the capillary height.

In particular, RE is made of compacted soil, so to better estimate the capillary rise, an approach used in real soil will be adopted. Soil comprises a range of different particle sizes with complex packing and pores distribution. Analytically evaluating the height of capillary rise is quite difficult. Various empirical equations have been developed for soil by considering the particle size distribution, void ratio, and air-entry head. Peck et al. (1974) [143], for example, describe an empirical equation expressing the height of capillary rise *hc* (mm), with the void ratio e, and the 10% finer particle size, D_{10} (mm) as;

$$h_c = \frac{C}{eD_{10}} \tag{5.3}$$

Where C is a constant varying between 10 and 50 mm² depending on surface impurities and the grain shape. However, the coefficient C is difficult to choose because the range of C is relatively large. Lane and Washburn (1946) [144] proposed a formula after conducting an experiment for eight different soil, they found that the maximum capillary height h_c (mm) is linear with D_{10} (mm):

$$h_c = -990(\ln D_{10}) - 1540 \tag{5.4}$$

Where both D_{10} ranges from 0.006 to 0.2 mm. On the other hand, Kumar and Malik (1990) [145] by carrying out indoor tests summarized the following equation:

$$h_c = h_a + 134.84 - 5.16\sqrt{r} \tag{5.5}$$

Where h_a (mm) is the air-entry head defined as the height up to which the soil remains saturated during the capillary rise, *r* (μm) equivalent pore radius. The unit of r is very small, so it has little influence on the calculation of h_c. Therefore, h_a is the only key parameter which can be determined by the soil-water characteristic curve.

To conclude, these empirical formulas will be used to estimate the *hc* of the soil used in this study. Then by using *hc*, the rate of capillary rise will be estimated by using the Terzaghi approach as explained in the next part.

b) Rate of capillary rise

In order to predict the rate of capillary rise in soil, a conceptual model of a soil sample placed on a water table is considered in Figure 5.2, placed along with its soil-water retention curve. It is important to define the term that will be used: capillary front, ultimate height of capillary rise, and air-entry head.

The distance measured upward from the elevation of the water table to a wet zone is known as the capillary wetting front or simple capillary front (z). The capillary front can be observed at the interface between wetted soil which takes a darker colour in contrast to its original dry soil. The capillary front will keep rising until reaches a maximum height known as the ultimate height of capillary rise (hc). Air-entry head (h_a) is defined as the height at which air enters the largest soil pore, and soil begins to desaturate. In other words, the air-entry head is the height up to which the soil remains saturated, it can be calculated from the soil-water retention curve (Figure 5.2).

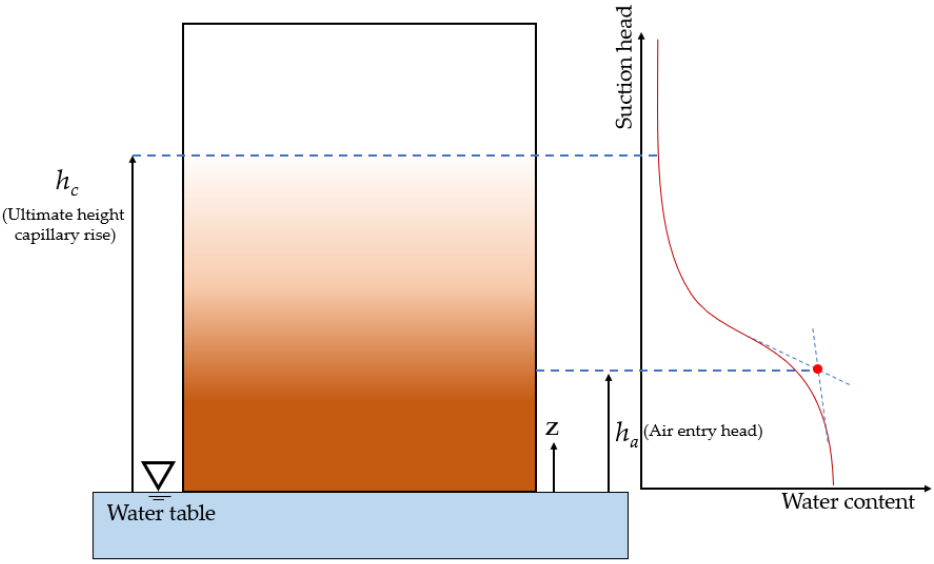

Figure 5.2: Conceptual model for the capillary rise and associated soil-water retention curve

Terzaghi (1943) proposed an analytical solution to predict the rate of capillary rise, and the following two major assumptions were considered: that Darcy's law for saturated fluid flow is roughly applicable to unsaturated soil and that the hydraulic gradient (i) responsible for capillary rise can be described as follows:

$$i = \frac{h_c - z}{z} \tag{5.6}$$

where hc is the ultimate height of capillary rise; and z is the capillary wetting front. Darcy's law can be expressed as:

$$q = k_s i = n\frac{dz}{dt} \tag{5.7}$$

Where q is the discharge velocity (m/s), k_s is the saturated hydraulic conductivity (m/s) of the soil, i is the hydraulic gradient and n is the soil porosity. Solving Eqn. (5.6) and (5.7) and imposing an initial condition of zero capillary rise at zero time, Terzaghi arrived at the following solution describing the location of the capillary wetting front z as an implicit function of time:

$$t = \frac{nh_c}{k_s}\left(ln\frac{h_c}{h_c - z} - \frac{z}{h_c}\right) \tag{5.8}$$

However, the hydraulic conductivity (k_s) to be nonlinear from the point where the soil ceases to be saturated and enters the unsaturated zone. Lu and Likos (2004) developed an alternative solution for the rate of capillary rise by incorporating the Gardner (1958) one-parameter model to estimate the unsaturated hydraulic conductivity function. Gardner's model may be expressed as:

$$k = k_s \exp(\beta h) \tag{5.9}$$

where k is the unsaturated hydraulic conductivity at suction head h (cm) and β is a pore size distribution parameter (cm^{-1}) representing the rate of decrease in hydraulic conductivity with increasing suction head. Incorporating the Gardner model to represent hydraulic conductivity at the wetting front, a governing equation for the rate of capillary rise can be written as:

$$\frac{dz}{dt} = \frac{k_s}{n}\exp(-\beta z)\frac{h_c - z}{z} \tag{5.10}$$

Then the analytical solution of equation 5.10 can be written in the series form:

$$t = \frac{n}{k_s}\sum_{j=0}^{m=\infty}\frac{\beta^j}{j!}\left(h_c^{j+1}\, ln\frac{z}{h_c - z} - \sum_{s=0}^{j}\frac{h_c^s z^{j+1-s}}{j+1-S}\right) \tag{5.11}$$

Therefore, the modified Terzaghi equation 5.11 will be used in this study to estimate the rate of capillary rise.

In the next section, the experimental part of this chapter will be presented. The schematic plan of the methodology is illustrated in Figure 5.3.

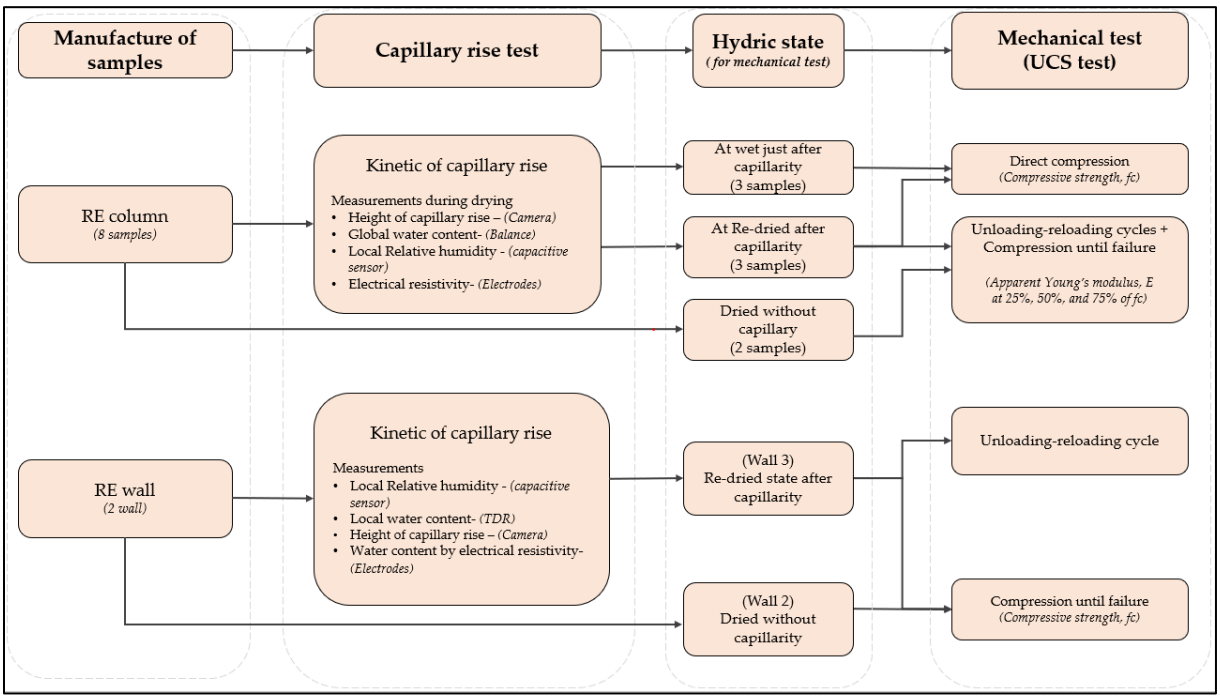

Figure 5.3: Schematic plan of the experimental protocol

5.2 Experiments at a column scale

The experimental campaign started with RE columns, six prismatic samples of size 15 cm x 15 cm x 45 cm were used in this study, and two more dry samples were used as reference. The physical properties of these samples are summarized in Table 5.1, with an average dry density and porosity of 1873.7 ± 1.4% $kg{\cdot}m^{-3}$ and 0.295 ± 3.5% respectively. More about the physical properties and preparation of these samples can be found in Chapter 3, section 3.4.2.

Samples were dried at ambient conditions before the capillary test for 16 weeks. To follow the hydric state during the test, five samples were equipped with capacitive sensors and only one was equipped with electrical instrumentation, more on this will be detailed later on. After the capillary rise test, samples were subjected to mechanical testing. The mechanical test was performed in a wet state, just after capillary rise (sample S16, S17, and S18) and re-dried after capillarity (S19, S20, and S21) (see Table 5.1).

Table 5.1**:** Summary of six RE columns used for capillarity, kinds of instrumentation used and hydric state during mechanical test.

Sample label	Dry density ($kg{\cdot}m^{-3}$)	Porosity (-)	Type of instrumentations	Hydric state during Mechanical test
S14	1881	0.27	-	Dry
S15	1912	0.29	-	Dry
S16	1850	0.30	Capacitive sensors	Wet
S17	1836	0.31	Electrical measurements	Wet
S18	1859	0.30	Capacitive sensors	Wet
S19	1896	0.28	Capacitive sensors	Re-dried
S20	1870	0.29	Capacitive sensors	Re-dried
S21	1889	0.29	Capacitive sensors	Re-dried
Mean	1873 ± 1.4%	0.29 ± 4.3%		

5.2.1 Experimental protocol

The global protocol consists in evaluating the mechanical capacity of 6 RE samples through the capillary rise. Then, 8 samples are considered. 2 of them are tested in the dry test after 19 weeks after manufacture. They are the reference of the experimental campaign. 3 of them will be subjected to the capillary rise and mechanically tested just after capillary equilibrium. Finally, 3 of them will be subjected to the capillarity rise, and tested once gone back to a dry state (16 weeks).

a) Capillary rise setup

Different methods have been developed in the literature to measure the capillary rise of RE. Generally, they involve plunging the RE sample into the water and recording the capillary rise in function of time, this method has been adapted from different standards for capillary rise tests for concrete and compressed earth bricks (AFNOR NF EN 13057 [146] and AFNOR XP P 13-901 [147]).

For example, Chabriac, (2014) [98] used a capillary tank developed by the Civil Engineering and Building Laboratory at ENTPE. The bottom of this tank was covered with a bed of gravel, then sand held in place by a plastic grating. This layer of aggregates is submerged in a few centimetres of water (Figure 5.4). Rammed earth samples made from different soil were placed on the gravel with a sheet of filter paper in between. A basket was made using wire mesh and wire to be able to lift the sample. The sample was weighed at regular intervals to measure the amount of water absorbed by capillary action. Teixeira, (2020) [148] adopted a similar method by immersing the lower face of the sample in a 5 mm water bath and then measuring the mass of water absorbed at a regular time.

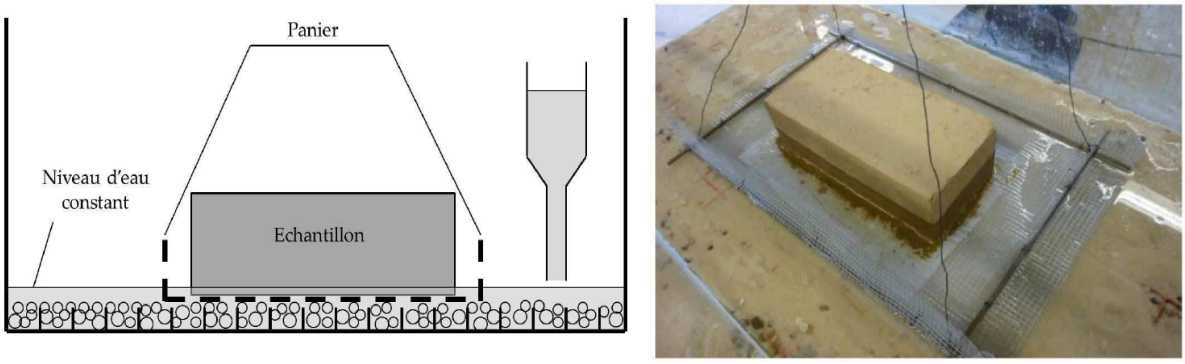

(a) (b)

Figure 5.4: Setup for measurement of coefficient of water absorption of rammed earth (Chabriac, 2014)

The capillary setup of Chabriac, (2014) [98] is quite useful since the actual mass of the sample can be measured directly from the overhanging wire mesh. However, the only problem with this setup is the risk of wearing edges at the base of the sample that is soaked in water. When RE samples are submerged in water, they tend to swell and disintegrate [99]. This decomposition results in the material being soaked through with water, thus the loss of mass of the sample during the test which brings a significant uncertainty in results.

This problem can be overcome by introducing a medium of contact between the sample and water. Various studies have introduced a wick and a filter paper to avoid the problem of disintegration. Wick is a porous material that sucks water up by capillary action with low or negligible capillary resistance.

Hall et al. (2004) [38] introduced a wick material which acts as a point of contact between the RE sample and water. They adopted the standard test for determining capillary suction of water into masonry materials, known as the initial rate of suction (IRS) test (See Figure 5.5a). RE cubical samples (100x100 x 100 mm) weighing around 2 kg, were placed on a platen allowing an opening for the wick. The platen is supported by using stands at a certain height. The whole assembly is placed in a tray containing water.

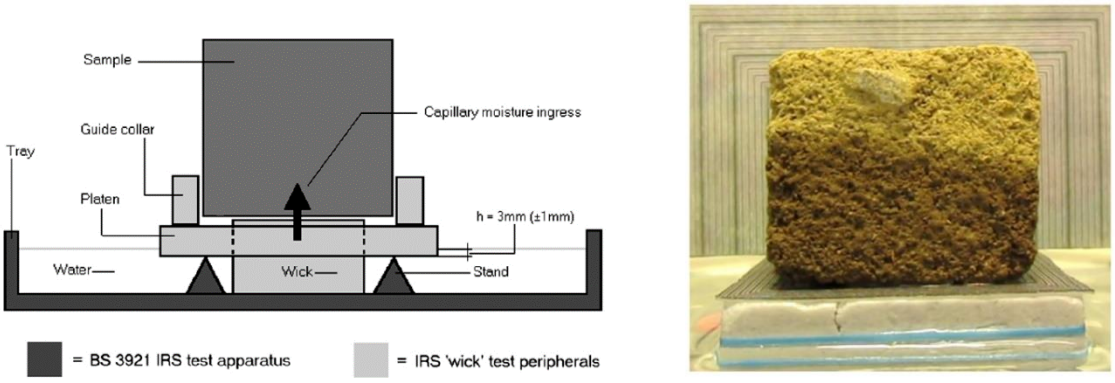

(a) (b)

Figure 5.5: Capillary rise test setup with wick material providing contact between water and the sample by (a) Hall et al., (2004) [73] and (b) Indekeu et al., (2021) [99].

The drawback of this setup is the reduced surface area of contact between the sample and the wick. This is due to the space taken by the plate that carries the sample. To overcome this, the best way is to place the sample directly on the wick, a strong wick material is required. A technique that was used by Indekeu et al. (2021) [99] during their experimental study on the capillary absorption characteristics of RE. Indekeu et al. (2021) [99] placed RE samples on top of a ceramic brick acting as a wick material. The contact between the ceramic brick and the sample was improved by using filter paper. Small samples 3.1 x 2.1 x 2.5 cm^3 were used (see Figure 5.5b).

However, this setup can be practically challenging for large and heavy samples. Therefore, there was a need to design a capillary setup that is practical for large RE columns, with better protection from disintegration and easy to control the constant boundary condition at the base of the sample.

Following these requirements, the capillary bench shown in Figure 5.6 was designed to study the capillary rise on a large RE column sample. The setup consists of two plastic containers connected by a siphon pipe to ensure a constant level of water [149]. As RE disintegrates when immersed in water [99], using fine sand as a medium of contact between the sample and water level was adopted to have a less intensive hydric boundary condition. The container on the left consists of the sample and fine sand all placed on high precision balance for continuous mass measurement. On the other hand, the water level was maintained constant thanks to the water reservoir system visible on the right container (Figure 5.6). The water level can be varied to change the height of capillary in sand hence imposing a certain suction at the base of the sample. In this study, the height of the capillary into the sand was maintained constant at 2 cm (equivalent to a suction value of 200 Pa = 0.2 kPa). Using this setup, dried samples covered with plexiglass (maintaining the same boundary conditions as in the drying experiment, chapter 4), were placed on top of saturated sand for the capillary rise. First, the two samples (S16, S17) were placed in capillary rise without plexiglass, then plexiglass was placed on the two opposite and the top of the samples (S18, S19, S20, S21).

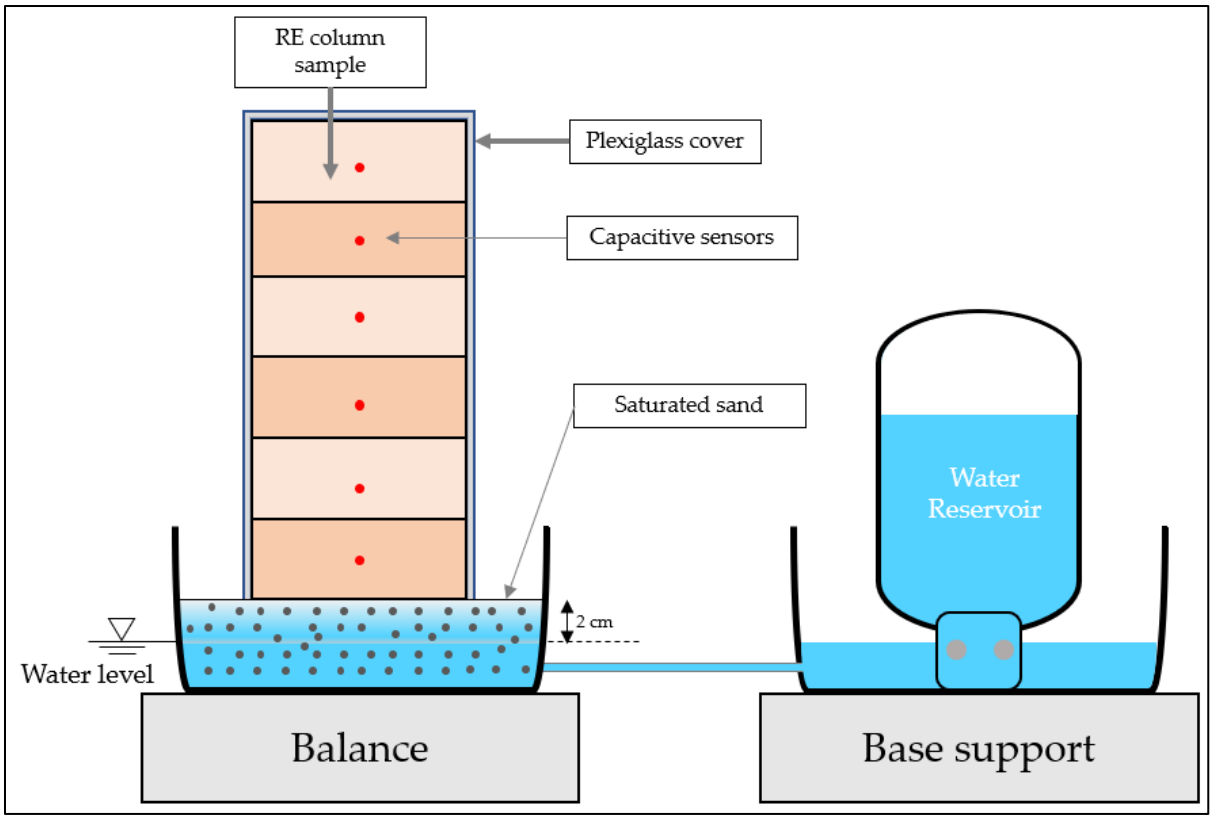

Figure 5.6: Design of experimental setup for capillary rise on RE column, adapted from Chitimbo et al. (2022) [149].

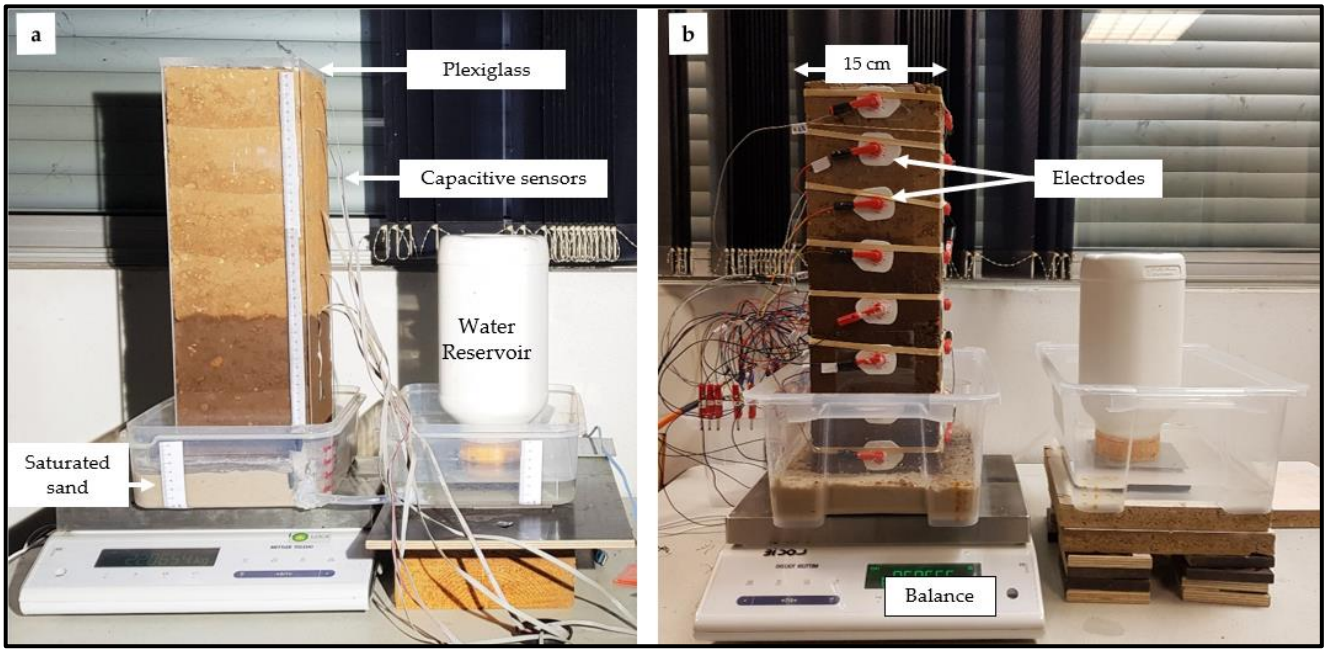

Figure 5.7: Experimental setup for capillary rise on RE column, (a) sample S16 equipped with capacitive sensors and (b) sample S17 equipped with electrodes for electrical measurements [149].

The tests were carried out in a closed room with a variation of temperature around 20/25°C and an average relative humidity of around 50/60%. The tests were carried out on samples in the dry state after they had spent more than three months drying at ambient conditions.

During this experimental campaign, the tests began immediately after the samples had been deposited on saturated sand (Figure 5.6). The tests ended in most cases when the water ingress on the samples no longer changed.

Samples were equipped with different instrumentation to follow the kinetics of capillary rise (more details on these instrumentations and calibration can be found in chapter 3, section 3.5);

- Capacitive sensors for relative humidity (RH) and temperature

In total six capacitive sensors were used per sample. Each sensor was placed in the middle of each layer of the RE column to provide the local evolution of RH with time (see Figure 5.7). This technique was applied to all samples except sample S17 which was reserved for electrical measurement technique. In addition, the capacitive sensors need to be installed during the manufacture and thus are not suited for the diagnostic of an existing structure.

- Electrical investigation

This geophysics method uses an electrical resistivity survey to measure the presence of water in the structure. Four electrodes were stuck with a gel around each layer to measure the local electrical resistivity as the water rise through capillarity. This method was applied only to sample S17 (see Figure 5.7b). This method is non-destructive since electrodes are only glued to the surface of the structure. It could be thus suited for the expertise of an existing structure.

- Balance and camera

Balance was used to measure the mass of the sample during capillary rise (see Figure 5.7). The mass of water absorbed was determined from the increment in the mass as the sample absorbs water at each time interval. Finally, a camera was used to take pictures of the sample at regular intervals during the capillary rise. These pictures were then analysed to determine the evolution of moisture rise at the surface of the sample observed.

b) Mechanical test

After the capillary rise test, where the kinetic of the capillary rise was followed, the experimental campaign was followed by a mechanical test. The test performed was the unconfined compressive strength (UCS) test to determine the compressive strength (fc) and Apparent Young's modulus (E_a). The UCS test was done using a compression machine and controlled at a constant rate of displacement of 1.2 mm/min according to standards [134]. More about the experimental protocol for the UCS test and DIC is explained in Chapter 4, sections 4.3.2.1 and 4.3.2.2). The UCS test was performed on three samples (sample S16, S17, and S18) in the wet state just after the capillary rise, and on the other three samples re-dried after capillarity (sample S19, S20, and S21) (see table 5.1).

5.2.2 Results and discussion

5.2.2.1 Water monitoring during the capillary rise

a) Evolution of mass of water absorbed

Thanks to the balance, a gravimetric determination of absorbed water in RE columns was done. Results of the evolution of the mass of water absorbed with time for all samples are represented in Figure 5.8. The test lasted for about three weeks and equilibrium was reached when there was no significant change in the mass of water absorbed in one day. The equilibrium was attained when the difference in water absorbed was less than 10 g in a day. It can be observed that most of the samples attained equilibrium at around 18 days showing that the total mass of water absorbed ranged from 1.5 kg to 1.8 kg for samples S18 to S21. The variation in results may be driven by the fluctuation of the ambient conditions, also considering that the tests were not done at the same time. Samples S16 and S17 showed a relatively low value of water absorbed because they were not covered by plexiglass, thus there was more surface evaporation loss as compared to the rest of the sample. Figure 5.9 shows the initial rate of absorption for each day, it represents the rate of water absorbed at each day. From this curve, it can be seen that the rate of absorption is significantly higher in the first two days.

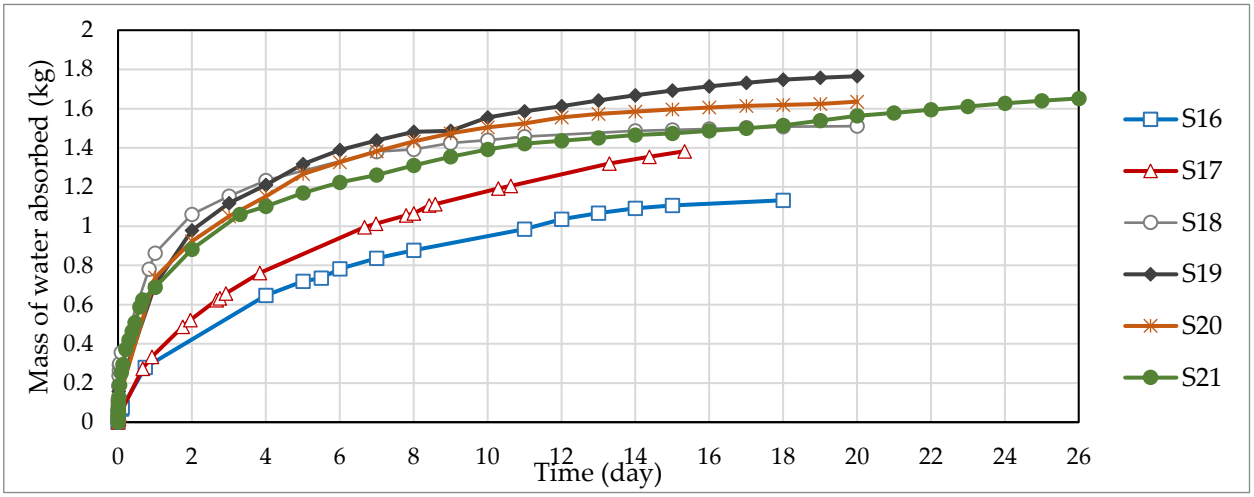

Figure 5.8: Evolution of mass of water absorbed in the sample during the capillary rise.

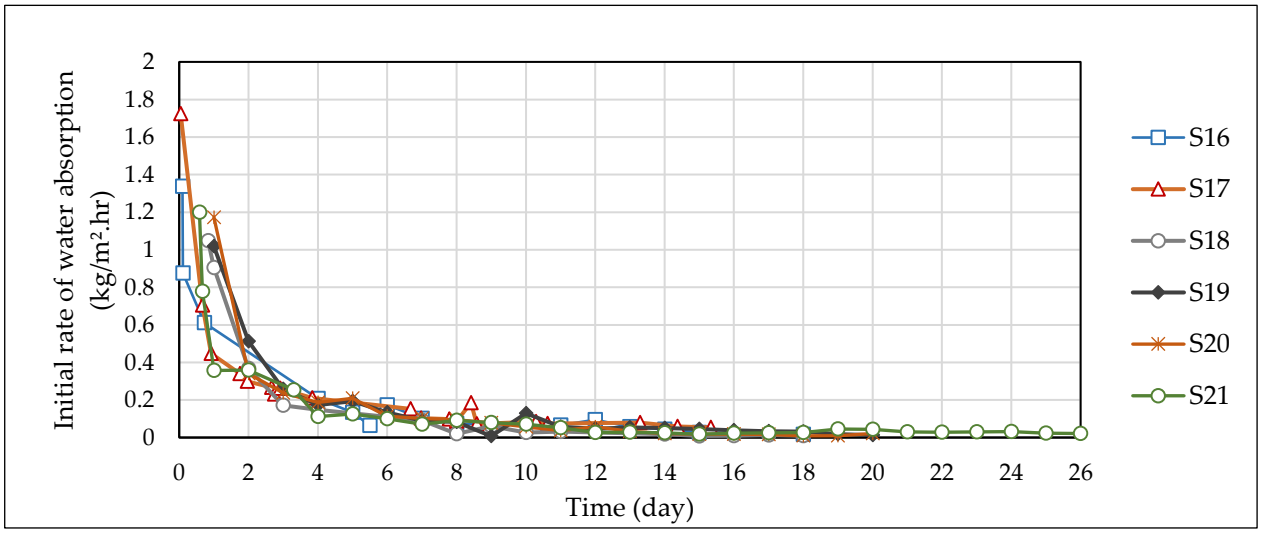

Figure 5.9: Evolution of the initial rate of water absorbed by the sample on each day during the capillary rise.

A parameter that is used to characterise the capillary behaviour of porous material is known as the coefficient of absorption (A). It is used to indicate the amount of water a porous material absorbs on first coming into contact with the water. The A coefficient comes from a property of porous material that when placed onto water, the cumulative absorbed mass of water per unit area of the inflow surface increases linearly against the square root of the elapsed time [95]. This coefficient reflects the quantity of water absorbed (in kg) per unit area (m²) and per root of the immersion time (√s).

The coefficient of absorption was determined over the first 10 minutes of capillary rise according to the standard (AFNOR XP P 13-901) [147]. Figure 5.10 shows the cumulative mass of water absorbed per plotted against the root of time on the first 10 minutes of capillary rise, the relationship is linear and the coefficient of absorption was calculated from this curve. After ten minutes the behaviour is non-linear as shown in Figure 5.11, the relationship is linear.

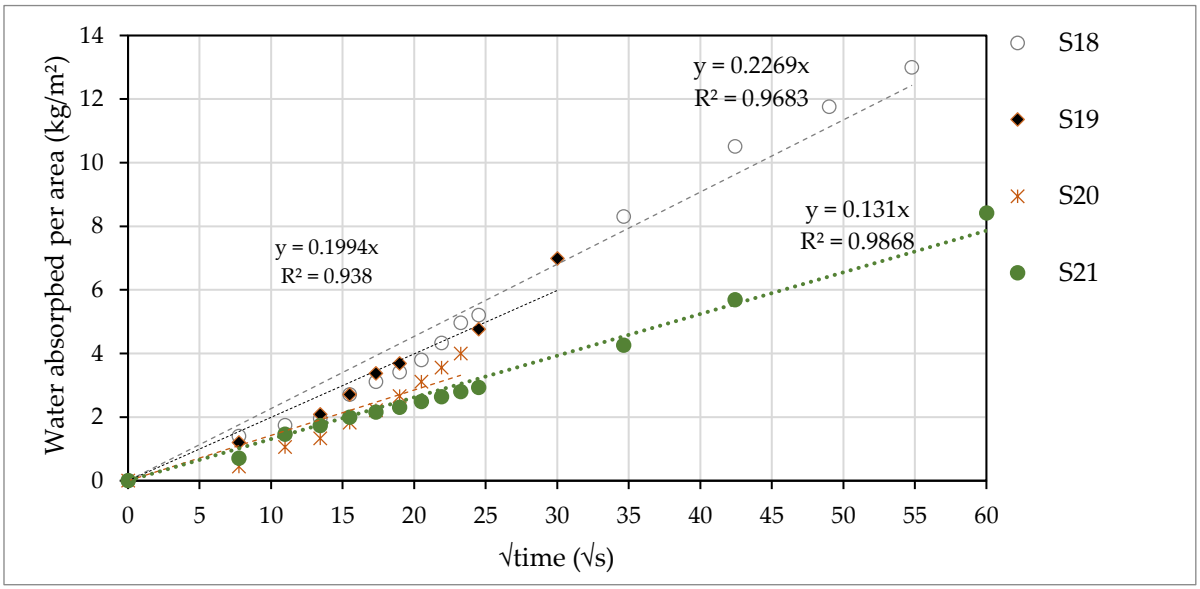

Figure 5.10: Relationship between mass of water absorbed per area and the square root of time at the first ten minutes of capillary rise.

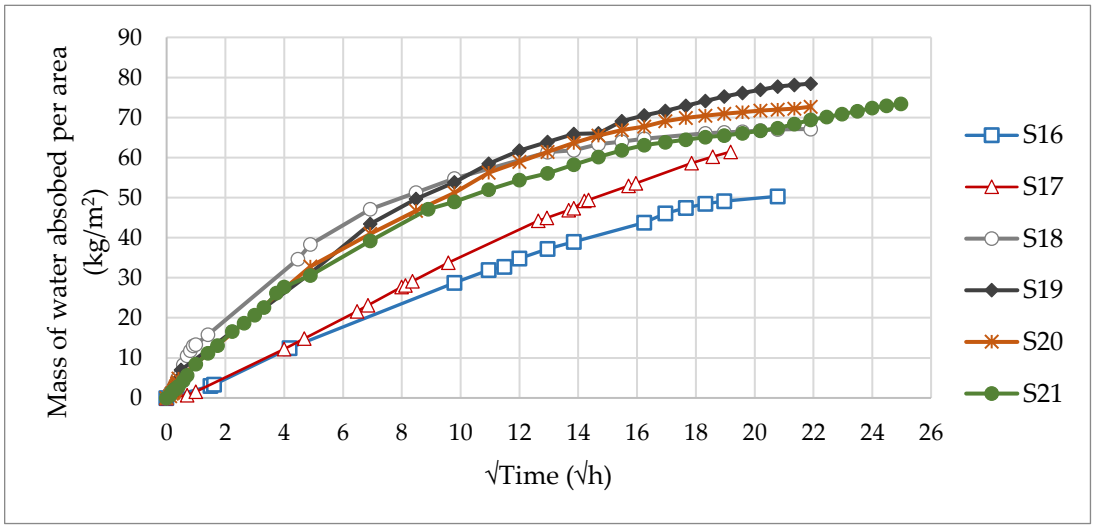

Figure 5.11: Mass of water absorbed per area plotted against the square root of time for the entire capillary rise.

Table 5.2: Results of total water absorbed and coefficient of capillary absorption(A)

Sample name	A (kg/m²/√s)	R²	Total water absorbed (kg)
S18	0.227	0.9683	1.5
S19	0.199	0.938	1.765
S20	0.143	0.8792	1.635
S21	0.131	0.9868	1.65
Mean	0.175± 26%		1.683±4.2%

Therefore, the coefficient A obtained ranges from 0.13 to 0.23 kg/m²/√s, with a mean value of 0.175 kg/m²/√s (table 5.2). One can notice a wide spread of results of the tests with a standard deviation of 26%. The coefficient of absorption obtained in this study is in the same order of magnitude as the one obtained by Guiheneuf, (2021) [150] who reported A values ranging from 0.03 to 0.23 kg/m²/√s. But the lower range of the values determined by Chabriac, (2014) [98] ranges between 0.2 to 0.6 kg/m²/√s. This big discrepancy in the coefficient of absorption value results from the difference in material compositions used, method, and conditions of a particular experiment.

b) Height of capillary rise

At the beginning of the test, the height of capillary rise was recorded by observing directly, as the bottom part of the sample could not be well captured by a camera. Then a high-resolution camera was used to record pictures each day during the capillary rise. Figure 5.12 show the image recorded during the capillary rise. From these images, the height of capillary rise was observed on the difference of the grayscale with the help of a ruler scale that is attached to the plexiglass (Figure 5.7a).

It can be observed that moisture rose at a uniform level at the beginning, for example, from day 1 to day 7 (see Figure 5.12), but diffused at the near end of the test on day 20. The results of the evolution of the height of capillary rise for all samples are presented in Figure 5.13. A higher rate of capillary rise is observed at the early stage of capillary rise, for example, in just two days the water has reached half of the height of the sample around 22 cm (see Figure 5.13), similarly observed in Figure 5.12 where a sample has reached the 3rd layer of the sample. Then this rate will gradually reduce until equilibrium is reached where there is no significant change in height, and then the test was stopped. Equilibrium for samples covered with plexiglass was reached after around 18 days showing the water rose by about 32 cm to 40 cm. While samples 16 and S17, which were not covered by plexiglass, reached a maximum height of 26 cm and 35 respectively.

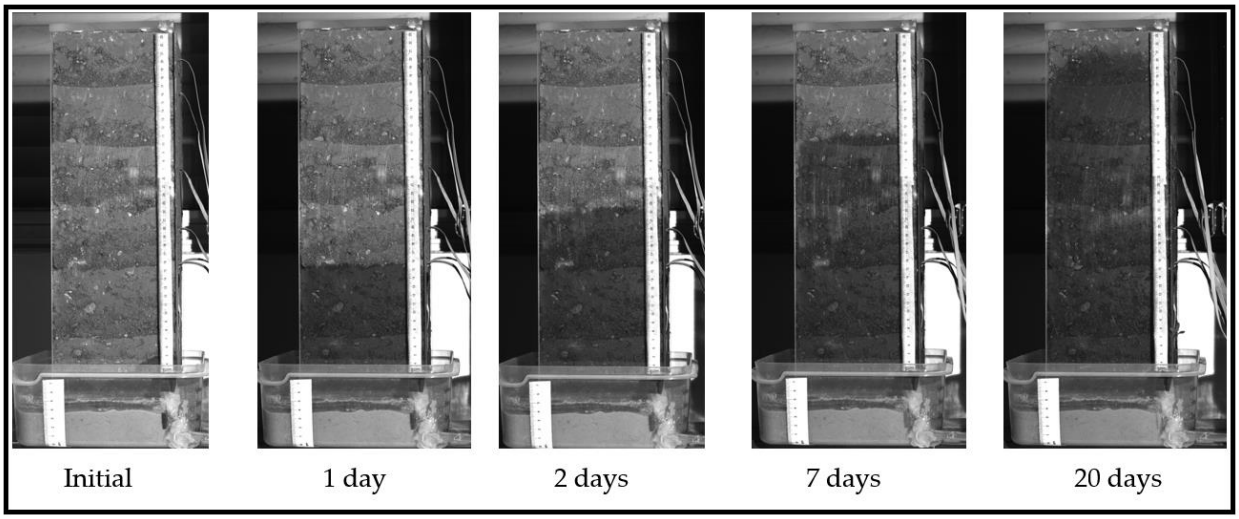

Figure 5.12: Image of capillary rise in RE samples showing the evolution of height of moisture rise for 20 days.

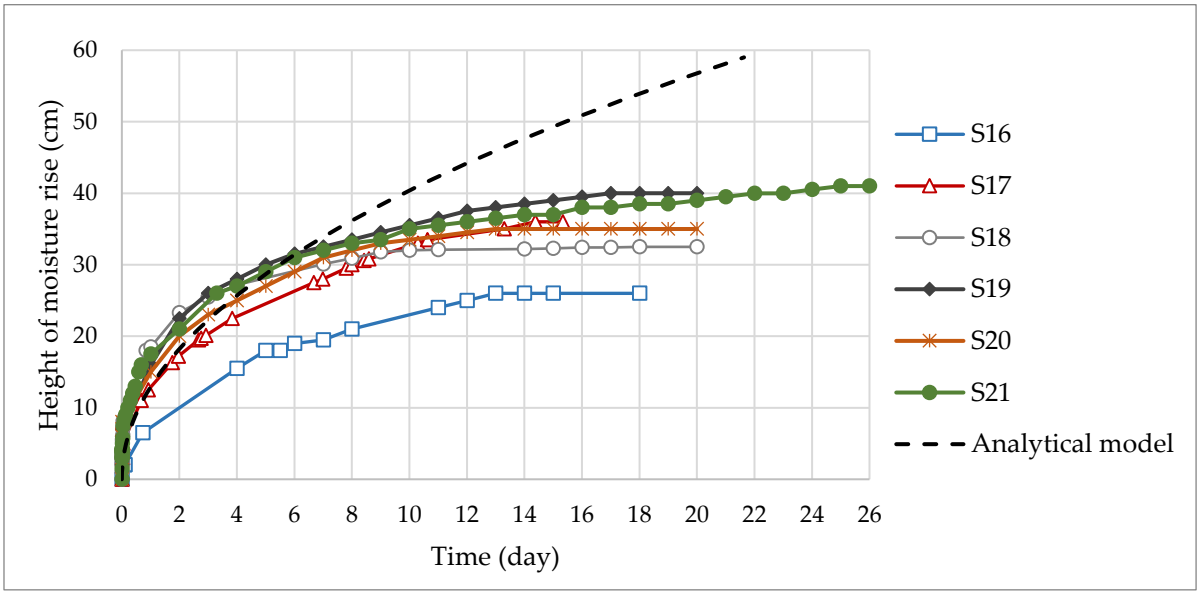

Figure 5.13: Evolution of height of capillary rise for all samples during capillary rise along with the analytical model.

Analytical solution for the rate of capillary rise

The experimental results of height capillary rise were then compared with the analytical solution proposed in equation 5.11. First, the ultimate height was determined, and then the rate of capillary rise.

The ultimate height of capillary rise (*hc*) was estimated using equation 5.3 formulated by Peck et al. (1974). The input parameters of soil used were, D_{10} was equal to 0.002 mm (from the granulometry), porosity (n) of 0.295, and void ratio (e) of 0.42. The hydric properties include the air-entry of 0.3 MPa and the saturated hydraulic conductivity of 2.4 x 10^{-8} m/s.

By using equation 5.3, the C parameter of 10 mm² was chosen by considering the proportion of coarse grains are more than fine grains in the soil used, hence we expect a lower value of *hc*, thus the value of *hc*:

$$h_c = \frac{C}{eD_{10}} = \frac{10\ mm^2}{0.42 \times 0.002\ mm} = 11904mm \approx 11.9\ m$$

Another empirical equation 5.4 by Lane and Washburn (1946) gives a value of *hc* of 4.6 m while Kumar and Malik (1990), equation 5.5, gives *hc* around 32 m. A huge variation in the prediction of *hc* is observed, some provide an overestimated value of *hc*, making these predictions not so reliable. So, we chose the value of *hc* of 11.9 m obtained from Peck et al. (1974).

Using the modified Terzaghi equation (5.11), the rate of capillary rise can be estimated analytically as shown in Figure 5.13. One can observe a good correlation between the experimental results and the analytical model in the first week of capillary rise. After a week, the capillary rise starts to stabilize due to mainly evaporations on the surface of the sample, while in the analytical model, the capillary rise will continue until reaches a *hc* value. This analytical model is suited for the underground application, where the effects of evaporation are not considered, thus posing a limitation when applied to a building structure that is exposed to ambient conditions.

Table 5.3: Summary of maximum capillary height on RE column

Sample name	Maximum height (cm)
S16	26
S17	36
S18	32.5
S19	40
S20	35
S21	41
Mean	**37.1±11%**

c) Results of relative humidity and electrical resistivity

Figure 5.14 shows the evolution of the relative humidity (RH) in five samples S16, S18, S19, S20, and S21. Sample S17 was equipped with electrical measurements only so the RH of this sample was not presented. The test was done in a closed room with an RH of around 45/55% and a slightly varying temperature of 20/25°C (ambient conditions are visible in Figure 5.14).

At the beginning of the capillary test, all samples had RH ranging between 50% and 60% which is in equilibrium with the ambient RH. When water starts rising in the samples, RH on the first and second layer instantly rise to 100% indicating saturation. A high rate of capillary rise was observed on the first two days, the RH in the middle of the first, second, and third layers increased from an RH value of 50/60% to 100%. Similar to what has been observed in the height of capillary rise in Figure 5.11.

When the water reaches the 4th layer, the capillary front is more and more diffuse, represented by the slope that gradually reduces for the 4th, 5th, and 6th layers (see Figure 5.14). For example, in Figure 5.14, sample S21 the RH in the 6th layer took over two weeks to increase from ambient RH to 100%, which is longer compared to the first three layers that were saturated in two days. The reason behind this behaviour could be a manifestation of two phenomena: first, the hydraulic gradient (see Eqn. 5.6) reduces as the water rises on the sample, hence the rate of capillary rise reduces, and the second is the increasing proportion of pore water that find an equilibrium between capillary and gravity forces along the height.

A similar trend noted on RH was also observed in the evolution of electrical resistivity (Figure 5.15). This work has not been developed in the frame of the PhD but has been led by a post-doctorate (Feras Abdulsamad) during the ANR VBATCH project. The sample S17 was equipped with electrical measurements to survey the electrical resistance. A set of four electrodes was placed to obtain one measurement, in a total of 8 sets of electrodes were placed along the height of the sample. Figure 5.15 shows the evolution of electrical resistivity in sample S17 which is compared to the RH of sample S19 during the capillary rise. Initially, the sample's electrical resistivity was around 2000 Ω.m, as the sample gets in contact with water its resistance to electricity decreased, and thus a sharp decrease in resistivity of the sample from 2000 Ω.m to around 100 Ω.m on the first layers followed by a gradual drop in resistivity as seen on the sixth layer (Figure 5.15). More on electric measurement can be found in Annex 1.

Finally, by using both capacitive sensors and electrodes method (Figures 5.15 and 5.16), the evolution of the capillary front with time was deduced for each sample and presented in Figure 4.16. The capillary front was considered when the RH reached 100% for each sensor and around 100 Ω.m for electrodes. The positions of capacitive sensors and electrodes were known, capacitive sensors were placed in the middle of each layer (see Figure 5.6) and electrodes were placed 2 cm from the bottom and then at an interval of 6 cm high (see Figure 5.15). The capillary fronts in Figure 5.16 were compared to the ones obtained by using a camera (see Figure 5.13), and it was concluded that all methods (capacitive sensors, electrodes and camera) were coherent in the determination of the height of capillary rise. The electrical measurement has more advantages over capacitive sensors since its non-destructive and therefore can be applied in real RE buildings.

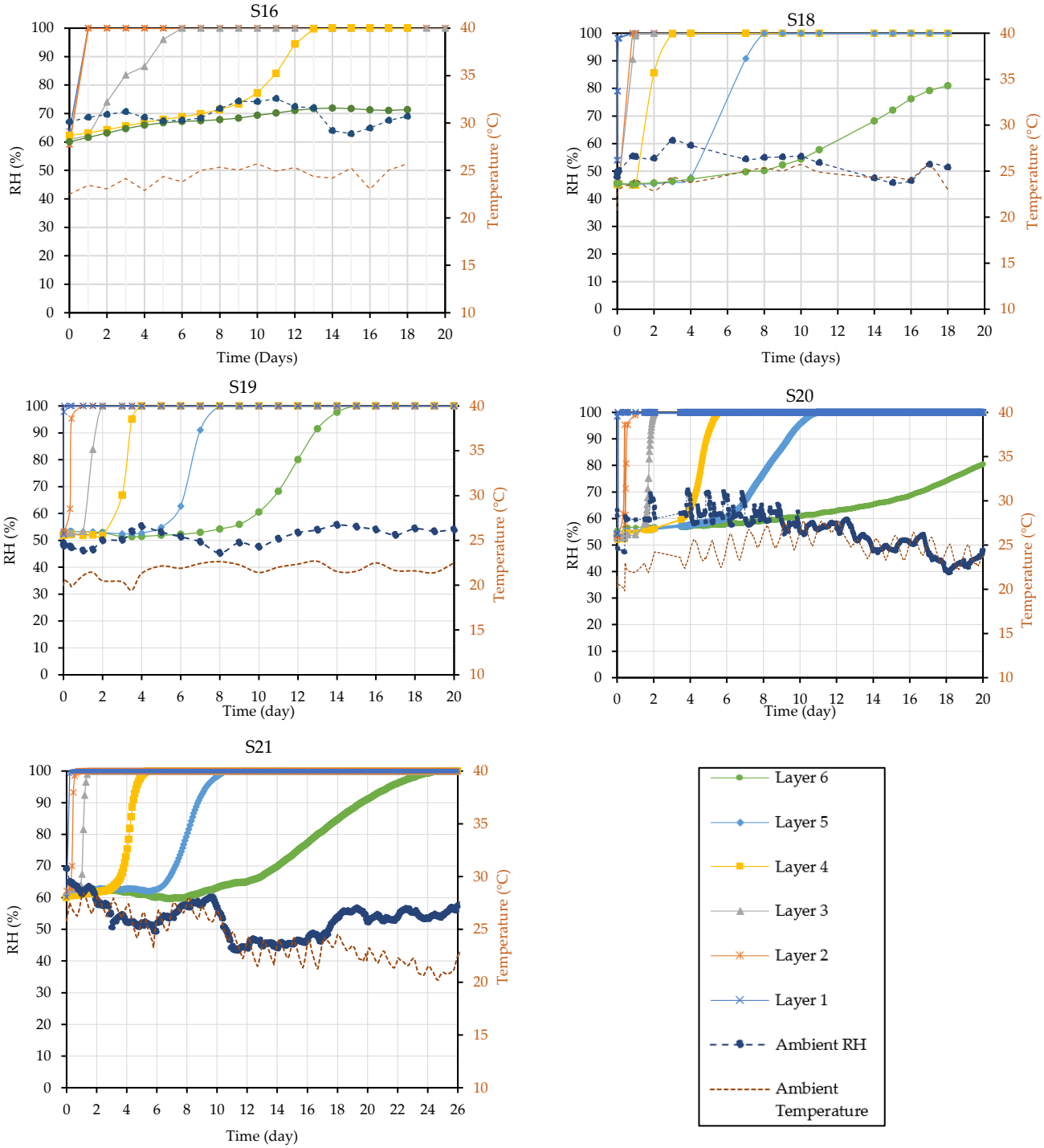

Figure 5.14: Evolution for capillary rise recorded by capacitive sensor inside RE columns.

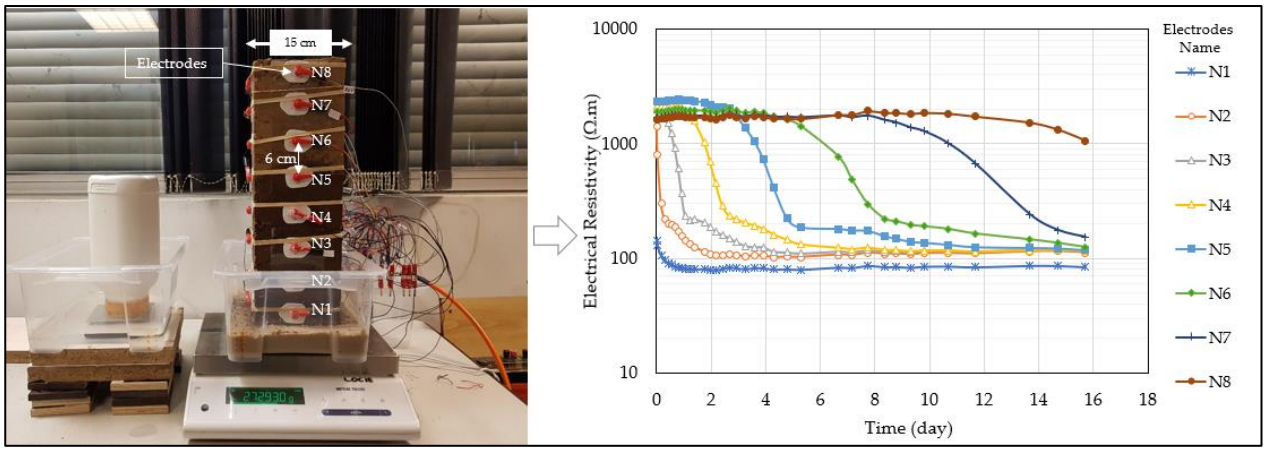

Figure 5.15: Evolution of electrical resistivity during capillary rise. Electrodes are arranged from bottom N1 to the near top N8 of the sample.

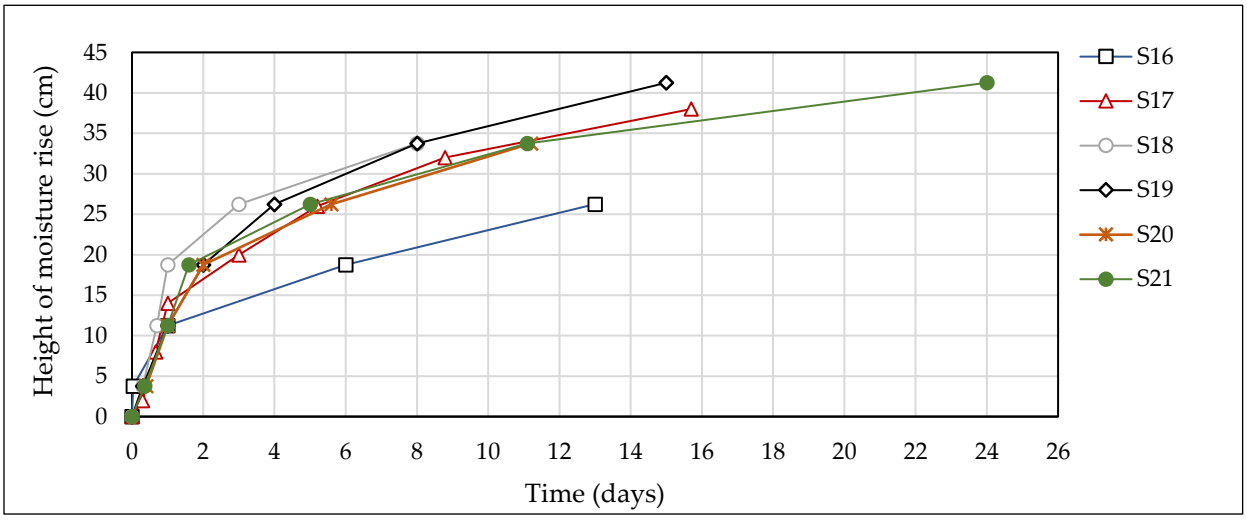

Figure 5.16: Evolution of height of capillary rise deduced from capacitive sensors (S16, S18, S19, S20, S21) and electrodes (for S17).

d) Other observation

It was observed at the beginning of the capillary test that the water rises in a curved dome shape (n-shape) whereas, in the middle part, the water rose faster than at the borders (Figure 5.17a). This can be explained by two factors; first, the layers of the sample are more compacted in the middle than at the border. Second, is the water loss at the border due to the effect of evaporation at the surface, causing to have a higher rate of capillary rise in the middle part. At the end of the capillary test, where the sample is wet, there was a development of mould and growing plants, showing the presence of organic matter in the soil (Figure 5.17b). This development of the biological activity shows that mould may appear and grow and that the earth building is also vulnerable from an air indoor quality point of view.

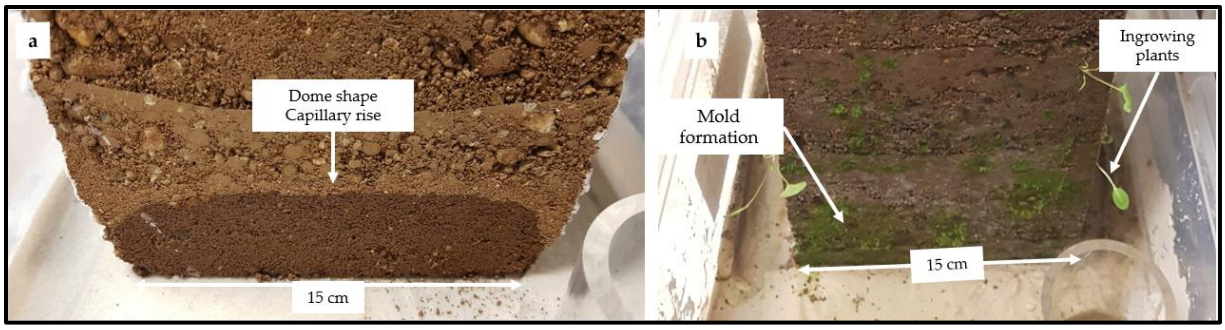

Figure 5.17: (a) capillary rise in a dome shape at the beginning of the test, (b)In-growing plants and mould at the end of capillary rise.

5.2.2.2 Results of mechanical test after capillary test

Among the six samples used for capillarity (see Table 5.4), three samples were tested mechanically just after the capillary test in a wet state and the other three were tested after being re-dried. Figure 5.18 presents the results of the UCS test on a total of 6 samples.

The results of samples tested after the capillary rise showed a significantly low fc of 0.065 MPa, 0.077MPa, and 0.068MPa for samples S16, S17, and S18 respectively. These values are considerably lower than the required minimum strength recommended for RE building. This means that a RE building will have a higher risk of collapsing when it is wet, near saturation, due to capillary rise or other similar conditions. The values of E_a cannot characterize a wet state, since the sample was partly wet and partly dry and hence not representative. Thus, the values E_a are not presented for samples S16, S17, and S18. Samples that were re-dried after capillarity, showed an fc of 1.11 MPa, 1.17 MPa and 1.27 MPa for samples S19, S20 and S21. All the samples showed strengths with an average of 1.18 MPa, which is above the required strength of at least 1 MPa according to New Mexico Code, 2001 [37].

In order to check the effect of capillary rise on the mechanical behaviour of RE, the results of compressive strength and modulus were compared to one of the samples that were tested at a dried state without capillarity. For this case, two samples S14 and S15 were used, these samples have been previously used in the drying experiment in Chapter 4 (see Table 4.2). The compressive strength was 1.36 MPa and 1.39 MPa for samples S14 and S15 respectively, with an average compressive strength of 1.375 MPa for the dried sample without capillary rise.

Figure 5.19 shows the evolution of fc at different state during the capillarity test. Samples tested after capillary rise show a decrease in average compressive strength to 0.07 MPa, this represents a reduction in strength by 95% from the initial dry state. For the samples (S19, S20, and S21) that after capillarity dried in a closed room, similar drying conditions to the original dry samples, show an average compressive strength of 1.18 MPa. This account for restoration in compressive strength by 86% of the dry original samples. The reduction in strength after a cycle of drying-wetting could be explained by the possible viscous flow that disorganizes the grain packaging.

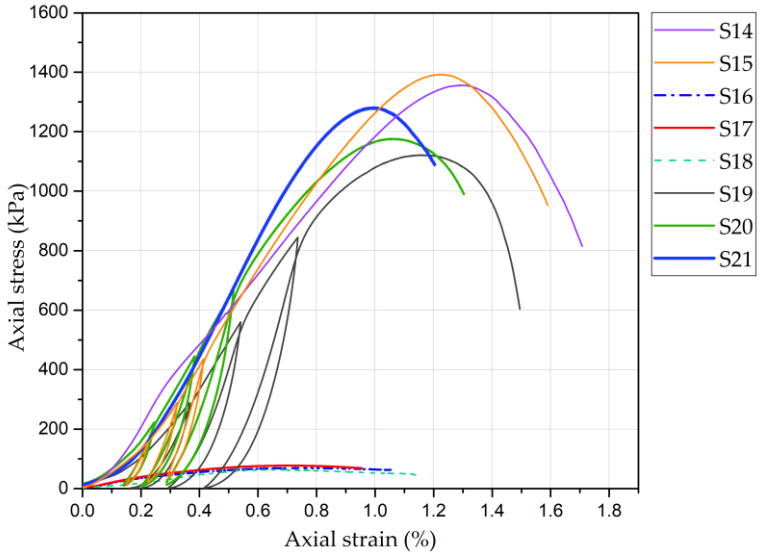

Figure 5.18: Stress-strain curve for samples used in capillarity

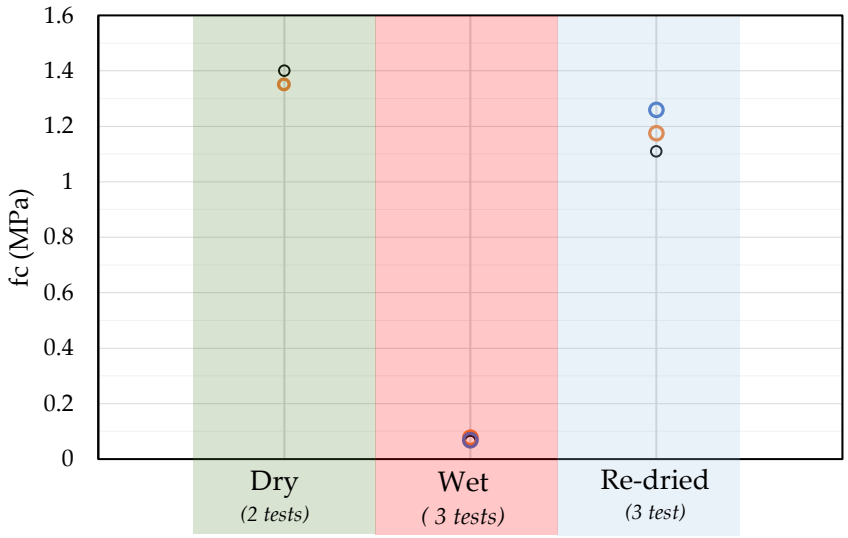

Figure 5.19 Compressive strength of RE columns at dry state, wet, and re-dried after capillary rise.

Table 5.4: Results of UCS test on samples after capillary rise test.

Sample label	Hydric state during Mechanical test	Compressive strength, *fc* (MPa)
S14	Dried	1.356
S15	Dried	1.392
S16	Wet	0.065
S17	Wet	0.077
S18	Wet	0.068
S19	Re-dried	1.11
S20	Re-dried	1.175
S21	Re-dried	1.269

5.2.3 Synthesis of capillary rise experiment on columns

The effect of capillary rise on the mechanical behaviour of RE has been studied experimentally. A suitable capillary bench was designed suited for a large RE sample. RE columns equipped with different instruments for hydric measurement were placed on a capillary bench to start the capillary rise test.

During the capillary rise, the mass of water absorbed was followed by using a precise balance. The evolution of water absorbed was determined showing a high rate of water absorbed during the initial time which reduced gradually until equilibrium was reached. The total mass of water absorbed was observed to a maximum value of 1.8 kg, for all samples an average of 1.63 kg. From the evolution of water absorbed, the coefficient of absorption was determined, ranging from 0.13 to 0.23 kg/m²/√s, with a mean value of 0.175 kg/m²/√s for the coefficient. A good correlation between different methods: the evolution of RH and the electrical resistivity of the sample was observed.

After the capillary rise, the samples were subjected to the UCS test. Results of the UCS test after capillarity show a drop in mechanical resistance by 95% (a compressive strength of 1.375 MPa decreased to 0.07 MPa). Other samples dried after the capillarity test, show restoration of strength by 86% of the original sample. This suggests that a cycle of wetting and drying might have an effect on the mechanical performance of the RE structure, and thus reduces the durability of the RE building. However, resistance stays suitable after this cycle.

In the next section, experiments at a wall scale of 0.20 m × 0.75 m × 1.5 m will be done as a continuation of this experimental campaign. Thus, size effects on the kinetic of capillary rise and evolution of moisture content could be highlighted.

5.3 Experiment at wall scale

After interesting results from the RE column, the experimental campaign continued at the scale of a large wall of 1.5 m high.

The principle is to investigate the mechanical behaviour through an exceptional water entry, i.e. capillary rise. Thus, the global protocol includes 2 walls: one tested in a dry state (W2, already presented in the previous chapter), one initially dry, then weakened by a capillary rise and finally dried again and mechanically tested (W3). W3 is previously presented in Chapter 4 (section 4.6). This wall was manufactured and left to dry at ambient conditions.

5.3.1 Experimental protocol

a) Capillary rise setup

Given that wall W3 is large (1.5 m) and heavy (460 kg) it was challenging to design a suitable experimental bench for the capillary rise. The first challenge was how to introduce water at the bottom of the wall without moving it, and then obtain the mass of water absorbed for the determination of capillary characteristics.

To solve these challenges, the experimental setup shown in Figure 5.19 was designed. The setup consists of a RE wall that was constructed on a concrete beam. On the bottom, the wall is covered by paraffin up to a height of 10 cm, then the tank was filled with fine sand up to 12 cm. Therefore, there is a 2 cm high contact between fine sand and the wall. Finally, the water level was maintained at 8 cm thanks to the water reservoir system visible on the right (Figure 5.20a). By controlling the water level, the height of the capillary into the sand in contact with the wall was maintained between 2 and 4 cm (equivalent to a suction value of 200 to 400 Pa), which is similar to the RE column. The designed setup was implemented as shown in Figure 5.21. The wall was instrumented by capacitive sensors, TDR, and electrodes (Induced Polarization method) to monitor the hydric state. On the other hand, a camera was used to record the capillary rise and a balance was used to measure the amount of water absorbed. The capillary rise experiment lasted for 21 days (from 07/07/22 to 28/07/22).

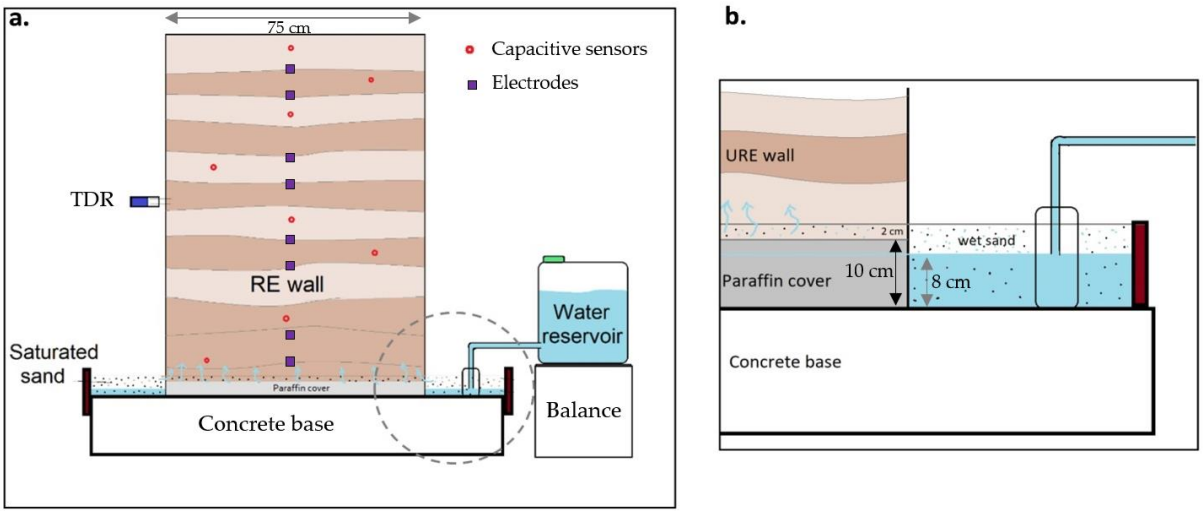

Figure 5.20: Design of **c**apillary rise experiment adopted for large wall. (a) Sketch of the experimental setup. (b) Zoom of the setup showing different levels for the water infiltration at the basis of the wall.

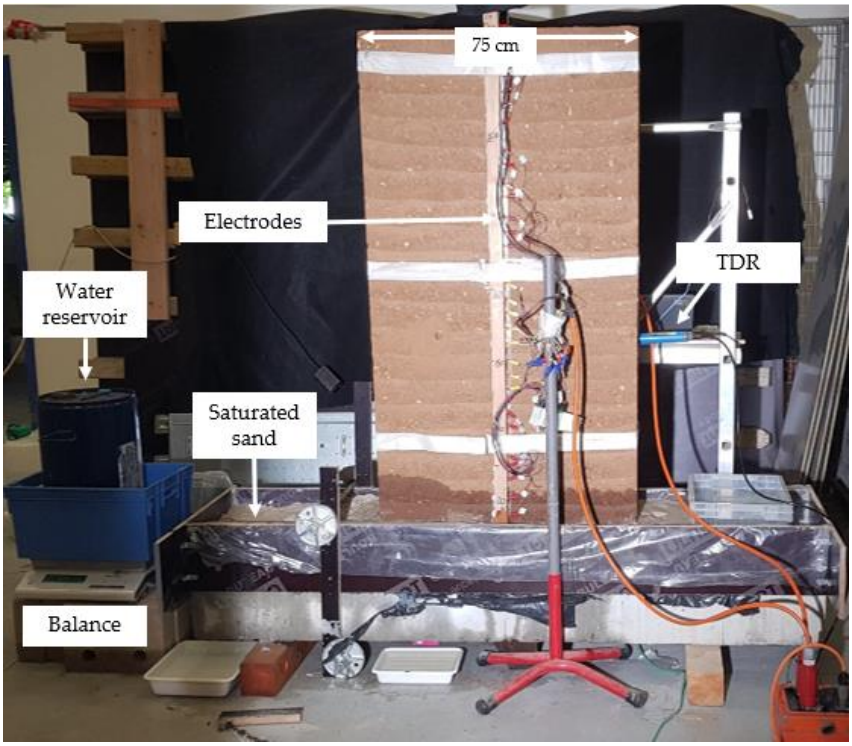

Figure 5.21: Experimental setup of RE wall subjected to capillary rise.

b) Mechanical test

After the capillary rise test, the wall W3 was left to dry in ambient conditions. The mechanical test was done upon drying for over 3 months. The test performed was the unconfined compressive strength (UCS) test to determine the compressive strength (*fc*) and Apparent Young's modulus (*Ea*). The experimental protocol for the test was similar to wall W2 in the previous chapter. More about the experimental protocol for the UCS test is explained in Chapter 4, sections 4.5.1b. The mechanical results of re-dried after capillarity wall W3 were then compared to the one of wall W2 which was tested at a dry state without capillarity.

5.3.2 Results and discussion

5.3.2.1 Results of capillary kinetics

i. Evolution of Relative humidity (RH)

The RH was measured by capacitive sensors, the position of the sensors in the wall is shown in Figure 5.20b. Figure 5.22a shows the evolution of RH in the wall and the ambient RH conditions. First, it was observed that the ambient RH was varying between 40% to 50% and remained relatively constant during the capillary rise. A high rate of capillary rise was observed on the first day, the RH of the sensors (S1 and S2) that were placed on the first and third layers increased from a RH value of 60% to 100%. After a week of capillary rise, the RH value of sensor S3, placed at a height of 36.5 cm from the base of the wall, increased from 60% to 100%, showing that the capillary head reached this point. Between two to three weeks when the capillary front seems to stabilise (see Figure 5.22), the RH recorded by sensors S4 gradually increased from 60% to 100%. However, it doesn't seem consistent with the evolution of the

capillary front on the earth's surface, measured at 42 cm with the camera. This suggests that the moisture level in the middle of the wall was possibly higher than that on the surface. The rest of the sensors (S5 to S10) recorded an RH value fluctuating around the ambient conditions since they stay above the capillary zone.

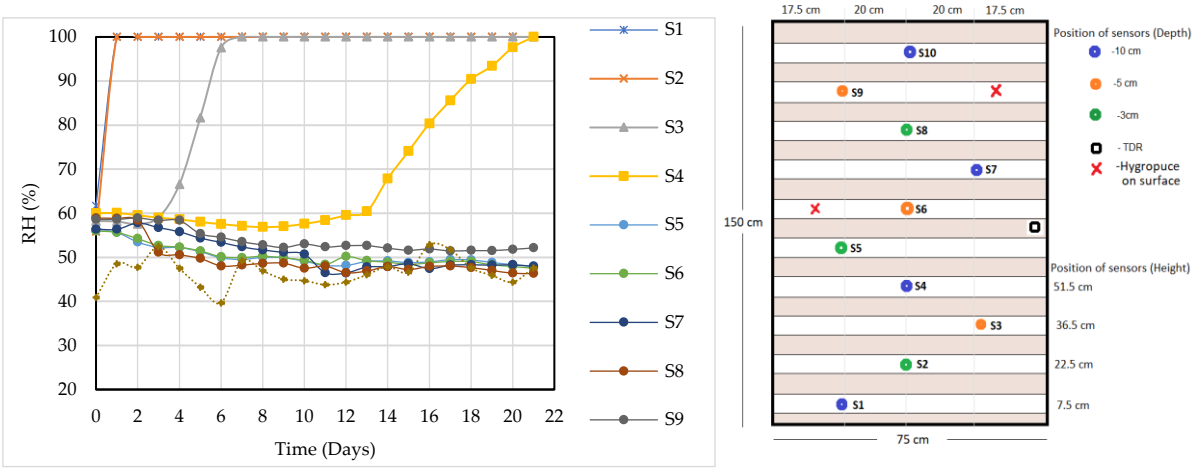

(a) (b)

Figure 5.22: (a)Evolution of Relative Humidity (RH) in the wall along with the ambient condition. (b)The right panel displays the layout of the RH sensors and the position of the layers is also indicated.

i. Height of capillary rise

The capillary wetting fronts are recorded using a fixed camera that takes photos over time. The change in the grey scale of the pictures is used to monitor the evolution of the water level in the wall over time (Figure 5.22). Figure 5.23 shows the evolution of moisture level. At the beginning of the test, water was allowed into the sand up to a height of 8 cm, and started seeping through capillarity at a height of 10 cm above the paraffin cover (see Figure 5.19b). The moisture level was observed to increase from 10 cm to 25 cm after two days, then stabilises after two weeks at a height between 40 cm to 42 cm above the base of the wall. The analytical model for the rate of capillary rise developed previously for RE columns was applied to the wall since they are both made up of the same soil. In Figure 5.23, it is observed that the analytical model seems to be closer to the experimental results. Another way of putting determining the height of moisture rise was by using the position of capacitive sensors (see Figure 5.21b). Since the position of the sensor is known, and the time for the sensors to reach 100% can be obtained from Figure 5.21a, the rate of moisture rise was determined and presented in Figure 5.23.

It was observed that the height of capillary rise from RH sensors was always slightly higher than the one recorded on the surface (see Figure 5.23), at the end of the test the height of capillary rise on the surface was from 42 cm while 51.5 cm from the RH sensors. This could be due to the fact that the observation on the surface or the measurements in the sub-surface are affected by evaporation. This suggests that the moisture level inside the wall was higher than that on the surface. We recall that this could be due to two reasons. First, the wall layers are denser in the middle than on the borders because of compaction. The second explanation is due to evaporation that occurs on the surface causing water loss on the surface and thus a lower rate of capillary rise.

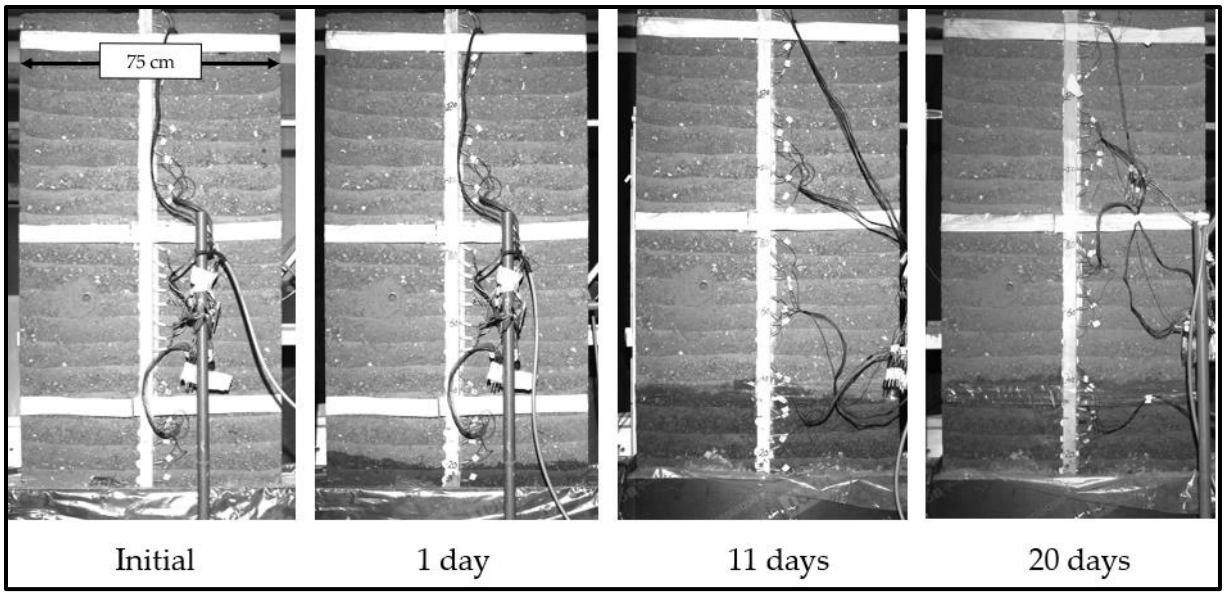

Figure 5.23: Image of capillary rise in RE samples showing the evolution of height of moisture rise up to 20 days.

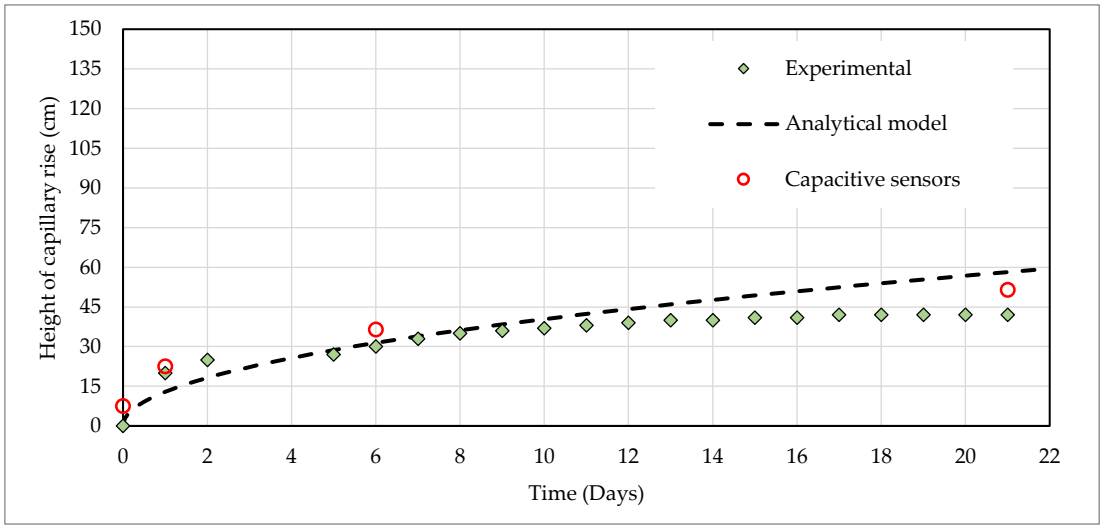

Figure 5.24: The rate of capillary rise, comparison between experimental data and analytical solution

ii. Evolution of water content

The capillary experimental setup (see Figure 5.20) was designed in a way that the mass of water leaving from the reservoir can be measured by a balance and thus the mass of water absorbed can be calculated. Unfortunately, there was unexpected leaking at the base of the concrete beam, which was difficult to seal once the experiment started. Therefore, due to the leaking problem, the evolution of water absorbed will not be presented.

Another method for measuring water content was by using Time Domaine Reflectometry (TDR) probe (more on this is described in Chapter 3.5.2). TDR was used to measure the volumetric water content which was then converted to gravimetric water content. The TDR was placed at the side centre of the

wall (see Figure 5.20) to monitor the local water content along a depth of 10cm. Figure 5.25 shows the evolution of gravimetric water content deduced from TDR during the capillary rise. A water content of around 2.4% was recorded during the entire experiment. No significant change in water content was observed since the moisture rose to 42 cm high (see Figure 5.23) while the TDR was placed in the middle of the wall (75 cm high).

The water content of the wall can also be calculated from the RH presented in Figure 5.22. The RH values were linked with suction using Kelvin's equation, and suction was finally linked to water content using the Van Genuchten model for the retention curve (more about this can be found in Chapter 3, section 3.3.2). The results of gravimetric water content deduced from RH are presented in Figure 5.26, the initial water content was about 1.3% and rose to 14.5% during the capillary rise.

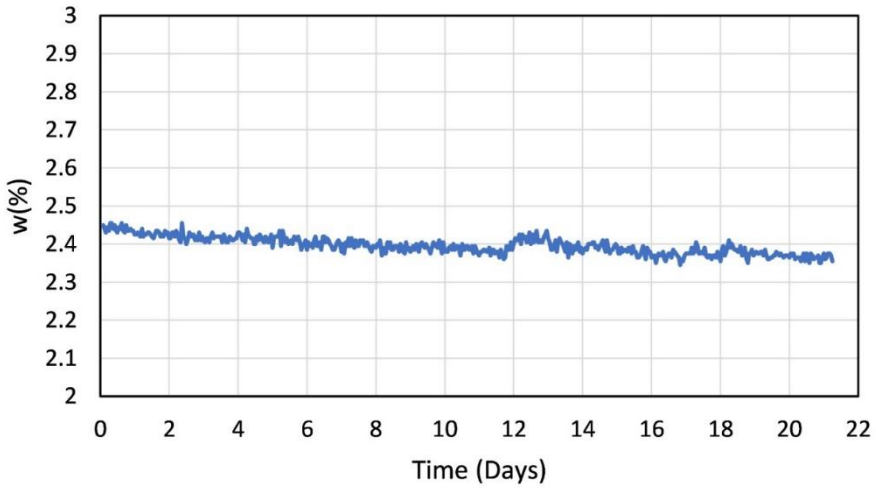

Figure 5.25: Evolution of local water content (in weight, w) at the middle of the wall.

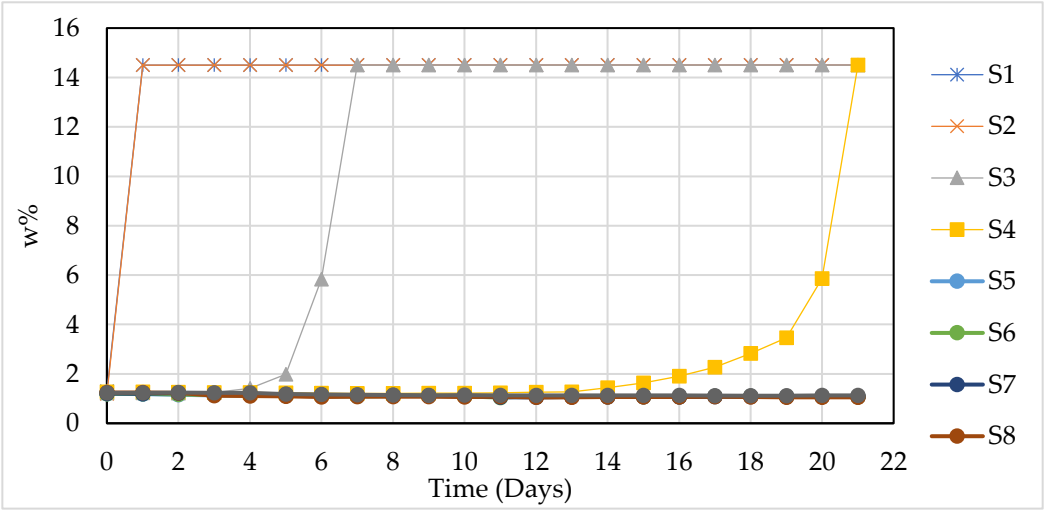

Figure 5.26: Evolution of gravimetric water content computed from RH.

Another method for measuring water content was by using the Induced Polarization technique. This part of the work was done by experts from geophysics (Feras Abdulsamad, Ahmad Ghorbani and Andre Revil) in collaboration with this PhD work. More details about this technique and calculations can be found in Annex 2 [151]. The experimental setup was shown in Figures 5.19 and 5.20, the wall

shown here is in its dry state, before adding water to the sand. 64 self-adhesive electrodes are placed on one line in the middle of the wall, the distance between the electrodes is 4.5 cm. Two supports were used to keep the electrodes in contact with the wall during all days of the experiment.

A device "ABEM Terrameter SAS-4000" was used to perform both the resistivity and time domain-induced polarization data measurements. From these measurements, water content was deduced. The tomograms along time are presented along the vertical mid-plane, beneath the position of the electrodes, in Figure 5.27 [151].

It can be observed that initially, before capillarity, the gravimetric water content was below 3% which is consistent with Figure 5.26. When the capillary test started, the water content at the bottom part rose to 14% (Figure 5.27), which is also consistent with w shown in Figure 5.26. The interface between the dry part and wet part is clearly visible showing the capillary wetting front. The capillary front from this method was then compared to the one recorded by using a camera, and a good correlation was observed between the two methods.

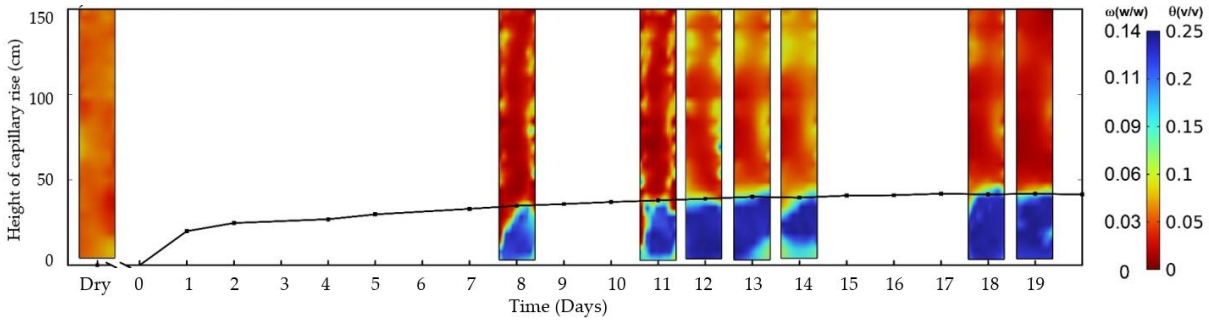

Figure 5.27: Water content (volumetric fraction) and (gravimetric fraction) tomograms obtain induced polarization method [151].

5.3.2.2 Results of mechanical test after capillary test

When dried after the capillary test, the wall W3 was subjected to a mechanical test where compressive strength and apparent Young's modulus were determined. A similar protocol for the mechanical test was followed as explained in Chapter 4, in section 4.6.3. The wall was compressed with reloading-loading cycles at 20% of the estimated maximum strength. The deformation was calculated by DIC. The result of the stress-strain curve of wall W3 is presented in Figure 5.27. It can be observed that the maximum compressive strength was 0.98 MPa for a wall that was re-dried after capillary rise. The apparent Young's modulus of the re-dried wall was equal to 1.11 MPa at 20% of compressive strength (fc).

Compared to the reference wall W2, tested at a dry state in the drying experiment (Chapter 4, section 4.6.4.1), without capillary rise, had a compressive strength of 1.15 MPa. From the values of compressive strength of the two walls, a possible restoration of strength by 85% can be observed on the wall re-dried after capillary rise.

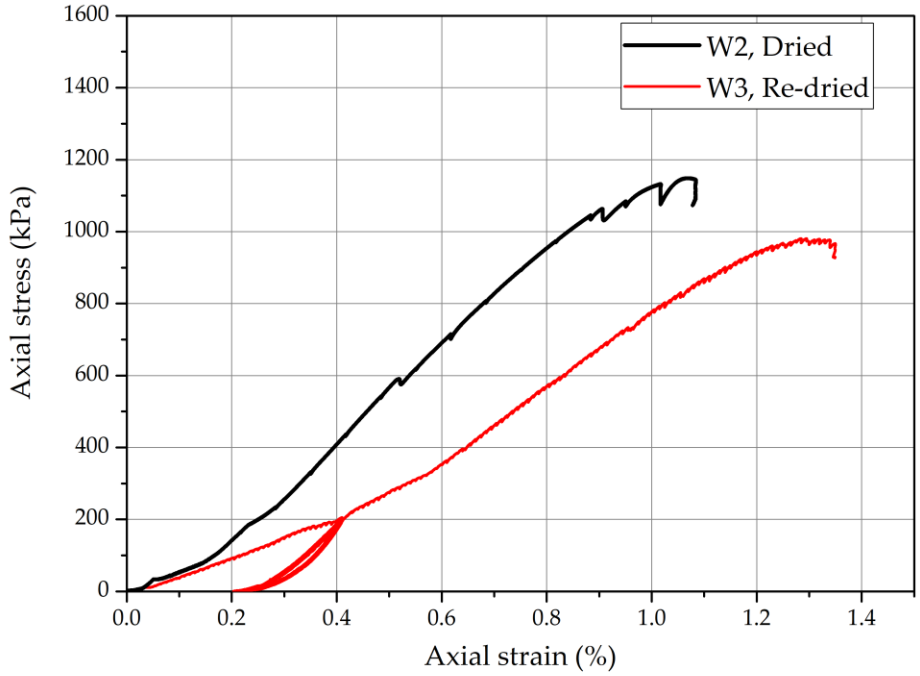

Figure 5.28: Stress-strain curve for RE walls, wall W2 tested without capillarity and W3 after re-dried from capillarity.

The results of compressive strength were further placed with the one at column scale as shown in Figure 5.29. First, we observe that the compressive strength of the RE walls is always lower than the one of the RE columns at both dry and after re-dried even though they are made of the same earth and have comparable density. A possible reason for this difference could be their size difference. In both RE columns and walls, there was a noticeable decrease in compressive strength when the samples were re-dried after capillary rise (see Figure 5.29). This shows that a wetting-drying cycle has a significant effect on the mechanical performances of RE structures.

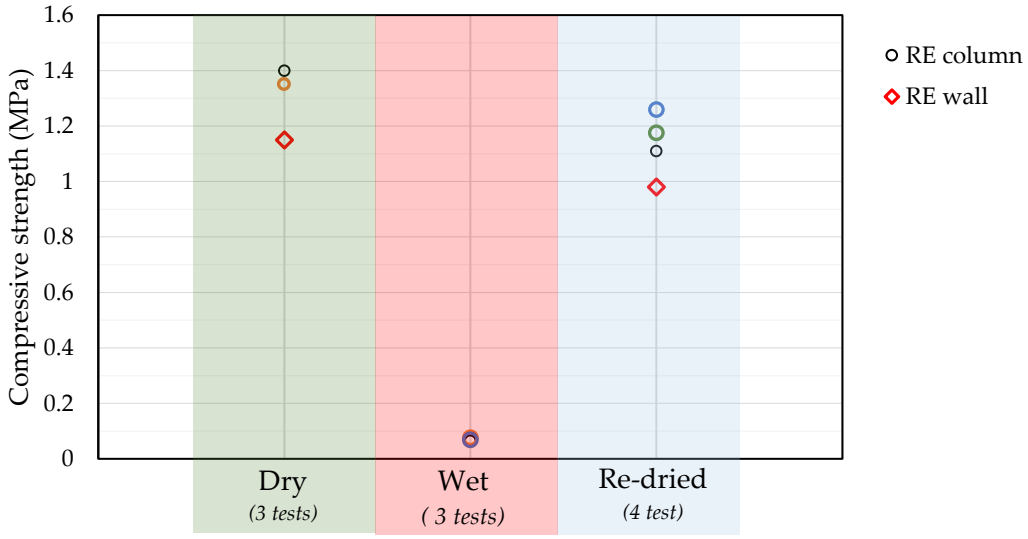

Figure 5.29: Compressive strength of 8 RE columns and walls (W2 and W3) before and after the capillary rise

5.3.3 Synthesis of capillary test on wall

The capillary rise was done in the RE wall of 1.5 m high, the aim was to investigate the mechanical behaviour of the wall through an exceptional water entry, such as capillary rise. Therefore, the hydric state was followed during the capillary rise and a mechanical test was performed.

The capillary rise setup was designed suited for large walls. The hydric state was followed by using methods such as capacitive sensors, TDR, and electrodes. A camera was used to record the height of the capillary rise. The test lasted for 21 days which the capillary fronts reaches equilibrium at a height of 42 cm. It was observed that the moisture rose faster inside the wall than on the surface. A similar analytical model was used, it seems to be closer to the experimental results. Different methods for monitoring water content were compared. It was observed that both capacitive sensors and electrodes showed a similar gravimetric water content of around 13% to 14.5% once the soil is in contact with water. Also, from the position of electrodes, the tomogram of w was determined, making it possible to determine the evolution of the capillary front. A good correlation of capillary front was observed from the one obtained using a camera.

The capillary rise test was stopped when equilibrium was reached, and the wall was left to be re-dried. The re-dried wall (W3) was subjected to a UCS test. The results were then compared to a wall dried without capillarity named W2. It was observed that the *fc* was 0.98 MPa for the wall W3 that was re-dried after capillary rise. Compared to the reference wall W2, tested at a dry state in the drying experiment which had fc of 1.15 MPa. From the values of compressive strength of the two walls, a possible restoration of strength by 85% can be observed on the wall re-dried after capillary rise.

5.4 Conclusion on capillary experiments

This chapter has highlighted the effect of capillary rise on RE building. The experimental campaigns were realised at two large scales (RE columns and a wall) aiming to reproduce what happens on a real RE building.

The development of an experimental setup at these two large scales was a challenge that was overcome by the use of saturated sand and a controlled water level, thus imposing a known value of suction at the base. Samples were place placed on top of the sand to start the experiment which lasted about three weeks.

During the capillary rise, the hydric state was monitored by using different instrumentations such as a capacitive sensor, TDR, balance, camera, and induced polarisation (a resistive technique used in geophysics). Thanks to these instrumentations, the kinetics of the capillary rise were followed by the evolution of water absorbed and the height of capillary rise.

A linear relationship was observed between the water absorbed and the square root of time elapsed, thus a coefficient of absorption was determined. The coefficient of absorption indicates the amount of water a porous material absorbs on first coming into contact with the water. The value of the coefficient of absorption ranged from 0.13 to 0.23 kg/m²/√s which was close to other RE found in the literature. The results of the mass of water absorbed were not presented for the RE wall due to experimental difficulties. Despite the lack of this data in a wall, water content was followed using another method. The wall was equipped with electrodes that permitted the wall's electrical resistivity to be surveyed, this method is known as Induced polarization. By using this technique, the evolution of water content and height of capillary rise were determined.

The height of capillary rise was also recorded by a camera for both columns and the wall. In both experiments, the evolution of the height of capillary rise was quite similar, the water level stabilized at a height of around 41 to 42 cm with an applied suction at the base between 200 and 400 Pa. An approach to deducing the analytical solution for the rate of capillary rise was performed by using unsaturated flow theory. This theory was modified from Terzaghi's assumption of saturated flow in the soil. By using the unsaturated theory, the rate of the capillary was determined. A good correlation was found between experimental data and analytical ones, but this can be improved because the ultimate height of capillary rise on columns or walls is much lower than the theoretical one.

Another observation was the RH inside the sample was monitored by capacitive sensors. The sensors were installed during sample preparation with protection from damage. The capacitive sensors were used in both RE columns and the wall. The evolution of RH was recorded with time, in the early days the RH of the bottom layer will shoot instantly as the water wet the sample while at the near top of the sample, the RH gradually increased, indicating that water was diffusing to vapour.

When the capillary rise reached equilibrium, the test was stopped and samples were subjected to drying. The aim was to answer a question like to what extent is the mechanical performance of RE building at critical conditions such as flood, and is there a restoration of strength upon drying after capillary rise?

Therefore, the UCS test was performed on three samples that were tested in a wet state just after the capillary rise and three other samples that were re-dried after capillarity. Results of the UCS test after capillarity shows a drop in mechanical resistance by 95% from the initial dry state, this means that the building is at a high risk of collapsing. After dying, both wall and column showed restoration of the strength by 85% of the original strength. In the future, further research is welcomed to study the effect of several drying-wetting cycles on the mechanical behaviour of RE.

General Conclusion and Perspectives

Conclusions

The effect of water in RE is one of the main reasons hindering the adaptation of this type of construction and earth construction in general. This problem is not new, and there exists various research to quantify the effect of water on the mechanical behaviour of RE, but only a few are done at a realistic scale. More research is needed to improve the design of RE with respect to varying hydric conditions. This thesis proposed to quantify experimentally the effect of water in the RE building, with the goal of facilitating the hydromechanical modelling.

The thesis begins with the characterisation of the earthen material used. The soil came from the recent construction of the RE building in the Rhone-Alpes region. The soil contained 10% clay which was adequate for RE construction. The clay activity was categorised as slightly active, meaning less sensitive to swelling and shrinkage. The hydric properties were characterised by determining the water retention curve and hydraulic conductivity of the earth.

Before the compaction of the sample, the manufacturing water content was determined by the proctor test. Two kinds of proctor tests were performed (i.e. Modified proctor test and In-situ proctor test) to determine the optimum water content. It was found that the results of the modified proctor test were close to the in-situ using on-site ramming equipment. Therefore, it was confirmed that the modified proctor provides a good representation of the on-site compaction, thus it is recommended for RE.

Samples were manufactured at three scales from material scale (small samples) to large scales (column and wall). Small samples were compacted with a homogeneous density since there were no layers. At large scales, columns and walls were made up of layers intentionally chosen to have a closer representation of a real RE and were mainly used in the experiments. After sample preparation, two kinds of experimental campaigns (drying experiments and capillary rise experiments) were performed to link the hydric state and the mechanical properties.

The drying experiment was done at all three scales, at the material scale samples after manufacture were dried in different uniform RH until reaches equilibrium, and then tested mechanically. At large scale (columns and walls) samples were dried in a closed environment before they were mechanically tested. The boundary conditions adopted constrained the moisture transfer in one direction. While drying, periodic monitoring of the hydric state was performed.

Capillary experiments were done on columns and walls. A design of a capillary setup suited for both scales was presented. Dried samples were placed for the capillary rise test, and the kinetic of capillary rise and the mechanical behaviour were followed.

The following conclusions were made from this thesis:

- The hydric condition inside the RE samples was monitored by the following methods; capacitive sensors (for RH), TDR, and Induced polarization method for water content. It was observed that capacitive sensors are not suitable for very humid conditions (RH >98%), but below that they were working fine. When using Induced polarization, it was observed that the evolution of electrical resistivity had a similar trend as the one of RH. Both the Induced Polarization method and capacitive sensors had a similar result in the determination of capillary fronts. The Induced Polarization method has more advantages over capacitive sensors since its non-destructive and allows to obtain the 3D field of hydric state, therefore can be applied in real RE buildings.

- Water has a very important influence on the mechanical behaviour of RE. The compressive strength which is considered the main parameter for strength was observed to increase by a factor of 12 from the moist state (manufacturing state) to the dry state. The modulus of elasticity was also observed to increase at a significant amount from the manufacturing state to the dry state for both walls and columns. Considering the realistic boundary conditions were adopted, the evolution of mechanical behaviour with drying time presented in this thesis is representative of a real RE. This is useful in practice to estimate the minimum drying time for RE structures to attain the required strength during construction. Here, for the earth considered, the geometry of the column and wall, and the indoor conditions, we found between 3 and 4 weeks.
- However, time alone does not account for the changes in mechanical performances but rather the varying drying environment. Therefore, the mechanical behaviours were linked with the hydric state, represented by a state variable "suction". The mechanical behaviour was observed to increase with suction. At an early stage of drying, where the sample is close to saturation, a little variation in suction has a greater influence on mechanical behaviour than a few variations of suction, for a low saturation degree (near dried state). Thus, a linear relationship was observed between mechanical capacity and logarithmic suction.
- The effect of scale and granulometry of samples was observed, and the results of compressive strength with the logarithm of suction at three scales were compared. it was concluded that the compressive strength at the material scale is significantly larger than column and wall scales. Whereas the apparent Young's modulus was in the same order of magnitude at all suction levels.
- New findings on the viscous behaviour of RE were reported in this thesis. The viscous part of the mechanical behaviour was quantified experimentally, at different hydric states. It was found that the coefficient of viscosity increased during drying, and this value will tend toward a constant value when the wall dried. The coefficient of viscosity was also related to suction. A linear relationship between the coefficient of viscosity and the logarithm of suction was observed. This work provides the order of magnitude for the coefficient of viscosity for RE, which is scarce in the literature. Considering that, none of the existing studies has ever shown the variation of the viscous behaviour of RE, this work will pave the way for taking into consideration the viscous part of the mechanical behaviour of RE.

- In the capillary experiment, it was found that the wet samples just after the capillary rise, showed a drop in mechanical resistance by 95% from the initial dry state, this means that at this state the building is at a high risk of collapsing. Upon drying after the capillary rise, both wall and column showed a restoration of the strength by 85% of the original strength. This implies that even though the building will lose strength during the capillary rise, most of it will be recovered upon re-drying.

Finally, a summary of parameters toward modelling is presented in the thesis work. A tremendous amount of experimental data on hydric conditions inside RE columns together with their corresponding mechanical capacity is provided. These data will improve the validation of the hydro-mechanical model.

Perspectives

- One of the main challenges in the drying experiment was the fluctuating environmental conditions, notably due to varying seasons. Improvement of drying conditions by designing a chamber that can maintain a steady RH and temperature, will solve this problem for future studies and assure a more accurate study of suction. Similar case for the capillary experiment, constant temperature ensures constant water viscosity, hence less uncertainty in results. It is worth noting that, at the beginning of this thesis project, a climatic chamber was developed where the humidity was controlled by saline solution. This is not an effective way for the moist sample as they tend to release a lot of water that can't be controlled by saline solution. A solution could be, designing a sealed climatic chamber, large enough to accommodate large samples, where the humidity and temperature are controlled through a humidity control machine.
- Numerical modelling and validation of existing Thermal Hydro-Mechanical models. The parameters required for modelling are summarized from the experiments. The numerous experimental results, at both small and large scales, showing the evolution of mechanical performances with suction as well as time, could facilitate the validation of existing RE models. In addition, the new findings on the coefficient of viscosity of RE and its evolution with the hydric state will facilitate the integration of viscous behaviour the in hydro-mechanical modelling.
- Further experimental studies on the viscous behaviour of RE for a long duration of time are recommended.
- In the capillary rise test, only one cycle of wetting and drying was done, and it was observed to influence the mechanical performance. Further research is welcomed to study the effect of several drying-wetting cycles on mechanical behaviour, thus the durability of RE can be assessed.

Reference

[1] ADEME, "Bâtiment Chiffres Clés," Nice, 2013.

[2] Global Alliance for Buildings and Construction, "Global Status Report: Towards a Zero Emission, Efficient and Resilient Buildings and Construction Sector," 2018.

[3] M. Adams *et al.*, "Bringing embodied carbon upfront: Coordinated action for the building and construction sector to tackle embodied carbon," *Bringing Embodied Carbon Upfront*, vol. 35, 2019.

[4] Ministère de la Transition écologique et solidair, "Stratégie National bas-carbone," 2020. [Online]. Available: http://www.ecologique-solidaire.gouv.fr/strategie-nationale-bas-carbone.

[5] C. Nicolas, "Guide RE 2020." https://www.ecologie.gouv.fr/reglementation-environnementale-re2020#scroll-nav__3 (accessed Jan. 20, 2023).

[6] L. Barcelo, J. Kline, G. Walenta, and E. Gartner, "Cement and carbon emissions," *Mater. Struct.*, vol. 47, no. 6, pp. 1055–1065, 2014.

[7] U. N. Environment, K. L. Scrivener, V. M. John, and E. M. Gartner, "Eco-efficient cements: Potential economically viable solutions for a low-CO2 cement-based materials industry," *Cem. Concr. Res.*, vol. 114, pp. 2–26, 2018.

[8] M. Sauvage, "LES DÉBUTS DE L ' ARCHITECTURE DE TERRE AU PROCHE-ORIENT," *1ére conférence méditerranéenne sur l'architecture terre*, 2009.

[9] C. S. Costa, F. Rocha, and A. L. Velosa, "Sustainability in earthen heritage conservation," *Spec. Publ.*, vol. 416, no. 1, pp. 91–100, 2016.

[10] J. Vyncke, L. Kupers, and N. Denies, "Earth as Building Material–an overview of RILEM activities and recent Innovations in Geotechnics," in *MATEC Web of Conferences*, 2018, vol. 149, p. 2001.

[11] J. C. Morel, A. Mesbah, M. Oggero, and P. Walker, "Building houses with local materials: Means to drastically reduce the environmental impact of construction," *Build. Environ.*, vol. 36, no. 10, pp. 1119–1126, 2001, doi: 10.1016/S0360-1323(00)00054-8.

[12] D. Gallipoli, A. W. Bruno, C. Perlot, and N. Salmon, "Raw earth construction: Is there a role for unsaturated soil mechanics?," *Unsaturated Soils Res. Appl. - Proc. 6th Int. Conf. Unsaturated Soils, UNSAT 2014*, vol. 1, pp. 55–62, 2014, doi: 10.1201/b17034-8.

[13] L. Soudani, "Modelling and experimental validation of the hygrothermal performances of earth as a building material," 2017.

[14] D. Allinson and M. Hall, "Hygrothermal analysis of a stabilised rammed earth test building in the UK," *Energy Build.*, vol. 42, no. 6, pp. 845–852, 2010.

[15] ADEME, "Déchets Chiffres Clés," Angers, 2017.

[16] M. Menegaki and D. Damigos, "A review on current situation and challenges of construction and demolition waste management," *Curr. Opin. Green Sustain. Chem.*, vol. 13, pp. 8–15, 2018, doi: 10.1016/j.cogsc.2018.02.010.

[17] A. N. Daza, E. Zambrano, and J. A. Ruiz, "Acoustic performance in raw earth construction techniques used in Colombia," *EuroRegio2016, Eur. Assoc. Acoust.*, pp. 1–10, 2016.

[18] L. Birznieks, "Design and building with compressed earth." MSC Thesis, 2013.

[19] NZS-4297, "Engineering design of earth buildings," *Stand. New Zeal.*, vol. 4297, p. 63, 1998.

[20] J. . Tibbets, *Emphasis on rammed earth—The rational*, 9th ed. Interaméricas Adobe Build, 2001.

[21] Q. B. Bui, J. C. Morel, B. V. Venkatarama Reddy, and W. Ghayad, "Durability of rammed earth walls exposed for 20 years to natural weathering," *Build. Environ.*, vol. 44, no. 5, pp. 912–919, 2009, doi: 10.1016/j.buildenv.2008.07.001.

[22] R. E. L. Nabouch, "Mechanical behavior of rammed earth walls under Pushover tests," Université Grenoble Alpes., 2017.

[23] E. Hamard, B. Cazacliu, A. Razakamanantsoa, and J. C. Morel, "Cob, a vernacular earth construction process in the context of modern sustainable building," *Build. Environ.*, vol. 106, pp. 103–119, 2016, doi: 10.1016/j.buildenv.2016.06.009.

[24] D. R. Hill, *A history of engineering in classical and medieval times*. Psychology Press, 1996.

[25] E. Bıcakci, M. Özdoğan, H. Hauptmann, and N. Basgelen, "Observations on the Early Pre-Pottery Neolithic Architecture in the Near East: 1. New Building Materials and Construction Techniques," *From Village to Cities: Early Villages in the Near East*. Yayinlari Istanbul, pp. 385–414, 2003.

[26] R. Anger and L. Fontaine, "Bâtir en terre, du grain de sable à l'architecture, éditions Belin," *Cité des Sci. l'industrie, Parigi*, 2009.

[27] J. M. C. Ongpeng, E. Gapuz, and C. L. C. Roxas, "Optimization of mix proportions of compressed earth blocks with rice straw using artificial neural network," in *Proceedings of the 2017 World Congress on Advances in Strucural Engineering and Mechanics (ASEM17), Seoul, Korea*, 2017, pp. 1–14.

[28] F. Ávila, E. Puertas, and R. Gallego, "Characterization of the mechanical and physical properties of unstabilized rammed earth: A review," *Constr. Build. Mater.*, vol. 270, 2021, doi: 10.1016/j.conbuildmat.2020.121435.

[29] K. J, *Building Without Borders*. Gabriola Island, BC, Canada,: New Society Publishers, 2004.

[30] B. V. V. Reddy and P. P. Kumar, "Embodied energy in cement stabilised rammed earth walls," *Energy Build.*, vol. 42, no. 3, pp. 380–385, 2010.

[31] G. Minke, "Building with Earth: Design and Technology of a Sustainable Architecture." DE GRUYTER, 2006.

[32] L. Miccoli, U. Müller, and P. Fontana, "Mechanical behaviour of earthen materials: A comparison between earth block masonry, rammed earth and cob," *Constr. Build. Mater.*, vol. 61, pp. 327–339, Jun. 2014, doi: 10.1016/j.conbuildmat.2014.03.009.

[33] D. Gallipoli *et al.*, "Durability of Earth Materials: Weathering Agents, Testing Procedures and Stabilisation Methods," in *Testing and Characterisation of Earth-based Building Materials and Elements: State-of-the-Art Report of the RILEM TC 274-TCE*, A. Fabbri, J.-C. Morel, J.-E. Aubert, Q.-B. Bui, D. Gallipoli, and B. V. V. Reddy, Eds. Cham: Springer International Publishing, 2022, pp. 211–241.

[34] S. Australia, "The Australian earth building handbook," *Sydney, Aust.*, 2002.

[35] Standards Association of Zimbabwe, *SAZS 724: Zimbabwe Standard Rammed Earth Structures.* Harare, Zimbabwe, 2001.

[36] G. F. Middleton, *Revised by Schneider, LM (1992)*, Fourth Edi. North Ryde, Australia: Construction and Engineering, 1987.

[37] G. C. Bureau, "New Mexico adobe and rammed earth building code," *Gen. Constr. Bur. USA*, vol. 311, p. 312, 1991.

[38] M. Hall and Y. Djerbib, "Rammed earth sample production: Context, recommendations and consistency," *Constr. Build. Mater.*, vol. 18, no. 4, pp. 281–286, 2004, doi: 10.1016/j.conbuildmat.2003.11.001.

[39] D. M. Lilley and J. Robinson, "Ultimate strength of rammed earth walls with openings," *Proc. Inst. Civ. Eng. Build.*, vol. 110, no. 3, pp. 278–287, 1995.

[40] V. Maniatidis, P. Walker, A. Heath, and S. Hayward, "Mechanical and thermal characteristics of rammed earth," 2007.

[41] V. Maniatidis and P. Walker, "Structural Capacity of Rammed Earth in Compression," *J. Mater. Civ. Eng.*, vol. 20, no. 3, pp. 230–238, Mar. 2008, doi: 10.1061/(asce)0899-1561(2008)20:3(230).

[42] Q. B. Bui, J. C. Morel, S. Hans, and P. Walker, "Effect of moisture content on the mechanical characteristics of rammed earth," *Constr. Build. Mater.*, vol. 54, pp. 163–169, 2014, doi: 10.1016/j.conbuildmat.2013.12.067.

[43] Q. Piattoni, E. Quagliarini, and S. Lenci, "Experimental analysis and modelling of the mechanical behaviour of earthen bricks," *Constr. Build. Mater.*, vol. 25, no. 4, pp. 2067–2075, 2011, doi: 10.1016/j.conbuildmat.2010.11.039.

[44] P. Walker, R. Keable, J. Martin, and V. Maniatidis, *Rammed earth : design and construction guidelines*. IHS BRE, 2005.

[45] V. Maniatidis and P. Walker, "A review of rammed earth construction," *Dev. rammed earth UK Hous.*, no. May, p. 109, 2003, [Online]. Available: http://staff.bath.ac.uk/abspw/rammedearth/review.pdf.

[46] V. Mollion, "Etude du comportement mécanique du pisé," *Internsh. report. Master, Lyon ENTPE*, 2009.

[47] F. Champiré, A. Fabbri, J. C. Morel, H. Wong, and F. McGregor, "Impact of relative humidity on the mechanical behavior of compacted earth as a building material," *Constr. Build. Mater.*, vol. 110, pp. 70–78, 2016, doi: 10.1016/j.conbuildmat.2016.01.027.

[48] L. Fontaine, "Cohésion et comportement mécanique de la terre comme matériau de construction," *DPEA Report, Lyon Insa. 115p*, 2004.

[49] L. Miccoli and D. V Oliveira, "Static behaviour of rammed earth : experimental testing and finite element modelling," pp. 3443–3456, 2015, doi: 10.1617/s11527-014-0411-7.

[50] T. T. Bui, Q. B. Bui, A. Limam, and S. Maximilien, "Failure of rammed earth walls: From observations to quantifications," *Constr. Build. Mater.*, vol. 51, pp. 295–302, 2014, doi: 10.1016/j.conbuildmat.2013.10.053.

[51] R. A. Silva, D. V Oliveira, L. Schueremans, and P. B. Lourenço, "Modelling the Structural Behaviour of Rammed Earth Components," pp. 1–13, 2014.

[52] L. E. Yamin, C. A. Phillips, J. C. Reyes, and D. M. Ruiz, "Seismic Behavior and Rehabilitation Alternatives for Adobe and Rammed Earth Buildings," *13 th World Conf. Earthq. Eng.*, no. 2942, p. 10, 2004.

[53] P. Chauhan, A. El Hajjar, N. Prime, and O. Plé, "Unsaturated behavior of rammed earth: Experimentation towards numerical modelling," *Constr. Build. Mater.*, vol. 227, p. 116646, 2019, doi: 10.1016/j.conbuildmat.2019.08.027.

[54] R. El-nabouch, Q. Bui, O. Plé, and P. Perrotin, "Characterizing the shear parameters of rammed earth material by using a full-scale direct shear box," *Constr. Build. Mater.*, vol. 171, pp. 414–420, 2018, doi: 10.1016/j.conbuildmat.2018.03.142.

[55] H. Houben and H. Guillaud, "Earth Construction: A Comprehensive Guide, Intermediate technology." Publications, London, 1994.

[56] O. Helson, A. L. Beaucour, J. Eslami, A. Noumowe, and P. Gotteland, "Physical and mechanical properties of soilcrete mixtures: Soil clay content and formulation parameters," *Constr. Build. Mater.*, vol. 131, pp. 775–783, 2017, doi: 10.1016/j.conbuildmat.2016.11.021.

[57] M. I. Gomes, T. D. Gonçalves, and P. Faria, "Unstabilized rammed earth: Characterization of material collected from old constructions in south portugal and comparison to normative requirements," *Int. J. Archit. Herit.*, vol. 8, no. 2, pp. 185–212, 2014, doi: 10.1080/15583058.2012.683133.

[58] J. Keable, *Rammed earth structure - A code of practice*. London, UK: Intermediate Technology Publications, 1996.

[59] J. Norton, *'Building with Earth: a handbook,'* Second Edi. London, UK: Intermediate Technology Publications, 1997.

[60] L. Keefe, *"Earth building- methods and materials, repair and conservation,"* 1st Editio. London, UK: Taylor & Francis, 2005.

[61] A. W. Skempton, "The colloidal activity of clays," *Sel. Pap. soil Mech.*, vol. 1, pp. 57–61, 1953.

[62] M. Olivier and A. Mesbah, "Le matériau terre: Essai de compactage statique pour la fabrication de briques de terre compressées," *Bull. Liaison Lab. Ponts Chaussées*, vol. 146, pp. 37–43, 1986.

[63] C. H. Kouakou and J. C. Morel, "Strength and elasto-plastic properties of non-industrial building materials manufactured with clay as a natural binder," *Appl. Clay Sci.*, vol. 44, no. 1–2, pp. 27–34, 2009, doi: 10.1016/j.clay.2008.12.019.

[64] S. S. D. Raavi and D. D. Tripura, "Predicting and evaluating the engineering properties of unstabilized and cement stabilized fibre reinforced rammed earth blocks," *Constr. Build. Mater.*, vol. 262, p. 120845, 2020.

[65] J. C. Morel, A. Pkla, and P. Walker, "Compressive strength testing of compressed earth blocks," *Constr. Build. Mater.*, vol. 21, no. 2, pp. 303–309, 2007, doi: 10.1016/j.conbuildmat.2005.08.021.

[66] A. W. Bruno, "Étude du comportement hygro-mécanique de la terre crue hyper-compactée pour la construction durable." Pau, 2016.

[67] A. W. Bruno, D. Gallipoli, C. Perlot, and J. Mendes, "Mechanical behaviour of hypercompacted earth for building construction," *Mater. Struct. Constr.*, vol. 50, no. 2, 2017, doi: 10.1617/s11527-017-1027-5.

[68] F. Menasria, A. Perrot, D. Rangeard, and A. Le Duigou, "Mechanical enhancement of casted and compacted earth-based materials by sand, flax fiber and woven fabric of flax," *Acad. J. Civ. Eng.*, vol. 35, no. 2, pp. 148–153, 2017.

[69] A. Perrot, D. Rangeard, F. Menasria, and S. Guihéneuf, "Strategies for optimizing the mechanical strengths of raw earth-based mortars," *Constr. Build. Mater.*, vol. 167, pp. 496–504, 2018.

[70] O. D. Martínez, "Preservation and repair of rammed earth constructions," *Univ. do Minho, Braga*, 2015.

[71] S. Burroughs, "Recommendations for the Selection, Stabilization, and Compaction of Soil for Rammed Earth Wall Construction," *J. Green Build.*, vol. 5, no. 1, pp. 101–114, 2010, doi: 10.3992/jgb.5.1.101.

[72] C. Beckett, "The Effect of Relative Humidity and Temperature on the Unconfined Compressive Strength of Rammed Earth The Effect of Relative Humidity and Temperature on the Unconfined Compressive," no. May 2014, 2012, doi: 10.1007/978-3-642-31116-1.

[73] M. Hall and Y. Djerbib, "Moisture ingress in rammed earth : Part 1 — the effect of soil particle-size distribution on the rate of capillary suction," vol. 18, pp. 269–280, 2004, doi: 10.1016/j.conbuildmat.2003.11.002.

[74] Q. B. Bui, J. C. Morel, S. Hans, and N. Meunier, "Compression behaviour of non-industrial materials in civil engineering by three scale experiments: The case of rammed earth," *Mater. Struct. Constr.*, vol. 42, no. 8, pp. 1101–1116, 2009, doi: 10.1617/s11527-008-9446-y.

[75] P. A. Jaquin, C. E. Augarde, D. Gallipoli, and D. G. Toll, "The strength of unstabilised rammed earth materials," *Géotechnique*, vol. 59, no. 5, pp. 487–490, Jun. 2009, doi: 10.1680/geot.2007.00129.

[76] P. Gerard, M. Mahdad, A. R. Mccormack, and B. François, "A unified failure criterion for unstabilized rammed earth materials upon varying relative humidity conditions," *Constr. Build. Mater.*, vol. 95, pp. 437–447, 2015, doi: 10.1016/j.conbuildmat.2015.07.100.

[77] U. Röhlen and C. Ziegert, *Earth building practice: Planning-design-building*. Beuth Verlag, 2011.

[78] D. Ciancio, P. Jaquin, and P. Walker, "Advances on the assessment of soil suitability for rammed earth," *Constr. Build. Mater.*, vol. 42, pp. 40–47, 2013, doi: 10.1016/j.conbuildmat.2012.12.049.

[79] P. A. Jaquin, C. E. Augarde, and C. M. Gerrard, "Analysis of historic rammed earth construction. Structural analysis of historical constructions," 2006.

[80] T. Bui, "Modeling rammed earth wall using discrete element method," pp. 523–538, 2016, doi: 10.1007/s00161-015-0460-3.

[81] R. El-nabouch, Q. Bui, O. Plé, and P. Perrotin, "Assessing the in-plane seismic performance of rammed earth walls by using horizontal loading tests," *Eng. Struct.*, vol. 145, pp. 153–161, 2017, doi: 10.1016/j.engstruct.2017.05.027.

[82] H. Nowamooz and C. Chazallon, "Finite element modelling of a rammed earth wall," *Constr. Build. Mater.*, vol. 25, no. 4, pp. 2112–2121, 2011, doi: 10.1016/j.conbuildmat.2010.11.021.

[83] X. Zhang and H. Nowamooz, "Effect of rising damp in unstabilized rammed earth (URE) walls," *Constr. Build. Mater.*, vol. 307, no. June, 2021, doi: 10.1016/j.conbuildmat.2021.124989.

[84] P. Chauhan, N. Prime, and O. Plé, "Benefit of Unsaturated Soil Mechanics Approach on the Modeling of Early-Age Behavior of Rammed Earth Building," *Materials (Basel).*, vol. 15, no. 1, 2022, doi: 10.3390/ma15010362.

[85] L. Xu, F. Champiré, A. Fabbri, H. Wong, and D. Branque, "Hydro-Mechanical Triaxial Behaviour of Compacted Earth at Different Temperatures," in *Poromechanics VI*, 2017, pp. 164–171.

[86] W. J. Lu, N. and Likos, *Unsaturated Soil Mechanics*. Hoboken: John Wiley & Sons, Inc., 2004.

[87] M. T. van Genuchten, "A Closed-form Equation for Predicting the Hydraulic Conductivity of Unsaturated Soils," *Soil Sci. Soc. Am. J.*, vol. 44, no. 5, pp. 892–898, 1980, doi: https://doi.org/10.2136/sssaj1980.03615995004400050002x.

[88] B. François, L. Palazon, and P. Gerard, "Structural behaviour of unstabilized rammed earth constructions submitted to hygroscopic conditions," *Constr. Build. Mater.*, vol. 155, pp. 164–175, 2017, doi: 10.1016/j.conbuildmat.2017.08.012.

[89] A. W. Bishop, "The principle of effective stress," *Tek. Ukebl.*, vol. 39, pp. 859–863, 1959.

[90] P. Chauhan, "Influence of hydric solicitations on the mechanical behavior of rammed earth: early-age behavior," Doctoral dissertation, Université Savoie Mont Blanc, 2021.

[91] L. M. Gil-Martín, M. A. Fernández-Ruiz, and E. Hernández-Montes, "Mechanical characterization and elastic stiffness degradation of unstabilized rammed earth," *J. Build. Eng.*, vol. 56, no. May, 2022, doi: 10.1016/j.jobe.2022.104805.

[92] P. Kelly, "Solid mechanics part I: An introduction to solid mechanics," *A Creat. Commons Attrib. Mt. View, CA*, vol. 94042, 2013.

[93] E. Franzoni, "Rising damp removal from historical masonries: A still open challenge," *Constr. Build. Mater.*, vol. 54, pp. 123–136, 2014.

[94] P. Scarato and J. Jeannet, *Cahier d'expert bâti en pisé: connaissance, analyse, traitement des pathologies du bâti en pisé en Rhône Alpes et Auvergne: base d'un référentiel du bâti existant en pisé*. ABITerre, 2015.

[95] C. Hall, "Water movement in porous building materials-IV. The initial surface absorption and the sorptivity," *Build. Environ.*, vol. 16, no. 3, pp. 201–207, Jan. 1981, doi: 10.1016/0360-1323(81)90014-7.

[96] M. Krus and A. Holm, "Simple methods to approximate the liquid transport coefficients describing the absorption and drying process," 1999.

[97] B. S. 3921, "British Standard Specification for Clay Bricks, British Standards Institution." BS London, UK, 1985.

[98] P.-A. Chabriac, "Mesure du comportement hygrothermique du pisé." ENTPE; CNRS-LTDS (UMR 5513), 2014.

[99] M. L. Indekeu, C. Feng, H. Janssen, and M. Woloszyn, "Experimental study on the capillary absorption characteristics of rammed earth," *Constr. Build. Mater.*, vol. 283, p. 122689, 2021, doi: 10.1016/j.conbuildmat.2021.122689.

[100] D. C. Drucker and W. Prager, "Soil mechanics and plastic analysis or limit design," *Q. Appl. Math.*, vol. 10, no. 2, pp. 157–165, 1952.

[101] R. B. J. Brinkgreve, "Selection of soil models and parameters for geotechnical engineering application," in *Soil constitutive models: Evaluation, selection, and calibration*, 2005, pp. 69–98.

[102] J. B. Burland, "Some aspects of the mechanical behaviour of party saturated soils," *Moisture equilibria moisture Chang. soils beneath Cover. areas*, pp. 270–278, 1965.

[103] R. J. Jardine, A. Gens, D. W. Hight, and M. R. Coop, "Developments in understanding soil behaviour," in *Advances in geotechnical engineering: The Skempton conference: Proceedings of a three day conference on advances in geotechnical engineering, organised by the Institution of Civil Engineers and held at the Royal Geographical Society, on 29–31 March 2004*, 2004, pp. 103–206.

[104] P. NF, "94-057-Analyse granulométrique des sols-Méthode par sédimentation," *Norme Française, AFNOR, Paris*, 1992.

[105] NF, *P 94-093. Soils: Investigation and Testing—Determination of the Compaction Characteristics of a Soil—Standard Proctor Test—Modified Proctor test*. Paris: AFNOR, 1999.

[106] P. NF, "94-051, Sols: Reconnaissance et Essais–Détermination des limites d'Atterberg–Limite de liquidité à la coupelle–limite de plasticité au rouleau," *Assoc. Française Norm. Fr. (in French)*, 1993.

[107] P. NF, "94–052-1 Soils: investigation and testing–atterberg limits determination–Part I: liquid limit–cone penetrometer method," *Assoc. Française Norm.*, 1995.

[108] T. Chitimbo, F. Abdul-Samad, N. Prime, and O. Plé, "Hydro-Mechanics Coupling on Rammed Earth Material: Drying Experiment at Structural Scale," *Bio-Based Build. Mater.*, vol. 1, pp. 698–706, 2022, doi: 10.4028/www.scientific.net/cta.1.698.

[109] LCPC, *Réalisation des remblais et des couches de forme*, 2 edition. Paris, 2000.

[110] P. NF, "94-068-Mesure de la capacité d'absorption de bleu de méthylène d'un sol ou d'un matériau rocheux-Détermination de la valeur de bleu de méthylène d'un sol ou d'un matériau rocheux par l'essai à la tache," *Norme Française, AFNOR, Paris*, 1998.

[111] E. E. Stapel and P. N. W. Verhoef, "The use of the methylene blue adsorption test in assessing the quality of basaltic tuff rock aggregate," *Eng. Geol.*, vol. 26, no. 3, pp. 233–246, 1989, doi: 10.1016/0013-7952(89)90011-2.

[112] D. Aran, A. Maul, and J.-F. Masfaraud, "A spectrophotometric measurement of soil cation exchange capacity based on cobaltihexamine chloride absorbance," *Comptes Rendus Geosci.*, vol. 340, no. 12, pp. 865–871, 2008.

[113] J. F. Young, "Humidity control in the laboratory using salt solutions - A review," *J. Appl. Chem.*, vol. 17, pp. 241–245, 1967.

[114] K. A. Bocking and D. G. Fredlund, "Limitations of the axis translation technique," in *Expansive Soils*, 1980, pp. 117–135.

[115] S. Houston, W. N. Houston, and A.-M. Wagner, "Laboratory filter paper suction measurements," *Geotech. Test. J.*, vol. 17, no. 2, pp. 185–194, 1994.

[116] R. J. Chandler and C. I. Gutierrez, "The filter-paper method of suction measurement," *Geotechnique*, vol. 36, no. 2, pp. 265–268, 1986, doi: 10.1680/geot.1986.36.2.265.

[117] F. M. Baptestini, P. C. Corrêa, A. M. Ramos, M. da Silva Junqueira, and I. R. Zaidan, "GAB model and the thermodynamic properties of moisture sorption insoursop fruit powder," *Rev. Cienc. Agron.*, vol. 51, no. 1, pp. 1–9, 2020, doi: 10.5935/1806-6690.20200006.

[118] G. Instruments, "World leaders in the manufacture of laboratory systems for soil & rock." web: www.gdsinstruments.com (accessed Feb. 01, 2023).

[119] G. Asch, *Les capteurs en instrumentation industrielle-7ème édition*. Hachette, 2010.

[120] Sensirion, "Datasheet SHT75," 2011. https://www.mouser.com/datasheet/2/682/Sensirion_Humidity_SHT7x_Datasheet_V5-469726.pdf (accessed Mar. 02, 2020).

[121] C. F. Souza and E. E. Matsura, "Multi-wire time domain reflectometry (TDR) probe with electrical impedance discontinuities for measuring water content distribution," *Agric. water Manag.*, vol. 59, no. 3, pp. 205–216, 2003.

[122] A. Wilczek, A. Szypłowska, M. Kafarski, and W. Skierucha, "A time-domain reflectometry method with variable needle pulse width for measuring the dielectric properties of materials," *Sensors*, vol. 16, no. 2, p. 191, 2016.

[123] F. Abdulsamad, A. Revil, N. Prime, P. Y. Gnonnoue, M. Schmutz, and O. Plé, "Complex conductivity of rammed earth," *Eng. Geol.*, vol. 273, no. February, 2020, doi: 10.1016/j.enggeo.2020.105697.

[124] A. Ghorbani *et al.*, "Complex conductivity of volcanic rocks and the geophysical mapping of alteration in volcanoes," *J. Volcanol. Geotherm. Res.*, vol. 357, pp. 106–127, 2018.

[125] A. Revil *et al.*, "Complex conductivity of soils," *Water Resour. Res.*, vol. 53, no. 8, pp. 7121–7147, 2017.

[126] H. J. Vinegar and M. H. Waxman, "Induced polarization of shaly sands," *Geophysics*, vol. 49, no. 8, pp. 1267–1287, 1984.

[127] A. Revil, "Effective conductivity and permittivity of unsaturated porous materials in the frequency range 1 mHz–1GHz," *Water Resour. Res.*, vol. 49, no. 1, pp. 306–327, 2013.

[128] A. Revil, "On charge accumulation in heterogeneous porous rocks under the influence of an external electric field," *Geophysics*, vol. 78, no. 4, pp. D271–D291, 2013.

[129] C. Hall, W. D. Hoff, and M. R. Nixon, "Water movement in porous building materials-VI. Evaporation and drying in brick and block materials," *Build. Environ.*, vol. 19, no. 1, pp. 13–20, 1984, doi: 10.1016/0360-1323(84)90009-X.

[130] J. D. Gonçalves, T.D., Pel, L. & Rodrigues, "Worsening of dampness and salt damage after restoration interventions : use of water repellent additives in plasters and renders," *Proc. 1st Hist. Mortars Conf. 24-26 Sept. 2008, Lisbon, Port. LNEC, 24-26 Oct.*, no. March 2014, p. II.01, 2008.

[131] L. F. Cooling, "Contribution to the study of florescence. II. The evaporation of water from bricks," *Trans. Br. Ceram. Soc.*, vol. 29, pp. 39–54, 1930.

[132] P. Gerard, M. Mahdad, A. Robert McCormack, and B. François, "A unified failure criterion for unstabilized rammed earth materials upon varying relative humidity conditions," *Constr. Build. Mater.*, vol. 95, pp. 437–447, 2015, doi: 10.1016/j.conbuildmat.2015.07.100.

[133] T. Chitimbo, N. Prime, O. Plé, and F. Abdulsamad, "Drying experiment on rammed earth structure," *Eur. J. Environ. Civ. Eng.*, vol. 27, no. 9, pp. 2950–2966, 2022, doi: 10.1080/19648189.2022.2099983.

[134] D. ASTM, "2166. Standard test method for unconfined compressive strength of cohesive soil," *West Conshoshocken, PA, United States*, 2016.

[135] W. H. Peters and W. F. Ranson, "Digital imaging techniques in experimental stress analysis," *Opt. Eng.*, vol. 21, no. 3, pp. 427–431, 1982.

[136] J. Zhao, Y. Sang, and F. Duan, "The state of the art of two-dimensional digital image correlation computational method," *Eng. reports*, vol. 1, no. 2, p. e12038, 2019.

[137] P. Vacher, S. Dumoulin, F. Morestin, and S. Mguil-Touchal, "Bidimensional strain measurement using digital images," *Proc. Inst. Mech. Eng. Part C J. Mech. Eng.*, vol. 213, no. 8, pp. 811–817, 1999, doi: 10.1243/0954406991522428.

[138] J. Górszczyk, K. Malicki, and T. Zych, "Application of digital image correlation (DIC) method for road material testing," *Materials (Basel).*, vol. 12, no. 15, 2019, doi: 10.3390/ma12152349.

[139] F. Abdulsamad, T. Chitimbo, A. Revil, N. Prime, and O. Plé, "Imaging the water content of rammed earth materials with induced polarization," *Eng. Geol.*, p. 107182, 2023, doi: https://doi.org/10.1016/j.enggeo.2023.107182.

[140] D. Ciancio and J. Gibbings, "Experimental investigation on the compressive strength of cored and molded cement-stabilized rammed earth samples," *Constr. Build. Mater.*, vol. 28, no. 1, pp. 294–304, 2012, doi: 10.1016/j.conbuildmat.2011.08.070.

[141] T. Chitimbo, F. Abdulsamad, N. Prime, A. Revil, and O. Plé, "Impact of Moisture Content on the Elasto-Viscoplastic Behaviour of Rammed Earth Wall: New Findings," *Constr. Mater.*, vol. 3, no. 1, pp. 1–13, 2022, doi: 10.3390/constrmater3010001.

[142] J. Li and Y. Yang, "Creep behaviour of unsaturated Red clay under matrix suction.pdf," *KSCE J. Civ. Eng.*, vol. 2, no. 22, pp. 582–587, 2018.

[143] R. B. Peck, W. E. Hansen, and T. H. Thornburn, *Foundation Engineering*, 2nd Editio. New York: Wiley, 1974.

[144] K. S. Lane, D. E. Washburn, and D. P. Krynine, "Capillarity tests by capillarimeter and by soil filled tubes," in *Highway research board proceedings*, 1946, vol. 26, pp. 460–473.

[145] S. Kumar and R. S. Malik, "Verification of quick capillary rise approach for determining pore geometrical characteristics in soils of varying texture," *Soil Sci.*, vol. 150, no. 6, pp. 883–888, 1990.

[146] AFNOR NF EN 13057, *Produits et systèmes pour la protection et la réparation des structures en béton - Méthodes d'essai - Détermination de l'absorption capillaire.* 2002.

[147] AFNOR XP P 13-901, *Blocs de terre comprimée pour murs et cloisons*. 2017.

[148] E. R. Teixeira *et al.*, "Mechanical and thermal performance characterisation of compressed earth blocks," *Energies*, vol. 13, no. 11, 2020, doi: 10.3390/en13112978.

[149] T. Chitimbo, N. Prime, F. Abdulsamad, and O. Plé, "Effect of capillary rise on mechanical behaviour of unstabilized rammed earth," in *NOMAD 2022 - 4e conférence internationale francophone Nouveaux Matériaux et Durabilité, IMT Mines Alès; LMGC; LIFAM*, pp. 1–6.

[150] S. Guiheneuf, "Formulation et renforts de blocs en matériau terre pour une utilisation structurelle," L'INSTITUT NATIONAL DES SCIENCES APPLIQUÉES RENNES, 2021.

[151] A. Ghorbani *et al.*, "Non-intrusive monitoring of water content field during capillary rise within a rammed earth structure: potential of induced polarization method," *Eng. Geol.*, 2023.

Appendices

Appendix A: Results of UCS results at material scale. Samples were conditioned at five different RH by using saline solution.

s=3,8 MPa,HR=97,3%

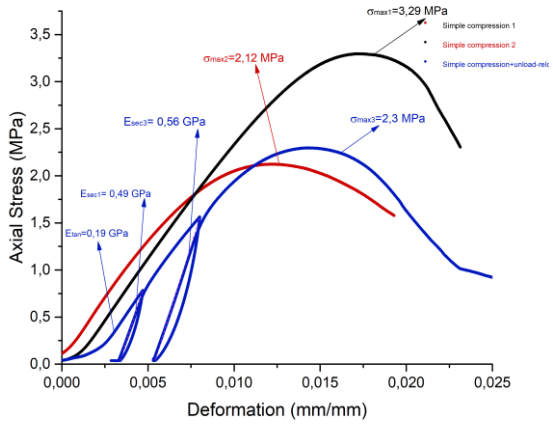

s=23,4 MPa,HR=84,34%

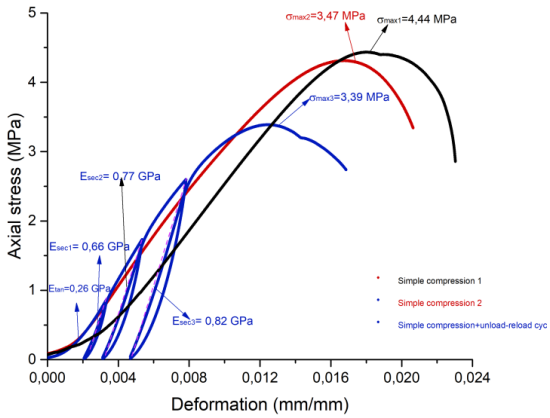

s=39 MPa,RH=75,3%

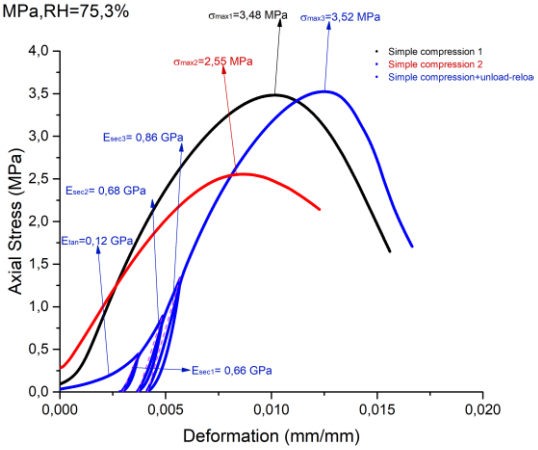

s=75,9 MPa,RH=57,6%

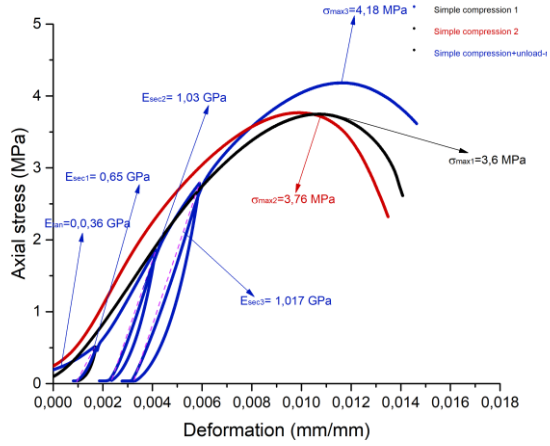

S=153,4 (MPa),RH=32%

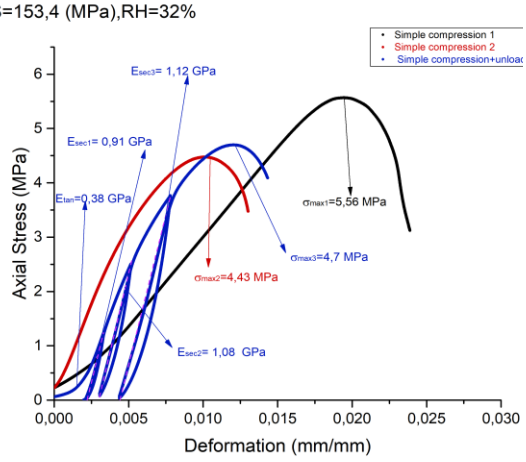

Initial condition w0

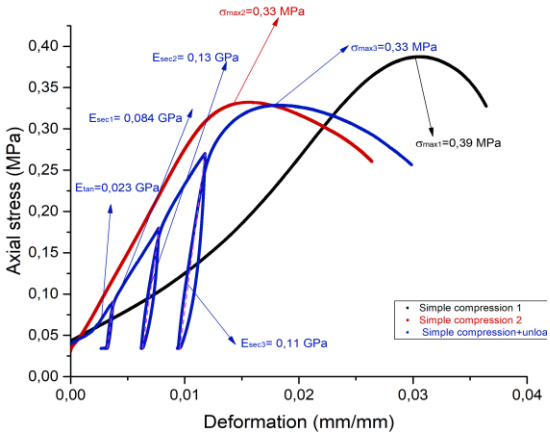

Appendix B: Calculation of Vertical strain for wall W2 during 8 weeks of frying. The strains were determined by using the vertical displacement (dy) along the vertical the height of the wall (y).

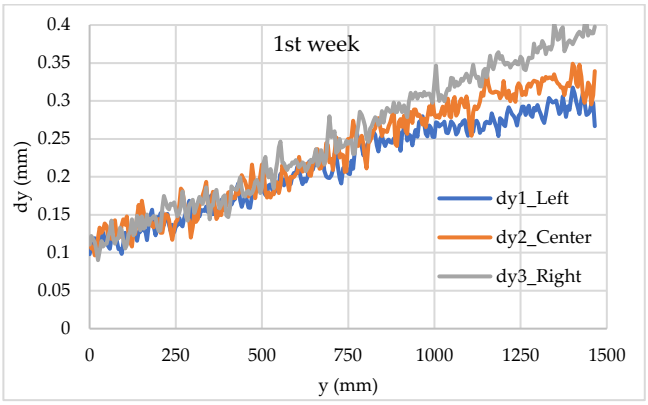

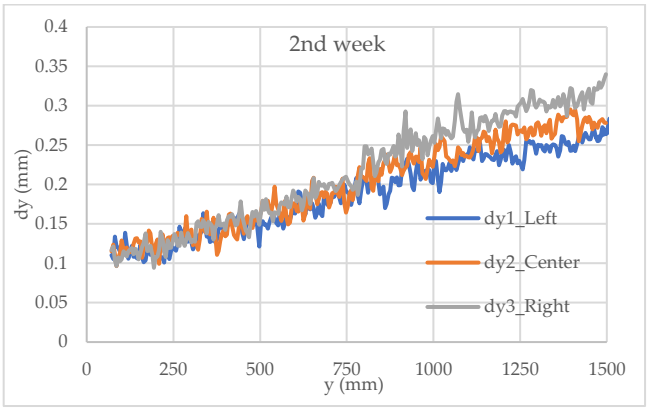

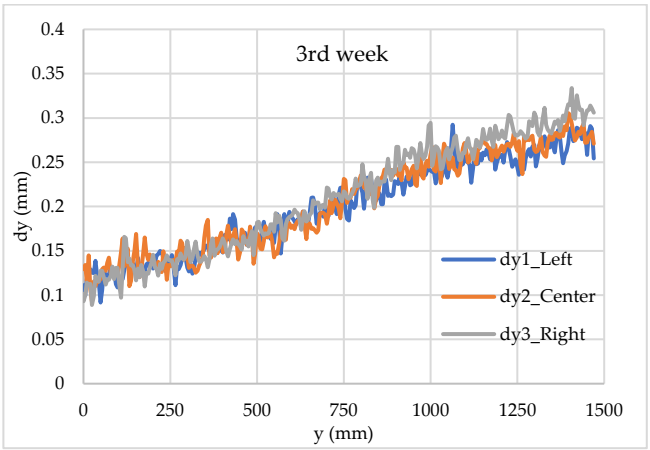

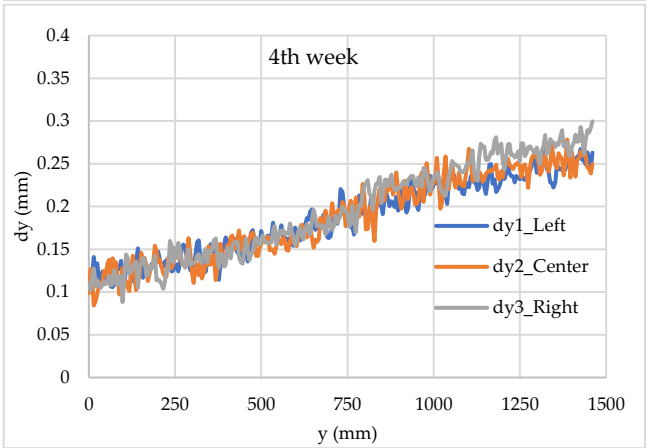

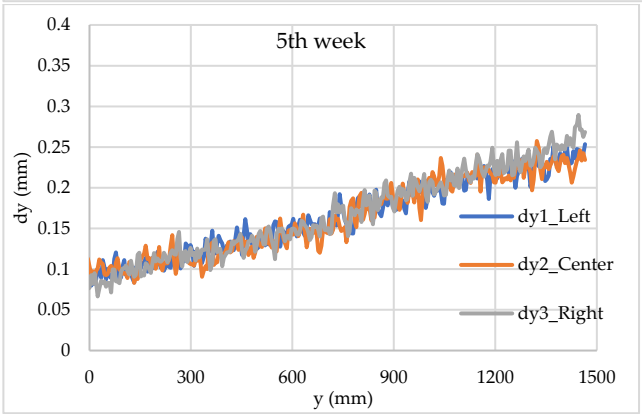

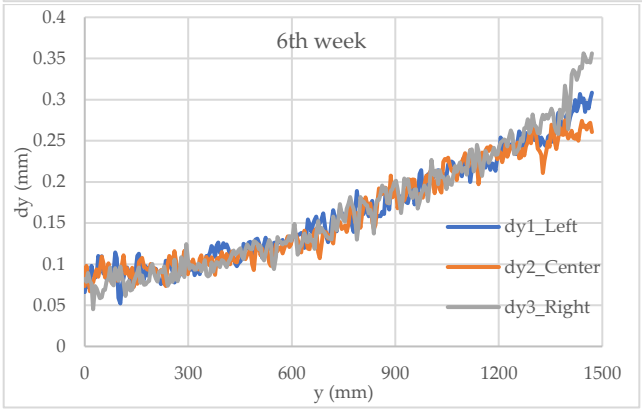

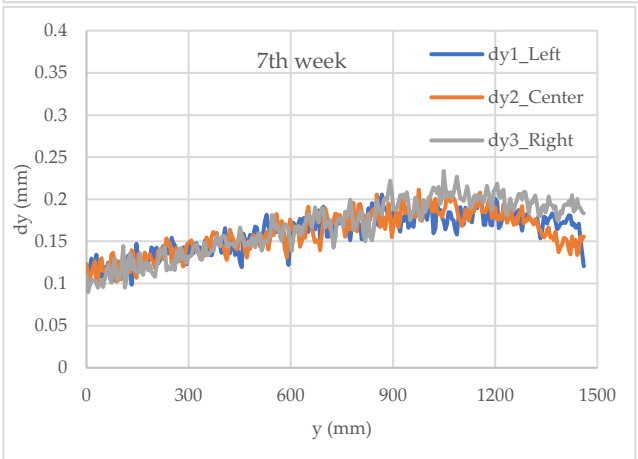

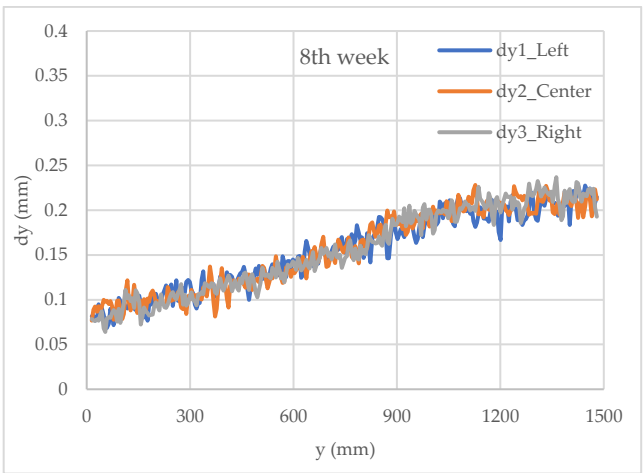

Annex 1

Article on Induced polarization technique applied in RE column while drying.

(Submitted to Engineering Geology Journal on Jan, 2023).

Imaging the water content of rammed earth materials with induced polarization

F. Abdulsamad (1), T. Chitimbo (1), A. Revil (2), N. Prime (1), and O. Plé (1)

(1) Université Savoie Mont-Blanc, CNRS, UMR CNRS 5271, LOCIE, 73370 Le Bourget du Lac, France

(2) Univ. Grenoble Alpes, Univ. Savoie Mont-Blanc, CNRS, UMR CNRS 5204, EDYTEM, 73370 Le Bourget du Lac, France

Short title: Water content in rammed earth element

Key-words: Rammed earth, time-domain induced polarization; chargeability; water content; capillary rise; diagnostic;

Emails: olivier.ple@univ-smb.fr; feras.abdulsamad@univ-smb.fr; andre.revil@univ-smb.fr; noemie.prime@univ-smb.fr; taini.chitimbo@univ-smb.fr;

Corresponding author: André Revil, andre.revil@univ-smb.fr

Abstract. Rammed earth is a traditional building material characterized by a low environmental impact. The variation of the moisture content of rammed earth can affect its mechanical properties. Therefore, the non-intrusive evaluation of the water content and its distribution inside rammed earth structures is of high interest to anticipate the risk of failure. A non-destructive geophysical method called induced polarization is used to evaluate its sensitivity to the water content distribution. Induced polarization properties are first connected to the water content and the cation exchange capacity using a petrophysical model. Induced polarization measurements are first performed on small cylindrical core samples of rammed earth in order to test the model. Then, the petrophysical model is used to estimate the water content in 3 cylindrical samples undergoing capillarity rise tests at 3 distinct heights. The data show the increase of the in-phase and quadrature conductivities as a result of capillary water rise over time. Finally, the sample was cut and its water content was determined by gravity and compared to that estimated from induced polarization measurements. A good correlation between the two estimates of the water contents was observed. In the second part of this study, induced polarization is used to image the water content distribution and its evolution over time in a rammed earth structural element. The monitoring is done for a period of 25 days strating from saturated conditions. We assess the evolution of the 3D distribution of the water content and we demonstrate that the geophysical results are in agreement with data from a Time Domain Reflectometry (TDR) probe. Such a probe provides a local measurement of the water content thanks to the measurement of the dielectric constant of the material.

1. Introduction

In order to mitigate climate change effects, humanity must decrease greenhouse gas emissions. In this spirit, the building industry is known to have a strong environmental impact and finding alternative construction materials is therefore a serious issue (Formoso et al., 2000). Rammed earth materials are sandy-clayey materials characterized by a moderate amount of clays (Walker et al., 2005). Raw earth materials have been broadly used for construction all around the world and over the history of mankind (Niroumand et al., 2013).

These materials are locally produced reducing the cost related to transport and therefore the environmental impact of the technique (Morel et al., 2001). It does not require any burning process during its manufacturing (Morella et al., 2001). The use of ecologic materials like rammed earth materials for construction is considered as an important challenge for the next decades (Hall and Allinson, 2009; Taylor and Luther, 2004). In addition, rammed earth materials are known for their durability (Bui et al., 2009, Hall, 2007). Other benefits of this construction material include (i) the ability to keep relative humidity and temperature pretty constant in the buildings (Hall, 2007), (ii) its energy consumption is lower in comparison to other construction materials (Taylor and Luther, 2004) and (iii) it is characterized by a significant durability (Bui et al., 2009). A detailed presentation of earth materials suitable for construction can be found in Walker et al. (2005). Among construction techniques with raw earth, one consists to compact successive layers of blocks using a mass water content w lower than the plastic limit of the material. This is why several studies have been recently performed to study the hydromechanical characteristics of rammed earth materials (Chauhan et al. 2019; Champiré et al. 2016).

Despite all these advantages, the use of rammed earth materials is scarce especially because their mechanical properties are highly influenced by hydric conditions. The increase of the water content in rammed earth structures decreases dramatically its mechanical strength and can lead to the collapse of the structure when a threshold in water content is reached. Estimation and evaluation of the water content and its distribution inside the rammed earth walls have a huge interest to anticipate risks and possibly to heal the structure before getting to the failure point. Hygrometers and relative humidity sensors are commonly used to get reliable information regarding the relative humidity. TDR (Time Domain Reflectometry) sensors provide intrusive and local measurements of the volumetric water content with quite a high accuracy (about ±2%, see Gong et al., 2003). That said, only the information at the position of the sensor is recorded and the presence of the sensor itself may perturb the measurement. A non-intrusive and non-destructive method able to image the water content would be therefore welcome.

In Abdulsamad et al. (2019), we proposed a geophysical method called induced polarization for imaging the water content distribution of rammed earth materials in a non-destructive way. Time-domain induced polarization method is based on the measurement of the electrical conductivity and normalized chargeability of a porous medium (Gazoty et al., 2012; Soueid Ahmed et al., 2020). The electrical conductivity describes the ability of a rock to conduct an electrical current, while the normalized chargeability describes the ability of a porous material to store reversibly electric charges under the action of an external (primary) electrical field (Vinegar and Waxman, 1984). These measured electrical properties can be connected to the density of the material, its clay content or cation exchange capacity, and its volumetric water content θ (Vinegar and Waxman, 1984; Revil, 2013a, b).

In the present study, we use induced polarization method to investigate its specific sensitivity to the water content of rammed earth samples. Induced polarization characterizes the ability of a material to store reversibly electrical charges through a petrophysical quantity called normalized chargeability (Kemna et al. 2012; Ghorbani et al. 2018; Revil et al. 2017; Tartrat et al., 2019). In Spectral Induced Polarization (SIP), we used a low-frequency electrical field (the frequency lies in the range 1 mHz to 10 kHz) and the resulting electrical current is measured as well as the phase lag between the two. The amplitude ratio and the phase are used to define a complex conductivity with an in-phase (real) component characterizing conduction and a quadrature (imaginary) component characterizing charge storage. A petrophysical model called the Dynamic Stern model was developed to connect the complex conductivity spectra to salinity, temperature, cation exchange capacity, and water content (Revil, 2013a, b). We can also use Time Domain Induced Polarization (TDIP) to investigate the material response.

In the present paper, we first perform SIP experiments on small rammed earth cylindrical samples to characterize the induced polarization properties of the material at different saturations. Then, the method is applied to follow the evolution of the water content associated with capillarity rise in cylindrical core samples and check the estimates of the water content with independent measurements. Finally, we monitor the drying of a rammed earth structure (45×15×15 cm in size) made of non-sieved rammed earth. This is made possible thanks to 3D TDIP

tomography. The water content distribution obtained by tomography is compared to a local measurement of the water content obtained using a Time Domain Reflectometry (TDR) probe.

2. Petrophysical model

2.1. Spectral Induced Polarization (SIP)

We summarize here the so-called dynamic Stern layer model used to represent the complex conductivity σ^* of a porous material. In spectral induced polarization, a sinusoidal current is injected between two (current) electrodes A and B and the potential difference measured between two voltage electrodes M and N. The voltage difference divided by the distance between M and N represents the component of the electrical field in the MN direction. The phase denotes the phase lag between the electrical current and the electrical field. The amplitude $|\sigma|$ (in S/m) and the phase φ (in rad) are used to define a complex conductivity σ^* according to Ohm's law

$$\mathbf{J}(\omega) = \sigma^*(\omega)\mathbf{E}(\omega), \tag{1}$$

$$\sigma^*(\omega) = |\sigma|e^{i\varphi} = \sigma'(\omega) + i\sigma''(\omega), \tag{2}$$

where **J** and **E** denote the current density and electrical field, respectively; i denotes the pure imaginary number ($i^2 = -1$), σ' denotes the in-phase component (in S m^{-1}), σ'' denotes the quadrature conductivity, and $\omega = 2\pi f$ denotes the pulsation frequency. Figure 1 describes the mechanisms of conduction and polarization associated with a clay particle in a rammed earth.

In order to interpret complex conductivity spectra in a metal-free partially-saturated porous material, a petrophysical model called the dynamic Stern layer model is used below (see details in Revil, 2013a, b, Revil et al., 2017, see also Figures 1b, c). When an harmonic electric field $\mathbf{E} = \mathbf{E}_0 \exp(+i\omega t)$ (t refers to time) is applied to a porous material, the complex conductivity of the porous material can be written as (Revil, 2013a, b; Revil et al., 2017).

$$\sigma^*(\omega) = \sigma_\infty - M_n \int_0^\infty \frac{h(\tau)}{1-(i\omega\tau)^{1/2}} d\tau, \tag{3}$$

$$\sigma_\infty = \frac{s_w^{\,n}}{F}\sigma_w + \frac{s_w^{\,p}}{F\phi}\rho_g B\,\mathrm{CEC}, \tag{4}$$

$$\sigma_0 = \frac{s_w^{\,n}}{F}\sigma_w + \frac{s_w^{\,p}}{F\phi}\rho_g (B-\lambda)\mathrm{CEC}, \tag{5}$$

$$M_n \equiv \sigma_\infty - \sigma_0 = \frac{s_w^{\,p}}{F\phi}\rho_g \lambda\,\mathrm{CEC}, \tag{6}$$

where $p = n$-1 (Revil et al., 2017), τ is a relaxation time (in s), $h(\tau)$ denotes the (normalized) probability density associated with the distribution of the time constants of the material (in turn related to its distribution of polarization length scales), σ_w (in S m^{-1}) denotes the conductivity of water, s_w, the saturation degree, ϕ, the porosity, F, the formation factor ($F = \phi^{-m}$, according to Archie's law, with m, the first Archie exponent, Archie, 1942), σ_∞ (S m^{-1}), the instantaneous conductivity of the soil while the real-valued term σ_0 (S m^{-1}) corresponds to its DC (Direct Current) conductivity (see Figure 1), M_n the normalized chargeability (S m^{-1}), equal to the difference between the instantaneous conductivity and the DC conductivity $M_n \equiv \sigma_\infty - \sigma_0$, $M = M_n / \sigma_\infty$ (dimensionless, see Cole and Cole, 1941), the chargeability, ρ_g is the grain density (in kg m^{-3}), CEC is the cation exchange capacity of the soil expressed in C kg^{-1} or in meq/100 g (1 meq/100 g = 963.20 C kg^{-1} in SI units), B (in m^{2}s^{-1}V^{-1}), the apparent mobility of the counterions for surface conduction (associated with the in-phase conductivity), and λ (in m^{2}s^{-1}V^{-1}), the apparent mobility of the counterions for the polarization associated with the quadrature conductivity (see Vinegar and Waxman, 1984; Revil et al., 2017a). The last term of Equation (4) corresponds to the

(instantaneous) surface conductivity, which at partial saturation is given by $\sigma_s = s_w^{n-1}\rho_g B\mathrm{CEC}/F\phi$ and at full saturation by $\sigma_S = \rho_g B\mathrm{CEC}/F\phi$. A dimensionless number R was introduced by Revil et al. (2017a, b, c) as $\mathbf{R} = \lambda / \boldsymbol{B}$. From Ghorbani et al. (2018), we have B(Na$^+$, 25°C) =3.1±0.3×10^{-9} m^{2}s^{-1}V^{-1} and λ(Na$^+$, 25°C) =3.0±0.7×10^{-10} m^{2}s^{-1}V^{-1}, and $R \approx 0.10\pm0.02$. The quantity B and λ have roughly the same temperature dependence (Vinegar and Waxman, 1984; Revil et al., 2017. Since we are working in isothermal conditions, here, this temperature dependence is not required here. The volumetric water content θ is also given by $\theta = s_w\phi$.

When the distribution of relaxation times is broad, then we can used another approximation called the constant phase model to interpret the real and imaginary components of the conductivity. This happens when the grain size distribution is broad and therefore the distribution of the relaxation times is also broad. This is quite typical of soils often associated with a self-affine structure and very broad grain size distributions. In this case, the associated complex conductivity spectra are rather flat (Vinegar and Waxman, 1984; Revil et al. 2017). In this case, we can approximate the in-phase conductivity by equation (4) whatever the value of the frequency. Regarding the quadrature conductivity, we consider that the quadrature conductivity at the geometric mean frequency of two frequencies f_1 and f_2 and the normalized chargeability defined as the difference between the in-phase conductivity at the frequency f_2 ($> f_1$) and the in-phase conductivity at the lower frequency f_1, are related each other by (Van Voorhis et al., 1973; Revil et al., 2017a)

$$\sigma''\left(\sqrt{f_1 f_2}\right) \approx -\frac{M_n(f_1, f_2)}{\alpha}, \tag{7}$$

$$\alpha \approx \frac{2}{\pi}\ln A, \tag{8}$$

and A denotes the number of decades between f_1 and f_2 (e.g., for 3 decades, $A = 10^3$ and $\alpha \approx 4.4$). Equations (7) and (8) provide the relationship between the quadrature conductivity and the CEC when combined with equation (6). Equation (7) is exact for the constant phase model and a reasonable approximation for the Cole Cole model whatever the value of c. At saturation (s_w=1) and assuming the conductivity of the pore water is known, equations (4) and (6) have one unknown parameter F (the formation factor). A measurement of electrical conductivity and chargeability of a saturated sample could be enough to get information about F.

From equations (4) and (6), we can also write directly a relationship between the instantaneous conductivity and the normalized chargeability as:

$$\sigma_\infty = \frac{s_w^{\ n}}{F}\sigma_w + \frac{M_n}{R}. \tag{9}$$

From previous studies (e.g., Ghorbani et al. 2018), we have B (Na$^+$, 25°C) =3.1±0.3×10^{-9} m^{-2}s^{-1}V^{-1}, λ (Na$^+$, 25°C) =3.0±0.7×10^{-10} m^{-2}s^{-1}V^{-1}, and R is typically around 0.10±0.01.

2.2. Time-Domain Induced Polarization (TDIP)

In time-domain induced polarization (TDIP), the primary and secondary voltages are measured at a set of bipoles M and N (voltage electrodes) during and after the injection/retrieval of an electrical current at a bipole A and B (current electrodes) (see Figure 1). The secondary voltage decay (obtained after shutting down the primary current) is sampled and integrated over a series of 10 windows to provide so-called partial chargeabilities M_i (expressed in ms). These partial chargeabilities are obtained by integrating the secondary voltage decay between two times t_i and t_{i+1} (t = 0 s corresponds to the time of the shutdown of the primary current, see Figure 1) according to:

$$M_i = \frac{1}{\psi_0}\int_{t_i}^{t_{i+1}} \psi(t)dt, \tag{10}$$

where y(t) denotes the secondary voltage measured between the electrode pair MN, ψ_0 denote the potential difference between the electrodes M and N just before the shutdown of the primary current (Figure 1), and $W_i = t_{i+1} - t_i$ indicates the duration of the time window (typically 100 ms).

Two tomograms can be obtained using TDIP data. An electrical conductivity (in S m^{-1}) tomogram and a chargeability (dimensionless) tomogram. For each cell of the tomogram, the multiplication of the electrical conductivity σ by the chargeability M provides the so-called normalized chargeability described in Section 2.1.

In the second part of this paper, we will investigate the drying of a rammed earth element. In the situation corresponding to drying a rammed earth structure from saturation, the salt is remaining segregated in the liquid pore water phase during drying. Consequently, the conductivity of the pore water is inversely proportional to the saturation itself when the sample is initially fylly water-saturated (i.e., the following transform should be used $\sigma_w \to \sigma_w / s_w$). Therefore in the case of drying, equations (4) and (6) should be written as:

$$\sigma_\infty = \frac{s_w^{n-1}}{F\phi}\left(\phi\sigma_w + \rho_g B\,\mathrm{CEC}\right), \tag{11}$$

$$M_n = \frac{s_w^{n-1}}{F\phi}\rho_g \lambda\,\mathrm{CEC}\,. \tag{12}$$

From equations (11) and (12), we can also write the conductivity and the normalized chargeability as,

$$\sigma_\infty(s_w) = s_w^{n-1}\sigma_\infty(s_w = 1)\,, \tag{13}$$

$$M_n(s_w) = s_w^{n-1}M_n(s_w = 1)\,, \tag{14}$$

and therefore the logarithm of the conductivity and normalized chargeability depends linearly on the log of the saturation. These expressions will be used in this paper to characterize how the conductivity and the normalized chargeability evolve with the degree of saturation of the rammed earth.

3. Method and materials

We used a soil from a site called St Quentin Fallavier located in The Auvergne-Rhone-Alpes region (France). This soil was used in the construction of an office building in France (Orangery building in Lyon) and for few houses around. We first characterize this soil in section 3.1 below. SIP measurements are described in Section 3.2.

3.1. Soil characterization and sample preparation:

The soil used in this study was first sieved at 5 mm to avoid the presence of large heterogeneities (gravels and peebles) in the core samples used for the measurements. The averaged grain size distribution curve of the core samples and the water saturation versus the relative humidity curve are shown in Figure 2. The analysis of the particle size distribution of the soil shows that the material contains about 50% gravels, 50% sand, 20% silt, and clay <15% (weight. fraction). To determine the optimum water content (i.e., the water content that insures getting the maximum dry density of the compacted material), a proctor test was performed. The optimum water content (in weight (g/g) was found to be about w = 10.7% for a static compaction at 5 MPa. The maximum dry density reached is 1990 kg m^{-3} (porosity $\phi \approx 0.24$ using a grain density ρ_g = 2650 kg m^{-3}).

A total of 20 samples of rammed earth materials were prepared under the same conditions with the same soil to obtain roughly the same porosity. Once prepared, the samples were placed in an air-tight container for moisture homogenization. Then, the partially saturated material was put in a cylindrical mold of 5 cm diameter and 10 cm height. Later, the mold was subjected to a compaction pressure (5 MPa). In order to get homogeneous density in the samples, 80% of the total compaction pressure, i.e., 4 MPa was applied gradually from one side, and then 100% of the total compaction pressure, i.e., 5 MPa was applied from both sides (a complete description of this double compaction method is described by Bruno et al., 2015, and Chauhan et al., 2019). The cation exchange capacity (CEC) of the material was measured with the cobalthexamine method (see Aran et al. 2008; Ciesielski and Sterckeman 1997). We obtain CEC = 9.2±0.4 meq/100 g.

3.2. Spectral Induced Polarization measurements

Two kinds of experiences were carried out on the cylindrical samples of rammed earth. The first experience aims petrophysical characterizing of the samples to evaluate the necessary parameters for water content estimation (i.e., the petrophysical parameters are F, m and n). The second experience consists of SIP measurements during capillary rise experiments.

Frequency-domain induced polarization measurements were performed over the frequency range 100 mHz - 45 kHz using the ZELSIP04-V02 impedance meter built by Egon Zimermann (Zimmermann et al., 2008, see Figure 3). The electrical current was injected between two electrodes (A and B), while the electrical potential was measured between two other electrodes (M and N). Medical electrodes of type carbone film was used for current injection and medical Ag/AgCl electrodes where used to measure the potential difference. The conversion of the measured impedance into the complex conductivity was performed using a geometric factor K (m^{-1}) depending on the position of the electrodes. The geometric factor was estimated by numerical modelling using the software COMSOL Multiphysics (see Jougnot et al., 2010, for details).

In order to get information about the formation factor, the porosity exponent and the saturation exponent, 6 cylindrical samples were saturated with pore water solution of different salinities. Figure 4 shows the dependency of the in-phase conductivity (at 1 Hz) versus the pore water conductivity. After fitting the data with equation (4), we get the values of parameters reported in Table 1 including the formation factor, and the surface conductivity $\sigma_S = \rho_g B \mathrm{CEC}/F\phi$. In Table 1, we also reported the porosity and CEC determined above and make a comparison with the properties of another soils used for construction (Sample ABD20, Table 1). We can easily check if the surface conductivity determined from the conductivity measurements at different salinities is consistent with the estimate obtained from the CEC. Using $\sigma_S = \rho_g B \mathrm{CEC}/F\phi$ with CEC = 9.2 meq/100 g, F = 14 (Figure 4), $\phi \approx$ 0.24 (see above Section 3.1), ρ_g = 2650 kg m^{-3}, m = 2.0, and B(Na^+, 25°C) =3.1±0.3×10^{-9} $m^2s^{-1}V^{-1}$, we obtain a surface conductivity of σ_S = 0.021 S m^{-1}, which can be compared to the value estimated in Figure 4, σ_S = 0.018 S m^{-1}. The agreement shows consistency between the predictions of the pretrophysical model and the laboratory data.

Another group of samples was confined in different relative humidities in humidity chambers. We use saturated solutions of different salts to control the relative humidity in the chambers. After about two months, the mass of samples was stabilized, and the water saturation of each sample could be calculated by a measurement of its weight. SIP measurements of those samples were carried out. Figure 5 shows the dependency of the in-phase and quadrature conductivities versus the saturation. We could notice a clear linear log-log relationship between the saturation and both the in-phase and quadrature conductivities (here reported at 1 Hz). The fitting of these data with equation (6) and (7) gives the second exponent of Archie's law (saturation exponent) n reported in Table 1. The high value of n (≅3.4 ±0.1) indicates disconnected pores possibly associated with the percentage of clays (15 vol.%) forming patches in the medium. We note that the value of $p = n-1 = 2.4$ is consistent with the exponent obtained in the plot (p = 2.3, Figure 5). Again the petrophysical model is consistent with the estimates. If we place the in-phase conductivity value at saturation in Figure 4, this implies that the pore water conductivity for the partially saturated samples is around 2 S m^{-1} (25°C). In turn, according to Figure 4, this justifies that the in-phase conductivity data are dominated by their bulk contribution.

3.4. Capillary rise experiment

SIP measurements during a capillary rise were carried out for 3 samples, named in what follows Sample 1, Sample 2 and Sample 3. A sandbox of dimension 22×30 cm and 5 cm in height, was filled by saturated sand of grain size varies between 100-200 µm. A capillary bench was created (Figure 3c), where the water level is at 1.5 cm under the sand surface, and the capillarity insures the saturation of sand upper the water level. The sandbox was connected to water reservoir for maintain the same water level in the sandbox. The rammed earth samples were put directly on the sand during the capillary rise. SIP measurements were carried out over the time at three levels of the sample (2.3, 5.3 and 8.3 cm from the base of the sample). At each level, the four electrodes (2 electrodes for current injection and 2 electrodes for measuring the potential difference, Figure 3c) were distributed radially around the sample at each level with 90° in between.

3.5. Results and interpretation

Figure 6 shows the variation of sample 1 weight during the capillary rise because of water suction and the advancement of wetting level over time. We could notice that the velocity of the wetting level is high (the slope is high) at the beginning of the experiment. The wetting head gets 4 cm in the first few hours (about 4 hours). Later, the velocity decreases (the slope is less than in the first part of the curve) and it continues linearly until the top of the sample after about 24h from the beginning of the experience.

Figure 7 show a series of spectral induced polarization spectra (in-phase and quadrature conductivities) in the frequency range 1 Hertz-10 kHz and taken over time at one level (Level 1) and for Sample 2. Similar data were obtained for the other levels and the two other samples.

Figures 8, 9, and 10 show the evolution of the in-phase conductivity (at 1 Hz) over the duration of the three capillary rise experiments. At the start of the experiment (t = 0 h), in-phase conductivities of the three levels are almost the same value, about 10^{-4} S m^{-1} for Sample 1, 10^{-3} S m^{-1} for Sample 2. No value were recorded for Sample 3. This initial difference could be explained by the ambient relative humidity controlling the hydric state of the earth by liquid-vapour equilibrium. The relative humidity curve shown in Figure 2b explains this observation. Indeed, the relative humidity of the room was recorded, and it was higher for Sample 2 (60-70%) than for Sample 3 (30-40%, see Figure 2b for the implication in terms of water saturation).

After the capillary rise starts, a quick elevation of in-phase-conductivity of first level (at 2.3 cm) occurs (before 2-3 hours), followed by the elevation of level 2 conductivity (5-6 hours), and finally by level 3 (between 10 and 20 hours). This increase corresponds to the wetting head rising which modifies the water content close to the measurements level. As the wetting head advance upward in the sample, the in-phase conductivity increases for each level, to get a stable value few hours after arriving the wetting head. By the end of the experience, all levels have almost the same value of in-phase conductivity, (1.0±0.2) ×10^{-4} S m^{-1}, and the sample is close to saturation. We could notice that the capillary rise is so fast at the beginning and the whole capillary rise test takes about 24 hours (the wetting head gets the top of the sample). In order to slow down the phenomena, the capillary rise is stopped during the time of measurements, we carried out the SIP measurements out of the sandbox (Samples 2 and 3, not for Sample 1).

Figures 8, 9, and 10 show the evolution of quadrature conductivity for the 3 samples during the capillary rise test. The same trend as that noticed for in-phase conductivity is visible. The quadrature conductivity increases over the development of the wetting head. At the end of the capillarity rise, we get almost the same level for the in-phase conductivity and the quadrature conductivity for all tested samples. From Figures 8, 9, and 10, it is clear that we have three phases, dry one at start, saturated at the end and transition phase in between.

At the end of capillary test, Samples 2 and 3 were cut off into three pieces (at the middle between the levels of SIP measurements). The water content in each piece was later measured by drying in oven at 100°C during 48 h. By using equation (6) and after replacing the values of all calculated and measured petrophysical parameters (Table 1) and the constants ρ_g (2650 kg m^{-3}) and λ(3.0×10^{-10} (m^{-2}s^{-1}V^{-1})), the water content could be estimated from SIP measurements. Figure 11 shows a comparison between the water content estimated from SIP measurements and the measured water content by weighting ($\theta = w\,\frac{\rho_{dry}}{\rho_w}$, where ρ_w is the density of water and w denotes the gravimetric water content). The correlation is good (less than 2% of θ) at low water contents. At high water content (saturation >0.85) the precision slightly decreases. The heterogeneity and local variations in porosity, cation exchange capacity or grain density could be responsible of the divergence at high saturation level.

Using the same approach as that used in Figure 11, it is possible to follow the increase of water saturation (or volumetric water content) over the time at each level (Figure 12). Additional studies should be conducted to evaluate the effect of clay percentage and clay type (CEC) on the results.

4. Application to a rammed earth structural element

4.1. Preparation of the rammed earth element

The material used in this section is the soil coming from a village of St Quentin Fallavier located in Auvergne-Rhone-Alpes region in Southeastern part of France and we will use here the method of time-domain induced polarization described in Figure 13 and section 2.2 above. This soil was used for the construction of different buildings. The particle size distribution was estimated using wet sieving and hydrometer analysis according to French standards (NF P 94-057) (French Standard NF P 94-057, 1992). In this study, soil sieved at 20 mm was used to make samples free of gravels. The particle size distribution curve of this soil is represented on Figure 14. The soil contains about 10% clay, 12% silt, 33% sand and 45% gravel (vol.%). An optimum mass water content of w=0.10 was obtained from a modified proctor test to obtain the plastic limit of the material. This optimum water content provides the highest dry density (2060 kg/m^3) for a fixed compaction energy.

Four prismatic samples were manufactured using the dynamic compaction method. Three samples were made with the following dimensions 15×15×45 cm. they are labeled S1, S2, and S3. A fourth sample with a size of 15×15×8 cm (S4) was prepared with an optimum water content, corresponding to normal proctor test, of w=0.10 and stored in a covered container for 1 day before the fabrication to assure the homogenization of the water content. Then, these four samples were dynamically compacted in a metal mold having a base of 15x15 cm. The rammed earth is compacted layer after layer: a mass of earth is poured loosely into the mold and rammed by a pneumatic hammer, which gives a layer of 7 to 8 cm of thickness. Samples S1, S2 and S3 were made with 6 layers with a final size of 15×15×H=45 cm. Sample S4 was made with a single layer of 8 cm. The four samples have an average dry density of 1884±32 kg m^{-3} (mean porosity of 29±2%) with a standard deviation of 1,75% which lies in the range of dry density for earthen structure 1700 kg m^{-3} to 2200 kg m^{-3} (Hall and Djerbib, 2004). The dry density of S1 is equal to 1840 kg m^{-3}. This gives (considering a grain density of 2650 kg m^{-3}) a porosity of 30% (ϕ=0.30).

Sample S1 is dedicated to geophysical investigation, as well as an independent measurement of the volumetric water content θ using a TDR probe (Figure 15). This local measurement is obtained for all the four times of investigation (0, 5, 13, and 25 days). Samples S2 and S3 are reference samples, dedicated to the survey of mass evolution with time. These experiments are more difficult to obtain on the instrumented sample S1. Sample S4 is used to investigate the petrophysical behavior of the porous medium at saturation and get a first idea of the formation factor (see Figure 16).

The petrophysical parameters of the samples are evaluated for the whole volume using the following equations: $\theta = \phi s_w = V_w / V_t = w\rho_{dry} / \rho_w$, $\rho_{dry} = (1-\phi)\rho_g$, and w = mass of water / mass of solid, where v_w, v_t , w are the volume of water, the total volume and the water content in weight fraction, respectively; ρ_w and ρ_{dry} denotes the density of water (1000 kg m^{-3}) and the dry density of the sample (kg m^{-3}), respectively. For S1, the volumetric water content (θ) once manufactured is equal to 18.4 %. For this sample, a measurement of the volumetric water content was also performed by using a TDR probe (Figure 15). The petrophysical parameters of the sample are reported in Table 2.

The rammed earth samples S1, S2, S3 were covered with Plexiglass on two opposite sides and on top, and a wooden impermeable surface at the bottom (Figure 15). This was done to constrain the drying of samples in the y-direction. Thin holes were let accessible on the side of the sample S1, at y =7,5 cm under the two drying surfaces, in order to have access for TDR (Time Domain Reflectometry) measures of volumetric water content θ at the core of the earth pile. The Plexiglas covering for short intervals of time was removed for the measurements for a short time (Figure 15c). The probe used in this study is a TRIME-PICO-32 TDR probe, which provides a measurement of the volumetric water content with accuracy of ±2% in the entire volumetric water content range (0 to 100%). The precision of the device was first tested by measurements on saturated sands and compacted soils of known volumetric water content.

The weights of samples S2 and S3 were daily recorded and introduced as a variation in water content w over the time (S1 was only weighted at the initial and final time). Electrical conductivity and chargeability were acquired during drying of rammed earth block S1, by using an ABEM Terrameter SAS-4000 resistivity meter. The box current has a box mode (+ I, 0, −I, 0) with a period T of 4s. The maximum injected current is I = 5 mA. A total of 10 partial chargeabilities were measured during the decay of the secondary voltages (T_{off} =1 s), after a dead time of 20 ms (i.e., 10 windows). Non-polarizable Ag/AgCl electrodes were used for the current injection and potential

measurement. 2 profiles of 32 electrodes were setup on the structure (15x2 electrodes on each open side, and 2x2 electrodes on the top of the block). The distance between electrodes is 3 cm and between profiles is 9 cm (see Figure 16a). At a given time, a set of data provides about 350 measurements of apparent chargeability and apparent resistivity. Figure 16b shows an example of the decay curves measured by two quadrupoles of electrodes (ABMN) at different times.

The electrical measurements were carried out at four distinct times during the drying process: first measurements were performed at time t_0=0, just at the manufacture, then at t1 = 5 days, t2 = 13 days, and t3 = 25 days. TDR measures were made at the same times. The apparent chargeabilities corresponding to the first window (M_1 (mV/V)) and the apparent resistivity were used in the inversion process. The ResIPY software (Blanchy et al., 2020) was used for the inversion of the recorded data. As the chargeability is proportional to the phase angle (Mwakanyamale et al., 2012), it was transformed before inversion to phase angle (φ in mrad): $\varphi = \alpha M_1$, and $\alpha \approx -1$). The results of inversion process are the distribution of conductivity (σ S/m) and distribution of chargeability (M, in V/V) in the block. From these two parameters (σ and M), the normalized chargeability M_n = σ M has been calculated. Then the diagram we used to integrate the petrophysical and geophysical data to get time lapse tomograms of the water content is shown in Figure 17.

In order to use equations 11 and 12 to evaluate the water saturation, the formation factor F(-) and the saturation exponent (n) need to be estimated. To do so, the same TDIP measurement was performed on sample S4, which was saturated by vacuum aspersion a saturated layer at three levels (2, 4 and 6 cm) from the bottom (Figure 16c). The electrical conductivity at saturation is 0.014±0.001 S m^{-1} and the formation factor is therefore 2.5∼3. The mean value of the formation factor will be used in equations (11) and (12) to calculate the saturation.

To evaluate the saturation exponent n, the in phase conductivity was extracted from the inversion results at the level of TDR (at z=20 cm height, Figure 15) and plotted versus the saturation (extracted from TDR measurement of water content) on Figure 18. The parameters used in equations (11) and (12) to calculate the water saturation from geoelectrical measurements are reported in Table 3.

4.2. Global drying kinetics and TDR measurements

Figure 19 shows the variation of weight of the sample (introduced here as a mass water content) over time. The water content curves for S1, S2, and S3 are consistent and we could notice on them two phases of drying. In the first phase, the drying is fast and the sample weight decrease linearly during approximately one week, which corresponds to a constant rate of evaporation (with regard to surface and time unit). In the second phase, the drying is slower and the rate of evaporation is decreasing.

TDR measurements on S1, provides the volumetric water contents at 0, 1, 5, 13 and 25 days which are equal to θ = 20%, 19,5%, 16.3%, 11% and 6.6% respectively. When θ is converted in mass water content w (accounting for a porosity of 30%, see above), it gives the curve presented in Figure 19. It is interesting to notice that this punctual value of w, measured at the core of the sample, evolve in the same way than the global water content, with an immediate adaptation of the hydric state, even at 7.5 cm depth from the drying surfaces.

4.3. Electrical measurements at initial time

Figure 20 results from the tomography reconstruction of electrical measurements at time 0, in 3D. A first observation is that, at time 0, the measures makes appear a variation of the conductivity and chargeability along the vertical direction. A contrast appears within the layers, with the top part of them having a value of σ_∞ globally between 0.01 and 0.03 S m^{-1}, and the bottom of them having a conductivity globally between 0.003 and 0.01 S m^{-1}. For the same nature of soil, and the same mass water content w, upper values of conductivity are linked with the saturation degree, which increases for a decrease of porosity. Indeed, it is known that the dynamical compacting could not impose a uniform dry density across and the earth layer rammed, and gives denser part at the top of each layers, and looser part at the bottom of them (Bui and Morel, 2009). At time 0, the saturation (s_w=water volume/pore volume) calculated from equations (11) and (12) and the measure, follows the dry density variation (thus porosity variation). An estimation of porosity is important to evaluate correctly the volumetric water content (Figure 17). We can also write a relationship between dry density and saturation as $\rho_{dry} = \rho_s \rho_w / \left[\rho_w + \rho_s w / s_w\right]$.

The distribution of saturation at time 0 was calculated using equatios (11) and (12), and used to evaluate the dry density and later the porosity. Figure 21 shows the variation of dry density and porosity with height at two

different points (x, y). First of all, the calculated dry density varies between 1750-2100 kg m^{-3} which is in the range of RE material (1700-2200 kg m^{-3}, see Hall and. Djerbib, 2004). Bui and Morel (2009) reported experimental evolution of the dry density in the upper part of RE layer (1980 kg m^{-3}) and in the lower part (1820 kg m^{-3}). The mean of dry density calculated is 1890 kg m^{-3} and the porosity is 28.4% (very close to the mean value estimated from weight of the sample and reported in Table 2).

4.4. Evolution of resistivity, chargeability and water content θ

From Figure 22, we could notice the electrical conductivity decreases with drying (loss of water content). At a global scale, we observe that the decrease is faster in the top part of the block. The normalized chargeability has the same trend as the electrical conductivity. Besides, only a small variation of chargeability during drying could be noticed (Figure 23) in correlation with the prediction of the dynamic Stern layer model developed in Revil (2013a, b). The volumetric water content ($\theta = \phi s_w$) was estimated using the water saturation calculated from the TDIP measurements and the estimated porosity curves. Figure 24 shows the distribution of water content (θ(-)) from 3D inversion inside sample S1, and Figure 25 presents the graph of θ vertical profiles for point (x=5 cm ; y=12 cm).

After 5 days of drying, the upper part of the block looks dried more than the lower part (Figures 23 and 24). Up to this time, it seems that loss of water content is not intenser at the drying surface than in the core sample (Figure 24). This is consistent with the observation made on w evolution, similar for the whole sample than for a point at 7.5 cm depth. This means that the water evaporation is not limited by the internal water transfer inside the porous material during this period. In the same time period, the influence of the layer porosity gradient is very important, as shown in Figure 25: the looser part of the block (at the base of the compacted layers) is losing more water by volume unit than the denser part of the block (at the top of each layer). After 13 days of drying, this effect starts to be less visible. After 25 days the block is almost dry with water content θ less than 7% ($w \approx 0.035$ g/g).

Finally, the water content at the level of TDR probe at position (y, z) = (7.5, 2 cm) was extracted at different points for x=3 to x=12 cm with TDIP. The mean values of the water content estimated from TDIP data is plotted versus the water content measured with TDR probe (Figure 26). A very good correlation could be noticed between both measurements.

5. Conclusion

Iin the first part of this paper, we perform frequency-domain induced polarization measurements of cylindrical core samples of rammed earth were used to evaluate the volumetric water content in case of a capillary rise experiment. First, the petrophysical parameters of the samples were identified and later used in the Dynamic Stern Layer model to estimate the change in the volumetric water content. A good correlation between the estimated water content (from induced polarization) and measured water content (by weight) was noticed. At low water content the precision is high enough (less than 2%). The results are promising and the approach is applied on a representative volume of rammed earth material manufactured in laboratory with dimensions of tens of centimeters. This application is essential in the context of the structural diagnosis and rehabilitation of rammed earth-made buildings.

In the second part of the paper, time domain induced polarization measurements were carried out on a rammed earth block during drying in order to evaluate the distribution of water content inside the block. The results of induced polarization were compared with precise measurements of TDR probe. The distribution of water in the block over the time shows that the upper part dried faster (under the gravitational effect), while the variation of water content with depth (i.e., in the drying direction) are less pronounced in the first drying phase. On the contrary, the variation of density in each layer has a significant influent at the first drying phase, and then blurs after 13 days. The estimated water content has a good correlation with the punctual measurements of carried out by TDR probe. The results are promising and the approach will be applied at a large scale, i.e. on a real wall. However, in real case other information is still needed to properly asses the distribution of water content (e.g., the porosity, the formation factor). Measurements of porosity (e.g., ultrasound measurements) could be worth to complete the image of the structure.

Acknowledgement. This work is part of the ANR project VBATCH “Raw earth construction vulnerability regarding hydric conditions” funded by Agence National de la Recherche in France. We thank Egon Zimmerman for the construction of the ZEL-SIP04-V02 impedance meter used in this work.

References

Abdulsamad, F., Revil, A., Prime, N., Gnonnoue, P.Y., Schmutz, M., Plé, O., 2020. Complex conductivity of rammed earth, Engineering Geology 273, 105697. https://doi.org/10.1016/j.enggeo.2020.105697.

Abdulsamad F., Revil A., Soueid Ahmed A., Coperey A., Karaoulis M., Nicaise S., Peyras L., 2019. Induced polarization tomography applied to the detection and the monitoring of leaks in embankments. Engineering Geology 254, 89–101. https://doi.org/10.1016/j.enggeo.2019.04.001.

Aran, D., Maul, A., Masfaraud, J.-F., 2008. A spectrophotometric measurement of soil cation exchange capacity based on cobaltihexamine chloride absorbance. Comptes Rendus Geoscience 340(12), 865–871. https://doi.org/10.1016/j.crte.2008.07.015.

Archie, G. E., 1942. The electrical resistivity log as an aid in determining some reservoir characteristics. SPE-942054-G 146, 54–62. https://doi.org/10.2118/942054-G.

Blanchy, G., Saneiyan S., Boyd J., McLachlan P., Binley A., 2020. ResIPy, an intuitive open source software for complex geoelectrical inversion/modeling in 2D space. Computer & Geosciences 137, https://doi.org/10.1016/j.cageo.2020.104423.

Bui Q. B., Morel J. C., 2009. Assessing the anisotropy of rammed earth. Construction and Building Materials 23(9), 3005-3011. https://doi.org/10.1016/j.conbuildmat.2009.04.011.

Bui, Q. B., Morel, J. C., Reddy, B. V. V., Ghayad, W., 2009. Durability of rammed earth walls exposed for 20 years to natural weathering. Building and Environment 44, 912–919.

Champiré, F., Fabbri, A., Morel, J. C., Wong, H., McGregor, F., 2016. Impact of relative humidity on the mechanical behavior of compacted earth as a building material. Construction and Building Materials 110, 70–78. https://doi.org/10.1016/j.conbuildmat.2016.01.027.

Chauhan. P, El Hajjar. A, Prime. N, Plé. O,. 2019. Unsaturated behavior of rammed earth: Experimentation towards numerical modelling, Construction and Building Materials, 227, 116646. https://doi.org/10.1016/j.conbuildmat.2019.08.027.

Champiré, F., Fabbri A., Morel J. C., Wong H., McGregor F., 2016. Impact of relative humidity on the mechanical behavior of compacted earth as a building material. Constr. Build. Material 110, 70–78. https://doi.org/10.1016/j.conbuildmat.2016.01.027.

Ciesielski, H., Sterckeman, T., Santerne M. Willery J.P., 1997. Determination of cation exchange capacity and exchangeable cations in soils by means of cobalt hexamine trichloride. effects of experimental conditions. Agronomie 17 (1), 1-7. https://doi.org/10.1051/agro:19970101.

Cole, K. S., Cole R. H., 1941. Dispersion and absorption in dielectrics. Journal of Chemical Physics 9, 341–351. https://doi.org/10.1063/1.1750906.

Formoso C.T., L. Soibelman, C. De Cesare, and E. L. Isatto, 2002, Material waste in building industry: main causes and prevention. Journal of Construction Engineering and Management, Vol. 128, No. 4, 50 pp. ISSN 0733-9364/2002/4-316–325/8.001.

French Standard NF P 94-057, 1992. Soil: Investigation and Testing – Grain Size Analysis. Hydrometer Method., AFNOR.

Ghorbani, A., Revil, A., Coperey, A., Soueid Ahmed, A., Roque, S., Heap, M. J., et al., 2018. Complex conductivity of volcanic rocks and the geophysical mapping of alteration in volcanoes. Journal of Volcanology and Geothermal Research 357, 106–127. https://doi.org/10.1016/j.jvolgeores.2018.04.014.

Gong, Y., Cao Q., Sun Z., 2003. The effects of soil bulk density, clay content and temperature on soil water content measurement using time-domain reflectometry. Hydrological processes 17.18, 3601–3614.

Gazoty A., Fiandaca G., Pedersen J., Auken E., Christiansen A., 2012. Mapping of landfills using time-domain spectral induced polarization data: the Eskelund case study. Near Surface Geophysics, 10. https://doi.org/.3997/1873-0604.2012046.

Ghorbani A., Revil A., Coperey A., Soueid Ahmed A., Roque S., Heap M. J., et al., 2018. Complex conductivity of volcanic rocks and the geophysical mapping of alteration in volcanoes. Journal of Volcanology and Geothermal Research 357, 106–127. https://doi.org/10.1016/j.jvolgeores.2018.04.014.

Hall, M., 2007. Assessing the environmental performance of stabilised rammed earth walls using a climatic simulation chamber. Building and Environment 42, 139–145.

Hall M., Djerbib Y., 2004. Rammed earth sample production: context, recommendations and consistency. Construction and Building Materials 18.

Hall, M., Allinson, D., 2009. Analysis of the hygrothermal functional properties of stabilised rammed earth materials. Building and Environment 44, 1935-1942.

Houben, H. Guillard H., 1994. Earth Construction: A Comprehensive Guide. Intermediate Technology Publications, London.

Jougnot D., Ghorbani A., Revil A., Leroy P., Cosenza P., 2010. Spectral Induced Polarization of partially saturated clay-rocks: A mechanistic approach. Geophysical Journal International 180(1), 210-224. https://doi.org/10.1111/j.1365-246X.2009.04426.x.

Kemna, A., Binley A., Cassiani G., Niederleithinger E., Revil A., Slater L., Williams K.H., Flores Orozco A., Haegel F.-H., Hördt A., Kruschwitz S., Leroux V., Titov K., Zimmermann E., 2012. An overview of the spectral induced polarization method for near-surface applications. Near Surface Geophysics 10, 453-468. https://doi.org/10.3997/1873-0604.2012027.

Kruschwitz, S., 2002. Detection and characterization of the disturbed rock zone in claystone with complex valued geoelectrics. MSc Thesis, Technical University Berlin, Germany.

Morela, J.C. Mesbah, A. Oggero, M. Walker, P. 2001. Building houses with local materials:means to drastically reduce the environmental impact of construction. Building and Environment 36, 1119–1126.

Morela, J.C., Mesbah A., Oggero M., Walker P.., 2001. Building houses with local materials:means to drastically reduce the environmental impact of construction. Building and Environment, 36, 1119–1126.

Mwakanyamale, K., Slater L., Binley A., Ntarlagiannis D., 2012. Lithologic Imaging using induced polarization: Lessons learned from the Hanford 300 Area. Geophysics 77, 397-409.

Niroumand, H., Zain M.F.M, Jamil M., 2013. Assessing of critical parameters on earth architecture and earth buildings as a vernacular and sustainable architecture in various countries. Procedia - Social and Behavioral Sciences 89, 248 – 260, 1877-0428, https://doi.org/10.1016/j.sbspro.2013.08.843.

Revil, A., 2013a. On charge accumulation in heterogeneous porous rocks under the influence of an external electric field. Geophysics 78 (4): D271–291. https://doi.org/10.1190/geo2012-0503.1.

Revil, A., 2013b. Effective conductivity and permittivity of unsaturated porous materials in the frequency range 1mHz-1GHz. Water Resour. Res. 49, 306-327, https://doi.org/10.1029/2012WR012700.

Revil, A., Coperey, A., Shao, Z., Florsch, F., Fabricius, L. I., Deng, Y., Delsman, J. R., 2017. Complex conductivity of soils. Water Resources Research, 53 (8), 7121–47. https://doi.org/10.1002/2017WR020655.

Soueid Ahmed A., Revil A., Abdulsamad F., Steck B., Vergniault C., Guihard V., 2020. Induced polarization as a tool to non-intrusively characterize embankment hydraulic properties. Eng. Geol. 271, 105604. https://doi.org/10.1016/j.enggeo.2020.105604.

Tartrat Y. T., Revil A., Abdulsamad F., Ghorbani A., Jougnot D., Coperey A., Yven B., de la Vaissière R., 2019. Induced polarization response of porous media with metallic particles – Part 10. Influence of desiccation. Geophysics 84 (5), A43-W32. https://doi.org/10.1190/geo2019-0048.1.

Taylor P, Luther M.B.. 2004. Evaluating rammed earth walls: a case study. Solar Energy 76(1):79–84.

Vinegar, H., Waxman, M., 1984. Induced polarization of shaly sands. Geophysics 49 (8), 1267–87. https://doi.org/10.1190/1.1441755.

Walker P, Keable R, Martin J, Maniatidis V. 2005. Rammed earth – design and construction guidelines. BRE Bookshop..

Zimmermann, E., Kemna, A., Berwix, J., Glaas, W., Münch, H. M., Huisman, J. A., 2008. A high-accuracy impedance spectrometer for measuring sediments with low polarizability. Measurement Science and Technology 19 (10), 105603. https://doi.org/10.1088/0957-0233/19/10/105603.

Tables

Table 1. Petrophysical properties of the rammed earth used in the present study and comparison with the data obtained using the core sample (reference ABD20) used in the study of Abdulsamad et al. (2020). The parameters *m* and *n* are the porosity and saturation exponents in the First and second Archie's law, respectively. The CEC denotes the Cation Exchange Capacity and σ_S the surface conductivity.

Sample	ϕ (-)	F (-)	m (-)	n (-)	σ_S (S/m)	CEC (meq/100g)
This study	0.25	14.3	2.0	3.8	0.018	9.2
ABD20	0.26	9.1	1.8	2.1	0.031	2.6

Table 2. Petrophysical parameters of the samples used in this study.

Parameter	Water content w (g/g)	Bulk density ρ (kg/m^3)	Dry density ρ_{dry} (kg/m^3)	Mean Porosity ϕ (-)	Volumetric water content θ (-)	Volumetric water content from TDR θ (-)	Saturation s_w (-)
Value	0.10	2024.3	1840.3	0.30	0.18 - 0.19	0.20	0.66

Table 3: Parameters used in equation (11) and 512) to evaluate the water content. *F* denotes the intrinsic formation factor, $m > 1$ denotes the porosity exponent (also called the first Archie's exponent), *n* is called the saturation exponent (second Archie's exponent), *R* the ratio of the normalized chargeability by the instantaneous surface conductivity (a constant independent of temperature, saturation, and salinity), and σ_w the pore water electrical conductivity. The pore water conductivity is obtained from the conductivity curve at saturation and the value of the conductivity at full saturation (see Figure 18). The initial conductivity of the tap water used to saturate the rammed earth is σ_w = 0.035 S m^{-1} (25°C). The porosity exponent *m* is obtained from the formation factor and the porosity while the saturation exponent *n* is obtained from Figure 18.

Parameter	F (-)	m (-)	n (-)	R (-)	σ_w(S/m^{-1})
Value	27.5	2.80	2.65	0.10	0.35

Figures

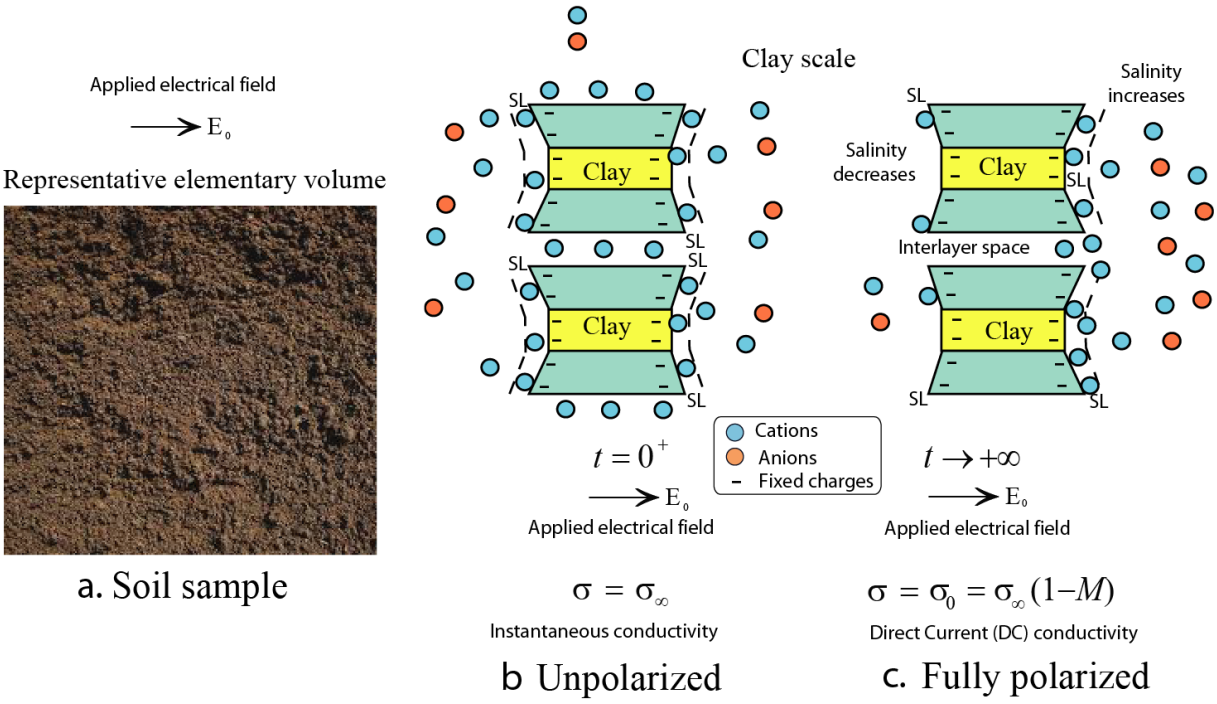

Figure 1. Polarization of a raw earth elementary volume under the action of an external (applied electrical field) $\mathbf{E}_0$. **a.** The raw earth material used in the present study is obtained after the compaction of a soil. This soil has a broad grain size distribution including clays. **b.** Just after the application of $\mathbf{E}_0$, all the charge carriers are mobile. This state defines the instantaneous (or high-frequency) electrical conductivity. **c.** After a long application of the external electrical field, the clay gets polarized and the charges associated with polarization do not participate any longer to the conduction process. This state defines the DC conductivity. The reduction in the conductivity corresponds to the chargeability *M*. The normalized chargeability is simply the difference between the instantaneous conductivity and the DC conductivity. SL stands for the Stern layer.

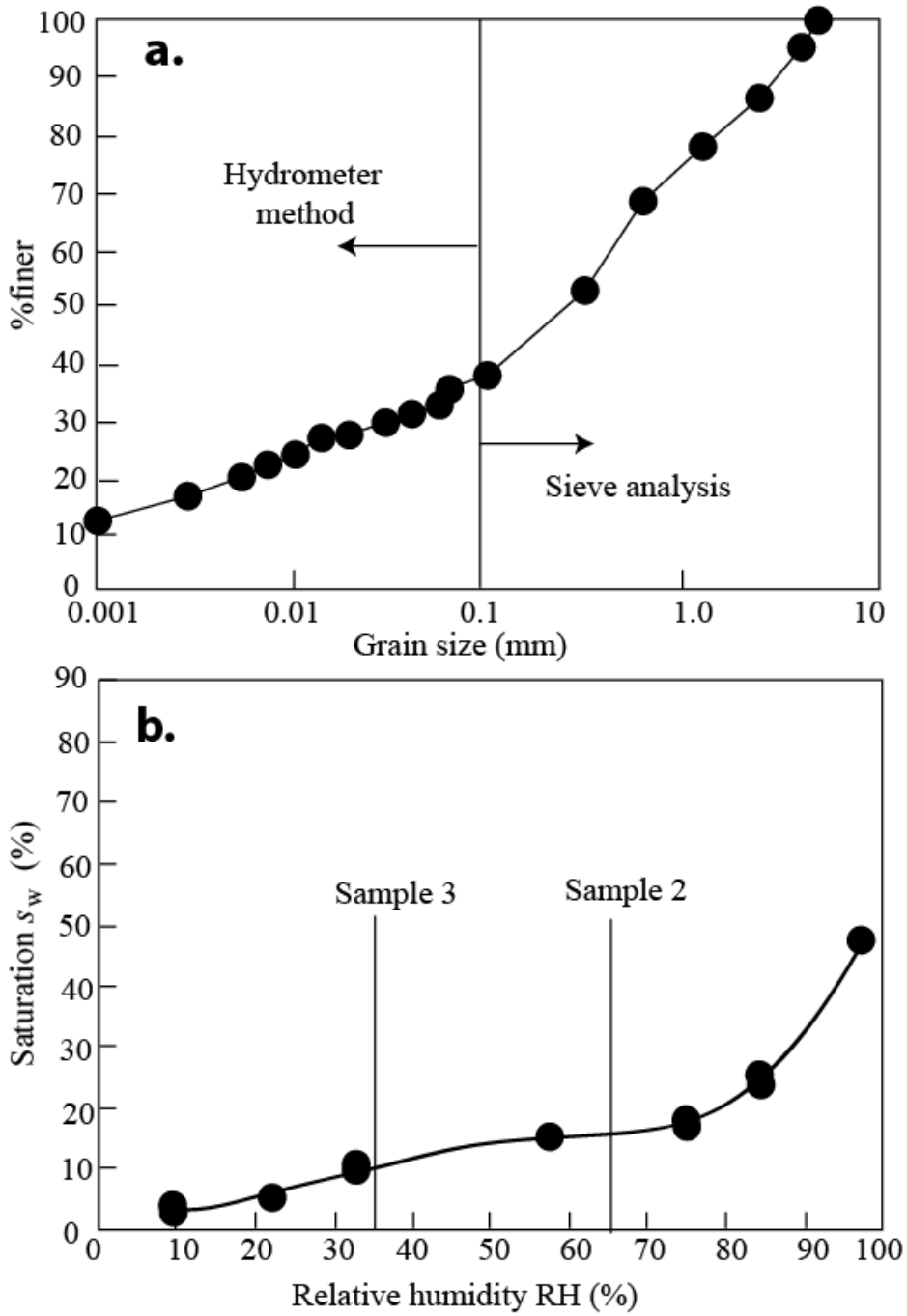

Figure 2. Properties of the compacted soil used as Earth raw material for construction. **a.** Grain size distribution of the sieved rammed earth material used in the present study. Approximately half of the grains are below 300 μm. During an induced polarization material, only the finest fraction of the material has the time to get polarized under the action of the low frequency-electrical field. **b.** Saturation versus relative humidity (RH).

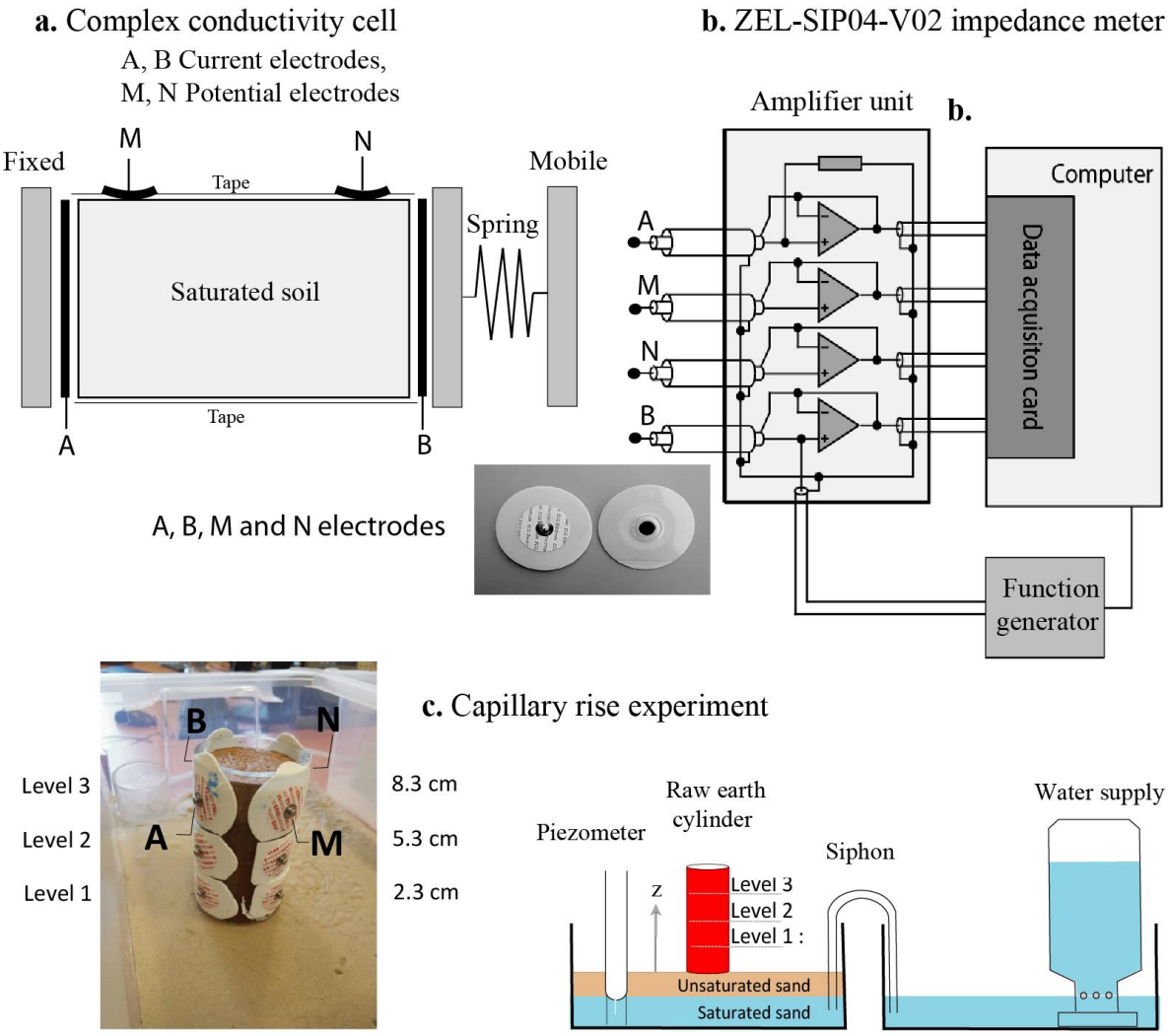

Figure 3. Complex conductivity measurements of rammed earth materials. **a.** Sketch of the experimental setup for the core sample experiments. The electrodes are self-adhesive super conductive carbon film-with biocompatible hydrogel. **b.** ZEL-SIP04-V02 impedance meter used for the laboratory experiments (see Zimmermann et al., 2008, for details). **c.** Capillary bench and position of injection electrodes (A and B) and voltage electrodes (M and N) in the Rammed earth cylinder lying on the partially saturated sand. Levels 1, 2 and correspond to three heights 2.3, 5.3 and 8.3 cm from the base of the sample, respectively.

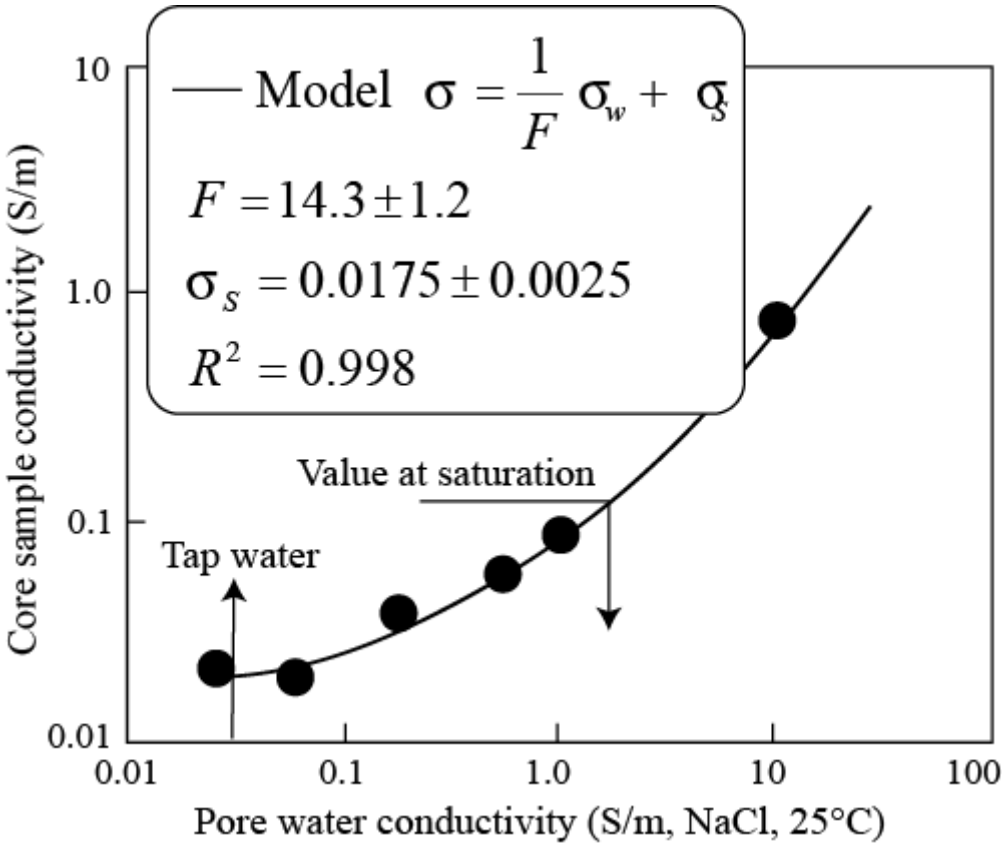

Figure 4. Variation of in-phase conductivity σ' of the core samples (at 1 Hertz) versus the pore water conductivity obtained at different salinities. Measurements are made with NaCl solutions at 25°C. The formation factor F is the inverse of the slope of the trend with σ_S denotes the surface conductivity of the grains. We also measure the value of the tap water used to saturate the other samples (0.035 S m^{-1} at 25°C).

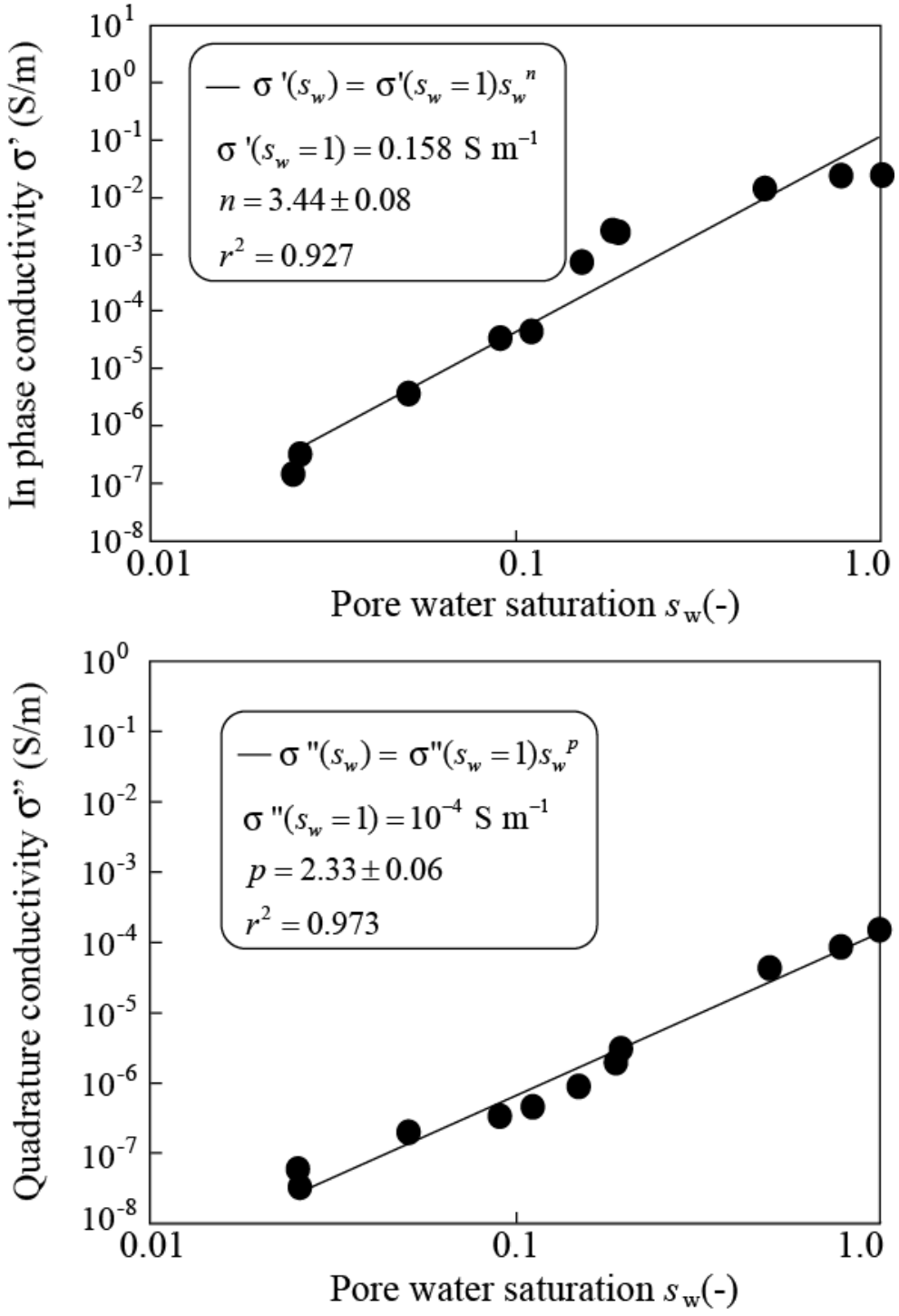

Figure 5. Variation of the in-phase (σ') and quadrature (σ'') conductivities (1 Hertz) versus the pore water saturation s_w with saturation performed with salts imposing different relative humidities. The solid lines correspond to the best fit using a power-law equation prescribed by the model. We obtain a saturation exponent n = 3.4 (assuming conductivity is controlled by its bulk component) and a quadrature conductivity saturation exponent p = 2.3.

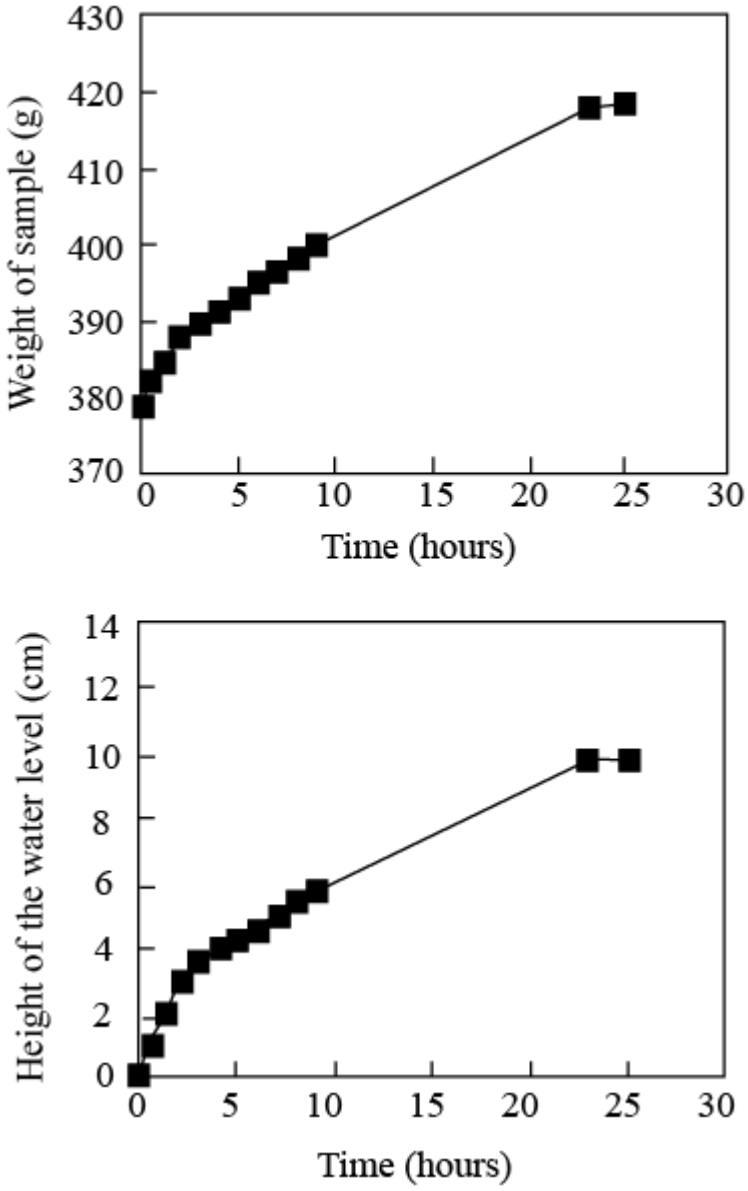

Figure 6. Evolution of the weight of the core sample and height of the water saturation front for Sample 1 versus the elapsed times during the capillary rise experiment. These data corresponds to the early time of the capillary rise.

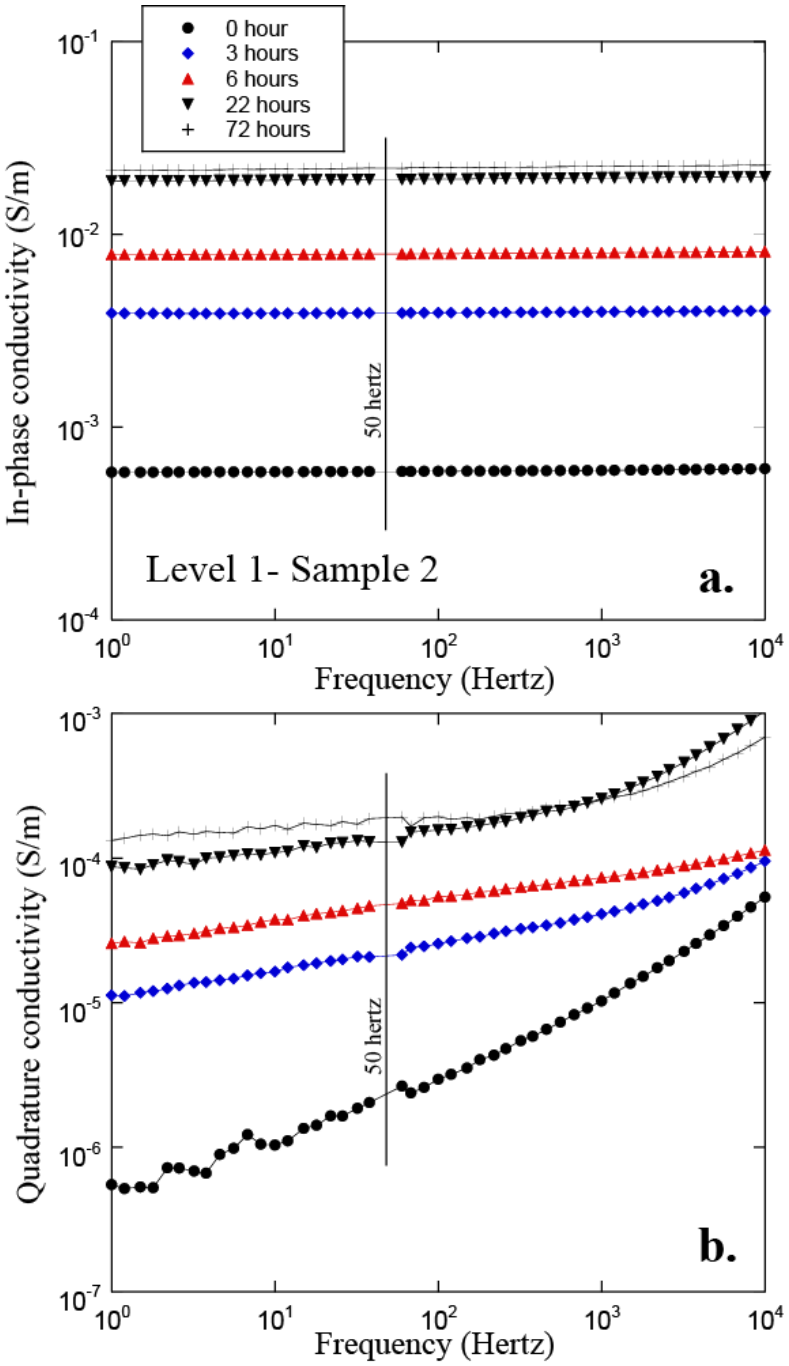

Figure 7. Typical variation of in-phase conductivity and quadrature conductivity spectra (in the range 1 Hertz – 10 kHz) over the time during the capillary rise experiment (Level 1, Sample 2). The in-phase conductivities show a minor dependence on the frequency. Such flat induced polarization spectra are characteristic of porous media having a very broad grain size distribution such as in the present case (see Figure 2a). For the quadrature conductivities, we start to see the influence of the Maxwell-Wagner interfacial polarization at high frequencies corresponding to the take-off of the quadrature conductivity values with frequency. The data are missing around 50 Hertz because of a bad signal-to-noise ratio.

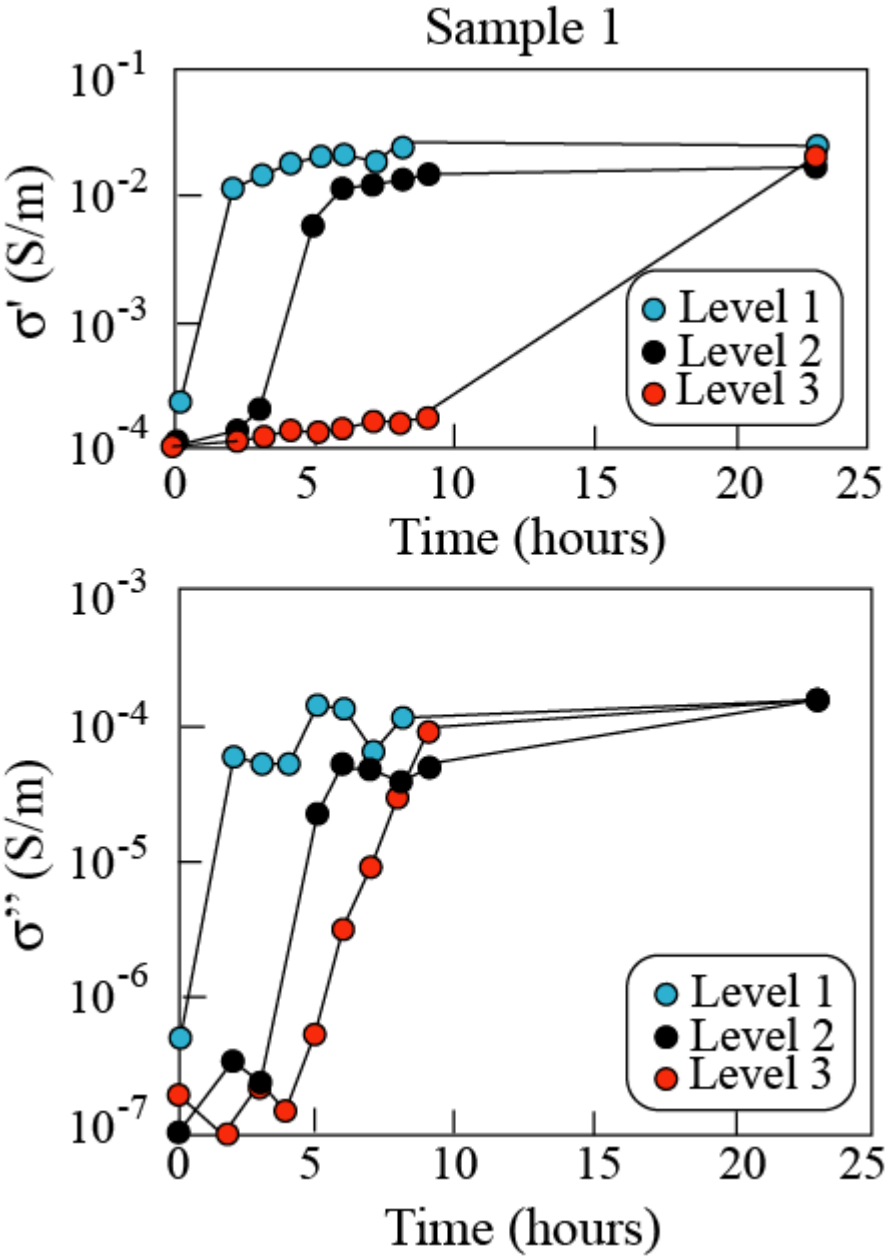

Figure 8. Evolution of the in phase conductivity σ' and quadrature conductivity σ" (at 1 Hertz) over time during the capillary rise experiment (Sample 1). Note that once the capillary rise has passed the third levels, both the in-phase and quadrature conductivities reach the same values at the end of the experiment. Levels 1, 2 and correspond to three heights 2.3, 5.3 and 8.3 cm from the base of the sample, respectively.

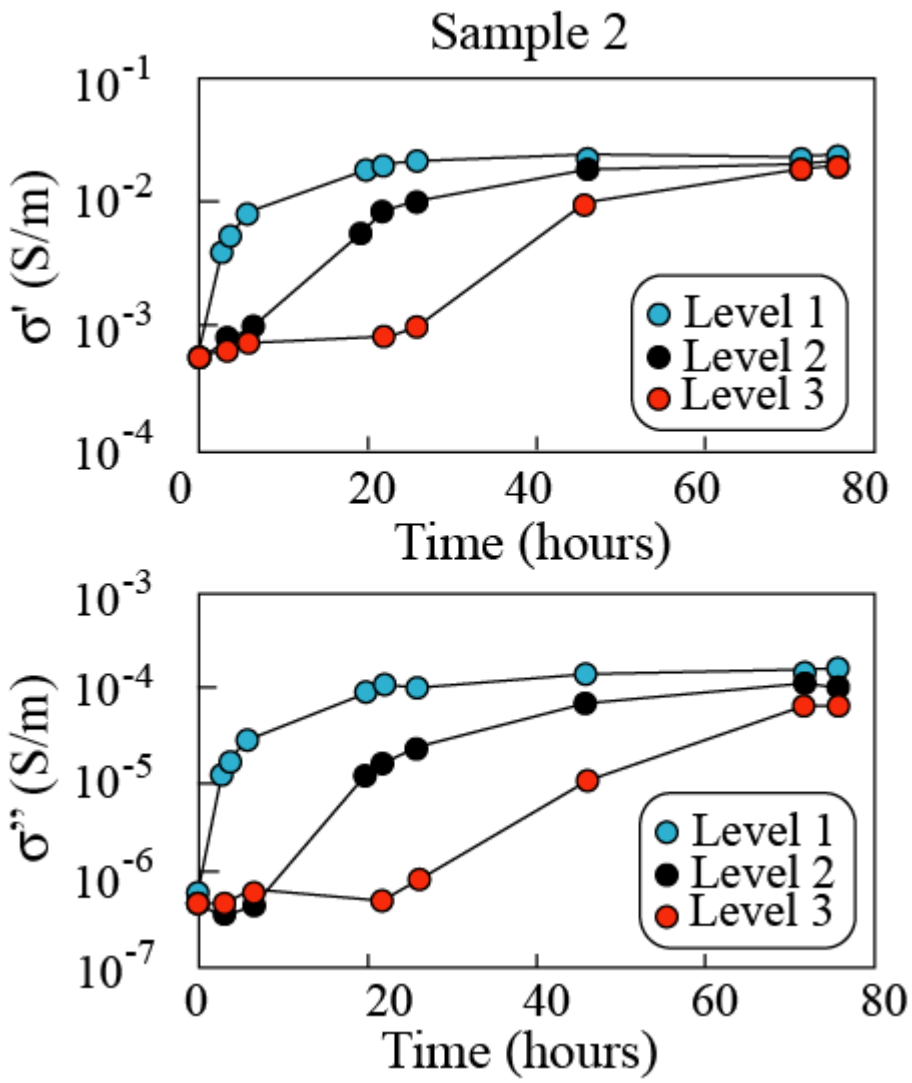

Figure 9. Evolution of the in-phase conductivity σ' and quadrature conductivity σ'' (at 1Hz) over time during the capillary rise experiment (Sample 2). Note that once the capillary rise has passed the third levels, both the in-phase and quadrature conductivities reach the same values at the end of the experiment. Levels 1, 2 and correspond to three heights 2.3, 5.3 and 8.3 cm from the base of the sample, respectively.

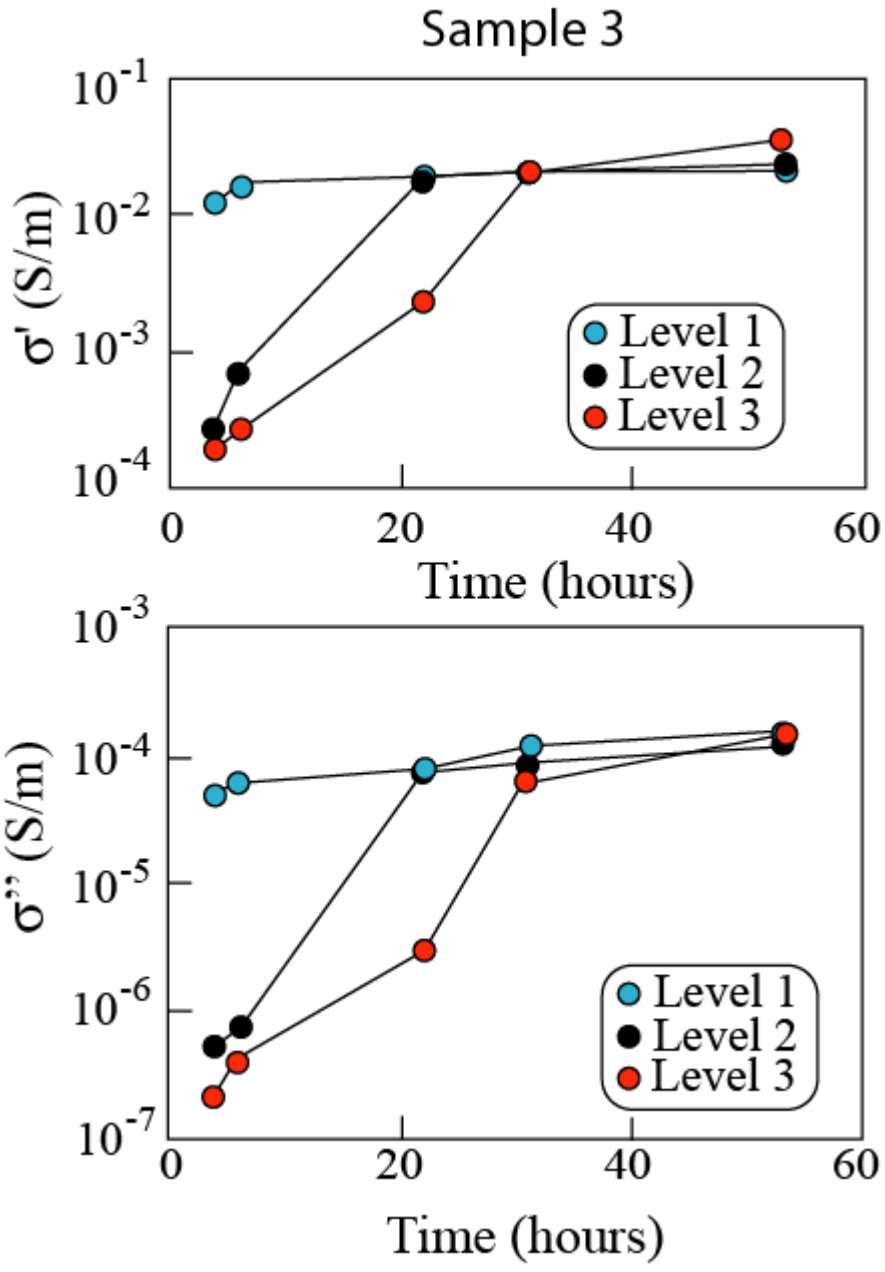

Figure 10. Evolution of in-phase conductivity σ' and quadrature conductivity σ'' (at 1Hz) over time during the capillary rise experiment (Sample 3). Note that once the capillary rise has passed the third levels, both the in-phase and quadrature conductivities reach the same values at the end of the experiment. Levels 1, 2 and correspond to three heights 2.3, 5.3 and 8.3 cm from the base of the sample, respectively.

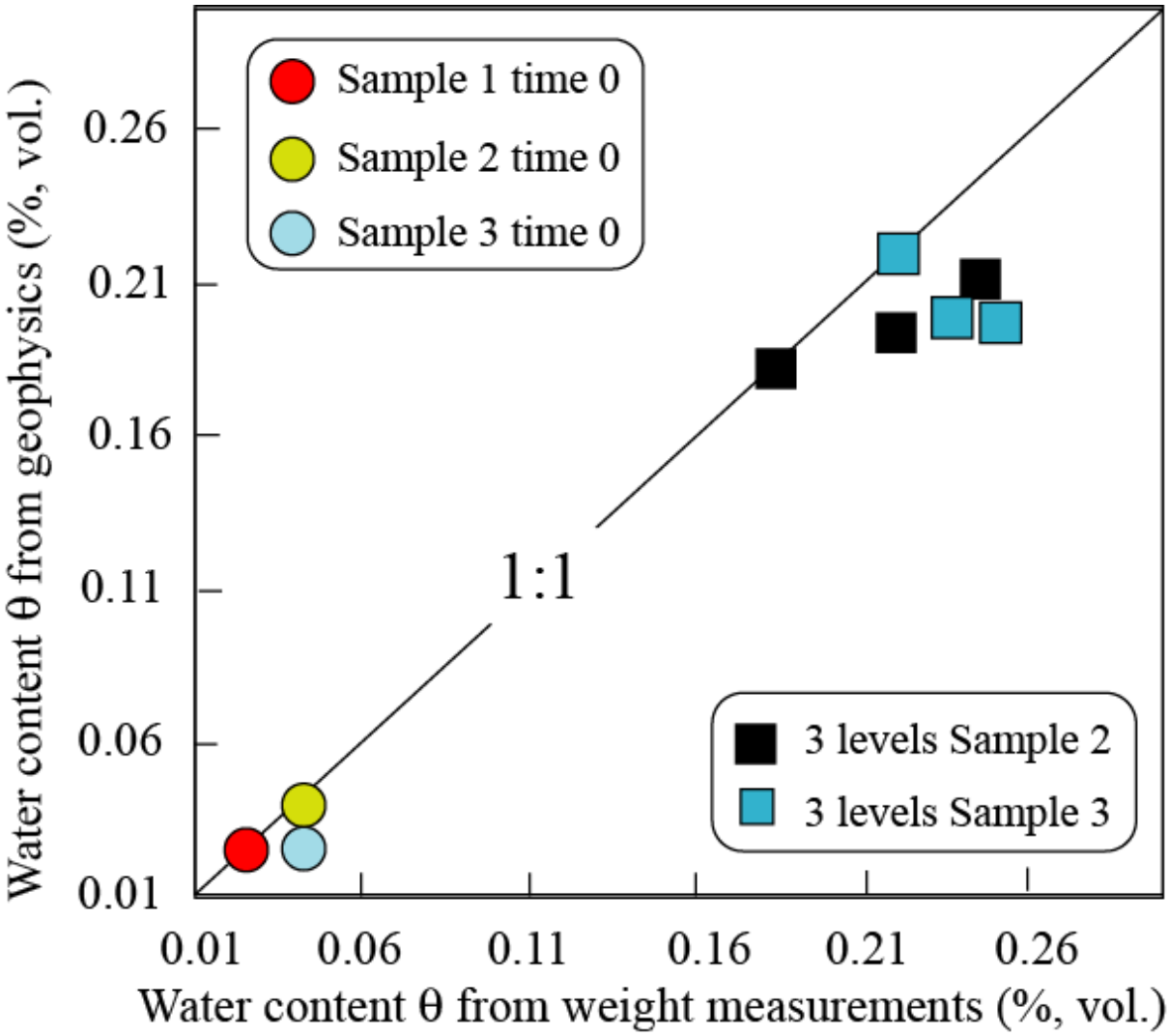

Figure 11. Comparison between the water content evaluated from the spectral induced polarization measurements and the water content measured by weighting at the end of the capillary rise experiment. We check that the spectral induced polarization measurements provide a reliable estimate of the water content.

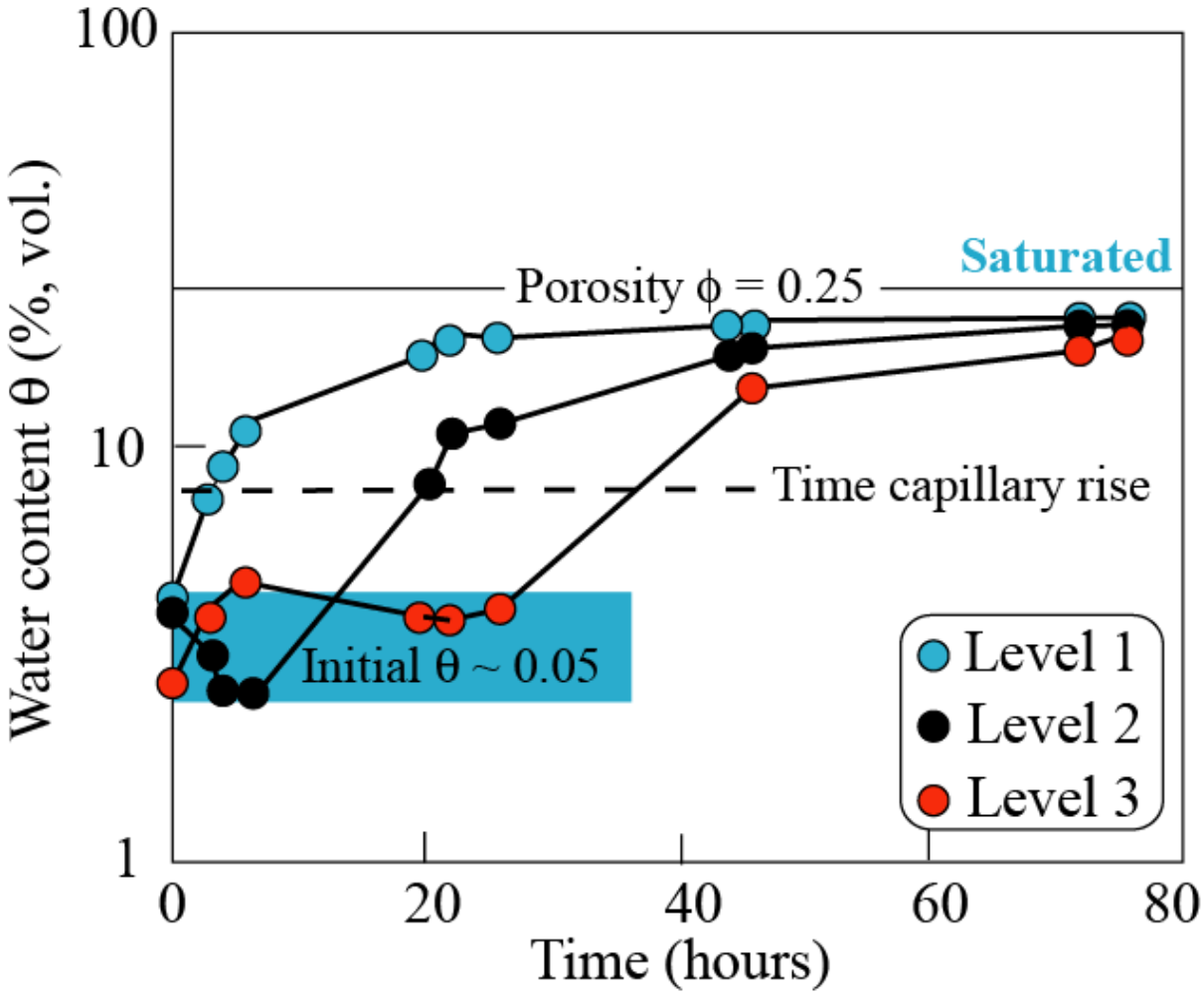

Figure 12. Variation of the water content θ (volume fraction) over time in the capillary rise experiment at three levels using the spectral induced polarization data (Sample 2). We use the spectra at 1 Hertz. The spectral induced polarization data can be used to reconstruct the capillary rise using non-intrusive measurements. Levels 1, 2 and correspond to three heights 2.3, 5.3 and 8.3 cm from the base of the sample, respectively. The porosity of the sample is around 25%. We observe that the water contents around 75 hours are slightly below this value.

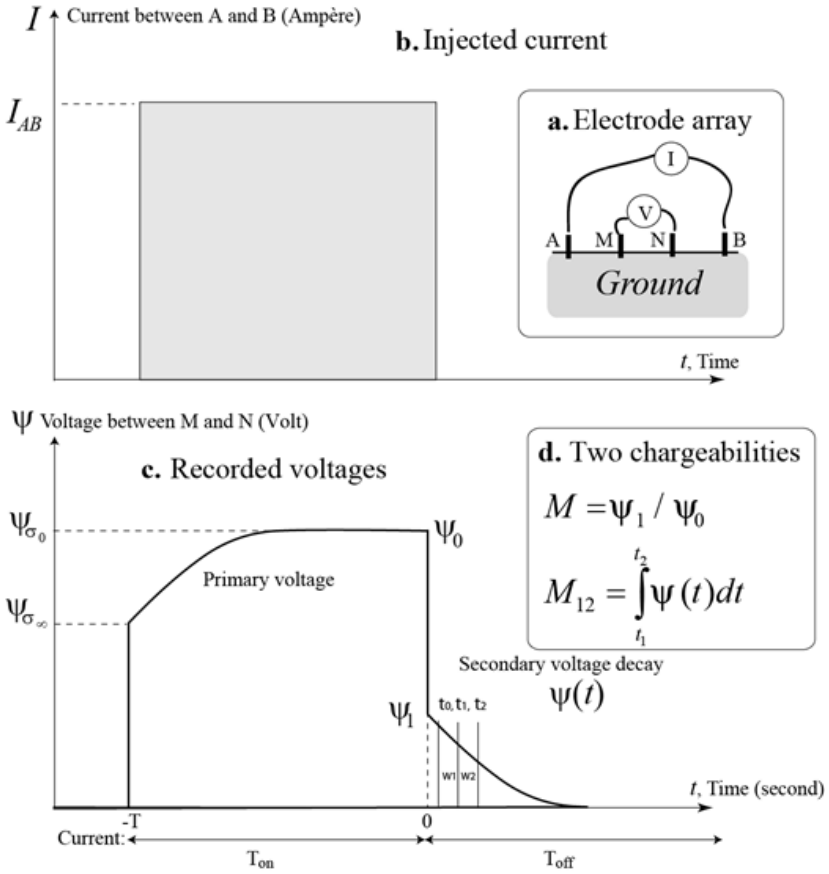

Figure 13. Principle of Time-Domain Induced Polarization (TDIP) measurements. **a.** A primary current is injected in the wall between two electrodes A and B. The associated response corresponds to the measured potential difference measured between two voltage electrodes M and N. **b.** The injected current *I* (in A) corresponds to a box signal of period *T*. **c.** The associated voltage response between the electrodes M and N is the sum of a primary voltage ψ_∞ (called the instantaneous potential) and a secondary voltage ψ_0-ψ_∞ where ψ_0 denotes the steady-state potential. Once the primary current is shut down (for t>0), only the secondary voltage persists and decays over time while the charge carriers are coming back to their equilibrium position at the grain scale. This decaying secondary voltage is measured between M and N for different windows (named W_1, W_2, etc.) separated by characteristic times (t_0, t_1, t_2, ...). The time t_0 is a delay time before starting the partial chargeability measurement (dead time). The dead-time is required to avoid the interference with spurious electromagnetic effects due to capacitive or inductive couplings. **d.** The partial chargeabilities are determined for each of these windows by integrating the secondary voltage over time. T_{on} and T_{off} denote the time of current injection and time for potential decay measurement, respectively. M denotes the chargeability (unitless or sometimes expressed in mV/V). The partial chargeability M_{12} is expressed in ms and needs to be normalized by the duration of the time window.

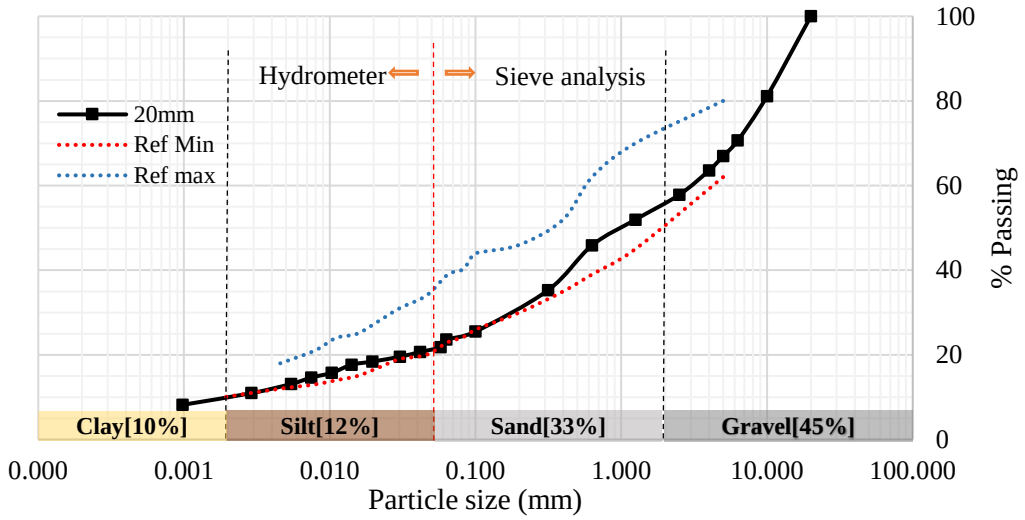

Figure 14. Particle size distribution curve of the soil used in the present study and sieved below 20 mm (i.e., gravels are removed). The two reference curves (min and max) are those proposed by Houben and Guillard (1994) for the construction of rammed earth made-structures. Note the very broad distribution of the grain sizes and D_{10} = 1 μm.

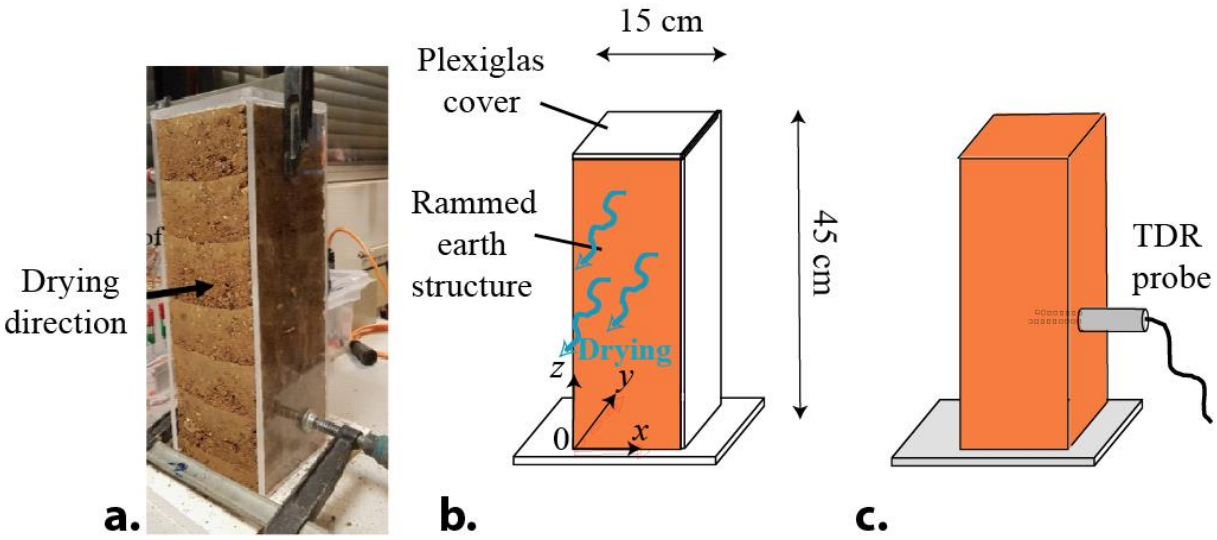

Figure 15. Rammed earth structural element. **a.** View of the earth structure S1 at manufacture with Plexiglas covering. We clearly see the six layers of rammed earth material. **b.** Sketch of the geometry for samples S1, S2, S3, with *x*, *y*, *z* axes. Drying is occurring from two lateral sides of the rammed earth element (the others being covered by Plexiglas layers). **c.** Sketch showing the position of the TDR sensor during the measurements for sample S1 (position *y* = 7.5 cm, *z* = 20 cm). The TDR probe is used to get an independent estimate of the water content.

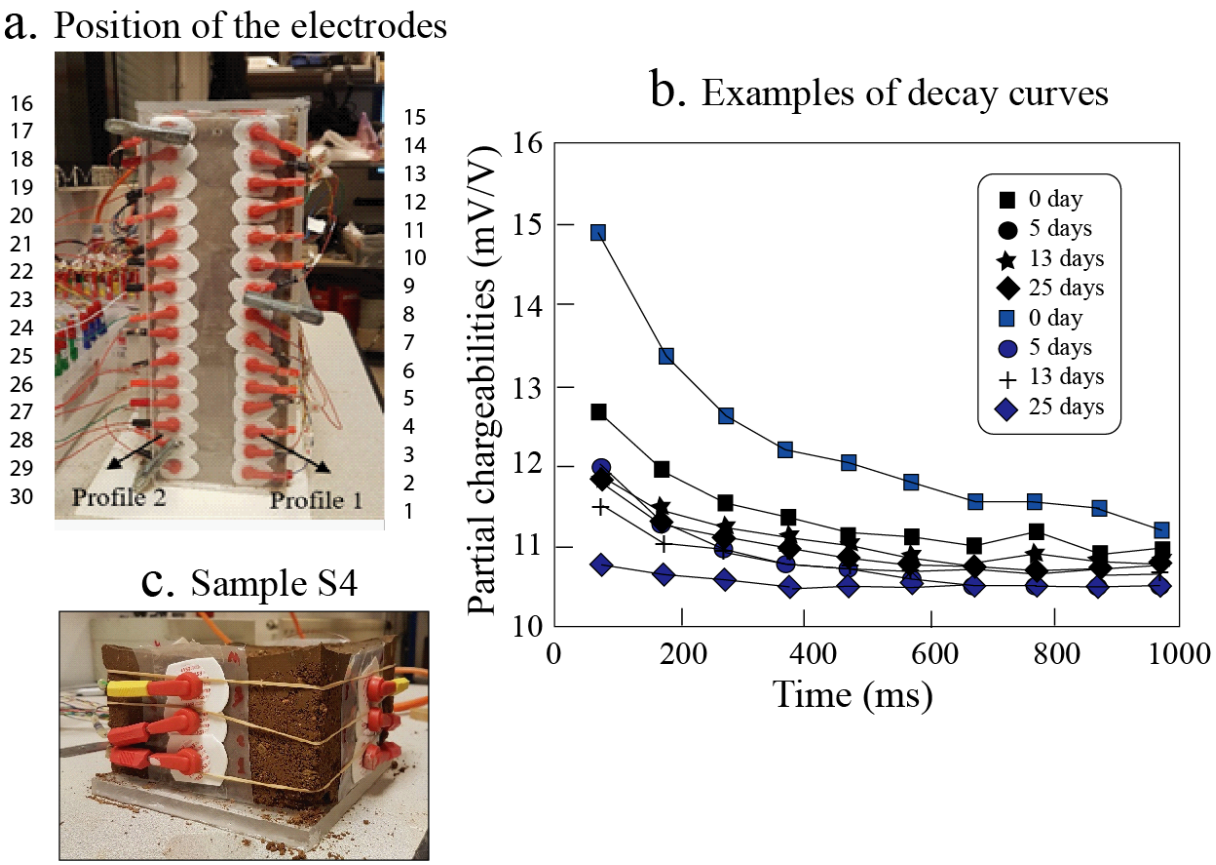

Figure 16. Electrode array and decay curves. **a.** Position of electrodes on the earthen block. 30 electrodes are distributed on each side plus 4 electrodes on the top. All the electrodes are non-polarizable medical electrodes. **b.** Examples of partial chargeability decay curves obtained by different combination of ABMN electrodes (AB current electrodes, MN voltage electrodes). The approximate exponential decays illustrate the quality of the recorded data. The measured partial chargeability over the time for two quadrupoles (ABMN=2,3,4,5, black curves at different elapsed time and ABMN=10,11,13,14, blue curves). **c**. Sample S4 (one layer of rammed earth) with instrumentation.

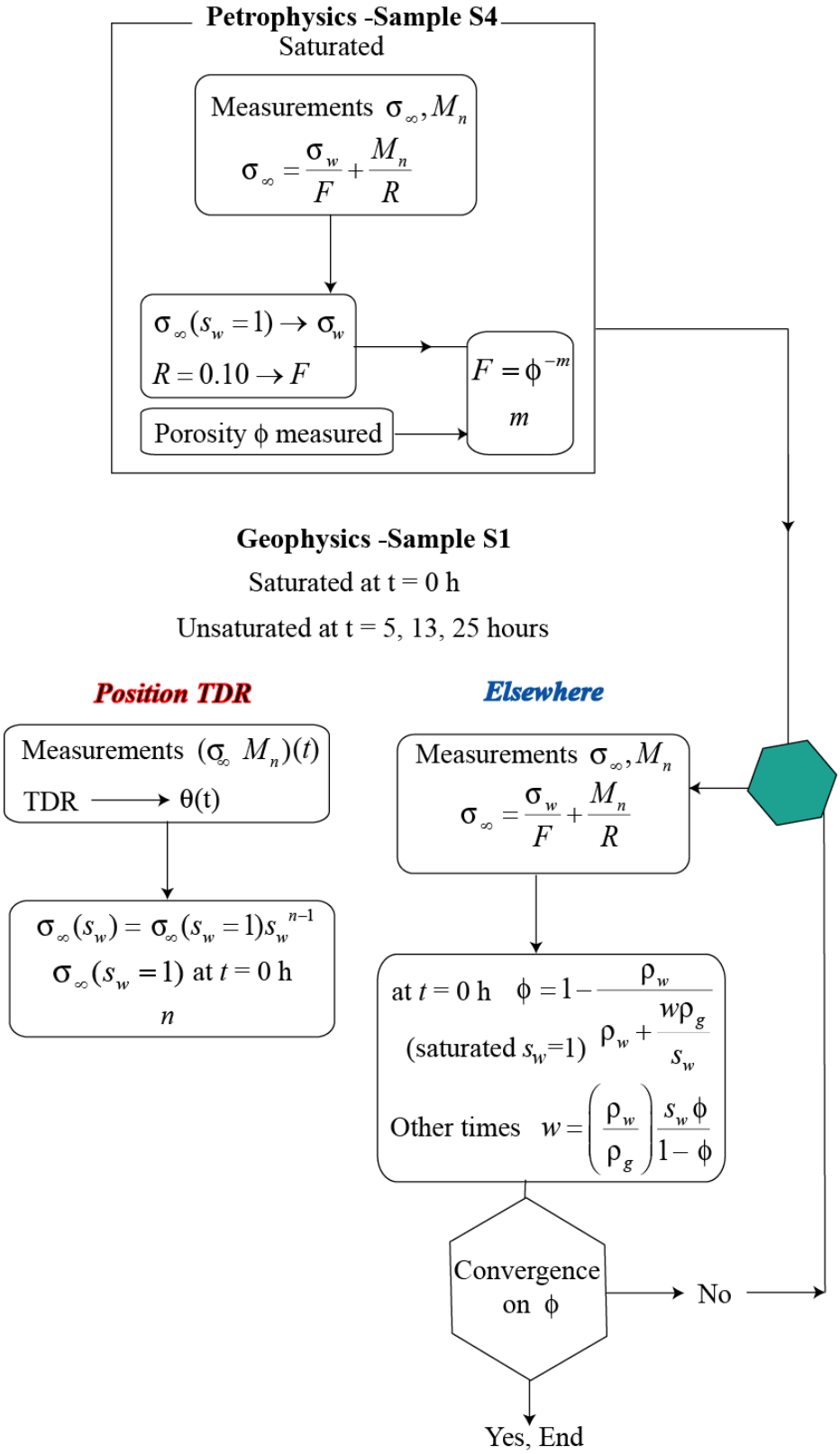

Figure 17. Diagram showing the analysis of the petrophysical and geophysical data and their integration to get tomograms of the water content in volume or weight. At the end of the analaysis, a comparison is made between the water content at the position of the TDR probe and then obtained from the tomography at the same position.

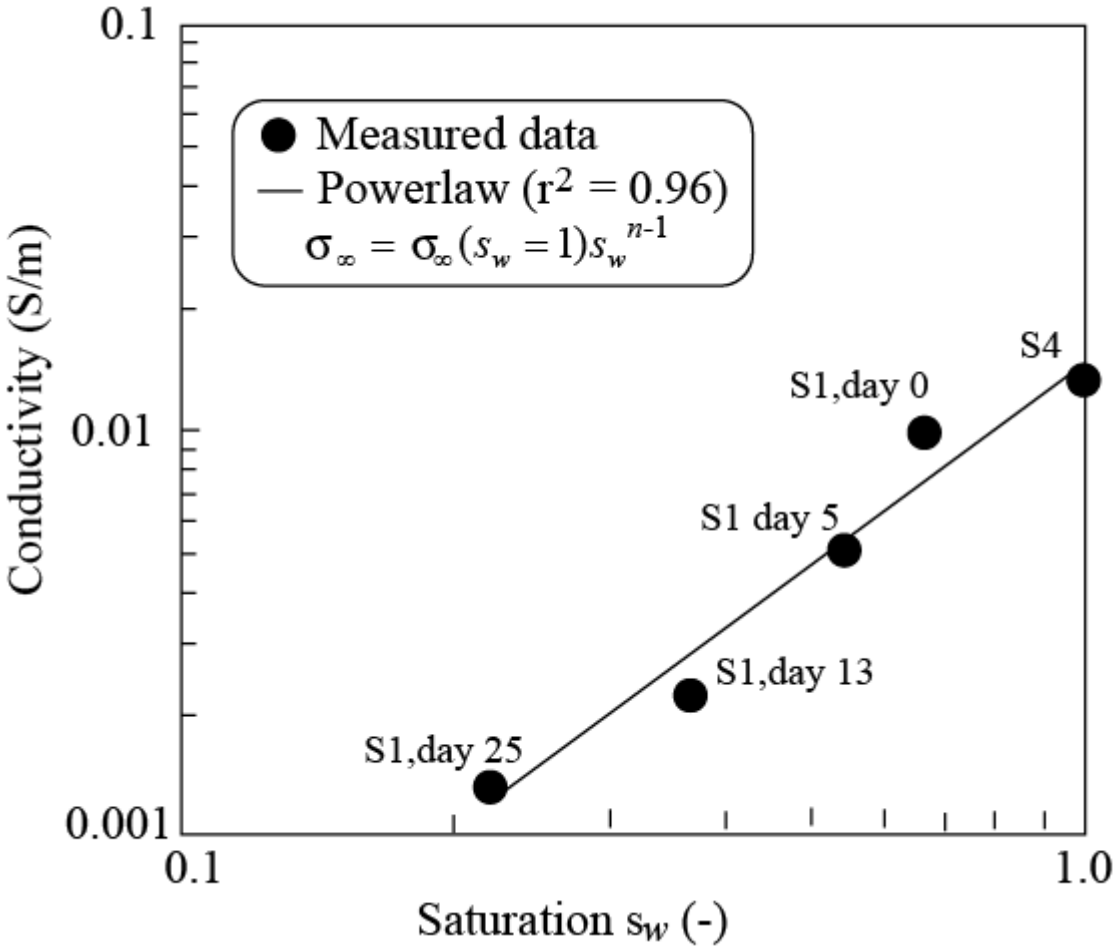

Figure 18. Relationship between the instantaneous electrical conductivity σ_∞ and water saturation S_w. The electrical conductivity data are here extracted from the inverted tomograms at the position of the TDR probes (at a height of 20 cm) while the saturation is determined from from the TDR measurements using a calibrated relationship between the dielectric constant and the saturation for the soil. The linear trend denotes a power-law relationship corresponding to equation (13) with a saturation exponent n = 2.65±0.15 (reported in Table 2) and $\sigma_\infty(s_w = 1)$ = 0.014±0.002 S m^{-1}.

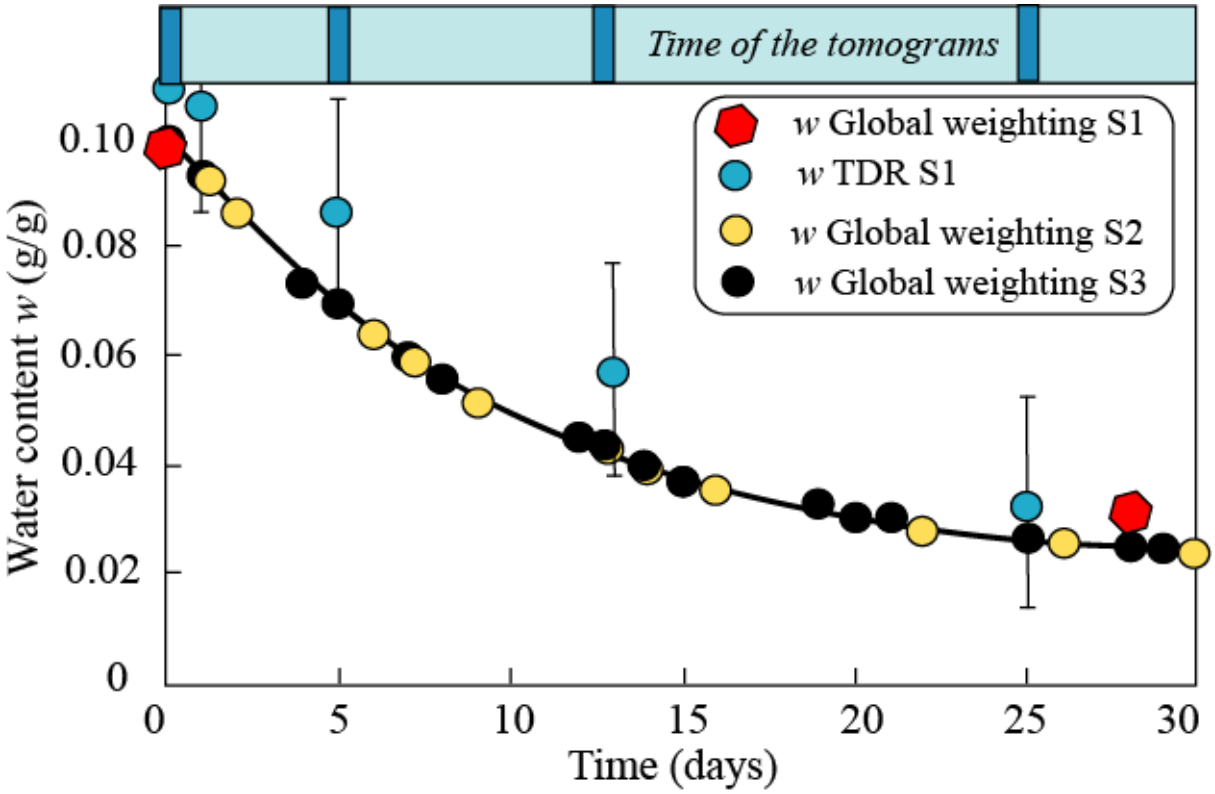

Figure 19. Dependence of the water content *w* over time using the variation of the weight of the samples with time and the TDR data (Samples S1, S2, S3, and S4). The line is just a guide for the eyes. Note the consistency between the different experiments.

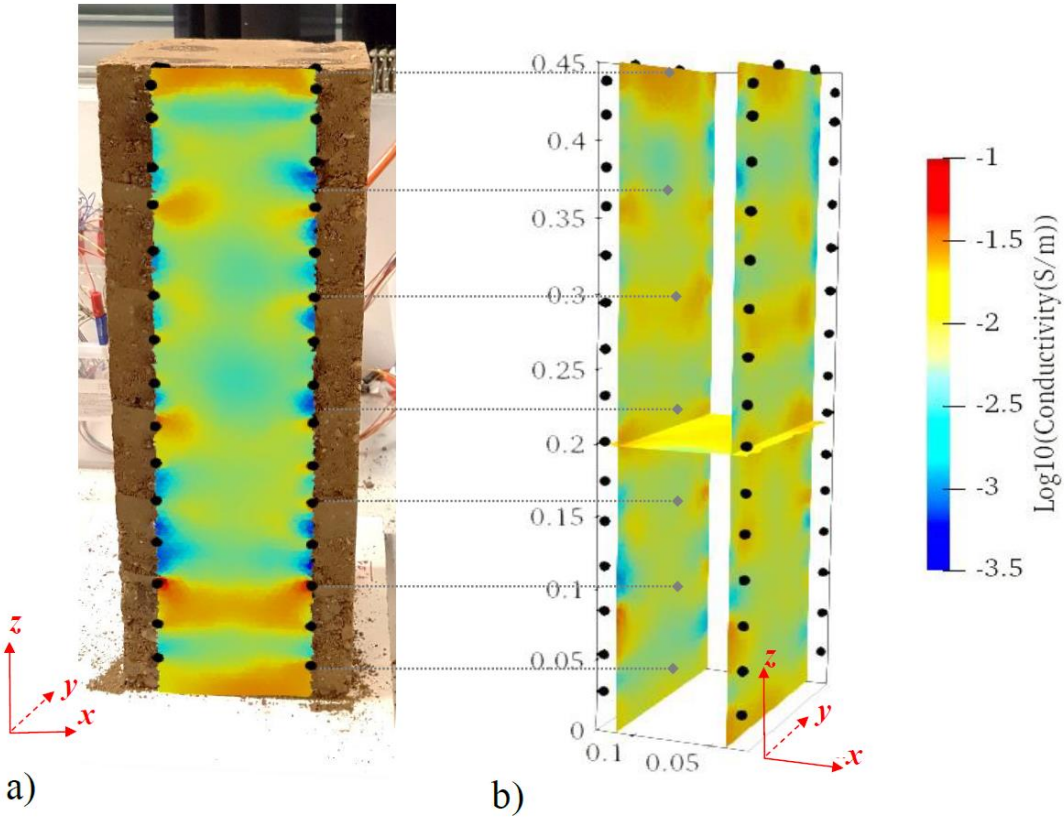

Figure 20. Tomograms of the electrical conductivity distribution at the manufacture (time 0, w =0.1). Overlay of conductivity field on the (O, x, z) plane, between the 2 lines of electrodes, figured in black **a.** Conductivity field on (O, y, z) planes at x =3 cm. **b.** Conductivity field on (Oyz) planes at x =12 cm. We see some of the heterogeneity associated with the 6 layers.

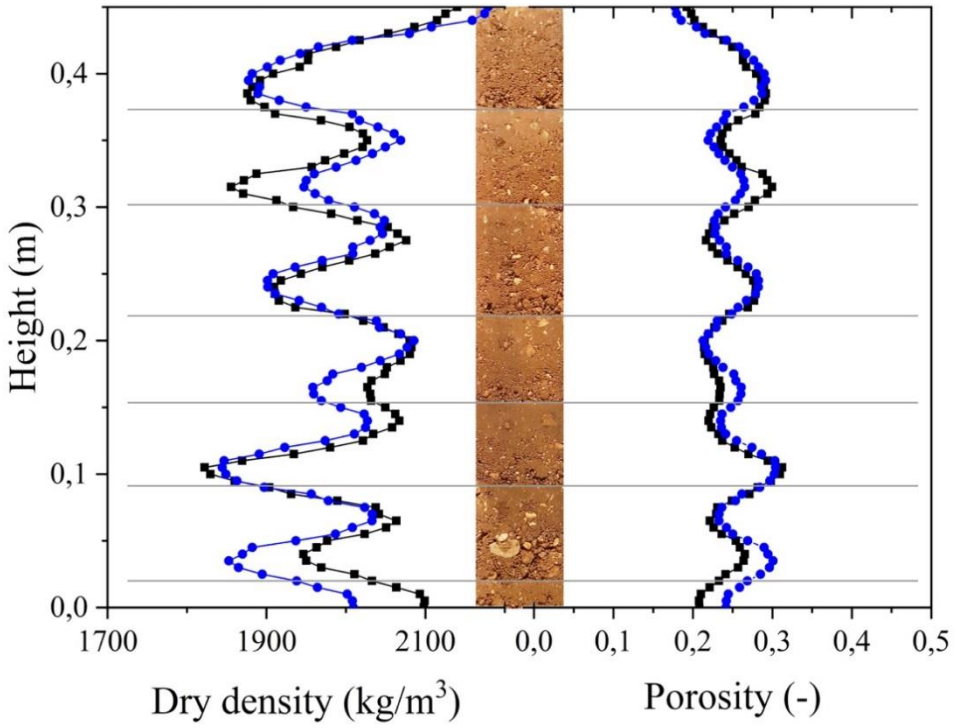

Figure 21. Variation of dry density and porosity with height in the block at two positions (X = 0.05 and Y = 0.12 cm, blue curve and X = 0.1 and Y = 0.12 cm, black curve). The figure includes a picture of the block showing the heterogeneities corresponding to the 6 layers of compacted rammed earth.

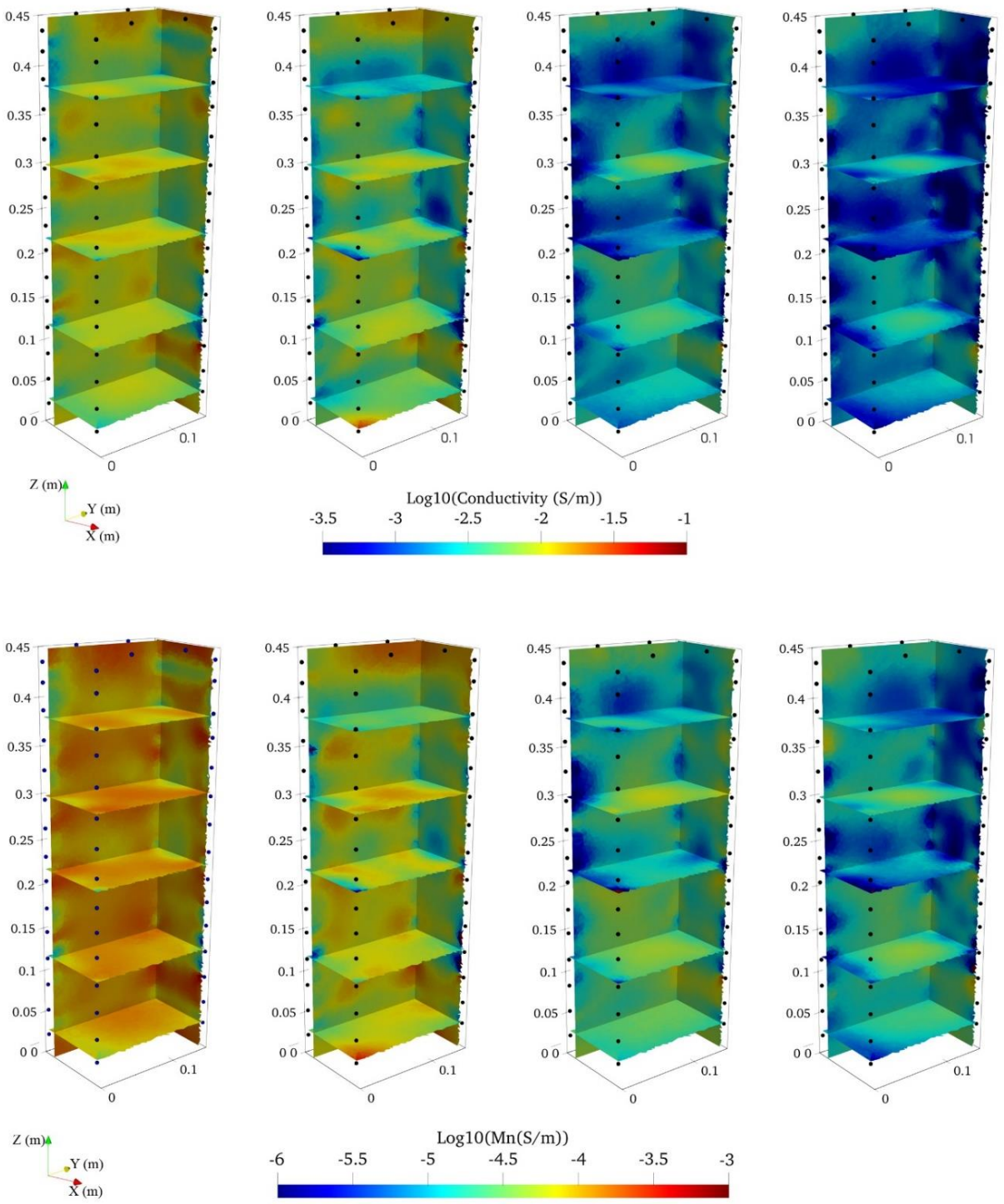

Figure 22. Tomograms of the electrical conductivity distribution (upper tomograms) and tomograms of the normalized chargeability (lower tomograms) at different elapsed times, For the two levels, the tomograms correspond to time 0 (manufactured wall), then for t = 5 days, t = 13 days and t = 25 days during the drying process, respectively. The Y-direction denotes the drying direction.

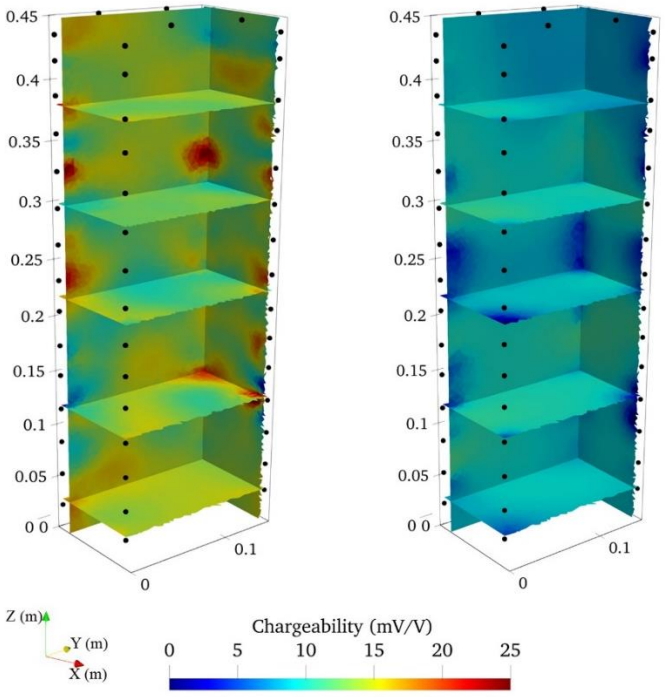

Figure 23. Tomograms of the chargeability distribution at Times 0 and 25 days. The chargeability is almost constant and a small variation could be noticed over the time. This is quite consistent with a conductivity dominated by its surface contribution at the surface of the grains.

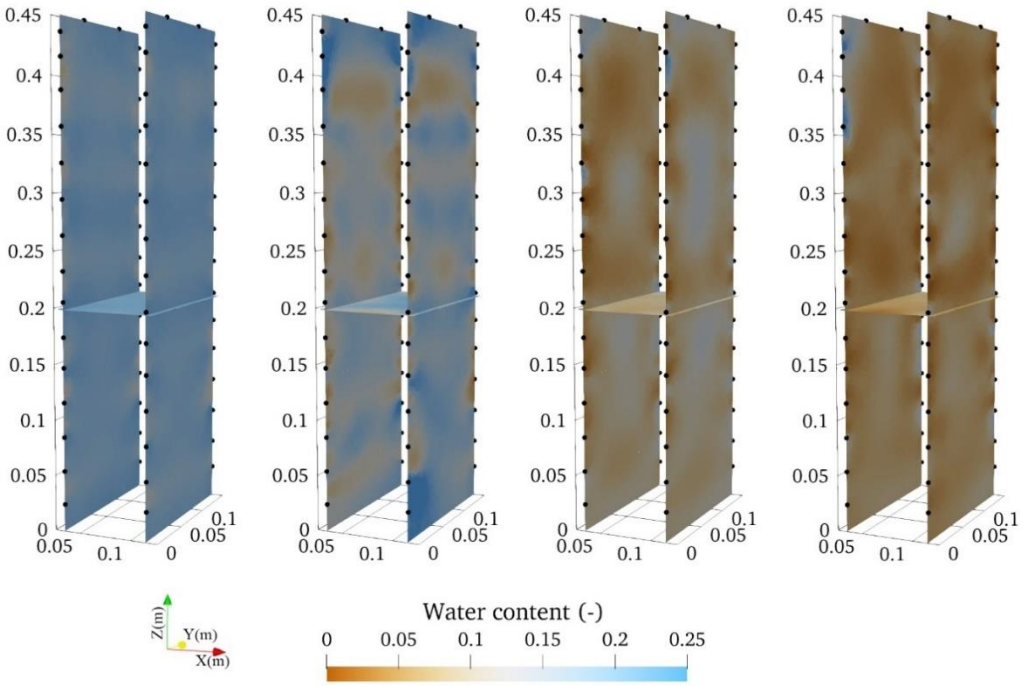

Figure 24. Distribution of volumetric water content at different elapsed time during the drying process. Panels from left to right corresponds to the following elapsed times t = 0, 5, 13, and 25 days, respectively.

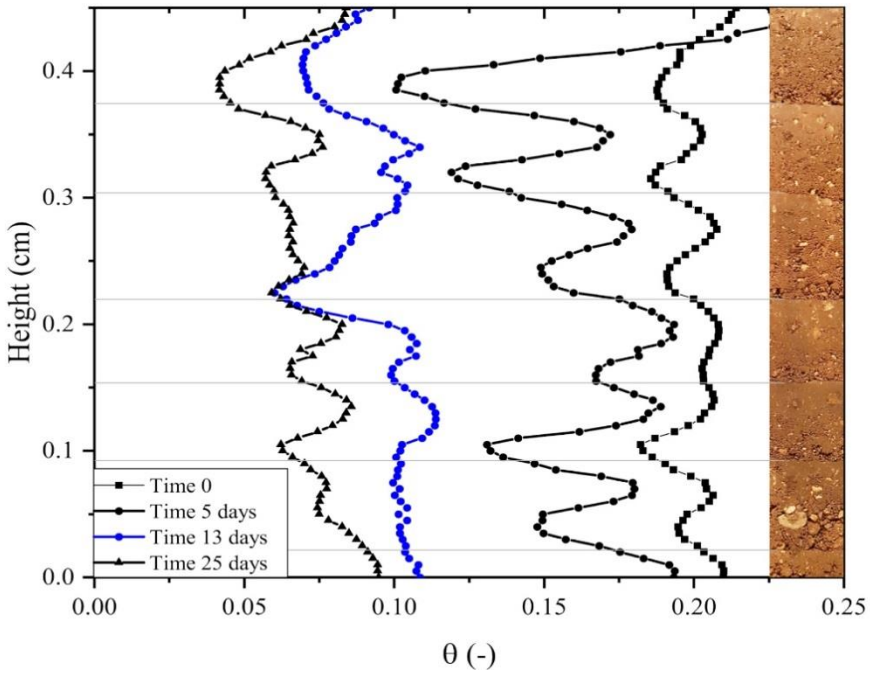

Figure 25. Variation of the volumetric water content over the height of the block (position X = 0.05 cm and Y = 0.12 cm) and at different elapsed time during the drying process.

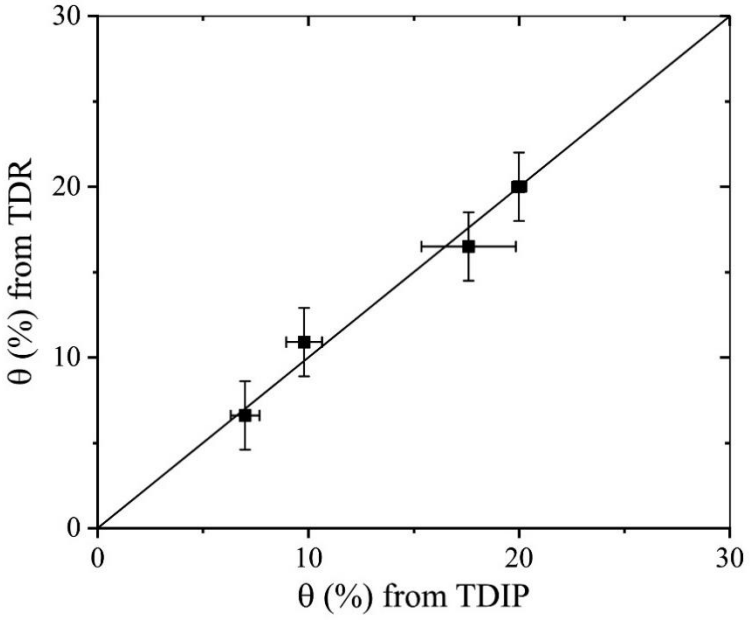

Figure 26. Comparison between the water content measured by the TDR probe and the estimated from geophysical measurements (TDIP). Water content from TDIP is the mean of the water content estimated at the position of the TDR probe using the induced polarization data. The vertical error bars are determined from the TDR probes (±2%), while the horizontal error bars are the standard deviation of the water content from the TDIP measurements at each elapsed times.

Annex 2

Article on Induced polarization technique applied in RE wall subjected to capillary rise

(Submitted to Engineering Geology Journal on Nov, 2022).

Non-intrusive monitoring of water content field during capillary rise within a rammed earth structure: potential of induced polarization method

A. Ghorbani (1), T. Chitimbo (2), A. Revil (3), N. Prime (2),

K. Zhang (4), T. Fu (5), and O. Plé (2)

(1) Naga Geophysics, Technolac, 73370 Le Bourget du Lac, France

(2) Université Savoie Mont-Blanc, CNRS, UMR CNRS 5271, LOCIE, 73370 Le Bourget du Lac, France

(3) Université Grenoble Alpes, Université Savoie Mont-Blanc, CNRS, UMR CNRS 5204, EDYTEM, 73370 Le Bourget du Lac, France

(4) Research Center of Geotechnical and Structural Engineering, Shandong University, Jinan 250061, Shandong Province, China

(5) Key Laboratory of Marine Geology and Metallogeny, First Institute of Oceanography, Ministry of Natural Resources, Qingdao 266061, China

Short title: Water content in rammed earth

Keywords: Rammed earth; water content field; capillary rise; time-domain induced polarization; resistivity; chargeability; non-destructive monitoring.

Emails: andre.revil@univ-smb.fr; olivier.ple@univ-smb.fr; noemie.prime@univ-smb.fr; taini.chitimbo@univ-smb.fr; futengfei@fio.org.cn; sdukaizhang@mail.sdu.edu.cn; ahmad.ghorbani@naga-geophysics.com;

Corresponding author: André Revil, andre.revil@univ-smb.fr

Under review in *Engineering Geology Journal*

Abstract. The capillary rise in earthen buildings is a factor of risk since it changes the mechanical properties of such class of materials. A laboratory-scale experiment is performed to see the ability of time-domain induced polarization to monitor the change in the water content during a capillary rise experiment in a rammed earth wall (150 cm in height and 75 cm in width). 64 self-adhesive Ag/AgCl electrodes are placed at the surface of the rammed earth wall. The contact between the electrodes and the wall is insured by a conductive gel. The distance between the electrodes is 4.5 cm. An ABEM Terrameter SAS-4000 is used to perform time-domain induced polarization measurements at 7 specific dates in July 2022. The raw data (apparent resistivity and chargeability) are inverted to produce tomograms through the wall. These tomograms are presented along the plane drawn by the position of the electrodes. A petrophysical model recently developed to interpret electrical conductivity and normalized chargeability data is used here to recover the water content distribution over time. The results are compared to the dielectric measurements made with a TDR (Time Domain Reflectometry) probe placed within the wall. In addition, the wet front associated with the capillary rise is monitored using a camera. The data shows a consistent position of the capillary rise between the various datasets. A methodology is described to obtain the distribution of the water content over space and time in the rammed earth structure.

1. Introduction

In the history of humankind, rammed earth materials have been used in many constructions worldwide (Easton and Easton, 2012) and its first recorded use is in ancient Northern China c. 2310-1810 BC (Jaquin et al., 2008). Rammed earth materials consist mostly of gravels, sand, clay, and water, compressed together between formworks to form a solid mass and let dried (Kebao and Kagi, 2012). This technique is called *pisé* in French, *tapial* in Spanish and *taipa* in Portuguese (Jaquin et al., 2008).

Nowadays, raw earth faces a revival of interest for houses and small buildings construction in the context of sustainable development and carbon footprint reduction which is more and more targeted by new regulations, as RE2020 in France (Taylor and Luther, 2004; Soebarto, 2009, Morel et al. 2001). As discussed by Abdulsamad et al. (2020, 2022), monitoring the water content of rammed earth structures is essential for predicting the evolution of the mechanical behavior of these materials (see also Chauhan et al., 2019; Champiré et al., 2016; Chitimbo et al., 2023).

Electrical resistivity/conductivity imaging is a geophysical method sensitive to the water content of porous materials (Waxman and Smits, 1968). That said the electrical conductivity of porous bodies has two contributions, one associated with conduction in the bulk pore space and one associated with the electrical double layer coating the surface of the grains (Vinegar and Waxman, 1984). The dependence on saturation (or water content) of these two contributions is different (Waxman and Smits, 1968). Therefore, electrical resistivity/conductivity imaging cannot be used as a stand-alone technique.

Induced polarization is a non-intrusive geophysical technique able to image two complementary properties of interest, namely the electrical conductivity and the normalized chargeability, of porous media (Kemna et al., 2012; Titov et al., 2002). The chargeability of porous media characterizes their ability of store reversibly electrical charges when submitted to an electrical field. Like electrical resistivity/conductivity imaging, this method has a long history in geophysics (Schlumberger, 1920). This technique is also known under terminologies such as low-frequency dielectric spectroscopy in colloidal chemistry and impedance spectroscopy in material science (Revil and Gresse, 2021). Nowadays, time-domain induced polarization tomography is broadly used in the field of hydrogeophysics as an efficient method to solve a number of environmental and geotechnical problems (e.g., Börner et al., 1993; Johnson et al., 2010; Schwartz and Furman, 2012; Nordsiek et al., 2015).

In Abdulsamad et al. (2020, 2022), we developed a specific physics-based petrophysical model describing both the electrical conductivity and normalized chargeability of rammed earth materials. This model was based on the so-called dynamic Stern layer model developed by Revil (2013a, b) providing a mechanistic description of the polarization of the double layer at the grain scale as well as electrical conductivity (see also Niu et al., 2016; Hao et al., 2016). Abdulsamad et al. (2020) connected the two properties of interest to the porosity, saturation and conductivity of the pore water and Cation Exchange Capacity (CEC). We then tested this petrophysical model on a drying block of rammed earth material in order to demonstrate the ability of this method to image the change of the water content over time starting from saturated conditions.

In the present paper, we go one step further in imaging the change of the water content on a whole-scale time-domain induced polarization to monitor the change of the water content in a capillary rise experiment applied to a wall made of rammed earth. Therefore the present study complements the two previous studies (Abdulsamad et al., 2020, 2022) in showing that the method can be applied to a large-scale experiments.

2. Theory

We consider a porous rammed earth material made of sand, clay, and water. The interface between the minerals and the pore water is the setting of an electrical double layer with an excess of charge in the pore water balancing the negative charge on the mineral surface. This double layer is composed of a Stern layer of weakly sorbed counterions and a Gouy-Chapan diffuse layer (e.g., Waxman and Smits, 1968). According to the dynamic Stern layer model and using harmonic current excitations behaving as $\exp(-i\omega t)$, Ohm's law and the complex conductivity of such porous material are given by (e.g., Revil, 2013a, b; Revil et al., 2017)

$$\mathbf{J}(\omega) = \sigma^*(\omega)\mathbf{E}(\omega), \tag{1}$$

$$\sigma^*(\omega) = \sigma_\infty - M_n \int_0^\infty \frac{h(\tau)}{1-(i\omega\tau)^{1/2}} d\tau \,, \tag{2}$$

where **J** and **E** denote the current density and electrical field, respectively, ω denotes the angular frequency (rad s^{-1}), τ is a time constant (also called a relaxation time since corresponding to a diffusion process), $h(\tau)$ denotes the (normalized) probability density associated with the distribution of the time constants of the material (in turn related to its distribution of polarization length scales), $M_n = \sigma_\infty - \sigma_0$ is the normalized chargeability (expressed in S m^{-1}), and σ_0 and σ_∞ denotes the DC (Direct Current, ω=0) and high-frequency (instantaneous) electrical conductivities (both expressed in S m^{-1} = A $V^{-1}m^{-1}$), respectively.

According to the dynamic Stern layer model, the normalized chargeability is proportional to the Cation Exchange Capacity (CEC) of the porous material (Revil et al., 2017). The high and low-frequency conductivities as well as the normalized chargeability can be obtained through a volume averaging method (see derivation in Revil, 2013a, b). In the so-called linear conductivity model, the following petrophysical relationships can be used to interpret the conductivity and normalized chargeability tomograms (Abdulsamad et al., 2020, 2022),

$$\sigma_0 = \frac{s_w^{\,n}}{F}\sigma_w + \left(\frac{s_w^{\,n-1}}{F\phi}\right)\rho_g(B-\lambda)\mathrm{CEC}\,, \tag{3}$$

$$\sigma_\infty = \frac{s_w^{\,n}}{F}\sigma_w + \left(\frac{s_w^{\,n-1}}{F\phi}\right)\rho_g B\mathrm{CEC}\,, \tag{4}$$

$$M_n = \left(\frac{s_w^{\,n-1}}{F\phi}\right)\rho_g \lambda \mathrm{CEC}\,. \tag{5}$$

In these relationships, F (dimensionless) denotes the intrinsic formation factor related to the porosity ϕ (dimensionless) by Archie's law (Archie, 1942) $F = \phi^{-m}$ ($m \geq 1.0$ is called the cementation or porosity exponent, see Waxman and Smits, 1968). The conductivity σ_w (in S m^{-1}) denotes the pore water conductivity, ρ_g is the grain density (in kg m^{-3}, typically ρ_g = 2700 kg m^{-3} for the rammed earth material made of silicates and alumino-silicates), and CEC denotes the Cation Exchange Capacity of the material (usually reported in meq/100 g but expressed in C kg^{-1} in the international system of units, 1 meq /(100 g) = 963.2 C kg^{-1}). The quantity B (in $m^2s^{-1}V^{-1}$) denotes the apparent mobility of the counterions for surface conduction and λ (in $m^2s^{-1}V^{-1}$) denotes the apparent mobility of the counterions for the polarization (Vinegar and Waxman, 1984). We also introduce a dimensionless number $R = M_n / \sigma_S$ where σ_S is the surface conductivity (last term of equation 4). This gives $R = \lambda / B$ = 0.09 independent of temperature and saturation.

This petrophysical model has been broadly tested on many types of porous media including soils (Revil et al., 2017), rammed Earth (Abdulsamad et al., 2020), and sandstones (Niu et al., 2016). It will be used to interpret the time-lapse geophysical data used below to monitor the capillary rise in the wall.

3. Materials and methods

3.1. Experimental setup

A capillary rise experiment was monitored for 21 days (from 07/07/2022 to 28/07/2022). The experimental setup consists of an Unstabilized Rammed Earth (URE) wall lying on a concrete base (see Figures 1 and 2). The wall is constructed using 20 layers of rammed earth material (~ 7.5 cm thick each). On the bottom, the wall is covered by (impervious) paraffin up to a height of 10 cm. Between 10 and 12 cm in height (over a thickness of 2 cm), the rammed earth wall is in contact with a layer of fine sand. Finally, the water level was maintained at 8 cm thanks to the water reservoir system visible on the right-side of Figure 1a. By controlling this constant water level into the sand, the height of capillary rise above the water reaches 2 cm at the sand surface, and it stays constant over time. This means that a suction value of 0,2 kPa is applied at the base of the wall.

Small relative humidity (RH) sensors (capacitive sensors of type Sensirion SHT75, Switzerland) are placed at 10 different levels, labeled s_1 to s_{10} from the bottom to the top of the URE wall (Figures 1 and 3). In addition, a Time Domain Reflectometry (TDR) method was used to measure the volumetric water content inside the wall (Top et al., 1958; Souza et al., 2003). The TDR probe used in this study was a TRIME-PICO-32 probe setup in one side of the wall (Figure 3), at mid-height of the wall, in the middle of a layer height, and down to a depth of 10 cm from the surface. Furthermore, a camera was used to automatically follow the capillary rise over time. Finally, a balance (Mettler Toledo) with a precision of 0.1g, was used to measure the amount of water in the wall by monitoring the change in the weight of the reservoir supplying water to the wall.

3.2. Geoelectrical measurements

At the start of the experiment, the wall is in a dry state (gravimetric water content is measured to be w = 2.4%, thanks to TDRs, cf. Figure 4). As the TDR probes records water content at the middle of a layer height (the density is supposed to have a mean value there), and as the wall has dried for sufficient time to be pseudo-dried (in comparison with the wet compacting state), it can be supposed that this value is representative of the global water content of the whole wall. In order to monitor the water content using time-domain induced polarization, 64 self-adhesive Ag/AgCl electrodes were placed along a vertical profile in the middle of the wall and along the two sides of the wall (see Figures 4 and 5). Two supports were used to keep the electrodes in good contact with the wall during the duration of the experiment. The distance between the electrodes is 4.5 cm. An ABEM Terrameter SAS-4000 is used for resistivity and time domain induced polarization data acquisition. Electrodes are installed on the wall and the first time domain induced polarization measurements are performed on July 2nd, 2022. Wenner array was used for electrical measurements with voltage electrodes in between the current electrodes to insure a good signal-to-noise ratio.

The experiment started on July 2nd, 2022 (Figure 1). Water is added to the sand tank at the bottom of the wall on 07 July 2022. Between July, 7th, 2022 to July, 14th, both apparent resistivity and chargeability measurements were measured but affected by high contact resistances. These data were not used further below. On July 14TH, we add a conductive gel (Transound, https://www.sonodis.fr/p24510036/gel-pour-ecg-et-eeg-transound) to improve the electrical contacts between the electrodes and the wall. In the array, the current electrode is used as the potential electrode after a long time (more than 5 minutes) from the current injection. This was done to reduce possible electrode charge buildups (and therefore electrode polarization) effects. 10 windows with a constant duration (100 ms) were used for the induced polarization measurements after the shutdown of the primary current.

3.3. Resistivity and chargeability tomograms

We first use the resistivity/conductivity inversion algorithm and code developed by Soueid Ahmed et al. (2018) and Qi et al. (2018). The injected current in a heterogeneous isotropic medium produces an electrical potential field that is described by Poisson's equation as:

$$-\nabla.(\sigma_\infty \nabla\psi) = I\delta(x - x_0)\delta(y - y_0)\delta(z - z_0) \quad (6)$$

with considering the normal component of the electrical field vanishes at the ground surface using Neumann boundary condition equal zero at the Earth's surface:

$$\frac{\partial\psi}{\partial\mathbf{n}} = 0 \quad (7)$$

and the Dirichlet type of boundary condition (the potential is taken equal to zero at the other boundaries placed far away from the domain of interest to infinity) and where σ_∞ denotes the instantaneous electrical conductivity; ψ the electrical potential; I the amplitude of current source points located at the coordinates x_0, y_0, and z_0; δ is the Dirac function and **n** is the unit normal vector to the ground surface.

The objective function for resistivity inversion can be represented with the Lagrange multiplier λ as follows:

$$\mathbf{E}(\mathbf{m}) = ||\boldsymbol{W}_d(\mathbf{d}(\mathbf{m}) - \mathbf{d}_{obs})||^2 + \lambda||\boldsymbol{W}_m\mathbf{m}||^2 \quad (8)$$

where $\boldsymbol{m}$ is the model vector corresponding to the logarithm of the conductivity of each cell, **d**(**m**) denotes the predicted data for a model vector **m**, $\mathbf{d}_{obs}$ denotes the observed apparent resistivity data, $\mathbf{W}_d$ is a weighting matrix

for data fitting, $\mathbf{W}_m$ is the roughness matrix and $\mathbf{d}(*)$ denotes the forward modeling operator based on the finite element method used to solve the electrical conductivity problem (Poisson equation with boundary conditions). In this study, the matrix $\mathbf{W}_d$ is generated from the measured standard deviations of observed data and the matrix $\mathbf{W}_m$ is the first-order gradient matrix. The quantity λ is the smoothness constraint, which helps model parameters update robustly in the iterative inversion process.

The model vector perturbation can be calculated by taking the derivative of the objective function via the Gauss-Newton method during a iterative process results in:

$$\delta\mathbf{m} = [\mathbf{J}^T(\mathbf{W}_d^T\boldsymbol{W}_d)\mathbf{J} + \lambda\mathbf{W}_m^T\boldsymbol{W}_m]^{-1}[\mathbf{J}^T(\mathbf{W}_d^T\boldsymbol{W}_d)(\boldsymbol{d}_{obs} - \mathbf{d}(\mathbf{m}_k) - \lambda\mathbf{W}_m^T\boldsymbol{W}_m\mathbf{m}_k] \quad (9)$$

where **J** is the Jacobian matrix which is calculated by the adjoint method (Soueid Ahmed et al., 2018) and *k* is the iteration number.

To define the calculated apparent chargeability, we run the forward problem for conductivity twice, one time considering the space conductivity σ_∞ and the other time using σ_0 as the space conductivity. The apparent chargeability is obtained from potentials $\Psi\sigma_0$ and $\Psi\sigma_\infty$; calculated from the forward model at the measured points. The apparent chargeability M_a is defined as

$$M_a = \frac{\psi_{\sigma_\infty} - \psi_{\sigma_0}}{\psi_{\sigma_\infty}}. \quad (10)$$

During the inversion, M_a is treated as the measured chargeability. The inversion process for the chargeability principally is the same as for the conductivity. The chargeability sensitivity matrix can be defined from modification of the conductivity sensitivity matrix that we have already computed during the conductivity inversion

$$\frac{\partial \mathrm{d}_i}{\partial \log \mathrm{M}_j} = \frac{-\mathrm{M}_j}{1-\mathrm{M}_j} \cdot \frac{\psi_{\sigma|_i}}{(\psi_{M|_i})^2} \cdot \frac{\psi_{M|_i}}{\partial \log \sigma_j}, \quad (11)$$

where $\partial d_i/\partial \log M_j$ denotes the chargeability sensitivity matrix and $\partial\Psi_{M|i}/\partial\log\sigma_j$ is the conductivity sensitivity matrix associated with $\sigma_0 = \sigma_\infty(1\text{-}M)$. $i=1,2,\ldots,N$ and $j=1,2,\ldots,M$ where N and M are the number of measured data and the number of model parameters used to discretize the wall, respectively. Usually, we have $N << M$ and therefore the problem is underdetermined. In this study, the vector parameter **m** considers the logarithm of the conductivity and the logarithm of chargeability as unknowns.

4. Results

Figure 2 shows the evolution of the moisture level in the wall (height of the capillary head) over time. The moisture level was observed to rapidly increase from 0 cm to 25cm in 2 days, then it stabilized during two weeks at a height between 40 cm to 42 cm. The evolution of moisture rise was directly followed by a camera. Figure 3 shows the evolution of the relative humidity (RH) in the wall and the ambient conditions. It was observed that the ambient RH was varying between 40% to 50% and remained relatively constant during the capillary rise. A high rate of capillary rise was observed on the first day, the RH of the sensors (S1 and S2) that were placed on the first and third layers increased from a RH value of 60% to 100%. We can also observe that the capillary front is more and more diffuse as long as the point is high: for S1, it takes less than one day to pass from an ambient RH to a saturated one, for S2 it takes 3 approximately days, and for S4 it takes 8 days. It is probably the manifestation of 2 phenomena: water rise velocity variation (according to the pore size), and increasing proportion of pore water that find an equilibrium between capillary/gravity forces along the height. After a week of capillary rise, the RH value of sensor S3, placed at a height of 36.5 cm from the base of the wall, increased from 60% to 100%, showing that the capillary head reached this point. Between two to three weeks when the moisture level seems to stabilize (see Figure 2), the RH recorded by sensors S4 gradually increased from 60% to 100%, which was installed at 51,5 from the base of the wall and at a depth of 10 cm within the earth. However, it doesn't seem totally consistent with the evolution of the capillary head on the earth surface, measured at 42 cm with the camera. This suggests that the moisture level in the middle of the wall was possibly higher than that on the surface. The rest of the sensors (S5 to S10) recorded an RH value fluctuating around the ambient conditions since they stay above the capillary zone.

The TDR placed at the middle high of the wall was used to monitor the local water content. Figure 4 shows the evolution of gravimetric water content during the capillary rise. A water content of around 2.4% was recorded during the entire experiment. Unfortunately the TDR was too high to be affected by the capillary rise and no significant change of water content was observed.

Each tomogram (at a given day) was based on 472 measurements for the electrical conductivity and chargeability for a single survey (i.e., at a given date). Because the primary injection time is short (1s), only the clay fraction of the rammed earth has the time to be fully polarized. The partial chargeability of the first window is used as induced polarization data in the 3D inversion algorithm described in the previous section. Figure 5 shows the electrodes and 3D finite element meshing used in the inversion process. Note that the mesh is refined around the electrodes to increase the accuracy of the forward computations for the electrical potential distribution. The relevant meshing is obtained by trial and error until the potential distribution is mesh independent. A total of 23,846 tetrahedral elements were used to numerically model the electrical properties of the wall.

Figures 6 to 8 show the results in terms of tomography. Figure 7 show that the secondary voltage data recorded after shutting down the primary current are good since they display exponential decays like expected for a discharging behavior in an RC circuit. Once the tomogram of the electrical conductivity and normalized chargeability are obtained (Figure 8), tomograms of the water content is obtained using equations (4) and (5) written as (assuming $m = n$)

$$\sigma_\infty = \theta^m \sigma_w + \theta^{m-1} \rho_g B \mathrm{CEC}\,, \tag{12}$$

$$M_n = \theta^{m-1} \rho_g \lambda \mathrm{CEC}\,. \tag{13}$$

In equations (12) and (13), and for each of the 23,846 tetrahedral elements, we can determined the CEC and the water content from the conductivity and the normalized chargeability using $m = 2$, σ_w = 595 μS cm^{-1} (~0.06 S m^{-1}, measured in the sand), ρ_g = 2700 kg m^{-3}, B(Na$^+$, 25°C) = 3.1±0.3×10^{-9} m^{2}s^{-1}V^{-1}, and λ(Na$^+$, 25°C) = 3.0±0.7×10^{-10} m^{2}s^{-1}V^{-1}.

Figures 6 and 8 displays the water content distribution over time in the portion of the wall comprised between the electrodes. The position of the infiltration front observed from the tomograms is in agreement with those determined by visual inspection using the camera.

We performed, using equations (12) and (13), a tomography of the CEC using the inverted conductivity and normalized chargeability data performed on the first day of the experience (i.e., on July 2nd, 2022). The mean value of the CEC for the CEC-tomogram is 2.3 meq/100 g (the CEC results are comprised between 1 and 7 meq/100 g). The inverted values are quite consistent with the values determined on the core samples using the cobalt hexamine method (3 meq/100 g).

Another way to check the validity of the result is to look at the importance of surface conductivity with respect to the bulk conductivity. From the results of the tomography, we check that the ratio $M_n = 0.05\ \sigma < R\ \sigma_S$ (Figure 10) where R has been previously defined. This point out that surface conductivity is close to be dominant in the conductivity response. This is confirmed by experimental data of the conductivity of the rammed earth performed with core samples at different salinities. The results are shown in Figure 11. At the conductivity of the tap water σ_w = 0.06 S m^{-1}, the conductivity of the rammed earth is dominated by the surface conductivity. It follows that the second Archie's law could be used as a simple conductivity equation to image saturation as done in many publications.

5. Conclusions

We have performed a capillary rise experiment on an earthen wall made of 20 compacted layers of rammed earth. The experiment is monitored using a network of 64 non-polarizing electrodes used to perform a time-lapse induced polarization tomography of the electrical conductivity and the normalized chargeability over a cross-section of the wall. The petrophysical model developed and tested in the first two papers of this series is used to image the change in the water content. The position of the capillary fringe is favorably compared to the position of the water level monitored with a camera. This study demonstrates the ability of the induced polarization method to monitor the variation of water content caused by the capillary rise in rammed earth-made structures in a quantitative way. This application of resistive methods, miniaturized from the geophysical scale to the building one, has thus a strong potential for building earth sector. Indeed it could bring a strong help for expert opinions in case of damage claims, or for insurance controlling in case of new construction, which are both key processes of building life.

Acknowledgement. This work is part of the ANR project VBATCH “Raw earth construction vulnerability regarding hydric conditions” funded by Agence National de la Recherche in France. We thank Egon Zimmerman for the construction of the ZEL-SIP04-V02 impedance meter used in this work and Pierre Vaudelet (Naga Geophysics) for its support. The grant to Tengfei Fu is funded by the National Natural Science Foundation of China (U1806212, 42276226). Kai Zhang and Tengfei Fu thank funding from China Scholarship Council.

References

Abdulsamad, F., Revil A., Prime N., Chitimbo T., Plé O., 2022. Imaging the water content of rammed earth materials with induced polarization. submitted to Engineering Geology.

Abdulsamad, F., Revil, A., Prime, N., Gnonnoue, P.Y., Schmutz, M., Plé, O., 2020. Complex conductivity of rammed earth, Engineering Geology 273, 105697. https://doi.org/10.1016/j.enggeo.2020.105697.

Archie, G. E., 1942. The electrical resistivity log as an aid in determining some reservoir characteristics: Petroleum Transactions of AIME, 146, 54-62.

Börner, F.D., Gruhne, M., Schön, J. H., 1993. Contamination indications derived from electrical properties in the low frequency range. Geophysical Prospecting, 41, 83–98.

Champiré, F., Fabbri A., Morel J. C., Wong H., McGregor F., 2016. Impact of relative humidity on the mechanical behavior of compacted earth as a building material. Constr. Build. Material 110, 70–78. https://doi.org/10.1016/j.conbuildmat.2016.01.027.

Chauhan. P., El Hajjar A., Prime N,. Plé O., 2019, Unsaturated behavior of rammed earth: Experimentation towards numerical modelling. Construction and Building Materials, 227, 116646. https://doi.org/10.1016/j.conbuildmat.2019.08.027.

Chitimbo, T., Abdulsamad, F., Prime, N., Revil, A., Plé, O., 2023. Impact of moisture content on the elasto-viscoplastic behaviour of rammed earth wall: new findings. Construction Materials 4, 1–14. https://doi.org/10.3390/constrmater3010001.

Easton, D. Easton T., 2012. 14 - Modern rammed earth construction techniques. Modern Earth Buildings, Materials, Engineering, Constructions and Applications, Woodhead Publishing Series in Energy, 364-384. https://doi.org/10.1533/9780857096166.3.364.

Hao, N., Moysey S.M.J., Powell B. A., Ntarlagiannis D., 2016. Comparison of the surface ion density of silica gel evaluated via spectral induced polarization versus acid–base titration. Journal of Applied Geophysics 135, 427-435. https://doi.org/10.1016/j.jappgeo.2016.01.014.

Johnson, T. C., Versteeg, R. J., Ward, A., Day-Lewis, F. D., Revil, A., 2010. Improved hydrogeophysical characterization and monitoring through parallel modeling and inversion of time-domain resistivity and induced-polarization data. Geophysics, 75, WA27–WA41.

Jaquin, P. A., Augarde, C., Gerrard, C. M., 2008. A chronological description of the spatial development of rammed earth techniques. International journal of architectural heritage: conservation, analysis, and restoration., 2 (4). 377-400. http://dx.doi.org/10.1080/15583050801958826.

Kemna, A., Binley A.,, Cassiani G.,, Niederleithinger E.,, Revil A.,, Slater L.,, Williams K.H.,, Flores Orozco A.,, Haegel F.-H.,, Hördt A.,, Kruschwitz S.,, Leroux V.,, Titov K., and Zimmermann E., 2012. An overview of the spectral induced polarization method for near-surface applications, Near Surface Geophysics, 10, 453-468. https://doi.org/10.3997/1873-0604.2012027.

Kebao, R., Kagi, D., 2012. 10 - Integral admixtures and surface treatments for modern earth buildings. Modern Earth Buildings, Materials, Engineering, Constructions and Applications, Woodhead Publishing Series in Energy 256-281. https://doi.org/10.1533/9780857096166.2.256.

Morel J., Mesbah A., Oggero, M., Walker P., 2001. Building houses with local materials: means to drastically reduce the environmental impact of construction, Build. Environ. 36 (10), 1119–1126, https://doi.org/10.1016/s0360-1323(00) 00054-8.

Niu Q., Revil A., Saidian M., 2016. Salinity dependence of the complex surface conductivity of the Portland sandstone. Geophysics 81 (2), D125-D140. https://doi.org/10.1190/GEO2015-0426.1.

Nordsiek, S., Diamantopoulos E.,, Hördt A., Durner W., 2015. Relationships between soil hydraulic parameters and induced polarization spectra, Near Surface Geophysics, 14, 23-37. https://doi.org/10.3997/1873-0604.2015048.

Schwartz, N., Furman A., 2012. Spectral induced polarization signature of soil contaminated by organic pollutant: Experiment and modeling, J. Geophys. Res., 117. https://doi.org/10.1029/2012JB009543.

Revil, A., 2013a. On charge accumulation in heterogeneous porous rocks under the influence of an external electric field. Geophysics 78 (4), D271–291. https://doi.org/10.1190/geo2012-0503.1.

Revil, A., 2013b. Effective conductivity and permittivity of unsaturated porous materials in the frequency range 1mHz-1GHz. Water Resour. Res. 49, 306-327. https://doi.org/10.1029/2012WR012700.

Revil A., Coperey A., Shao Z., Florsch F., Fabricius L. I., Y. Deng, Delsman J. R., 2017. Complex conductivity of soils. Water Resources Research 53 (8), 7121–47. https://doi.org/10.1002/2017WR020655.

Revil A., Gresse M., 2021. Induced polarization as a tool to assess alteration in volcanic areas: a review. Minerals 11 (9), 962. https://doi.org/10.3390/min11090962.

Schlumberger, C., 1920. Etude sur la prospection électrique du sous-sol, Gauthier-Villars, Paris. The second edition without modification is available at https://gallica.bnf.fr/ark:/12148/bpt6k64569898.texteImage. English version, translated by Sherwin F. Kelly: "Study of underground electrical prospection". Available at: https://archive.org/details/studyofundergrou00schlrich/page/n37.

Soebarto, V., 2009. Analysis of indoor performance of houses using rammed earth walls, Eleventh International IBPSA Conference, 1530-1537.

Souza, C.F., Matsura, E.E., 2003. Multi-wire time domain reflectometry (TDR) probe with electrical impedance discontinuities for measuring water content distribution. Agricultural water management 59(3), 205-216.

Topp, G.C. and Davis, J.L., 1985. Measurement of soil water content using time-domain reflectrometry (TDR): A field evaluation. Soil Science Society of America Journal 49(1),.19-24.

Taylor, P., Luther, M. B., 2004. Evaluating rammed earth walls: A case study. Solar Energy 76, 79-84.

Titov, K., Komarov, V. Tarasov, V., Levitski, A., 2002. Theoretical and experimental study of time domain-induced polarization in water-saturated sands. Journal of Applied Geophysics 50, 417-433.

Vinegar, H., Waxman M., 1984. Induced polarization of shaly sands. Geophysics 49 (8), 1267–87. https://doi.org/10.1190/1.1441755.

Waxman, M. H., Smits L. J. M., 1968. Electrical conductivities in oil-bearing shaly sands. Society of Petroleum Engineers Journal 8 (2), 107-122. https://doi.org/10.2118/1863-A.

Figures

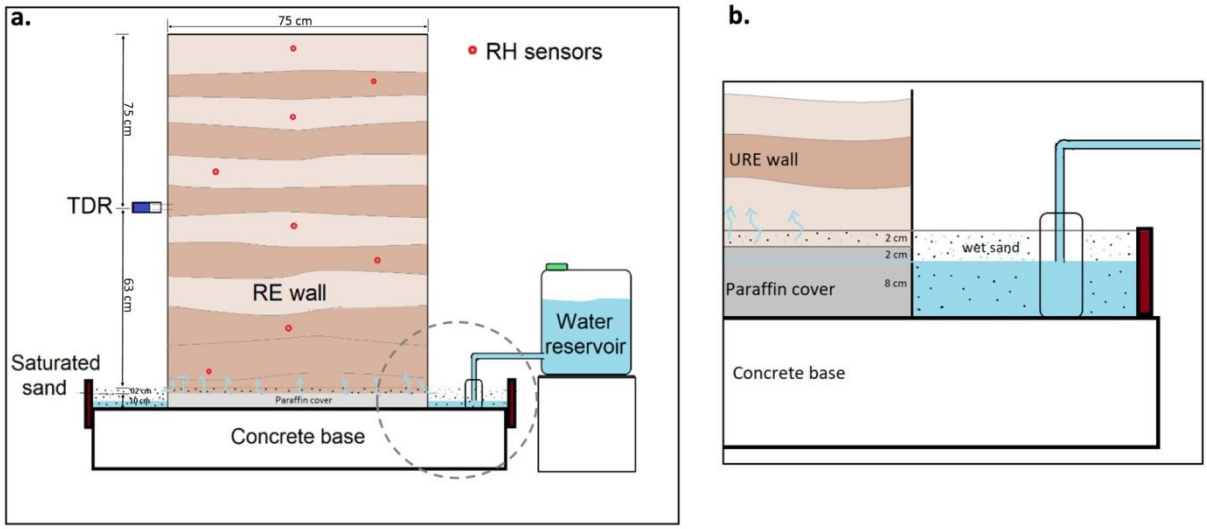

Figure 1. Capillary rise experiment. **a.** Sketch of the experimental setup. The wall is made of 20 layers of compacted rammed earth material. **b.** Zoom of the setup showing different levels for the water infiltration at the basis of the wall. TDR denotes a Time-Domain Reflectometry probe used to get an independent estimate of the water content. Saturation is imposed at the basis of the rammed earth wall.

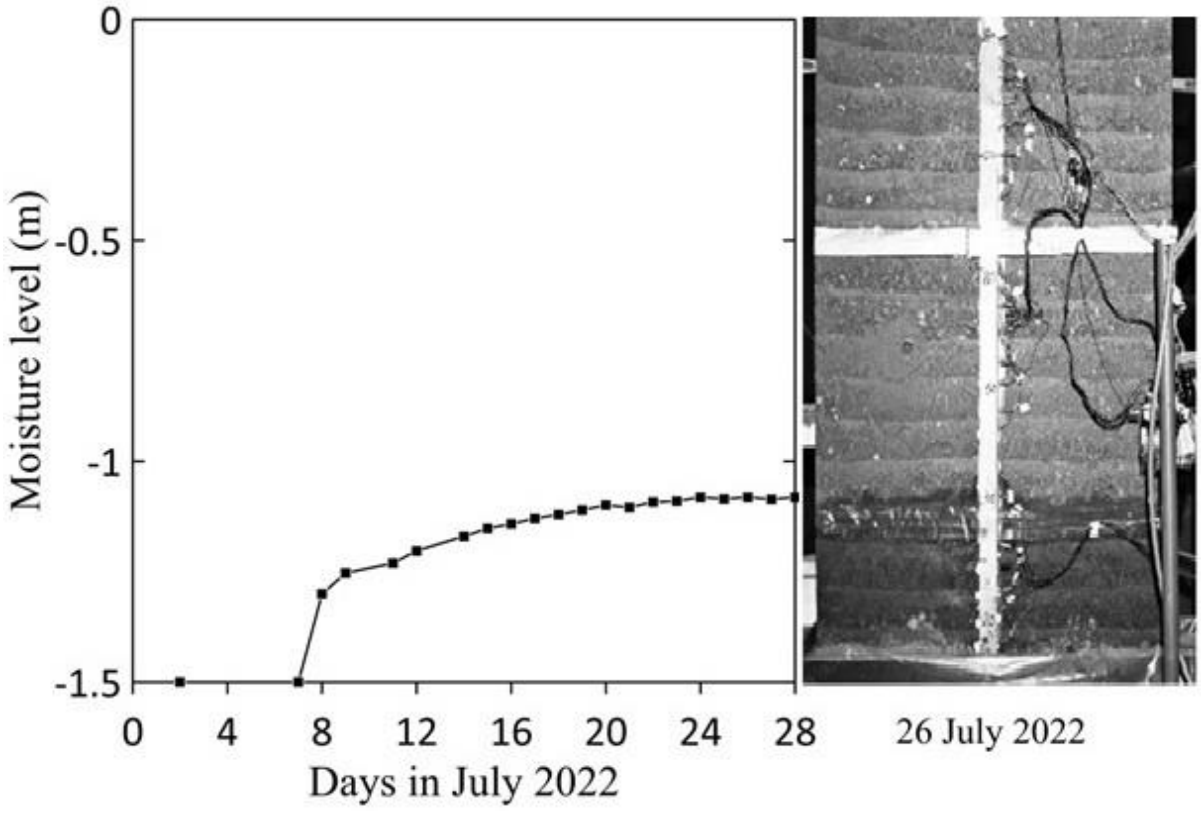

Figure 2. Evolution of moisture level in July 2022. The moisture changes are recorded using a fixed camera that takes photos during time. The change in the grey scale of the pictures is used to monitor the evolution of the water level in the wall over time. The picture shows that the layers of rammed earth material.

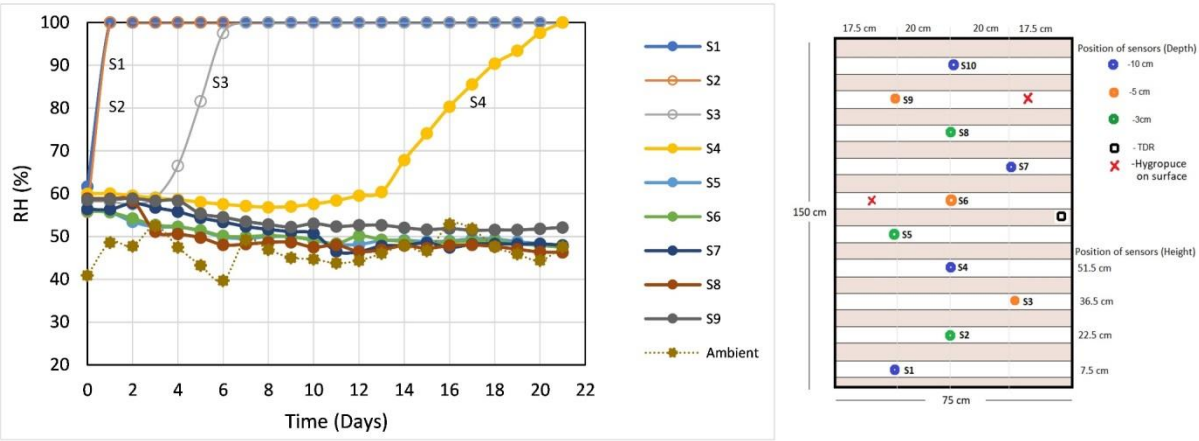

Figure 3. Evolution of Relative Humidity (RH) in the wall along with the ambient condition. The right panel displays the layout of the RH-sensors and the position of the layers is also indicated.

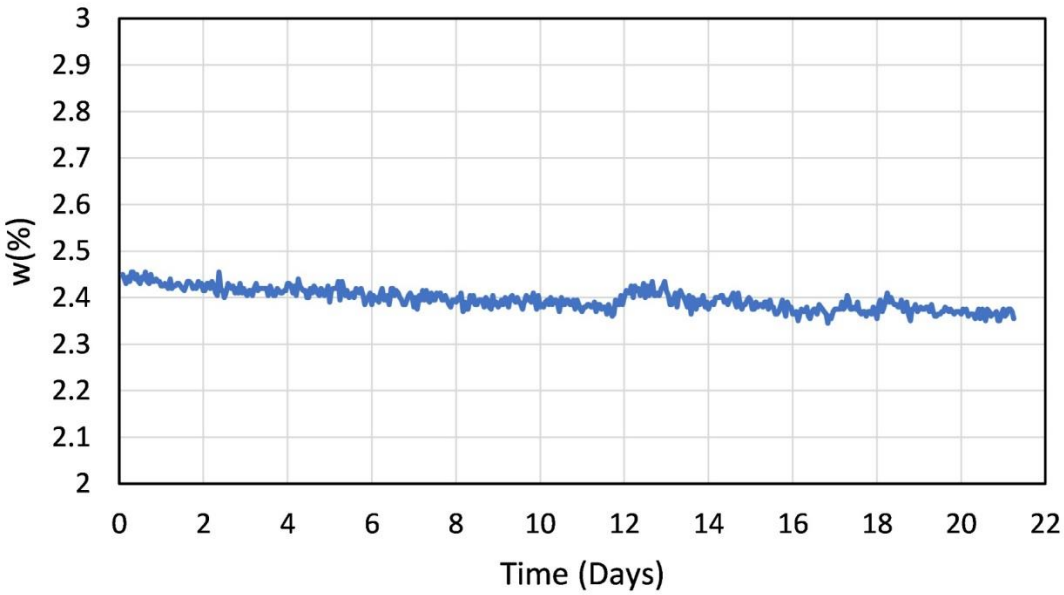

Figure 4. Evolution of local water content (in weight, *w*, weight fraction in %) at the middle of the wall. The experiment was done in July 2022, a period that was both dry and hot. We note therefore a slow drying of the wall above the capillary fringe.

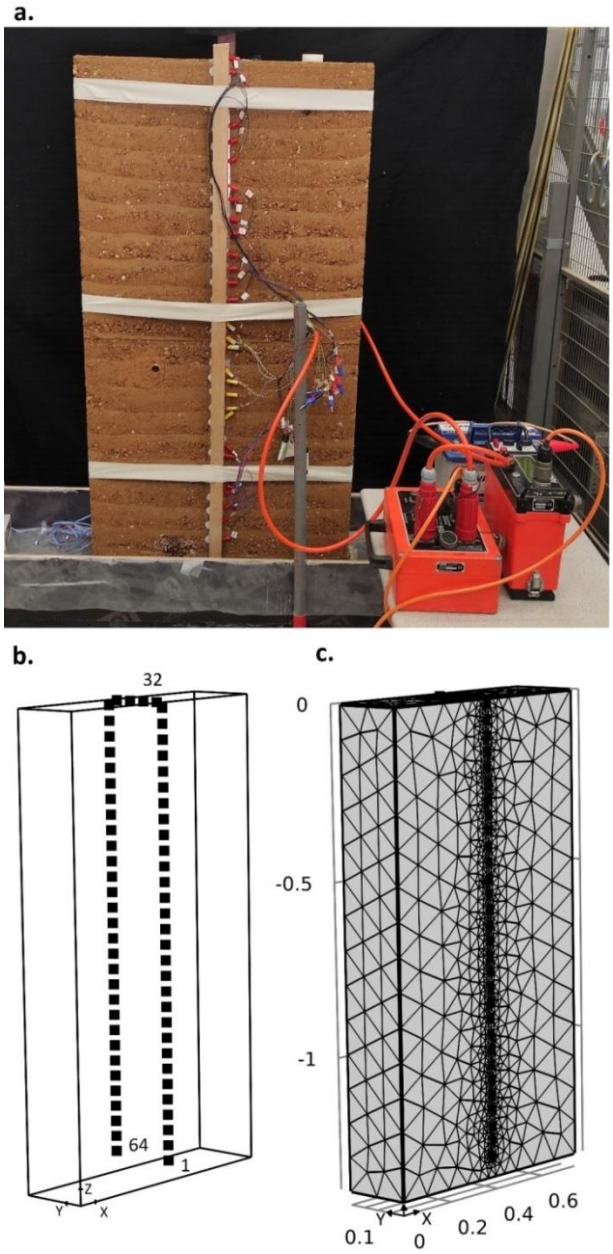

Figure 5. Sketch of the geometry of the electrode network. **a**. Rammed wall (width 0.75 m, high 1.5 m and thickness 0.2 m). Lying at the bottom of the wall, there is a plastic tank filled with sands. Sand is saturated during experiment. 64 self-adhesive Ag/AgCl electrodes are placed on one line at the middle of wall. The wall is shown here in its dry state, before adding water to the sand on July 2nd, 2022. Two supports were used to keep the electrodes in contact to the wall during all days of experiment. **b**. The black dots denote the locations of the electrodes. The distance between the electrodes is 4.5 cm. An ABEM Terrameter SAS-4000 is used to perform both the resistivity and time domain induced polarization data measurements. The tomograms are presented in the YZ section along the plane drawn by the position of the electrodes. **c**. Finite elements mesh used for the simulation domain. The mesh is refined around the position of the electrodes to increase the accuracy of the computations in the forward modeling. A total of 23,846 tetrahedral elements are used for the numerical simulations.

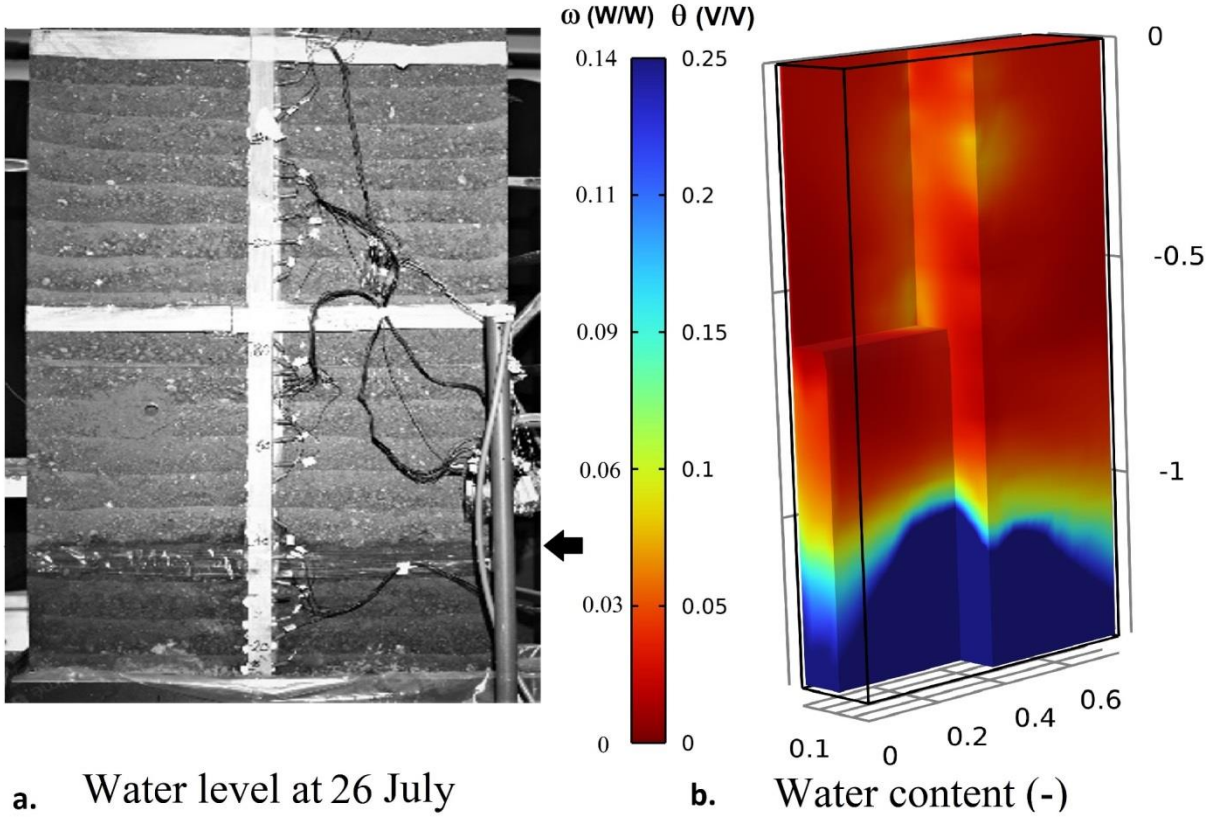

Figure 6. Tomogram of the water content associated with the capillary rise. **a**. Water level and capillary effect on rammed wall after 18 days' water feed from its bottom part using saturated sand tank. Water level is also mentioned by black arrow. The position of the infiltration front can be visually inspected and measured. **b**. Water content (by volume and weight) obtains from 3D inversion of the time domain induced polarization data (conductivity and normalized chargeability). Note that the sensitivity of the tomogram is good only in the plane characterized by the position of the electrodes.

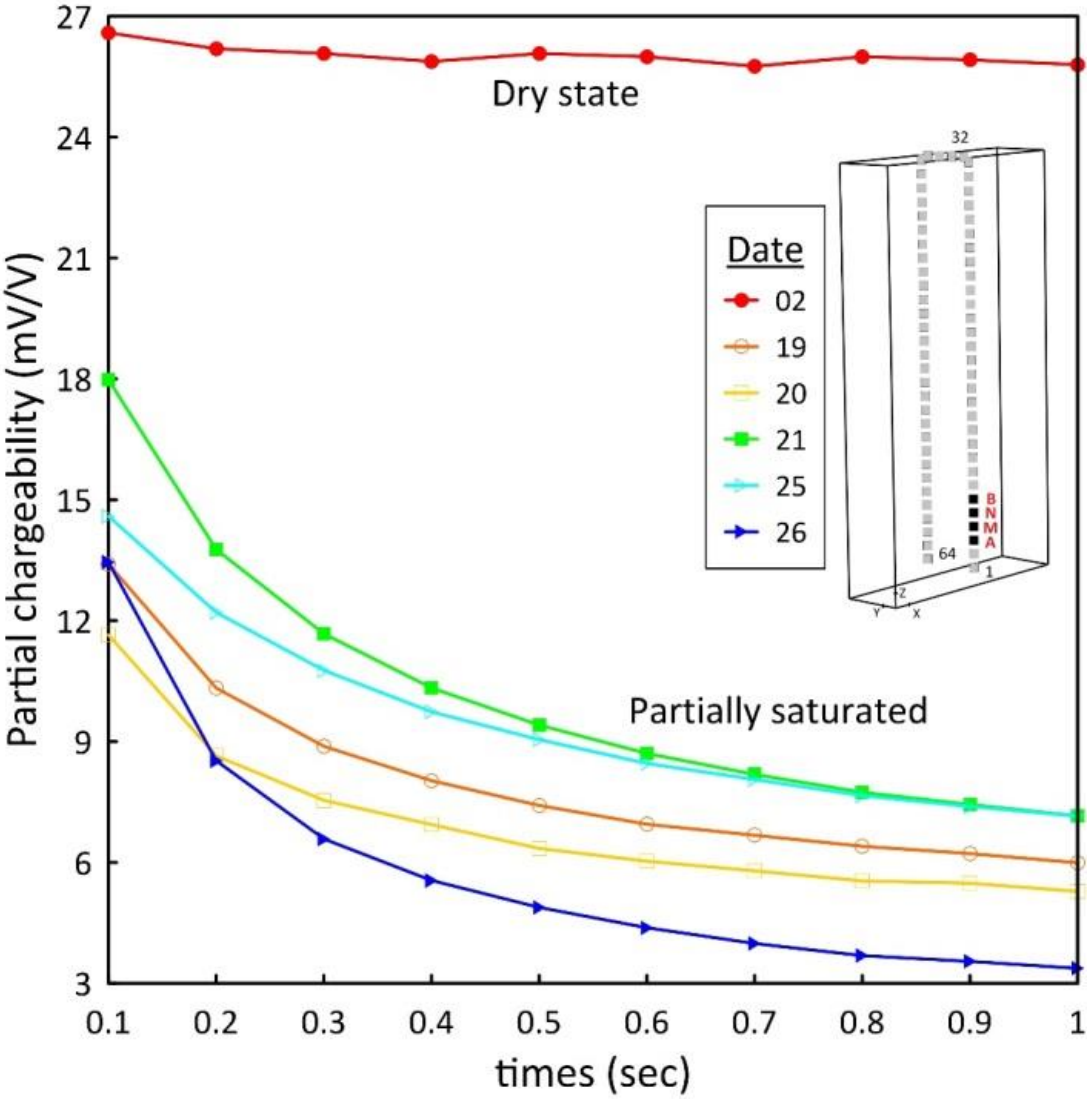

Figure 7. Partial chargeability decay curves during capillarity evolution. Partial chargeability curves are measured near the bottom of rammed wall that is affected by the change of the water content (Wenner array AMNB with equal distance between the electrodes, A and B are the current electrodes and M and N are the voltage electrodes). Except for July 2nd, 2022, for the other dates, this portion of the wall is humid. The dates correspond to the days in July 2022.

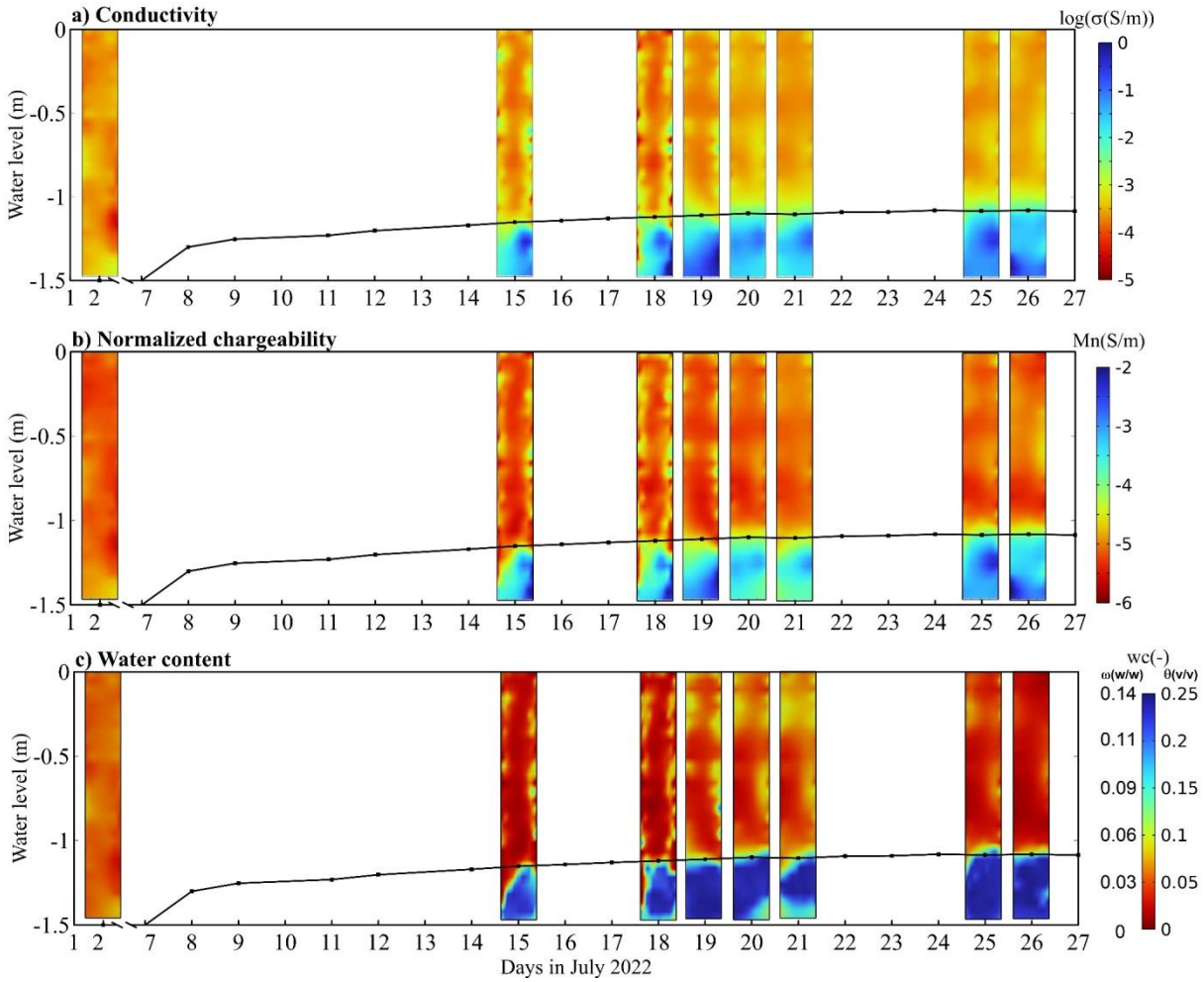

Figure 8. 3D tomograms along the cross-section in the plane of the electrodes in the rammed earth wall. The water level is measured and the curve (black line) is deducted from this measurements and direct observation. The results of the inversion are shown for the YZ section in the electrodes plan. **a**. Electrical conductivity tomography. **b.** Normalized chargeability tomography obtains from resistivity and chargeability data. **c**. Water content wc θ (vol. fraction) and w (weight fraction) tomograms obtain from petrophysical model using conductivity and normalized chargeability data (see Section 2).

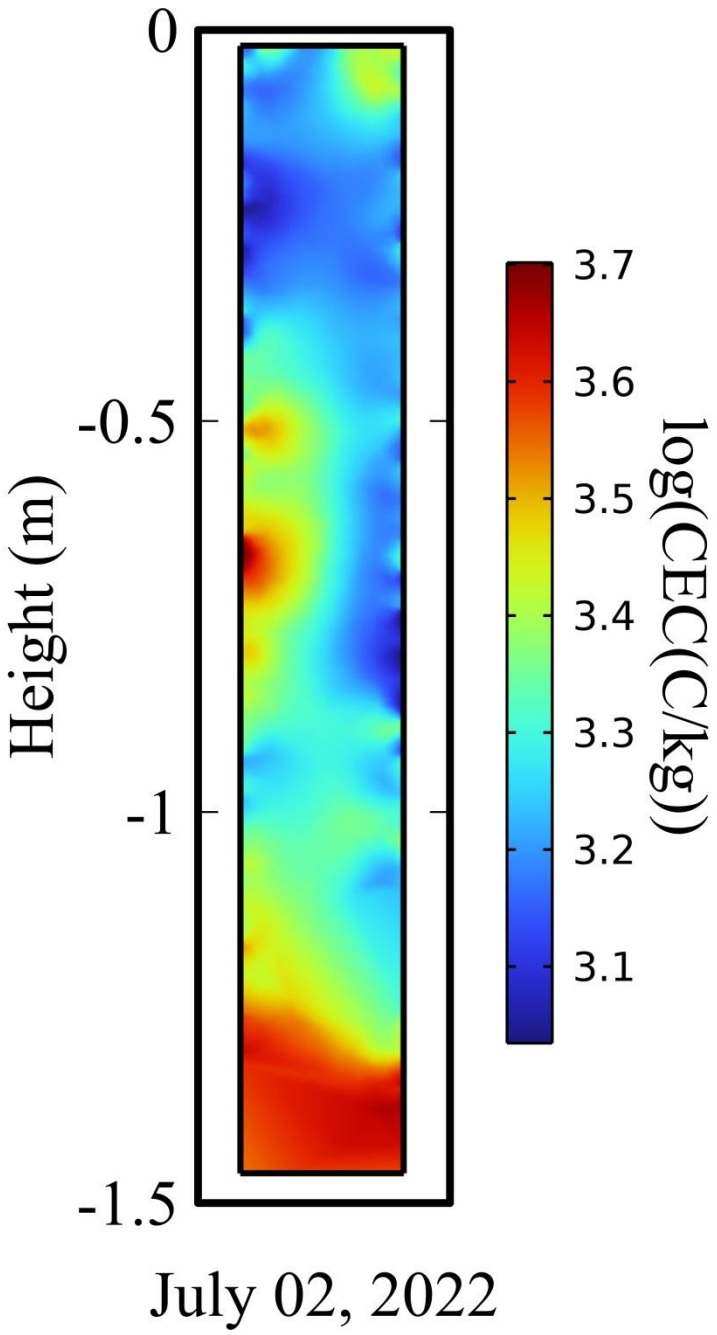

Figure 9. Tomography of the Cation Exchange Capacity performed on July 2nd, 2022, the first day of the experience. It is assumed that CEC is constant independent on saturation. The mean value of the CEC is around 2.3 meq/100g.

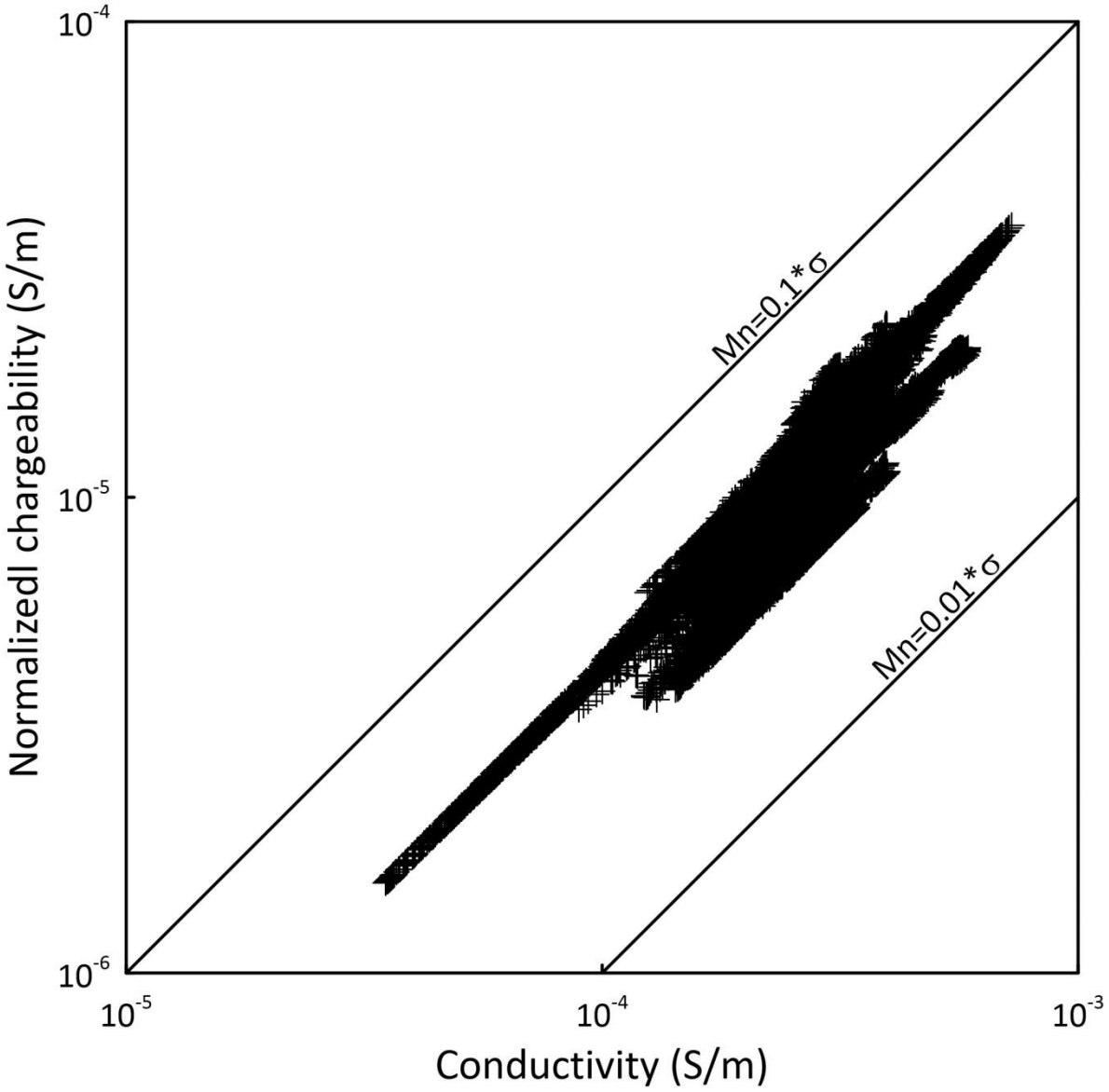

Figure 10. Normalized chargeability versus electrical conductivity. The position of the swarm of data points demonstrates that the surface conductivity represents 5 to 20% of the overall conductivity. Surface conductivity dominates when $M_n = R\,\sigma$ with $R = 0.09$.

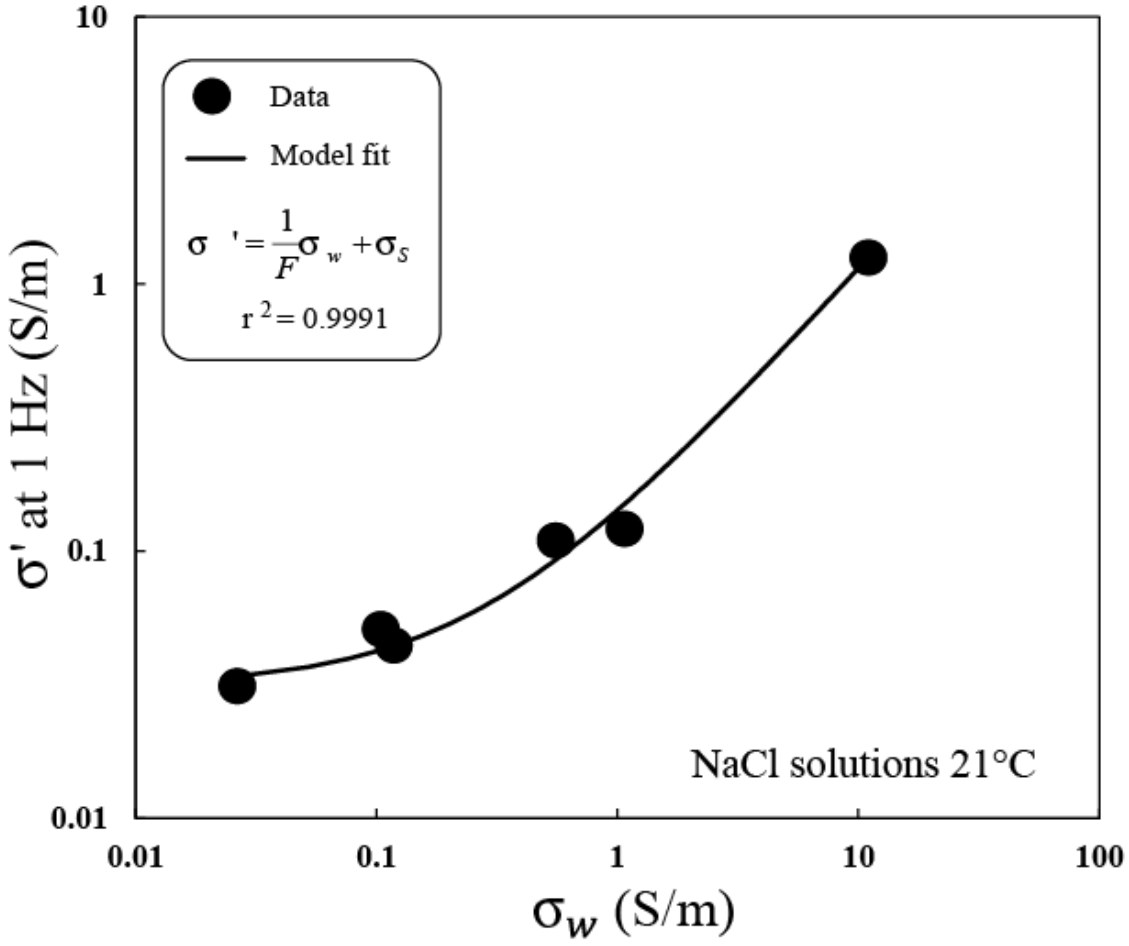

Figure 11. Electrical conductivity (1 Hertz) versus pore water conductivity σ_w. The measurements are obtained at saturation. The fit with a linear conductivity model (equation 2) yields the value of the formation factor F = 9.10 (at a porosity of 0.26) and the surface conductivity σ_S = 0.031 S m^{-1}. We see that at low salinities, the conductivity of the material is quickly dominated by its surface conductivity, which is in turn controlled by its cation exchange capacity.